NASA TECHNICAL MEMORANDUM

NASA TM X-3313

NASA TM X-3313

CASE FILE COPY

EFFECTS OF NOZZLE EXIT LOCATION AND SHAPE ON PROPULSION-INDUCED AERODYNAMIC CHARACTERISTICS DUE TO VECTORING TWIN NOZZLES AT MACH NUMBERS FROM 0.40 TO 1.2

Francis J. Capone

Langley Research Center
Hampton, Va. 23665

NATIONAL AERONAUTICS AND SPACE ADMINISTRATION • WASHINGTON, D. C. • JANUARY 1976

1. Report No.	2. Government Accession No.	3. Recipient's Catalog No.
NASA TM X-3313		

4. Title and Subtitle	5. Report Date
EFFECTS OF NOZZLE EXIT LOCATION AND SHAPE ON PROPULSION-INDUCED AERODYNAMIC CHARACTERISTICS DUE TO VECTORING TWIN NOZZLES AT MACH NUMBERS FROM 0.40 TO 1.2	January 1976
	6. Performing Organization Code
7. Author(s) Francis J. Capone	8. Performing Organization Report No. L-10493
9. Performing Organization Name and Address NASA Langley Research Center Hampton, Va. 23665	10. Work Unit No. 505-04-11-01
	11. Contract or Grant No.
12. Sponsoring Agency Name and Address National Aeronautics and Space Administration Washington, D.C. 20546	13. Type of Report and Period Covered Technical Memorandum
	14. Sponsoring Agency Code

15. Supplementary Notes

16. Abstract

An investigation has been conducted in the Langley 16-foot transonic tunnel to determine the induced lift characteristics of a vectored-thrust concept in which jet-exhaust nozzles were located in the fuselage at or near the wing trailing edge. The effects of moving twin rectangular nozzles rearward from the wing trailing edge and of round nozzles at the trailing edge only were studied at Mach numbers from 0.4 to 1.2, angles of attack up to 14°, and thrust coefficients up to 0.35. Nozzle deflection angle varied from 0° to 45°. Separate force balances were used to determine both total aerodynamic and thrust forces and thrust forces alone which allowed for a direct measurement of jet turning angle at forward speeds. The Reynolds number per meter varied from 8.20×10^{6} to 13.12×10^{6}.

17. Key Words (Suggested by Author(s))	18. Distribution Statement
Vectored thrust Induced lift Rectangular nozzle Round nozzle	Unclassified – Unlimited Subject Category 02

19. Security Classif. (of this report)	20. Security Classif. (of this page)	21. No. of Pages	22. Price*
Unclassified	Unclassified	205	$7.25

*For sale by the National Technical Information Service, Springfield, Virginia 22161

EFFECTS OF NOZZLE EXIT LOCATION AND SHAPE ON PROPULSION-INDUCED AERODYNAMIC CHARACTERISTICS DUE TO VECTORING TWIN NOZZLES AT MACH NUMBERS FROM 0.40 TO 1.2

Francis J. Capone
Langley Research Center

SUMMARY

An investigation has been conducted in the Langley 16-foot transonic tunnel to determine the induced lift characteristics of a vectored-thrust concept in which jet-exhaust nozzles were located in the fuselage at or near the wing trailing edge. The effects of moving twin rectangular nozzles rearward from the wing trailing edge and of round nozzles at the trailing edge only were studied at Mach numbers from 0.4 to 1.2, angles of attack up to 14°, and thrust coefficients up to 0.35. Nozzle deflection angle varied from 0° to 45°. Separate force balances were used to determine both total aerodynamic and thrust forces and thrust forces alone which allowed for a direct measurement of jet turning angle at forward speeds. The Reynolds number per meter varied from 8.20×10^{6} to 13.12×10^{6}.

The results show that moving the rectangular exits rearward from the wing trailing edge reduced jet-induced supercirculation lift but did not appreciably affect drag. The model with the round exits generated more induced lift at a Mach number of 0.7 than the model with the rectangular exits but had higher drag.

INTRODUCTION

A number of studies have indicated that thrust-induced supercirculation effects from thrust vectoring have a potential for not only increasing maneuverability of fighter aircraft but also improving cruise performance (refs. 1 to 5). These studies used a vectorable partial-span rectangular jet-exhaust nozzle located at the wing trailing edge to induce lift due to supercirculation similar to a jet flap. The configuration of references 1 and 2 had a highly swept wing, whereas that of references 3 and 4 used a wing more representative of current fighter aircraft. Reference 3 summarized a parametric investigation that included studying the effects on induced lift and drag of nozzle deflection angle, nozzle

exit location, nozzle shape (rectangular or round), and wing camber. Reference 4 presented detailed information concerning the effects of varying nozzle deflection angle with the rectangular nozzles located at the wing trailing edge.

This report presents results from those portions of the investigation concerning nozzle exit location, where the exit is moved aft from the wing trailing edge, and the induced lift characteristics of the model with round nozzle exits.

The investigation was conducted in the Langley 16-foot transonic tunnel at Mach numbers from 0.4 to 1.2, angles of attack up to 14°, and thrust coefficients up to 0.35. The test Reynolds number per meter varied from 8.20×10^6 to 13.12×10^6.

SYMBOLS

Model forces and moments are referred to the axis system shown in figure 1 with the model moment reference center located at $0.25\bar{c}$, which corresponds to FS 117.64 cm. A discussion of the data reduction procedure and definitions of the aerodynamic force and moment terms used herein are given in the appendix. All aerodynamic coefficients are based on $q_{\infty}S$ or $q_{\infty}S\bar{c}$ except at static conditions where p_a is substituted for q_{∞}.

A_{base} total cross-sectional area at nozzle exit including vane and nozzle base area, 78.513 cm^2

A_{max} maximum cross-sectional area of afterbody, 284.784 cm^2

A_{seal} cross-sectional area enclosed by seal strip, 266.000 cm^2

AR wing aspect ratio, 3.0

C_A axial-force coefficient (see fig. 1 and appendix)

C_D drag coefficient (see fig. 1 and appendix)

$C_{D,i}$ induced drag coefficient (see eq. (A13))

$C_{D,min}$ jet-off minimum drag coefficient

$C_{(F-A)}$ thrust-minus-axial-force coefficient (see fig. 1)

$C_{(F-D)}$ thrust-minus-drag coefficient (see fig. 1)

$C_{F,j}$	nozzle thrust coefficient along tailpipe center line (fig. 1)
C_L	total lift coefficient (see fig. 1)
ΔC_L	incremental lift coefficient, $C_{L,\Gamma} + C_{L,j}$
$C_{L,j}$	jet lift coefficient (see fig. 1)
$C_{L,o}$	jet-off lift coefficient
$C_{L,\Gamma}$	jet-induced supercirculation lift coefficient
C_m	total pitching-moment coefficient (see fig. 1)
$C_{m,j}$	jet pitching-moment coefficient (see fig. 1)
C_N	normal-force coefficient (see fig. 1)
$C_{N,j}$	jet normal-force coefficient
$C_{N,o}$	jet-off normal-force coefficient
$C_{N,\Gamma}$	jet-induced supercirculation normal-force coefficient
$C_{p,aft}$	afterbody pressure coefficient
C_T	gross thrust coefficient along jet axis (see fig. 1)
c_r	wing root chord at body, 37.08 cm
$\bar{c}$	mean geometric chord, 32.28 cm
e	wing efficiency factor at jet-off conditions
F_A	axial force, N
$F_{A,mom}$	momentum tare force due to bellows, N
$F_{A,Mbal}$	axial force measured by main balance along main balance axis, N

$F_{A,Tbal}$	axial force measured by thrust balance along thrust balance axis, N
F_j	thrust component along tailpipe or body axis, N
M	Mach number
$\dot{m}_i$	ideal mass-flow rate, kg/sec
$\dot{m}_p$	measured mass-flow rate, kg/sec
p_a	ambient pressure, Pa
$\bar{p}_{es}$	average static pressure at external seal, Pa
$\bar{p}_i$	average internal static pressure, Pa
$p_{t,j}$	average jet total pressure, Pa
p_∞	free-stream static pressure, Pa
q_∞	free-stream dynamic pressure, Pa
S	wing reference area including projection to model center line, 2599.89 cm^2
T_{rec}	thrust recovery (see eq. (A12))
w	half-width of body, 11.43 cm
X	afterbody length, cm (see fig. 8)
x,y	body ordinates, cm
x_e	exit location measured downstream from FS 138.68, cm (see fig. 3(a))
α	angle of attack, deg (see fig. 1)
α_{jo}	jet-off angle of attack, deg
α_n	angle of attack of tailpipe center line, deg (see fig. 1)

δ effective jet turning angle, deg

δ_d design or nominal nozzle deflection angle, deg

Abbreviation:

FS fuselage station, cm

APPARATUS AND PROCEDURE

Model

A sketch showing the external geometry of the model with rectangular exits is presented in figure 2. The wing had a leading-edge sweep of 50°, streamwise NACA 64A406 airfoil sections, an aspect ratio of 3.0, a taper ratio of 0.3, and a reference area of 2599.89 cm^2. The wing had no twist or dihedral.

The fuselage up to about FS 116.00 cm had essentially rectangular cross sections with rounded corners. The body lines were chosen to enclose the internal propulsion system and fair into the afterbodies enclosing the nozzles. The maximum width and height of the body were 22.86 cm and 12.7 cm, respectively, and the maximum body cross-sectional area was 284.78 cm^2. A 0.16-cm annular gap between the forebody and afterbody was required to prevent fouling between the nonmetric and metric portions of the model. A flexible teflon strip inserted into slots was used as a seal to prevent internal flow in the model. The low coefficient of friction of teflon minimized restraint between the metric and nonmetric portions of the model. Only that portion of the configuration aft of the metric break at fuselage station 99.06 is supported by the main force balance and hereinafter is referred to as the wind-tunnel model.

The afterbody used for the rectangular nozzles, shown in figure 3(a), had a boattail angle of 12.5°. When nozzle exit location was varied, the afterbody shell was moved in 2.54-cm increments rearward such that the afterbody terminated from FS 141.22 cm to 146.20 cm depending upon exit location. The three exit locations tested were 7, 14, and 21 percent of the wing root chord $\left(x_e/c_r = 0.07, 0.14, \text{ and } 0.21\right)$ aft of the wing trailing edge. The trailing edge of the wing always intersected the fuselage at FS 138.68 cm which corresponded to the configuration of reference 4 where the nozzle exit was at the trailing edge of the wing $\left(x_e/c_r = 0\right)$. Spacers of the appropriate length were added at FS 111.76 cm (fig. 3(a)) to obtain the configurations presented herein. Photographs of the model with the exit in the most aft location $\left(x_e/c_r = 0.21\right)$ are presented in figure 3(b).

The afterbody used for the round nozzles is shown in figure 3(c). Two design constraints placed on the round exit configuration were that the exits be at the wing trailing

edge ($x_e/c_r = 0$ corresponding to the location of the exit of the configuration used in ref. 4) and that the nozzle and tailpipe center lines be identical (which was not a constraint for rectangular exit configurations). In addition the afterbody boattail had to start downstream of FS 121.48 cm in order to enclose internal model hardware. One result of these design constraints was that the interfairing between the nozzles could have had a boattail angle in excess of 20° which can produce large increases in drag. The interfairing boattail angle can be reduced by allowing for a base between the nozzles. A trade-off can be made between interfairing and base drag. The results of reference 6 indicated that a base resulting from fixing the interfairing boattail angle at 12.5°, which was the approximate boattail angle of the afterbody nacelle at the nozzle exits, would result in lower overall drag. The data were adjusted to a condition of free-stream static pressure acting at this base. Photographs of this configuration are given in figure 3(d).

Twin-Jet Propulsion Simulation System and Exhaust Nozzles

A sketch of the twin-jet propulsion simulation system is presented in figure 4(a) and photographs without the force balances are shown in figure 4(b). The propulsion system internal performance characteristics are given in reference 4.

An external high-pressure air system provides a continuous flow of clean, dry air at a controlled temperature of about 306 K. This high-pressure air is brought through the support strut by six tubes into a high-pressure chamber. (See fig. 4(a).) Here the air is divided into two separate flows and is passed through flow control valves. These manually operated valves are used to balance the exhaust-nozzle total pressures to within 0.5 percent of each other. As shown in figure 4(c), the air in each supply pipe is then discharged perpendicular to the model axis through eight sonic nozzles equally spaced around the supply pipe. This method is designed to eliminate any transfer of axial momentum as the air is passed from the nonmetric to metric portion of the model. Two flexible metal bellows are used as seals and serve to compensate the axial forces caused by pressurization. The cavity between the supply pipe and bellows is vented to model internal pressure. The tailpipes are connected to the thrust balance whose loads are then transmitted to the main balance through the wing and thrust-balance support block. (See fig. 4(a).)

The air is then passed through the tailpipes to the exhaust nozzles as shown in figure 4(d). A transition section, located between FS 122.44 cm and FS 124.97 cm, was used to transform the exhaust flow from axisymmetric to two dimensional. Spacers of constant cross-sectional area were added at FS 126.75 cm to vary nozzle exit location (fig. 4(d)). Four sets of rectangular nozzles, each with a total exit area of 50.322 cm^2, were investigated with design deflection angles of 0°, 15°, 30°, and 45° as defined by δ_d on figure 4(d). The aspect ratio of the twin nozzles was 5.99, where the nozzle aspect ratio is

defined as the maximum nozzle width divided by maximum depth including vanes. Two sets of round nozzles were also investigated. These nozzles, shown in figure 4(e), had a total exit area of 51.623 cm^2 and had design deflection angles of 0° and 30°. Both the round and rectangular nozzles had the same internal cross-sectional duct area up to 4.04 cm forward of the nozzle exits.

Both types of nozzles used circular-arc turning vanes to turn the flow. This arrangement was chosen so that the turning vanes would be completely washed by the jet flow in order to minimize the influence of the external flow on vectored nozzle performance. Nozzle mass-flow and static-thrust characteristics are shown in figures 5 and 6, respectively. Figure 6 indicates that static turning was about 65 to 85 percent of the design deflection angle for $\delta_d > 0^o$ (similar to ref. 4). The variation of measured thrust coefficient with nozzle pressure ratio is given in figure 7. No data are presented for the round nozzles with $\delta_d = 0^o$ because the thrust balance was inoperative for this configuration.

Wind Tunnel and Support System

This investigation was conducted in the Langley 16-foot transonic tunnel which is a single-return atmospheric wind tunnel with a slotted octagonal test section and continuous air exchange. The wind tunnel has continuously variable airspeed up to a Mach number of 1.30. Test-section plenum suction is used for speeds above a Mach number of 1.10. From calibration of the wind tunnel, the test-section wall divergence is adjusted as a function of airstream dewpoint in order to eliminate any longitudinal static-pressure gradients in the test section that might occur due to condensation of atmospheric moisture. A complete description of the wind tunnel and operating characteristics can be found in reference 7.

The model was supported by a sting strut as shown in figure 2 with the model center of rotation indicated in figure 2. The strut had a leading-edge sweep of 45°, 50.8-cm chord, and a 5-percent-thick hexagonal airfoil in the streamwise direction. The model blockage ratio was 0.0015 (ratio of model cross-sectional area to test-section area) and the maximum blockage ratio including the support system was 0.0020. Strut interference effects are considered to be small on this model afterbody because of the low boattail angle (ref. 8).

Instrumentation

External aerodynamic and internal nozzle forces and moments were each measured by internal, six-component strain-gage balances (fig. 4). Eight external static pressures were measured at the sealed gap at approximately FS 100.00 cm, as shown in figure 8.

Four of these pressure orifices were located on the nonmetric forebody and four were located on the metric afterbody at meridian angles of every 90°. These pressure measurements were used to correct the measured axial forces for pressure-area force tares as described in the appendix. Four internal pressures were measured in the vicinity of the sealed gap and four internal pressures were located on the top and bottom of the nozzles at approximately FS 125.00 cm. One internal pressure measurement was made near the nose of the nonmetric portion of the model. These pressures are also used for determining pressure-area force tares.

A turbine flowmeter (external to the wind tunnel) was used to measure total mass-flow rate to the nozzles. In addition, the pressure and temperature in each supply pipe was measured prior to the discharge of the flow through the eight sonic nozzles in order to determine mass-flow rate to each nozzle. These flow measurements are used to independently check the mass-flow rate determined by the flowmeter. Two total pressures and one total temperature were measured at one axial location in each nozzle. These measurements were always made 5.38 cm forward of the nozzle exit.

Afterbody pressure distributions were measured on the top and bottom of the afterbody for the rectangular nozzles along axial rows located at the model center-line plane and at 8.89 cm from the center line during all force tests as indicated in figure 8. No afterbody pressures were measured for the model with the round nozzles. All pressures were measured with individual pressure transducers and temperatures were measured with iron-constantan thermocouples. At each test condition, approximately 10 samples of data were recorded on magnetic tape over a period of about 10 sec. The average of the 10 samples is used for computational purposes.

Tests

Four rectangular nozzles with geometric deflection angles δ_d of 0°, 15°, 30°, and 45° were tested at Mach numbers from 0.4 to 1.2 and angles of attack from -2° to 14°. Exit location varied from $x_e/c_r = 0.07$ to 0.21 (all nozzles not tested at all exit locations). Tests were also conducted with round nozzles at $x_e/c_r = 0$. Nozzle deflection angles tested were 0° and 30°. The average Reynolds number per meter, free-stream dynamic pressure, and stagnation temperature are summarized in the following table:

Mach number	Reynolds number per meter	Free-stream dynamic pressure, kN/m^2	Stagnation temperature, K
0.40	8.20×10^6	10.14	302.6
.70	11.68	24.96	316.5
.80	12.30	29.78	323.1
.90	12.63	33.92	328.7
.95	12.80	35.71	331.5
1.20	13.12	41.92	344.3

Balance load limits on pitching moment restricted the maximum angle of attack at high Mach numbers and the maximum obtainable jet pressure ratio for the nozzles with the larger deflection angles.

All tests were conducted with 0.25-cm-wide boundary-layer transition strips consisting of No. 100 silicon carbide grit sparsely distributed in a thin film of lacquer. These strips were located 2.54 cm from the tip of the forebody nose and on both the upper and lower surfaces of the wings at 5 percent of the wing chord at the wing-fuselage juncture to 10 percent of the local streamwise chord at the wing tip in accordance with the recommendations of references 9 and 10.

PRESENTATION OF RESULTS

The results of this investigation are presented in plotted coefficient form in the following figures:

	Figure
Model with rectangular exits:	
Basic aerodynamic characteristics:	
$x_e/c_r = 0.07, \quad \delta_d = 15^\circ$	9
$x_e/c_r = 0.14, \quad \delta_d = 0^\circ$	10
$x_e/c_r = 0.14, \quad \delta_d = 15^\circ$	11
$x_e/c_r = 0.14, \quad \delta_d = 30^\circ$	12
$x_e/c_r = 0.14, \quad \delta_d = 45^\circ$	13
$x_e/c_r = 0.21, \quad \delta_d = 15^\circ$	14
Basic nozzle thrust characteristics:	
$x_e/c_r = 0.14, \quad \delta_d = 0^\circ$	15
$x_e/c_r = 0.14, \quad \delta_d = 15^\circ$	16
$x_e/c_r = 0.14, \quad \delta_d = 30^\circ$	17
$x_e/c_r = 0.14, \quad \delta_d = 45^\circ$	18
Afterbody pressure distributions:	
$x_e/c_r = 0.07, \quad \delta_d = 15^\circ$	19
$x_e/c_r = 0.14, \quad \delta_d = 0^\circ$	20
$x_e/c_r = 0.14, \quad \delta_d = 15^\circ$	21
$x_e/c_r = 0.14, \quad \delta_d = 30^\circ$	22
$x_e/c_r = 0.14, \quad \delta_d = 45^\circ$	23
$x_e/c_r = 0.21, \quad \delta_d = 15^\circ$	24
Jet lift and induced lift characteristics:	
$x_e/c_r = 0.07, \quad \delta_d = 15^\circ$	25
$x_e/c_r = 0.14, \quad \delta_d = 0^\circ$	26
$x_e/c_r = 0.14, \quad \delta_d = 15^\circ$	27

Figure

$x_e/c_r = 0.14$, $\delta_d = 30^o$ 28
$x_e/c_r = 0.14$, $\delta_d = 45^o$ 29
$x_e/c_r = 0.21$, $\delta_d = 15^o$ 30
Lift augmentation factors 31
Drag and lift characteristics:
$x_e/c_r = 0.07$, $\delta_d = 15^o$ 32
$x_e/c_r = 0.14$, $\delta_d = 0^o$ 33
$x_e/c_r = 0.14$, $\delta_d = 15^o$ 34
$x_e/c_r = 0.14$, $\delta_d = 30^o$ 35
$x_e/c_r = 0.14$, $\delta_d = 45^o$ 36
$x_e/c_r = 0.21$, $\delta_d = 15^o$ 37
Thrust recovery characteristics 38
Summary of incremental lift 39
Summary of thrust recovery 40

Model with round exits, $x_e/c_r = 0$:
Basic aerodynamic characteristics:
$\delta_d = 0^o$ 41
$\delta_d = 30^o$ 42
Basic nozzle thrust characteristics, $\delta_d = 30^o$ 43
Jet lift and induced lift characteristics, $\delta_d = 30^o$ 44
Lift augmentation factors, $\delta_d = 30^o$ 45
Drag and lift characteristics, $\delta_d = 30^o$ 46
Thrust recovery, $\delta_d = 30^o$ 47

Comparison of incremental lift for rectangular and round exits 48

Comparison of thrust recovery for rectangular and round exits 49

The basic aerodynamic characteristics presented include the thrust forces measured by the main force balance. They consist of the variation with thrust coefficient of the total lift coefficient C_L, thrust-minus-drag coefficient $C_{(F-D)}$, pitching-moment coefficient C_m, and angle of attack α. Each curve on these figures as well as on subsequent data figures have been identified by the initial jet-off angle of attack α_{jo}. Ideally α would be fixed as pressure ratio or thrust coefficient is varied, but this was not possible because of the method of model support. For the model with the round exits and $\delta_d = 0^o$, the preceding coefficients are presented as a function of nozzle pressure ratio because the thrust balance was inoperative for that configuration. Basic thrust data are presented for the rectangular exits at $x_e/c_r = 0.14$ and nozzle deflection angles of 0° to 45° and for the round exits at $\delta_d = 30^o$ only. These data include the nozzle thrust

coefficient along the tailpipe center line $C_{F,j}$, jet normal-force coefficient $C_{N,j}$, jet pitching-moment coefficient $C_{m,j}$, and angle of attack of the nozzles α_n plotted as a function of thrust coefficient. Afterbody pressure distributions for the model with the rectangular exits only are presented at selected angles of attack and thrust coefficients.

Lift characteristics consist of the measured jet lift coefficient $C_{L,j}$, jet-induced supercirculation lift coefficient $C_{L,\Gamma}$, and incremental lift coefficient ΔC_L. Drag characteristics include drag coefficient C_D and total aerodynamic lift $C_{L,o} + C_{L,\Gamma}$. These data, along with lift augmentation factor $\Delta C_L/C_{L,j}$ and thrust recovery, are shown as a function of thrust coefficient. A discussion of these parameters is included in the appendix.

DISCUSSION OF RESULTS

Thrust-induced supercirculation effects from thrust vectoring have indicated a potential for not only increasing maneuverability of fighter aircraft but also improving cruise performance. References 3 and 4 indicated that significant increases in thrust-induced lift along with substantial decreases in drag were achieved by thrust vectoring. Since the results shown herein are similar to those detailed in reference 4, only a brief discussion is presented.

Effect of Nozzle Exit Location

The effects of varying nozzle exit location on the incremental lift characteristics of the rectangular nozzle configuration are summarized in figure 39 at two Mach numbers and thrust coefficients. The data for $x_e/c_r = 0$ were taken from reference 4. The results show a decrease in incremental lift as nozzle exit is moved aft from the wing trailing edge. This decrease in ΔC_L is due to a decrease in jet-induced supercirculation lift since the measured jet lift for a particular nozzle did not vary with exit location. The results of figure 39 were linearly extrapolated to the wings-off incremental lift level (ref. 4) represented by the heavy dashed line. The intersection of the extrapolated data with this level is represented by the solid symbol. At $M = 0.7$, no induced lift would probably be generated on the wings if the exit were moved 26 to 30 percent of the wing root chord. Since this is not indicated at $M = 0.9$ (exit must be moved $x_e/c_r > 0.5$), then it is quite possible that this linear extrapolation is not adequate to predict the effect of exit location at all Mach numbers.

Figure 40 presents a summary of thrust recovery characteristics for the model where thrust recovery is defined as that portion of the thrust recovered in the streamwise direction (see appendix). Since thrust recovery was a function of the thrust-minus-drag characteristics, variations in thrust recovery are a result of changes in external drag

because the internal nozzle performance was not affected by nozzle exit location. Positive values of recovery in terms of percent C_T indicate a drag reduction. For the nozzles deflected 15° and 30°, exit location had a small effect on recovery.

Effect of Round Nozzles

A comparison is made in figure 48 of the incremental lift characteristics for the model with round and rectangular nozzle exits. At $M = 0.7$, the model with the round exits induced more lift over the entire angle-of-attack range tested (jet lift was approximately the same for both nozzles).

Figure 49 presents a comparison of thrust recovery characteristics in percent thrust coefficient for the two nozzle shapes. The negative recovery values for the round nozzles at $C_T = 0.1$ indicate that the aerodynamic thrust term is negative and that $T_{rec} < \cos(\alpha + \delta)$ (see appendix). This, of course, is a drag increase that is probably attributable to an increase in afterbody drag due to adverse interference effects.

CONCLUDING REMARKS

An investigation has been conducted in the Langley 16-foot transonic tunnel to determine the induced lift characteristics of a vectored-thrust concept in which jet-exhaust nozzles were located in the fuselage at or near the wing trailing edge. The effects of moving twin rectangular nozzles rearward from the wing trailing edge and of round nozzles at the trailing edge only were studied at Mach numbers from 0.4 to 1.2, angles of attack up to 14°, and thrust coefficients up to 0.35. Nozzle deflection angle varied from 0° to 45°. The Reynolds number per meter varied from 8.20×10^6 to 13.12×10^6.

The results showed that moving the rectangular exits rearward from the wing trailing edge reduced jet-induced supercirculation lift but did not appreciably affect drag. The model with the round exits generated more induced lift at a Mach number of 0.7 than the model with the rectangular exits but had higher drag.

Langley Research Center
National Aeronautics and Space Administration
Hampton, Va. 23665
November 18, 1975

APPENDIX

DATA REDUCTION PROCEDURE

Data Adjustments

External aerodynamic and internal nozzle forces and moments were each measured by separate internal six-component force balances as shown in figure 4(a). The main balance measured total lift, thrust-minus-axial force and total pitching moment while the thrust balance sensed nozzle normal and axial forces and pitching moment. The center lines of these two force balances were located above and below the tailpipe center line (fig. 4(a)) and bellows flow transfer system (fig. 4(c)). Because of this offset, an effect of loading one balance on the other existed, primarily the main balance affecting the thrust balance.

Consequently, single and combined loadings of normal force and pitching moments were made with and without the jets operating with the 0° nozzle. These calibrations were performed with the jets operating because this gives a more realistic effect of pressurizing the bellows than capping off the nozzles and pressurizing the flow system. Thus, in addition to the usual balance interaction corrections that are applied for a single force balance under combined loads, another set of corrections was made to the data from this investigation for the combined loading effects of one balance on the other. However, loadings were also done in the axial-force direction with the flow system capped off and pressurized and this indicated no effect on the axial force measured by each balance.

The axial forces measured by both force balances must also be corrected for pressure-area tare forces acting on the model and momentum tare forces due to flow in the bellows in order to get desired thrust-minus-axial force (from the main balance) and thrust (from the thrust balance). The external-seal and internal pressure forces on the model were obtained by multiplying the difference between the average pressure (external or internal pressures shown in fig. 8) and the free-stream static pressure by the affected projected area normal to the model axis. The momentum tare force was determined from calibrations prior to the wind-tunnel investigation using standard calibration nozzles (appendix B of ref. 4).

Gross thrust-minus-axial force was computed from the main balance axial force with the following relationship:

$$F_j - F_A = F_{A,Mbal} + \left(\bar{p}_{es} - p_\infty\right)\left(A_{max} - A_{seal}\right) + \left(\bar{p}_i - p_\infty\right)A_{seal} - F_{A,mom} \tag{A1}$$

where $F_{A,Mbal}$ (positive upstream) includes all pressure and viscous forces, internal and external, on both the afterbody and thrust system. The second and third terms account for the forward seal rim and the interior pressure forces, respectively. In terms of an axial-force coefficient, the second term ranges from -0.0001 to -0.0007 and the third term varies ±0.0075 depending upon Mach number and pressure ratio. Reference 4 indicated that internal pressure at any given set of test conditions was uniform throughout the inside of the model indicating no flows. The fourth term is due to the momentum tare correction and is a function of the average bellows internal pressure. At an internal pressure of 1380 kN/m^2 (corresponding to $p_{t,j}/p_\infty = 4.0$), this tare is approximately 5 percent of the maximum static thrust and its repeatability is 0.25 percent. For the model with round exits, an additional adjustment is made to the condition of free-stream static pressure existing at the afterbody base between the two nozzle exits. This correction was a base axial force that varied from 0.0015 to 0.0040.

Gross thrust from the thrust balance is computed from a similar relationship:

$$F_j = F_{A,Tbal} - (\bar{p}_i - p_\infty)A_{base} - F_{A,mom} \tag{A2}$$

where $F_{A,Tbal}$ (positive upstream) includes nozzle thrust and the internal pressure forces acting on the thrust system.

Similar adjustments are made to the pitching moments measured by both balances since both the pressure-area and bellows momentum tare forces are assumed to act along the model center line and both balances are offset from the model center line. The pitching-moment tare is determined by multiplying the tare force by the appropriate moment arm and subtracting the value from the measured pitching moments.

External Forces Including Thrust

The adjusted forces and moments measured by the main balance are transferred from the main-balance axis to the body axis of the metric portion of the model where the body axis lies in the wing-chord plane (fig. 1). Angle of attack α, which is the angle between the wing-chord plane and the relative wind, was determined by applying to the sting pitch angle deflection terms due to model and balance bending under aerodynamic load. Calibrations were made with the propulsion simulation system in place in order to account for any restraints that might occur across the force balances. It should also be noted that some difference in angle between the nonmetric and metric portions of the model exists because of balance deflection. No adjustment has been made for wind-tunnel flow angularity which is approximately 0.1° for most sting-supported models in the Langley 16-foot transonic tunnel.

APPENDIX

The total force and moment coefficients including thrust about the body and stability axis are shown in figure 1 where the moment reference center is at the quarter-chord of the wing mean geometric chord (fuselage station 117.64 cm).

Nozzle Internal Forces

The adjusted forces and moments measured by the thrust balance are transferred from the thrust-balance axis to the parallel tailpipe center-line axis (fig. 1). The tailpipe center line will be at some angle with respect to the body axis because the thrust balance deflects, under load, relative to the body axis. Accordingly, α_n is defined as the angle between the tailpipe center line and the relative wind. This angle was determined by adding deflection terms to the previously determined value of angle of attack. Calibrations with the propulsion system in place were made in order to determine these deflection constants.

From the measured axial and normal components of the jet resultant thrust, the effective jet turning angle, thrust coefficient, and jet lift coefficient are defined, respectively, as

$$\delta = \tan^{-1} \frac{C_{N,j}}{C_{F,j}} \tag{A3}$$

$$C_T = \sqrt{C_{N,j}^2 + C_{F,j}^2} \tag{A4}$$

$$C_{L,j} = C_T \sin\left(\delta + \alpha_n\right) = C_{N,j} \cos \alpha_n + C_{F,j} \sin \alpha_n \tag{A5}$$

Thrust Removal

Nozzle internal forces are transferred from the tailpipe center-line axis to the body axis and then subtracted from the external forces resulting in the following aerodynamic loads:

$$C_{N,o} + C_{N,\Gamma} = C_N - \left[C_{N,j} \cos\left(\alpha - \alpha_n\right) - C_{F,j} \sin\left(\alpha - \alpha_n\right)\right] \tag{A6}$$

$$C_A = -C_{(F-A)} + \left[C_{F,j} \cos\left(\alpha - \alpha_n\right) + C_{N,j} \sin\left(\alpha - \alpha_n\right)\right] \tag{A7}$$

Transferring to the wind axis gives

$$C_{L,o} + C_{L,\Gamma} = \left(C_{N,o} + C_{N,\Gamma}\right) \cos \alpha - C_A \sin \alpha \tag{A8}$$

$$C_D = C_A \cos\alpha + \left(C_{N,o} + C_{N,\Gamma}\right) \sin\alpha \tag{A9}$$

where the normal force or lift coefficient with the subscript o refers to jet-off values and the subscript Γ refers to the jet-on normal or lift force induced as a result of supercirculation on the wing. The quantity $C_{L,o} + C_{L,\Gamma}$ represents the total aerodynamic lift of the wings.

Lift Augmentation

Generally, the total lift component is broken down into three parts: (1) jet-off lift, (2) jet-reaction lift, and (3) jet-induced supercirculation lift. Some experimental setups have a single force balance and thus are only able to measure thrust and turning angle at static conditions. In this case, values of thrust coefficient at forward speeds can be determined based on these static-thrust measurements. Since one of the purposes of the present investigation was to determine the components of the total lift, jet lift is measured directly with the thrust balance. However, first it was necessary to determine the jet-off or basic wing lift coefficient $C_{L,o}$. The basic wing lift varies with thrust coefficient and is different at each jet-on point because the model angle of attack is decreased with jet operation due to balance deflections. Figure 12 shows a typical variation of α with C_T. Therefore, in order to determine $C_{L,o}$, the average jet-off lift variation with angle of attack at each Mach number was fitted to a third-order polynomial curve as a function of angle of attack; $C_{L,o}$ was then computed at each power-on point for the particular model angle of attack measured.

Incremental lift is then defined as

$$\Delta C_L = C_L - C_{L,o} = C_{L,\Gamma} + C_{L,j} \tag{A10}$$

and the lift augmentation factor based on measured jet lift is simply

$$\frac{\Delta C_L}{C_{L,j}} = \frac{C_{L,\Gamma} + C_{L,j}}{C_{L,j}} \tag{A11}$$

Thrust Recovery

Thrust recovery has been defined as that portion of the total thrust recovered in the streamwise direction or the amount of propulsive thrust converted to aerodynamic thrust (ref. 4) and is given as

$$T_{rec} = \frac{C_{D,min} + C_{D,i} + C_{(F-D)}}{C_T} \tag{A12}$$

where T_{rec} is a thrust ratio. The average jet-off minimum drag coefficient $C_{D,min}$ for a particular configuration is determined and the induced drag coefficient $C_{D,i}$ is

$$C_{D,i} = \frac{\left(C_{L,o} + C_{L,\Gamma}\right)^2}{e\pi AR + 2C_T} \tag{A13}$$

where only the wing efficiency factor e, determined at jet-off conditions, is used to account for nonelliptic loading effects. Another efficiency factor can be applied to the entire denominator to account for jet effects but its value is not known.

In terms of the propulsive and aerodynamic thrust terms, thrust recovery is

$$T_{rec} = \frac{C_T\left[\cos(\alpha + \delta)\right] + C_{\Delta F}}{C_T} \tag{A14}$$

where $C_{\Delta F}$ is the aerodynamic thrust coefficient and represents the change in drag from the ideal jet-off drag polar. For zero thrust recovery, $C_{\Delta F} = 0$ and

$$T_{rec} = \cos(\alpha + \delta) \tag{A15}$$

For complete thrust recovery, $T_{rec} = 1$ and

$$C_{\Delta F} = C_T\left[1 - \cos(\alpha + \delta)\right] \tag{A16}$$

The aerodynamic thrust term can also be expressed as a ratio to C_T

$$\frac{C_{\Delta F}}{C_T} = T_{rec} - \cos(\alpha + \delta) \tag{A17}$$

which then can be easily converted to percent thrust coefficient.

REFERENCES

1. Corson, Blake W., Jr.; Capone, Francis J.; and Putnam, Lawrence E.: Lift Induced on a Swept Wing by a Two-Dimensional Partial-Span Deflected Jet at Mach Numbers From 0.20 to 1.30. NASA TM X-2309, 1971.
2. Capone, Francis J.: Exploratory Investigation of Lift Induced on a Swept Wing by a Two-Dimensional Partial-Span Deflected Jet at Mach Numbers From 0.20 to 1.30. NASA TM X-2529, 1972.
3. Capone, Francis J.: Supercirculation Effects Induced by Vectoring a Partial-Span Rectangular Jet. J. Aircraft, vol. 12, no. 8, Aug. 1975, pp. 633-638.
4. Capone, Francis J.: The Effects on Propulsion-Induced Aerodynamic Forces of Vectoring a Partial-Span Rectangular Jet at Mach Numbers From 0.40 to 1.20. NASA TN D-8039, 1975.
5. Capone, Francis J.: A Summary of Experimental Research on Propulsive-Lift Concepts in the Langley 16-Foot Transonic Tunnel. AIAA Paper No. 75-1315, Oct. 1975.
6. Maiden, Donald L.; and Runckel, Jack F.: Effect of Nozzle Lateral Spacing on Afterbody Drag and Performance of Twin-Jet Afterbody Models With Convergent Nozzles at Mach Numbers up to 2.2. NASA TM X-2099, 1970.
7. Corson, Blake W., Jr.; Runckel, Jack F.; and Igoe, William B.: Calibration of the Langley 16-Foot Transonic Tunnel With Test Section Air Removal. NASA TR R-423, 1974.
8. Reubush, David E.; and Runckel, Jack F.: Effect of Fineness Ratio on Boattail Drag of Circular-Arc Afterbodies Having Closure Ratios of 0.50 With Jet Exhaust at Mach Numbers up to 1.30. NASA TN D-7192, 1973.
9. Braslow, Albert L.; and Knox, Eugene C.: Simplified Method for Determination of Critical Height of Distributed Roughness Particles for Boundary-Layer Transition at Mach Numbers From 0 to 5. NACA TN 4363, 1958.
10. Braslow, Albert L.; Hicks, Raymond M.; and Harris, Roy V., Jr.: Use of Grit-Type Boundary-Layer-Transition Trips on Wind-Tunnel Models. NASA TN D-3579, 1966.

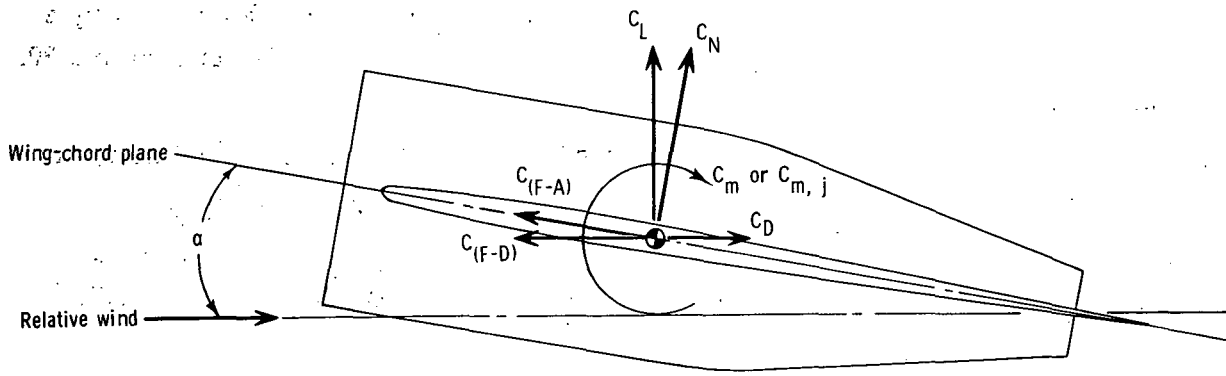

(a) External forces.

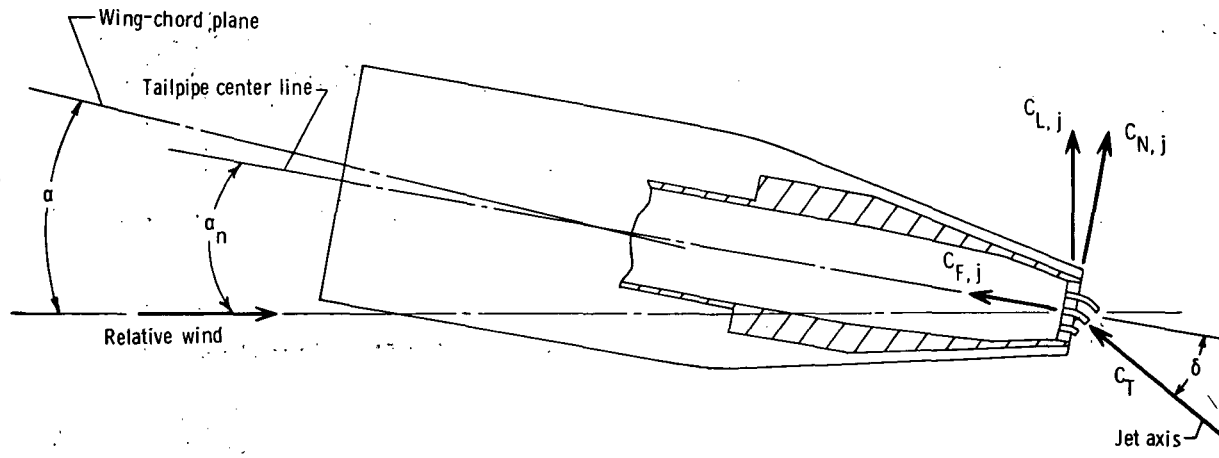

(b) Internal forces.

Figure 1.- Definition of model forces showing positive directions.

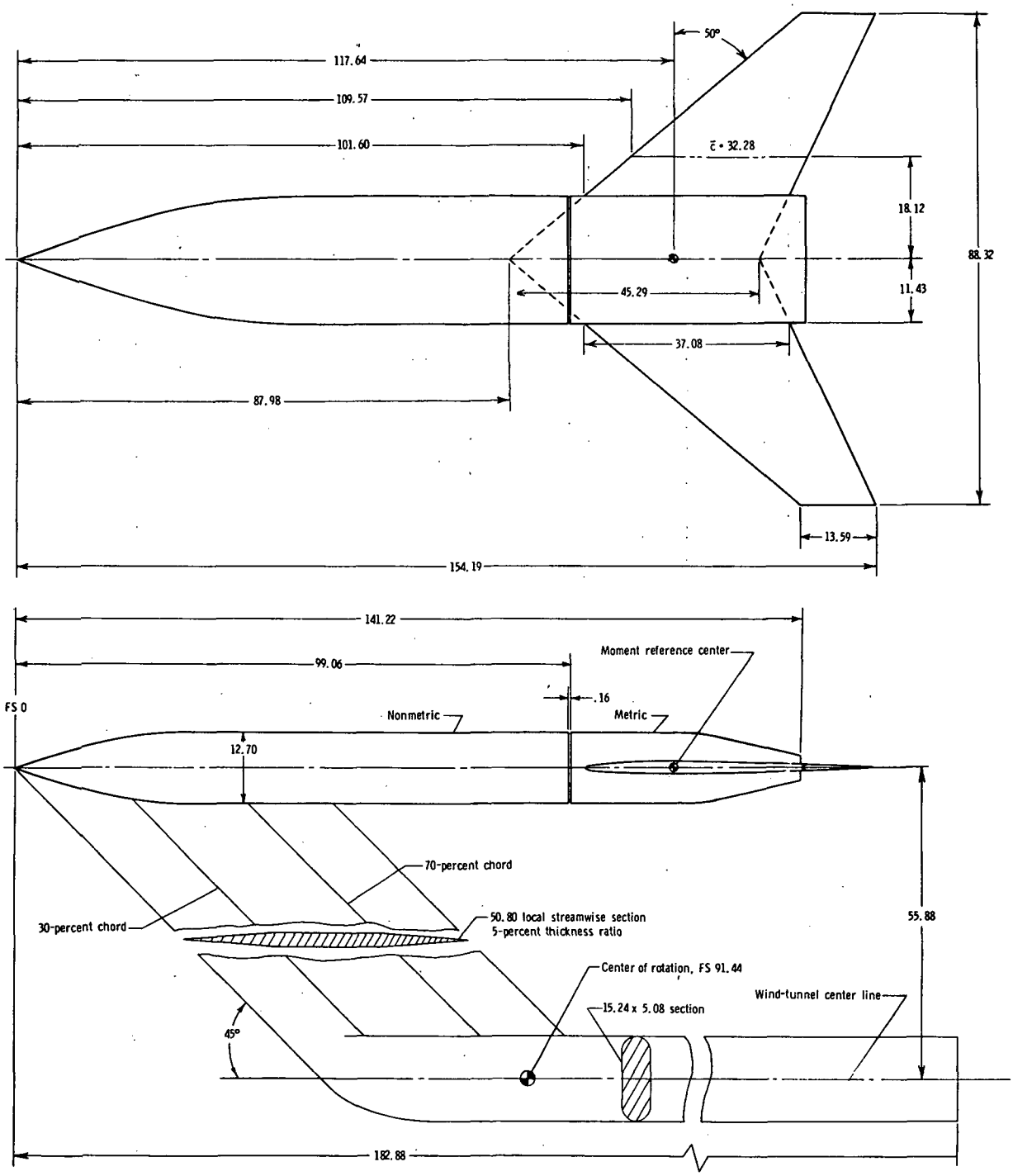

Figure 2.- General arrangement of model. All dimensions are in centimeters unless otherwise noted.

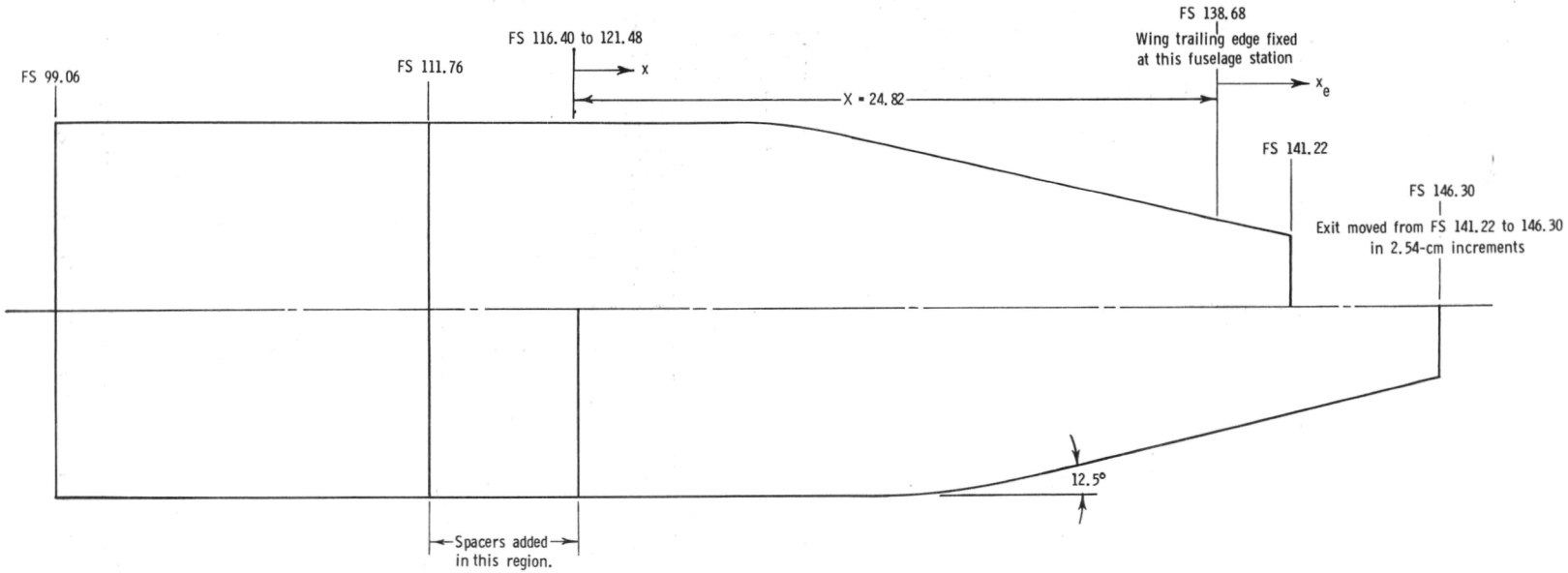

(a) Afterbody (nozzle exit) spacing.

Figure 3.- Afterbody geometry. All dimensions are in centimeters unless otherwise noted.

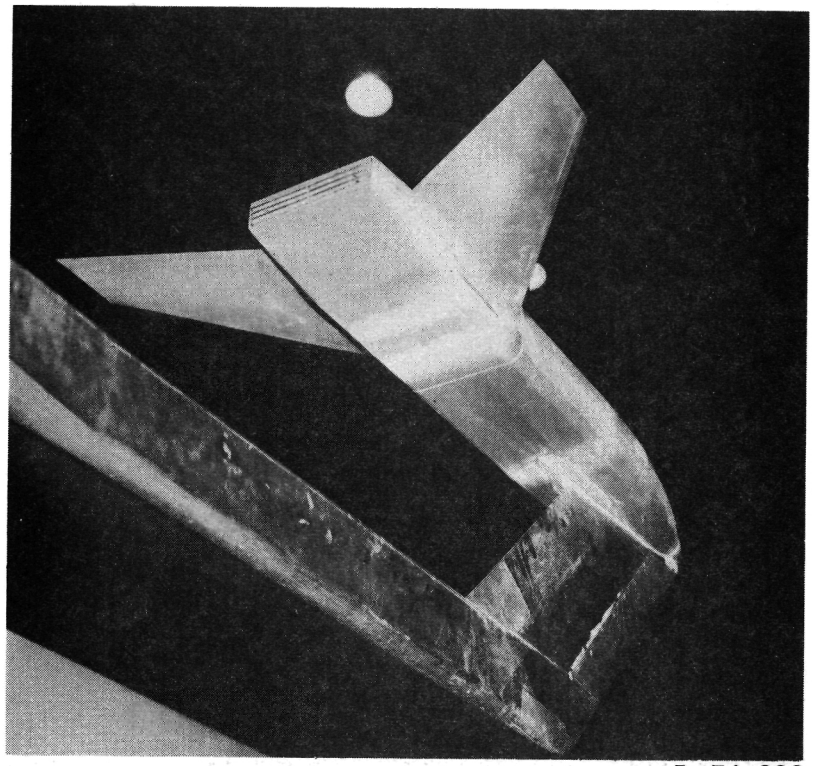

L-74-228

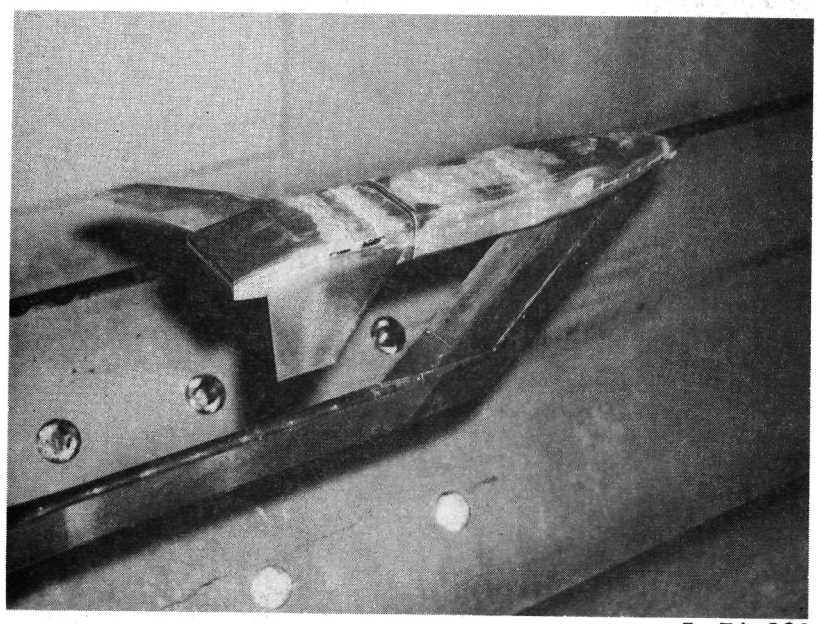

L-74-230

(b) Photographs of model with rectangular nozzles; $x_e/c_r = 0.21$.

Figure 3.- Continued.

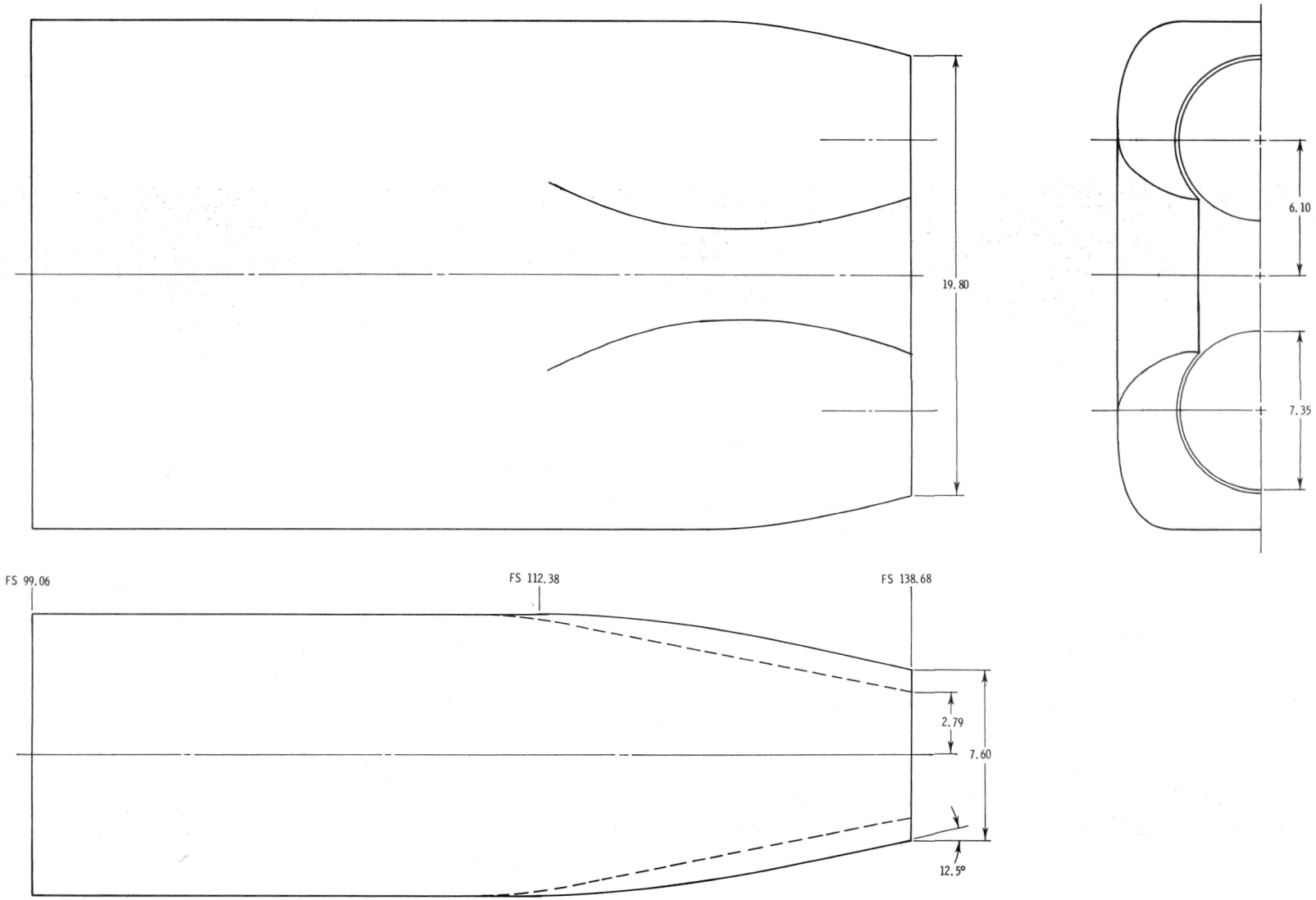

(c) Afterbody for round exits.

Figure 3.- Continued.

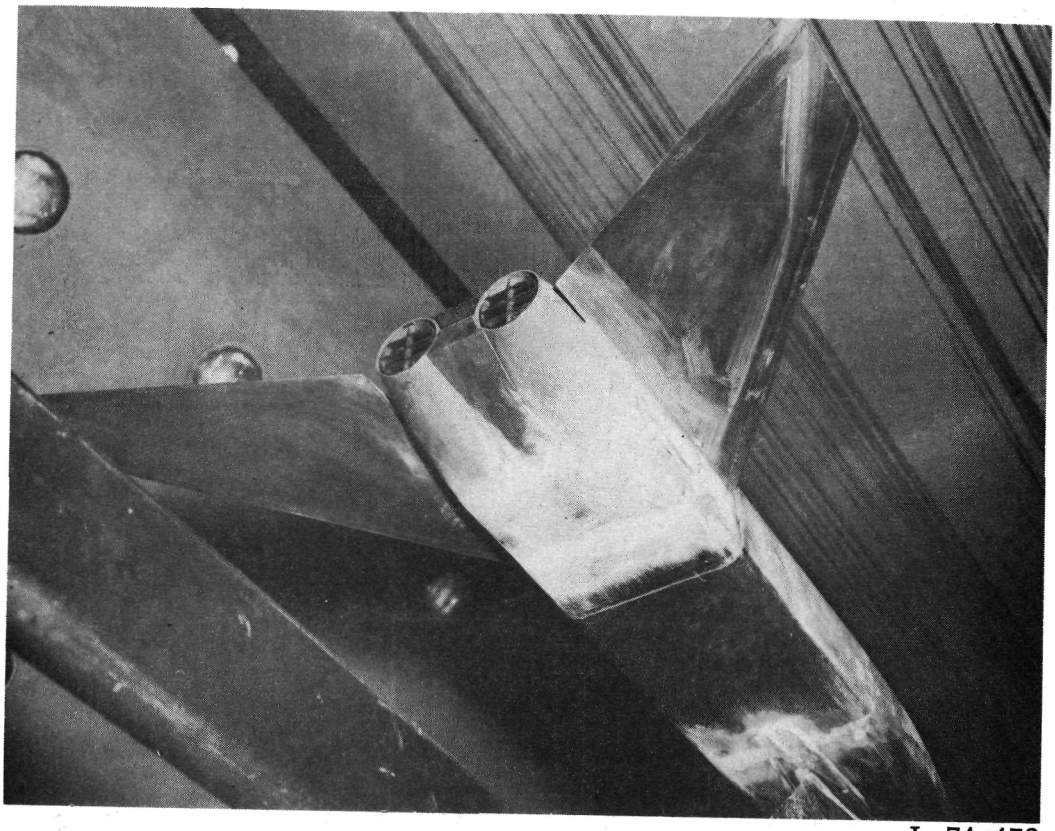

L-74-472

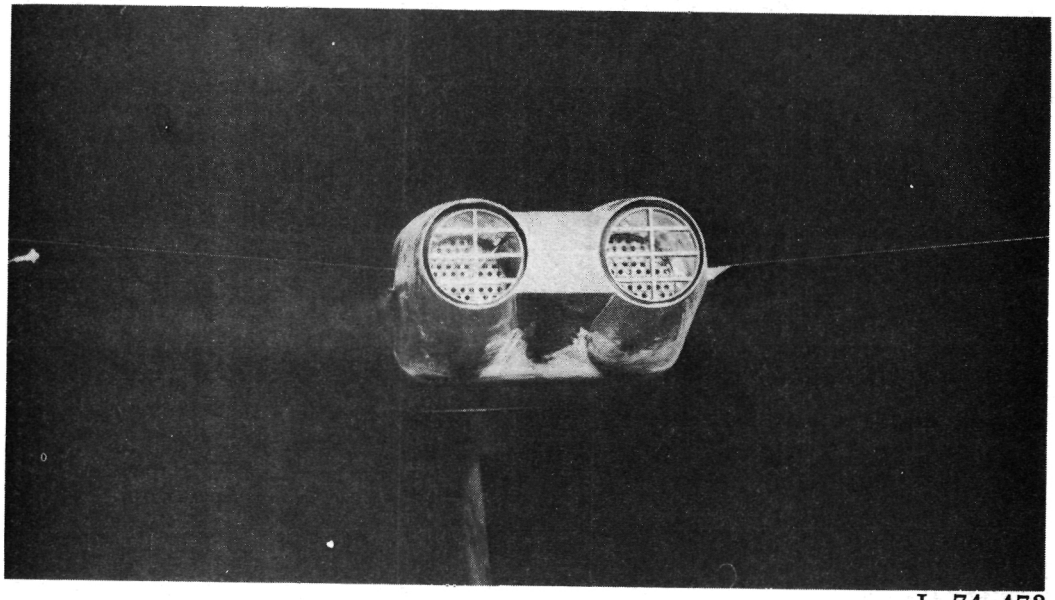

L-74-473

(d) Photographs of model with round exits; $\delta_d = 0^o$.

Figure 3.- Concluded.

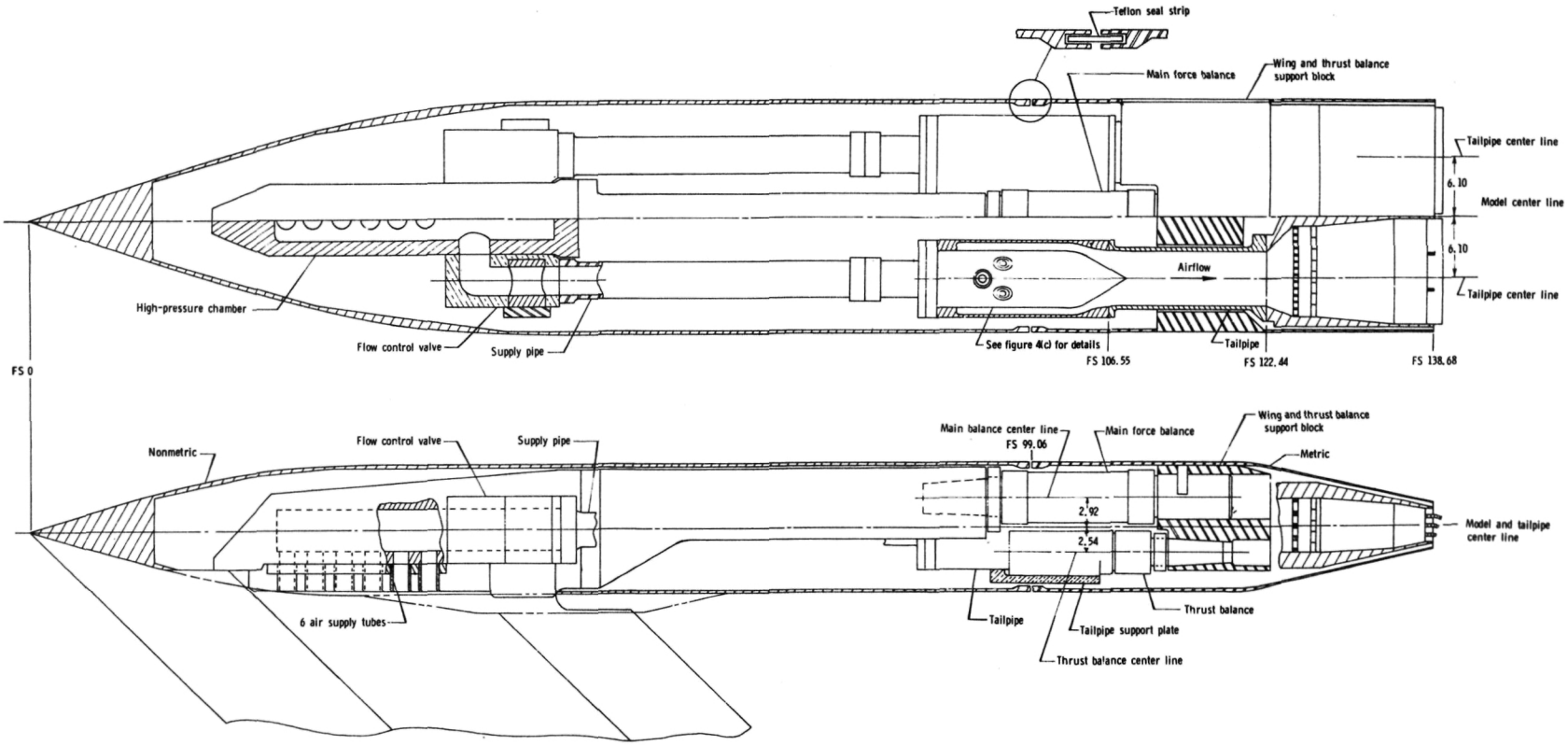

(a) Sketch of system; $x_e/c_r = 0$ (this configuration not tested).

Figure 4.- Details of twin-jet, exhaust-nozzle, simulation system. All dimensions are in centimeters unless otherwise noted.

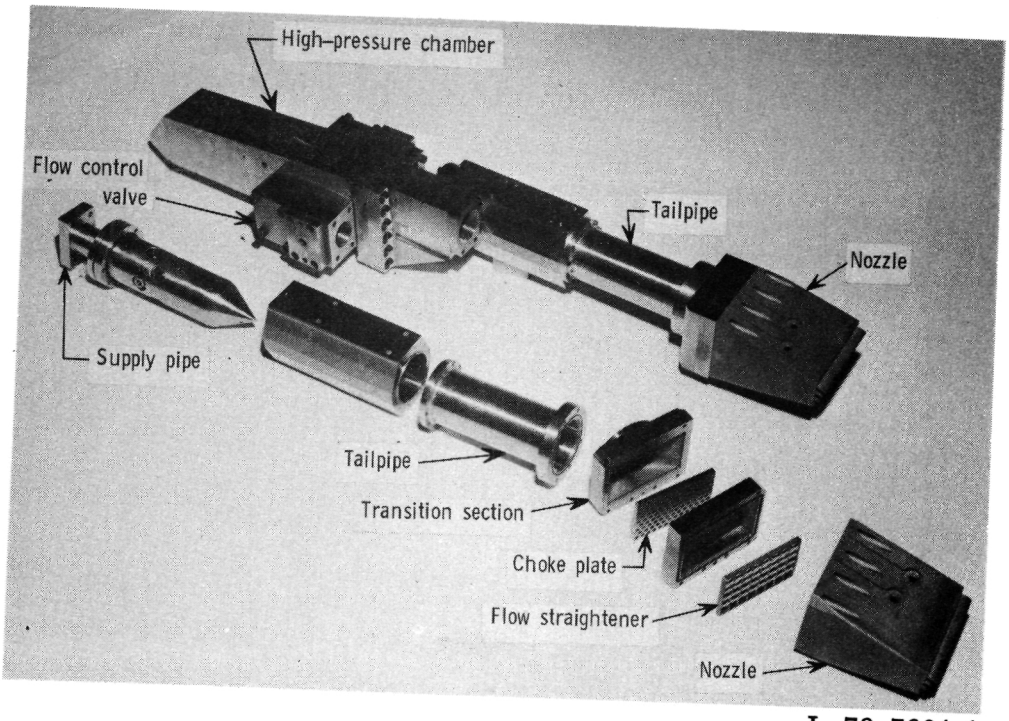

L-70-7604.1

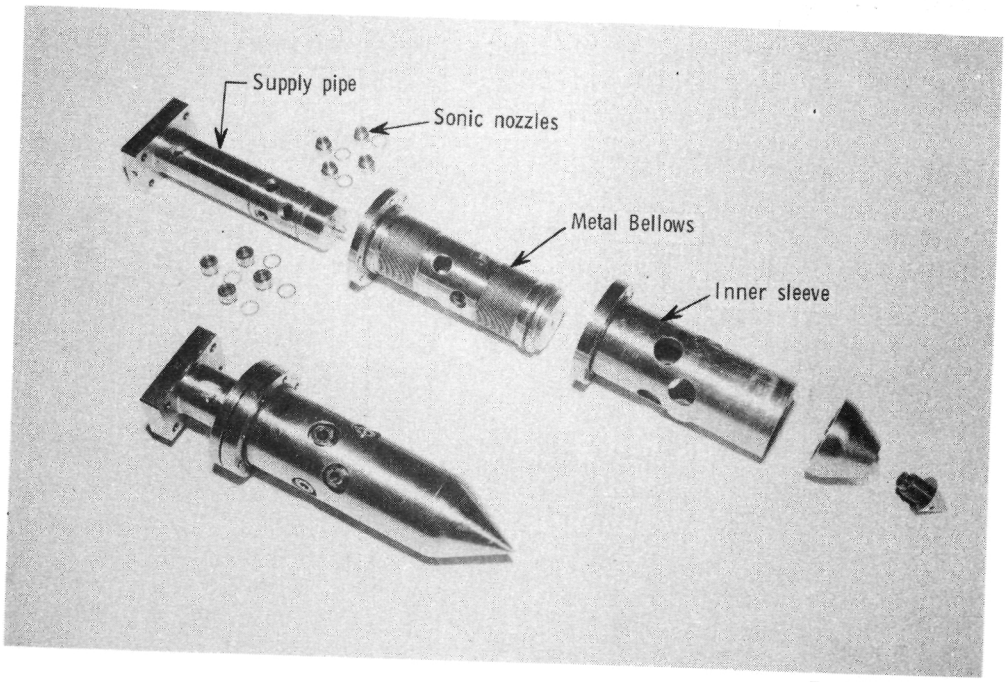

L-70-7605.1

(b) Photographs of propulsion simulation system.

Figure 4.- Continued.

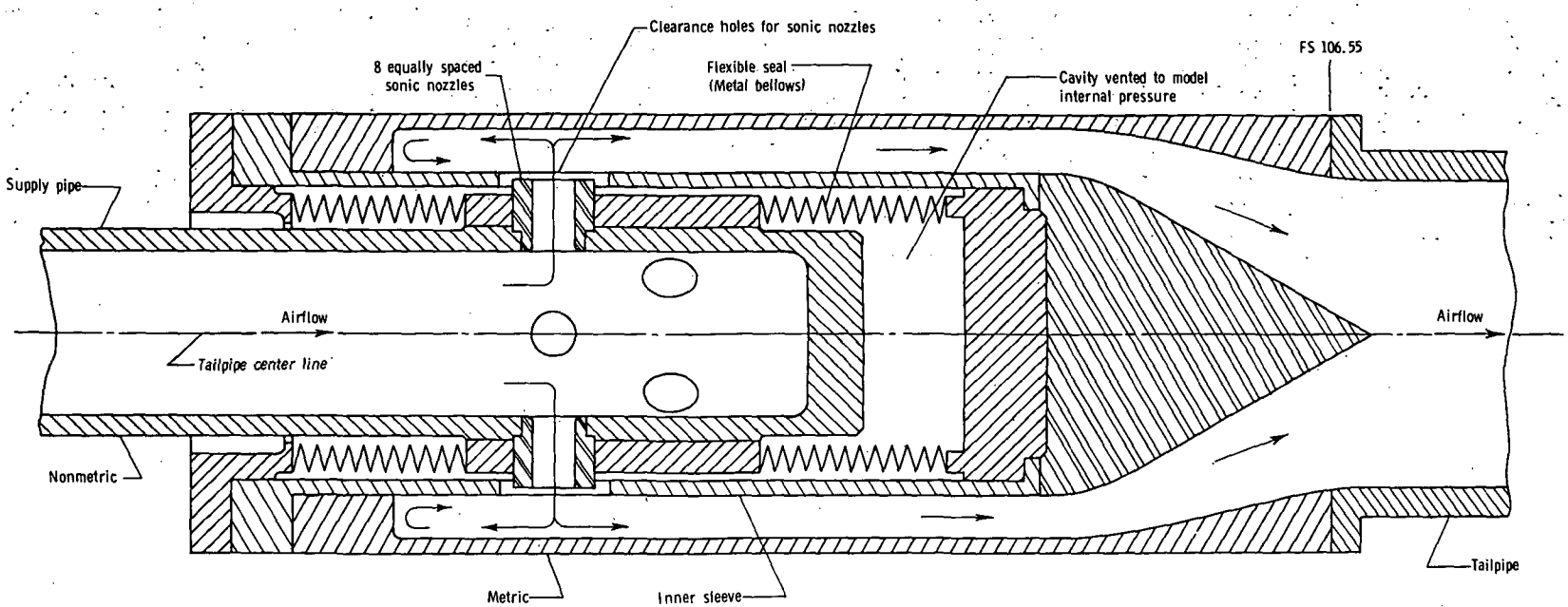

(c) Details of bellows arrangement used to transfer air from nonmetric to metric portions of model.

Figure 4.- Continued.

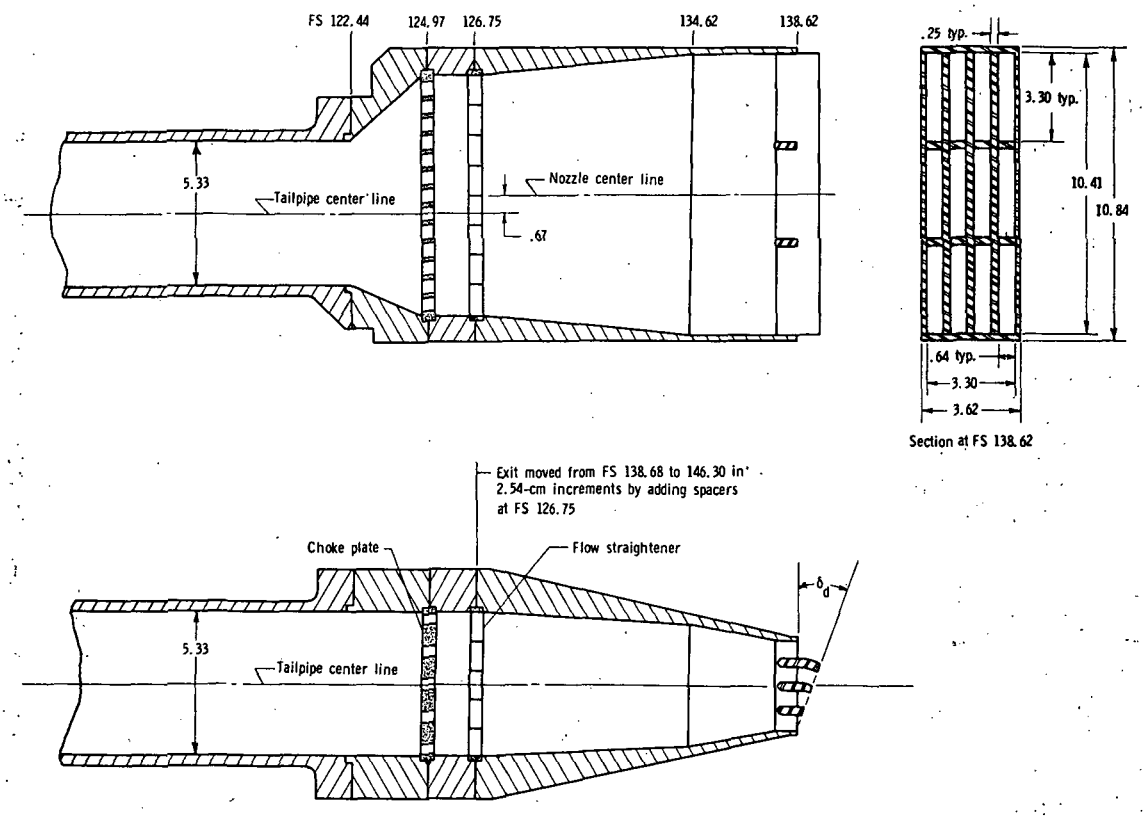

(d) Rectangular exits.

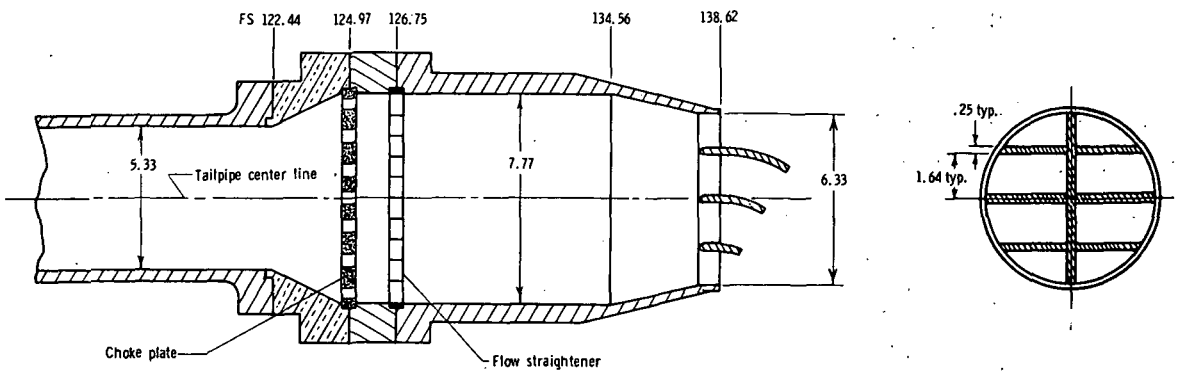

(e) Round exits.

Figure 4.- Concluded.

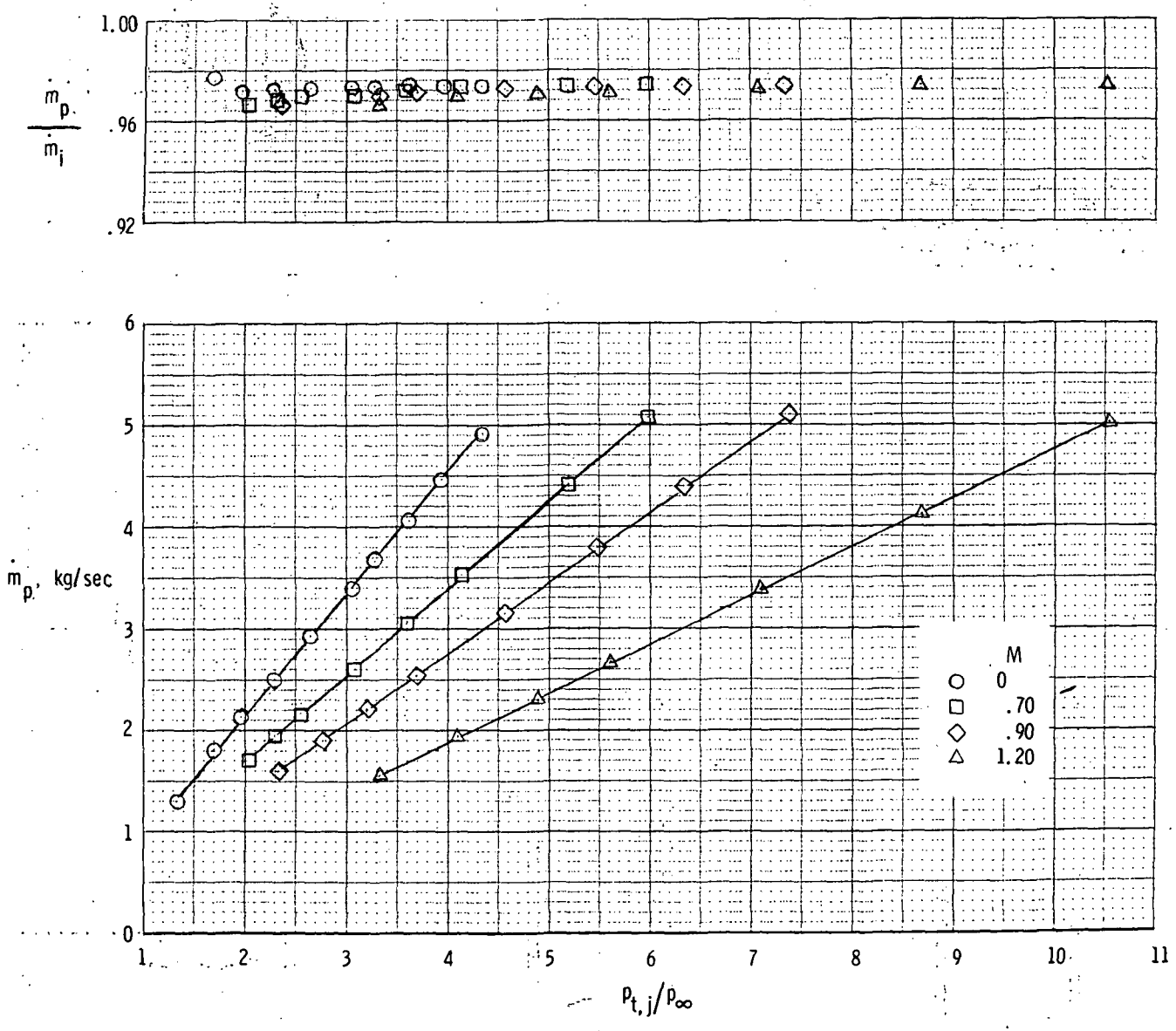

Figure 5.- Typical mass-flow rate and discharge coefficient characteristics, rectangular nozzles.

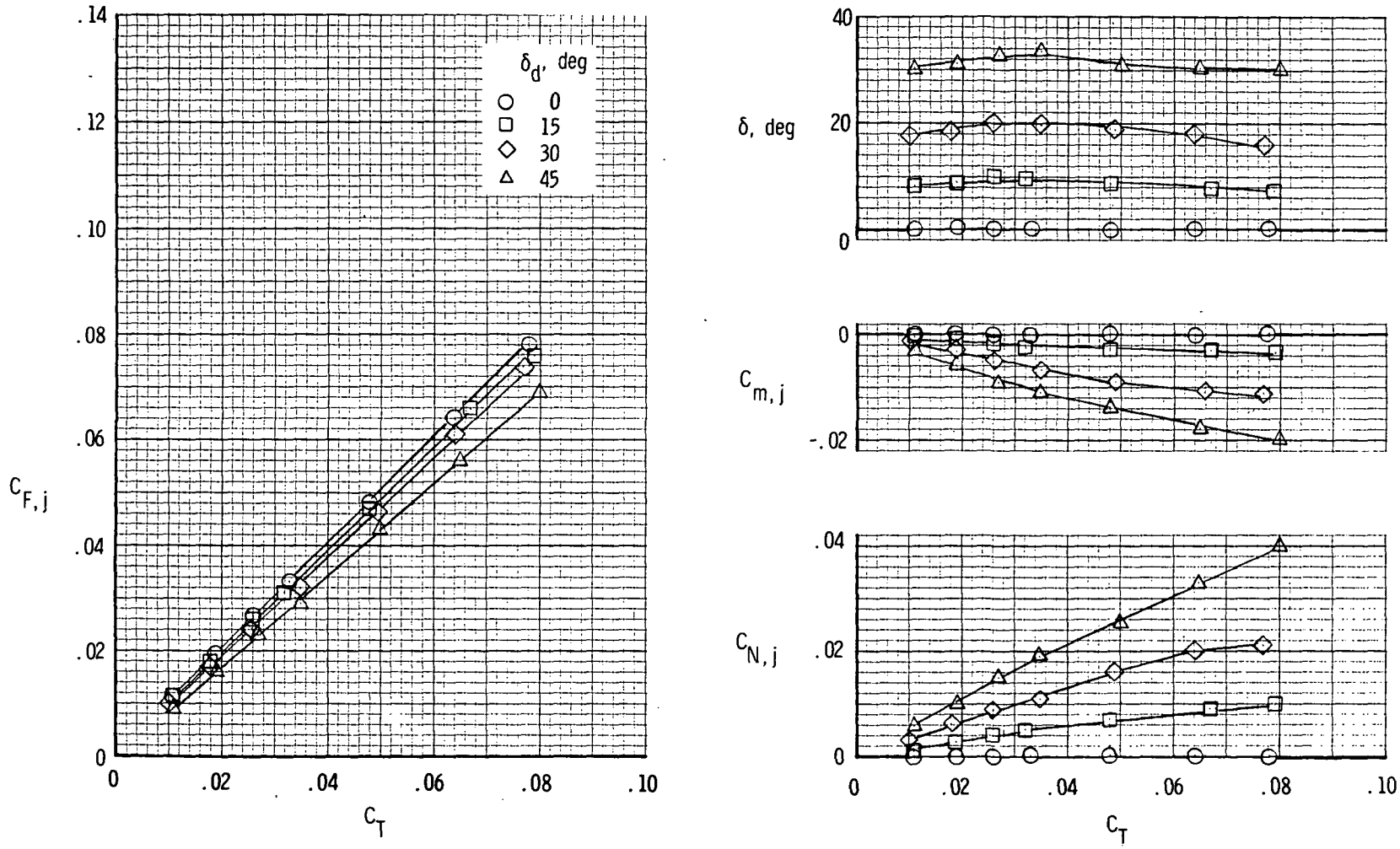

(a) Rectangular exits.

Figure 6.- Static thrust and effective turning angle characteristics.

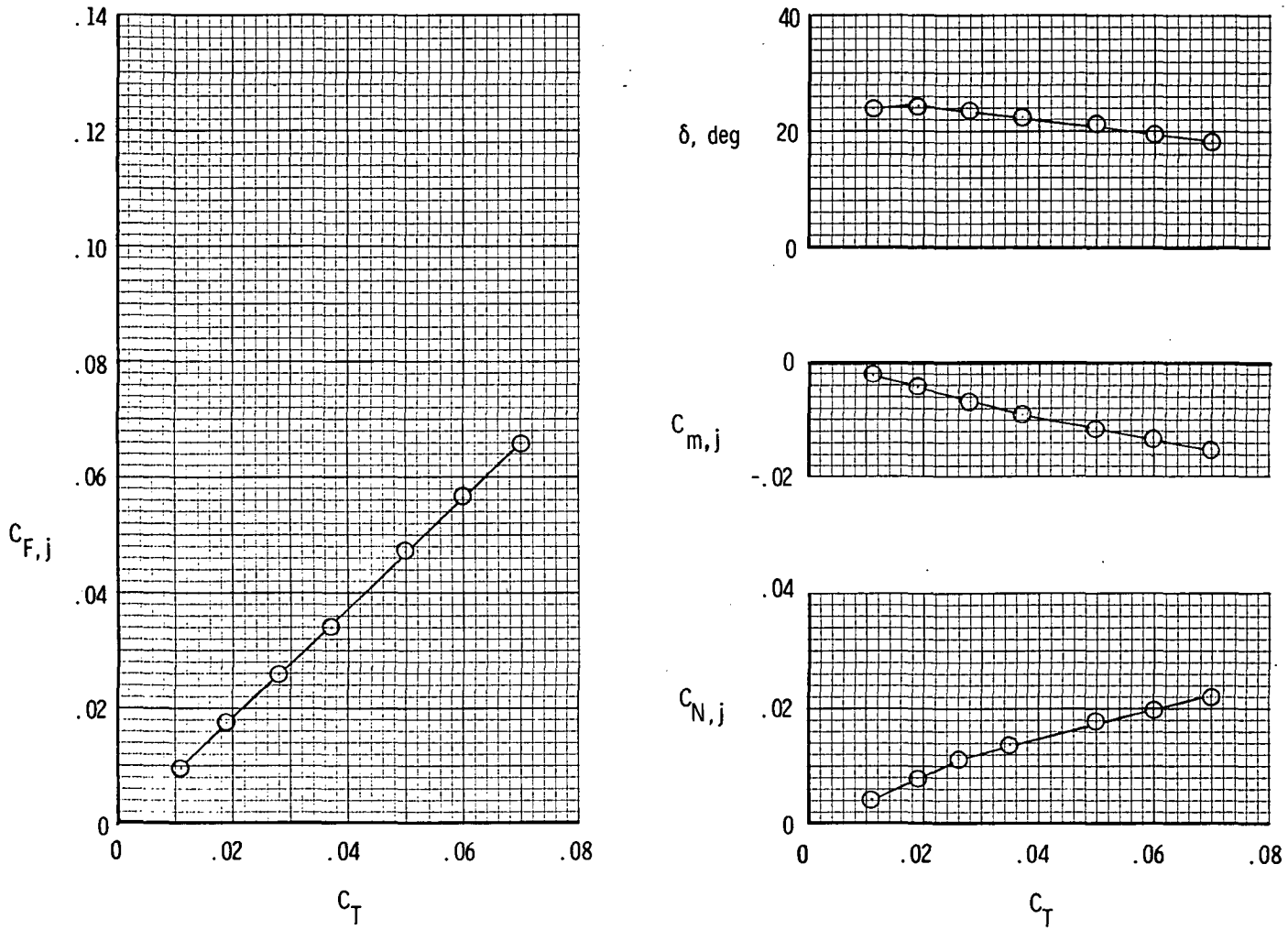

(b) Round nozzles; $\delta_d = 30^\circ$.

Figure 6.- Concluded.

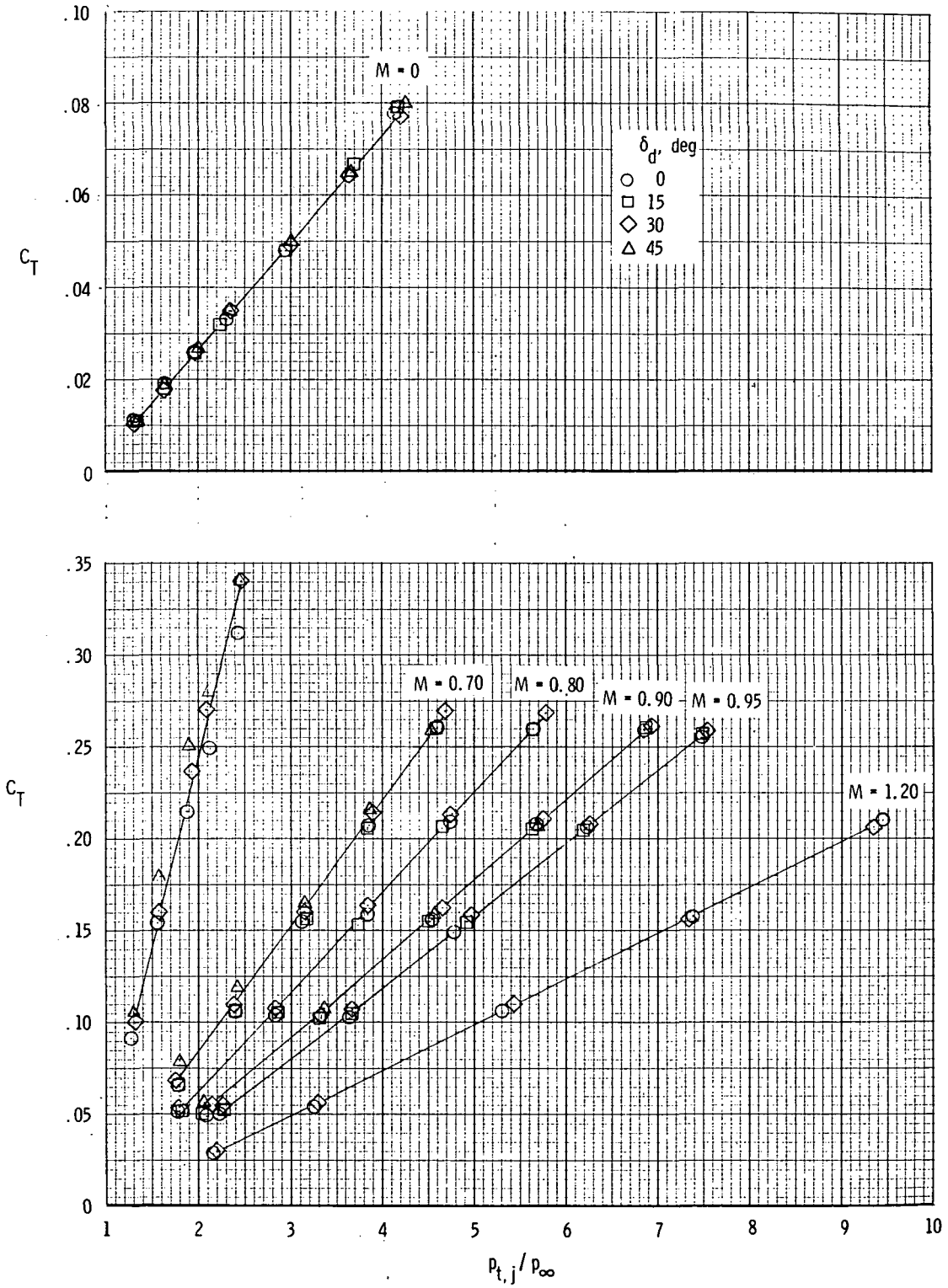

(a) Rectangular exits.

Figure 7.- Variation of measured thrust coefficient with nozzle pressure ratio.

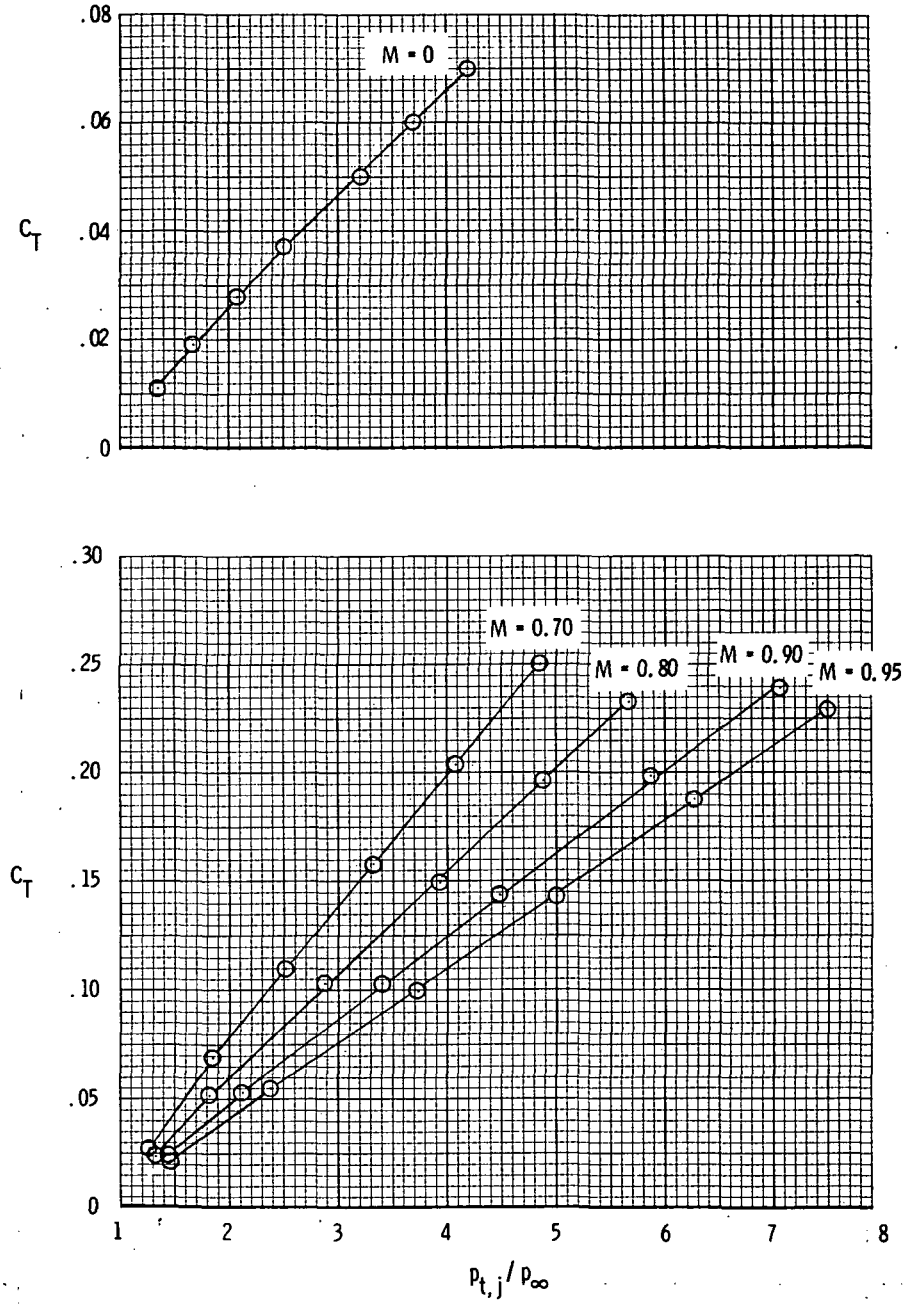

(b) Round nozzles; $\delta_d = 30^\circ$.

Figure 7.- Concluded.

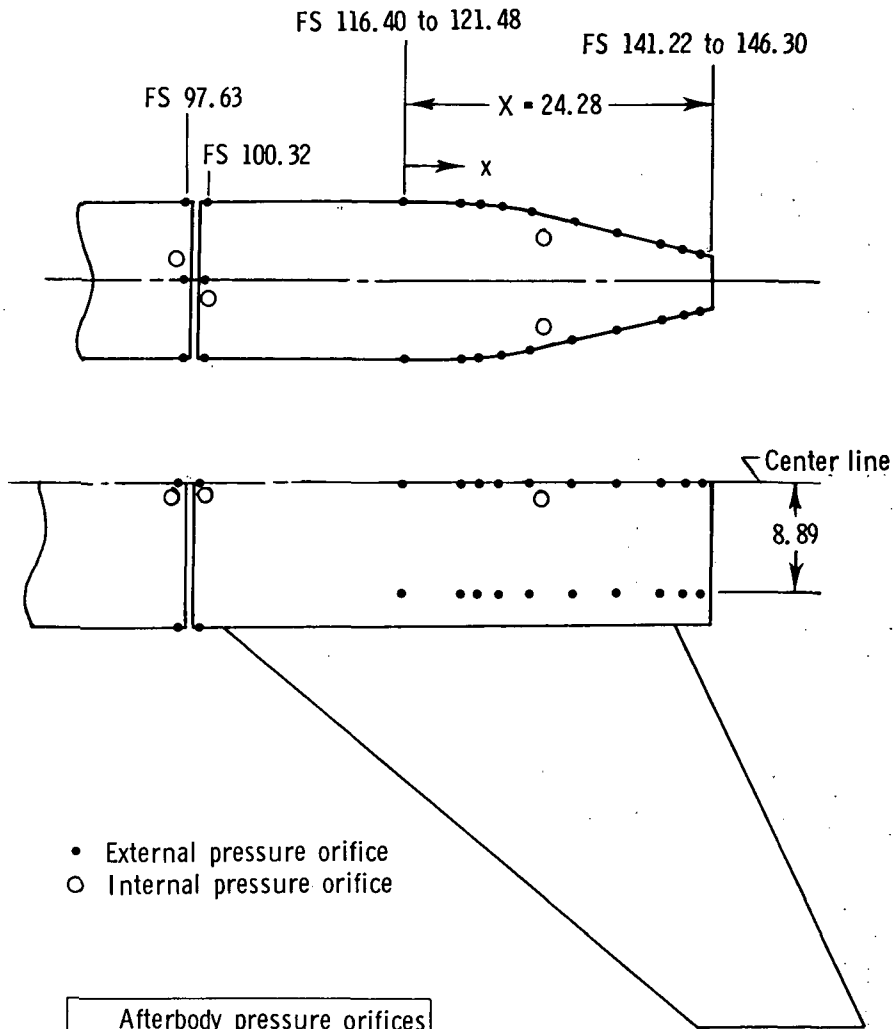

Afterbody pressure orifices	
x, cm	x/X
0	0
4.88	.200
6.25	.257
7.64	.315
10.41	.429
13.89	.572
17.35	.714
20.83	.858
22.88	.943
23.77	.980

Note: x/X locations identical for three exit locations tested.

Figure 8.- Sketch showing location of various pressure orifices. Typical internal pressure orifices shown at approximate locations. All dimensions are in centimeters.

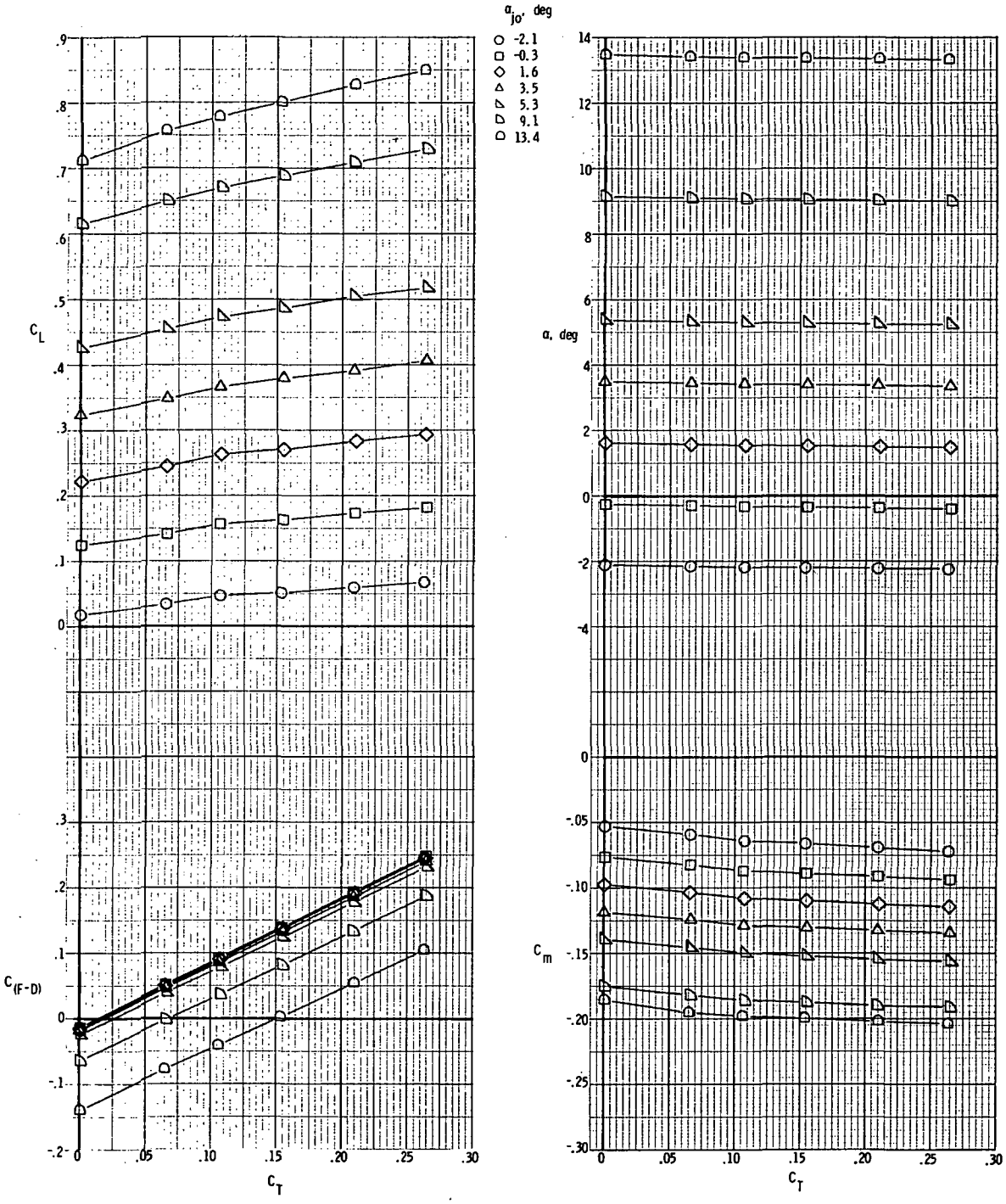

(a) M = 0.70.

Figure 9.- Basic aerodynamic characteristics for model with rectangular exits; $x_e/c_r = 0.07$; $\delta_d = 15^{\circ}$.

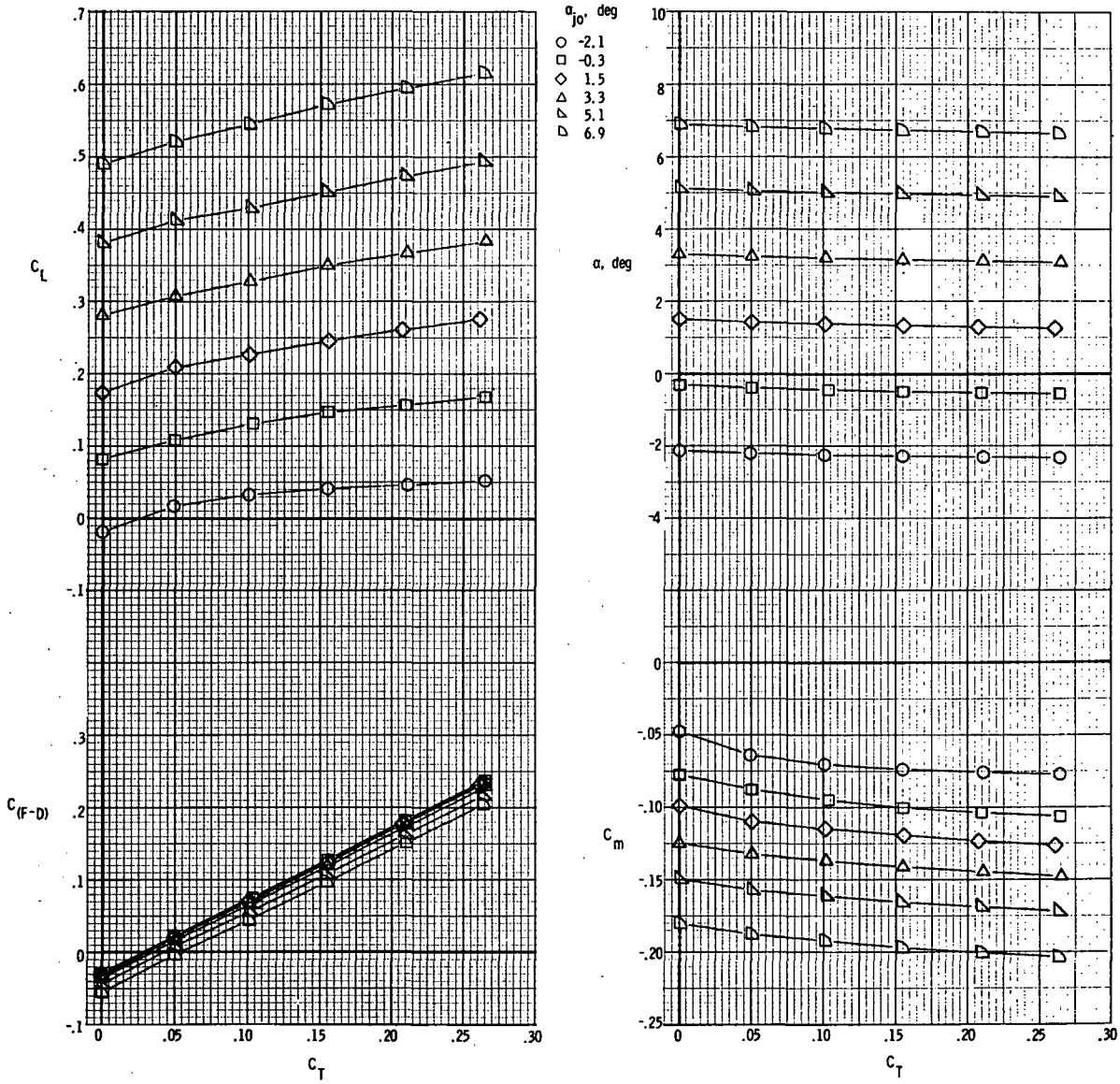

(b) M = 0.90.

Figure 9.- Concluded.

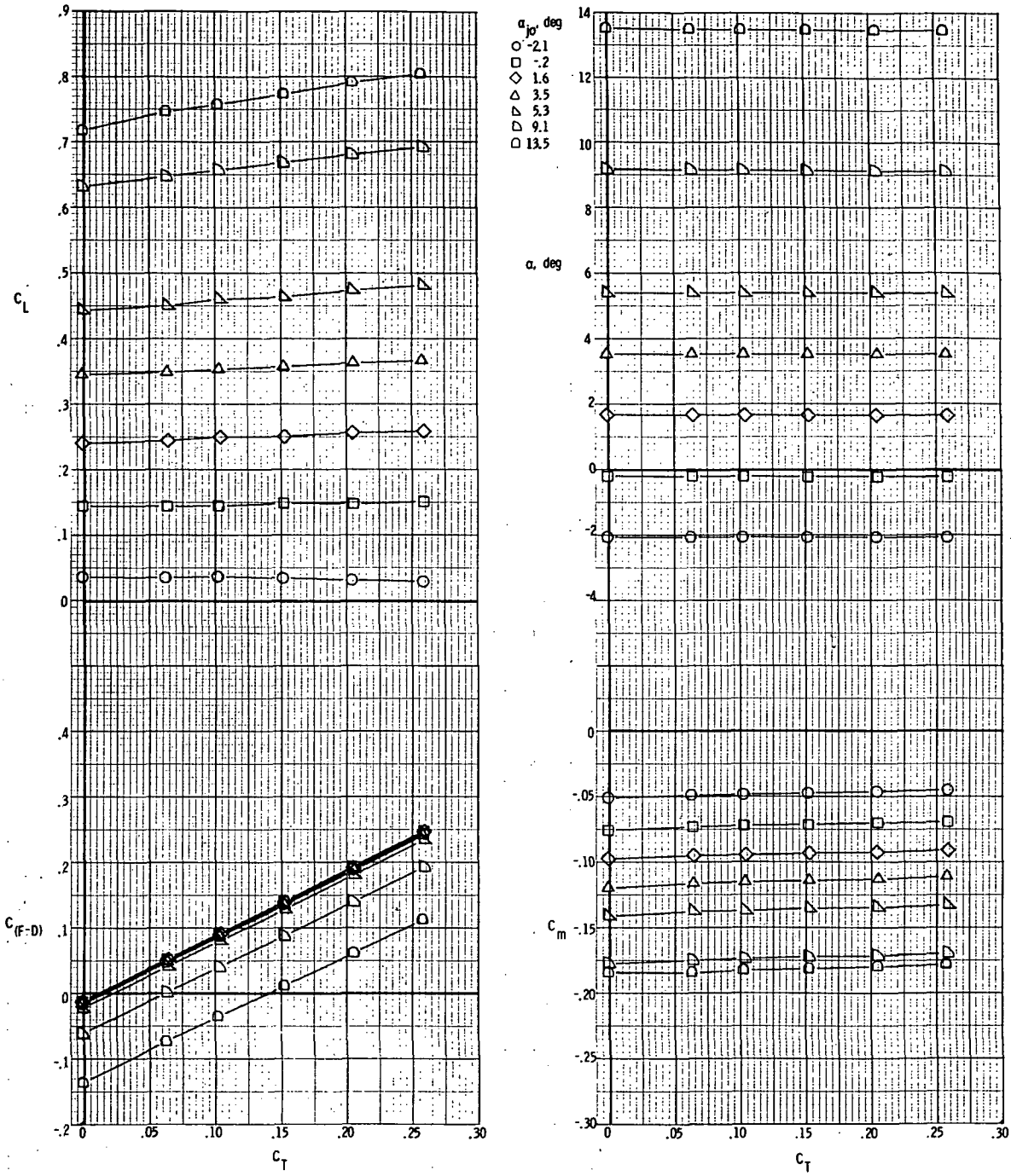

(a) M = 0.70.

Figure 10.- Basic aerodynamic characteristics for model with rectangular exits; $x_e/c_r = 0.14$; $\delta_d = 0^o$.

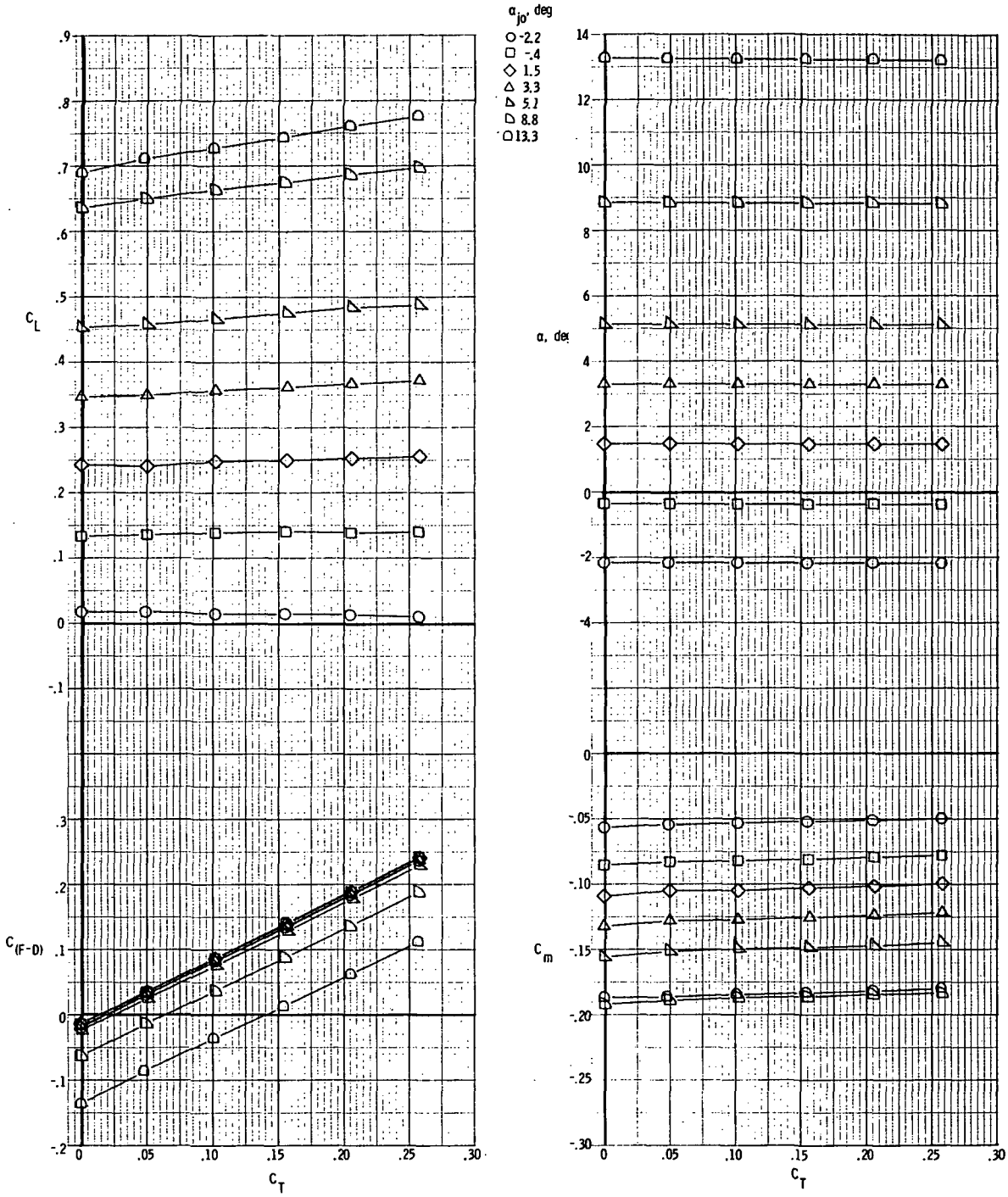

(b) M = 0.80.

Figure 10.- Continued.

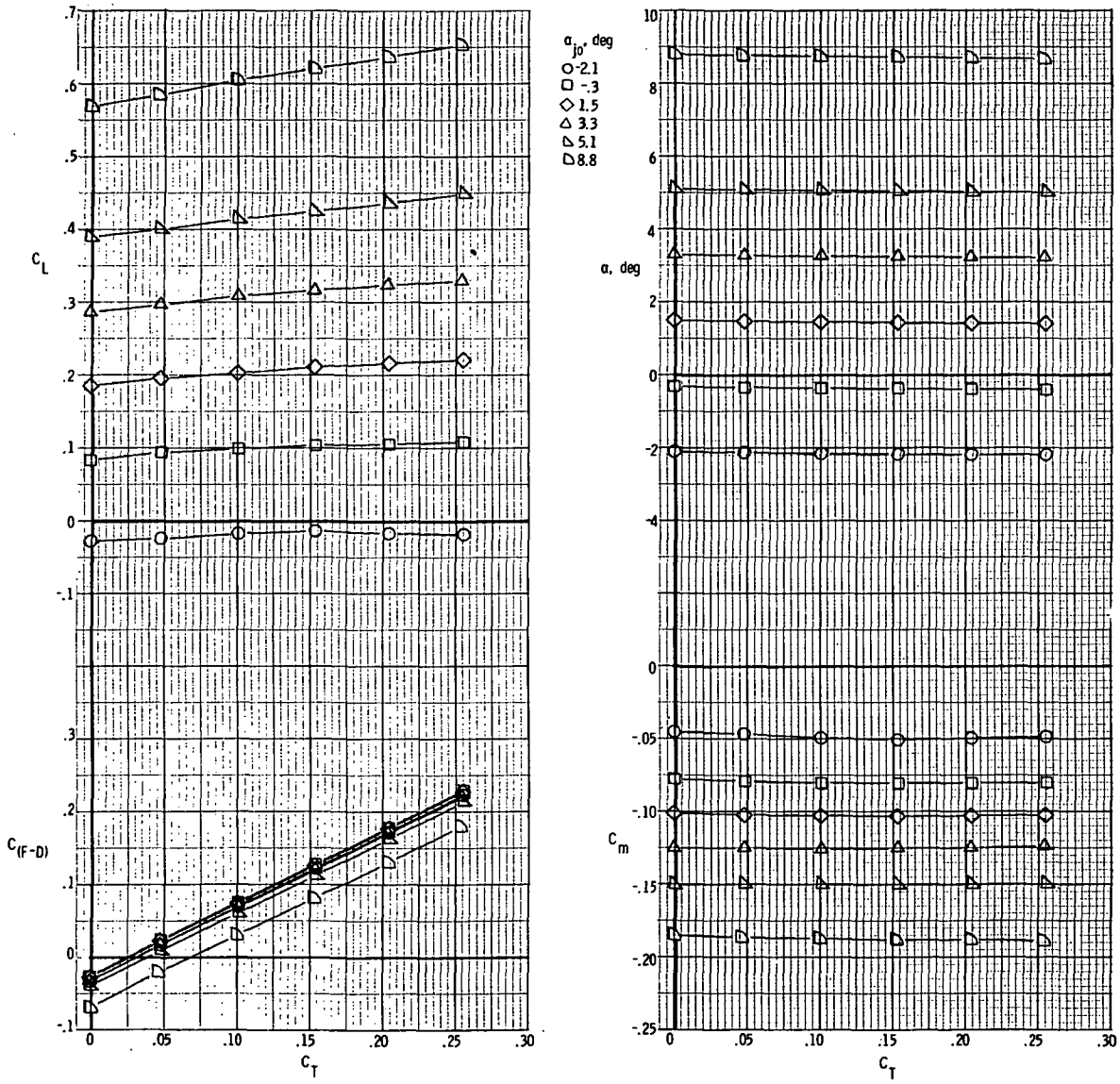

(c) M = 0.90.

Figure 10. - Continued.

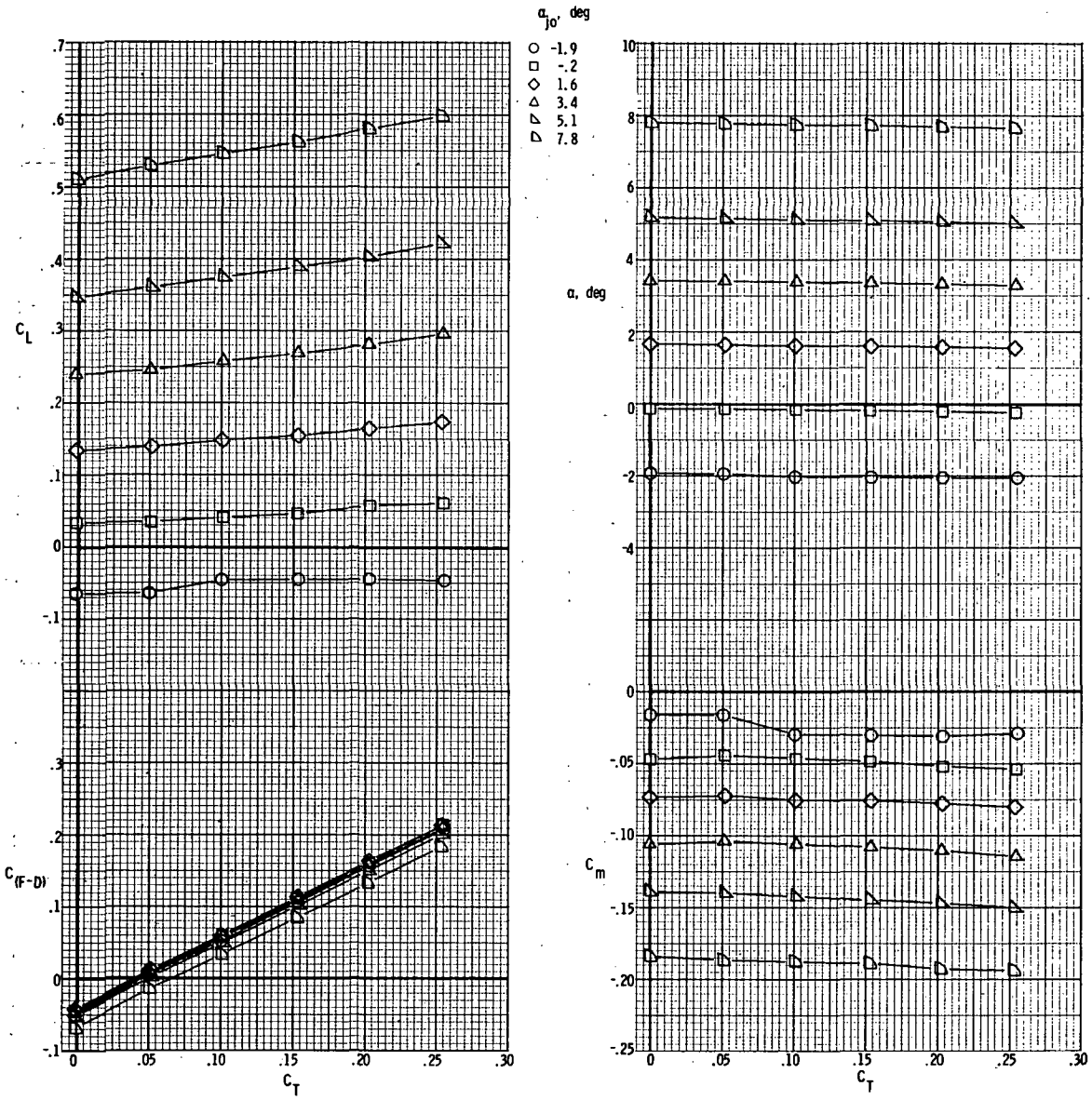

(d) M = 0.95.

Figure 10.- Continued.

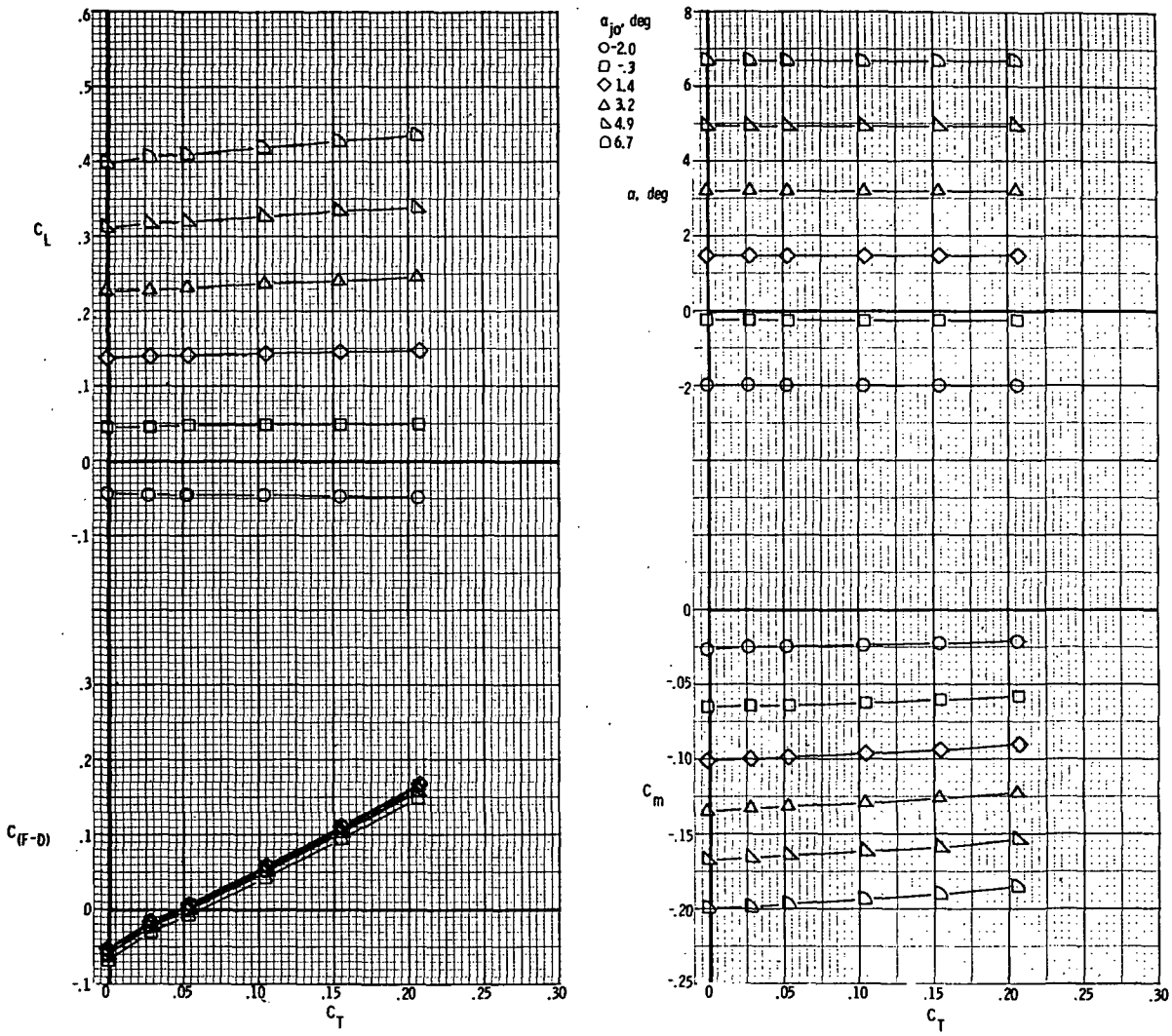

(e) M = 1.20.

Figure 10.- Concluded.

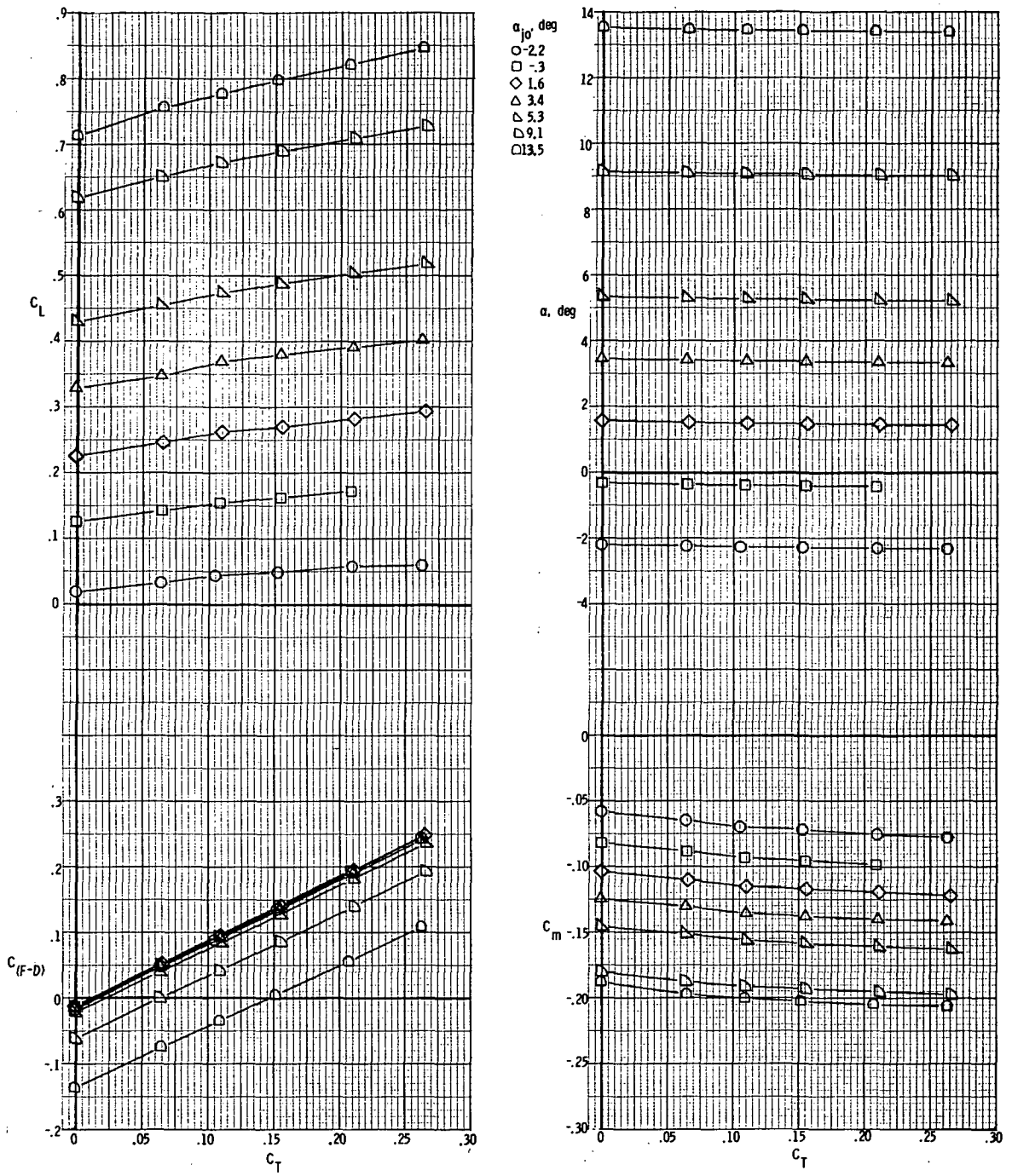

(a) M = 0.70.

Figure 11.- Basic aerodynamic characteristics for model with rectangular exits; $x_e/c_r = 0.14$; $\delta_d = 15^{\circ}$.

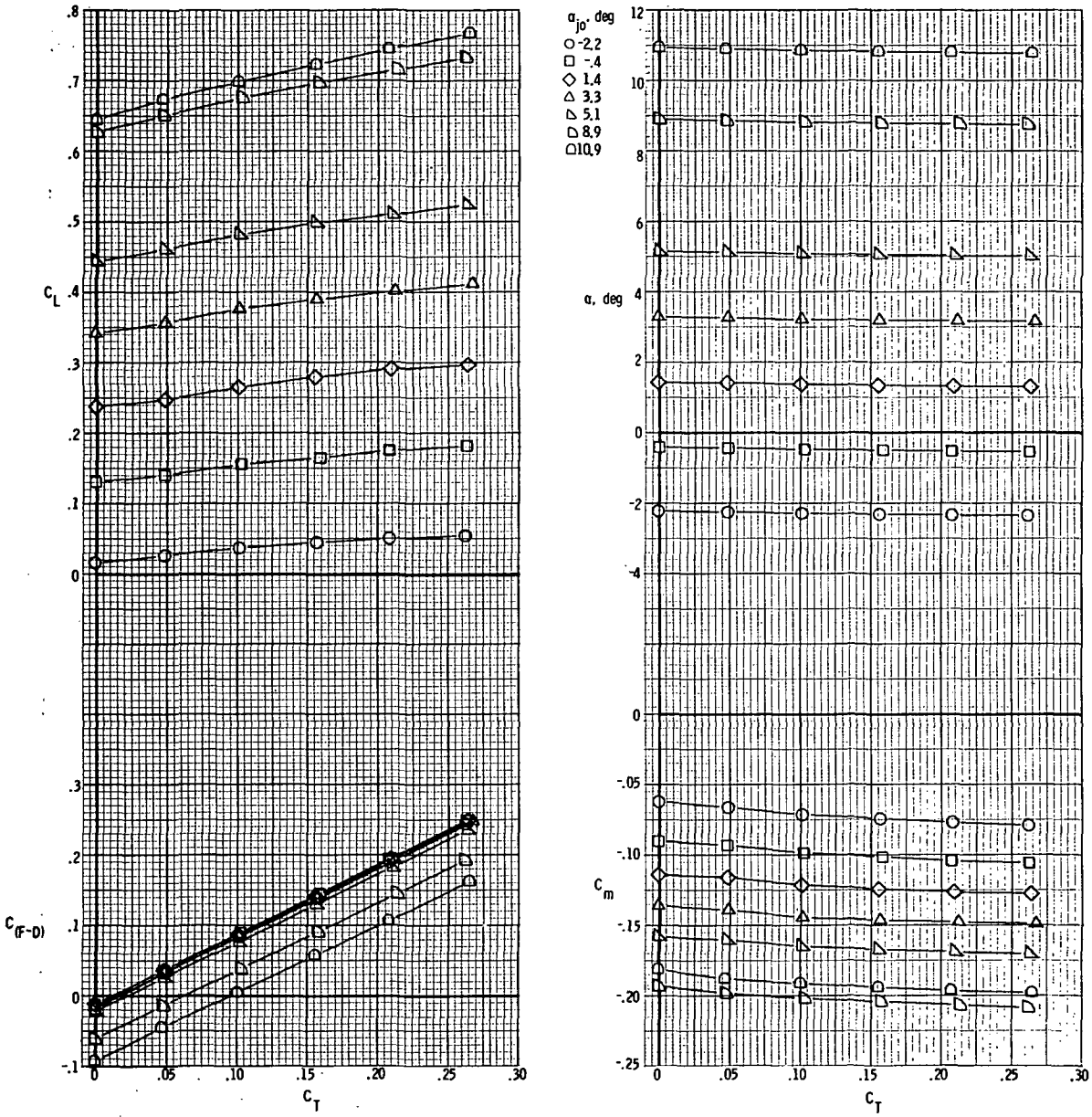

(b) M = 0.80.

Figure 11.- Continued.

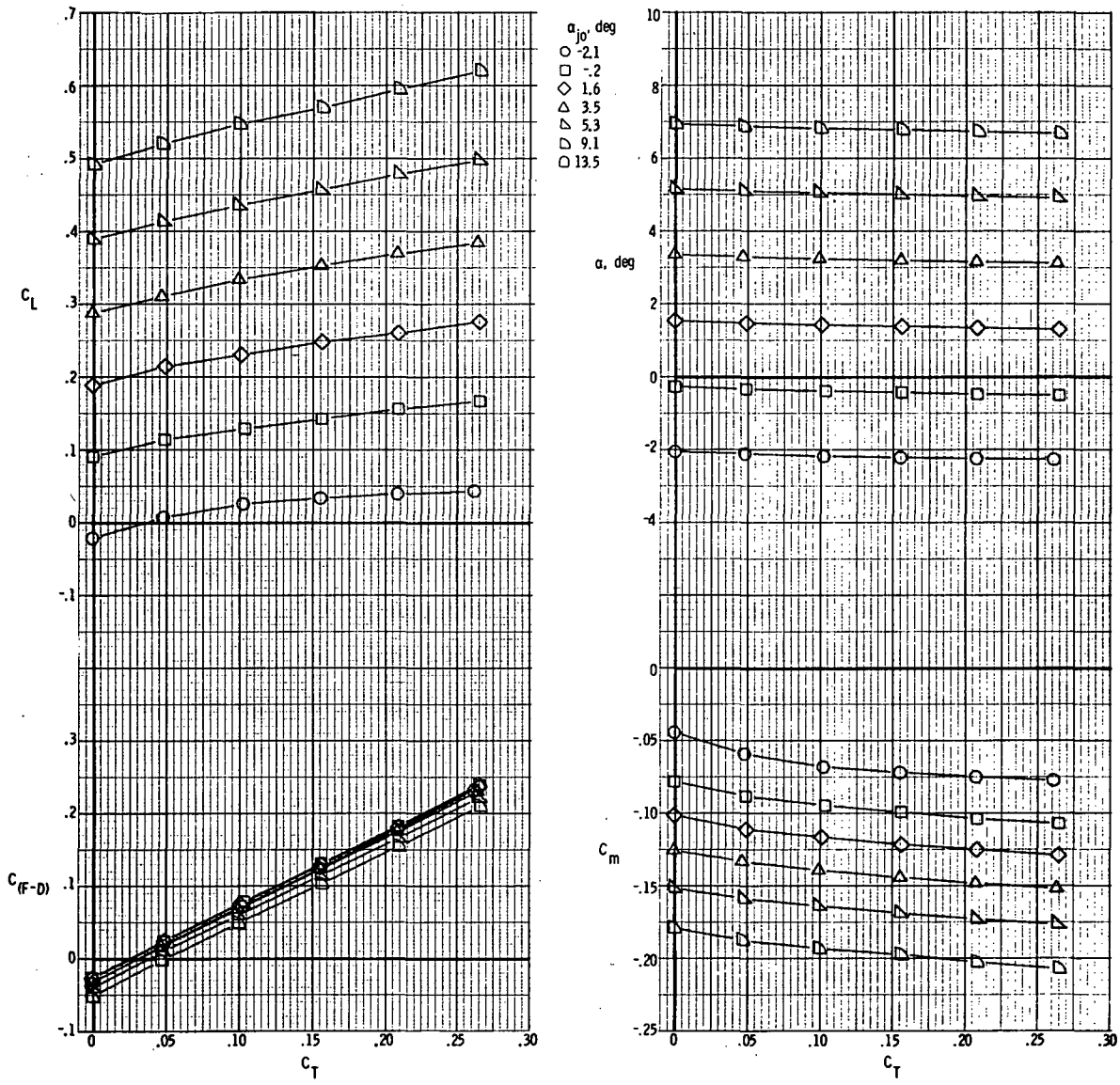

(c) M = 0.90.

Figure 11. - Continued.

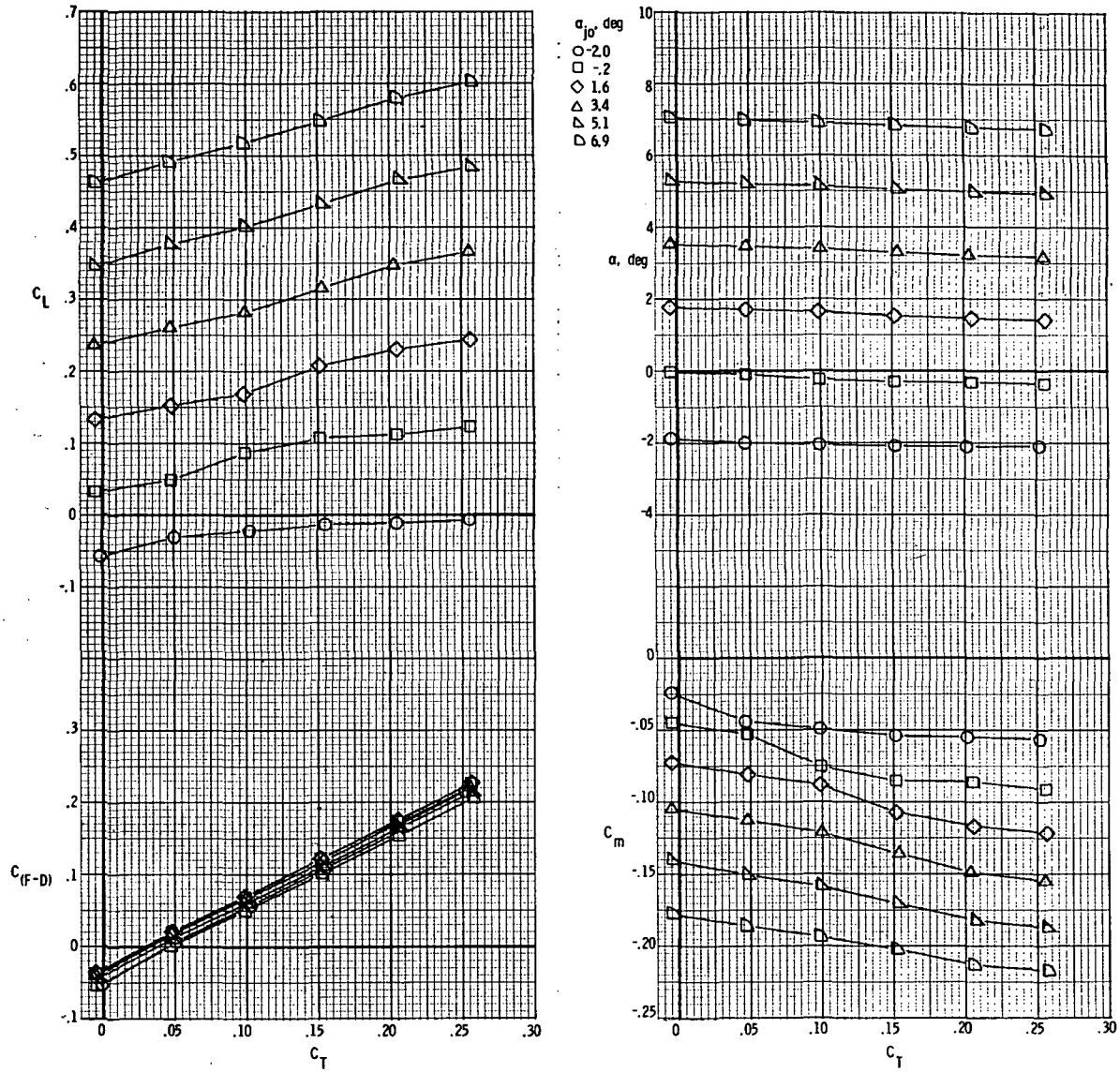

(d) M = 0.95.

Figure 11.- Concluded.

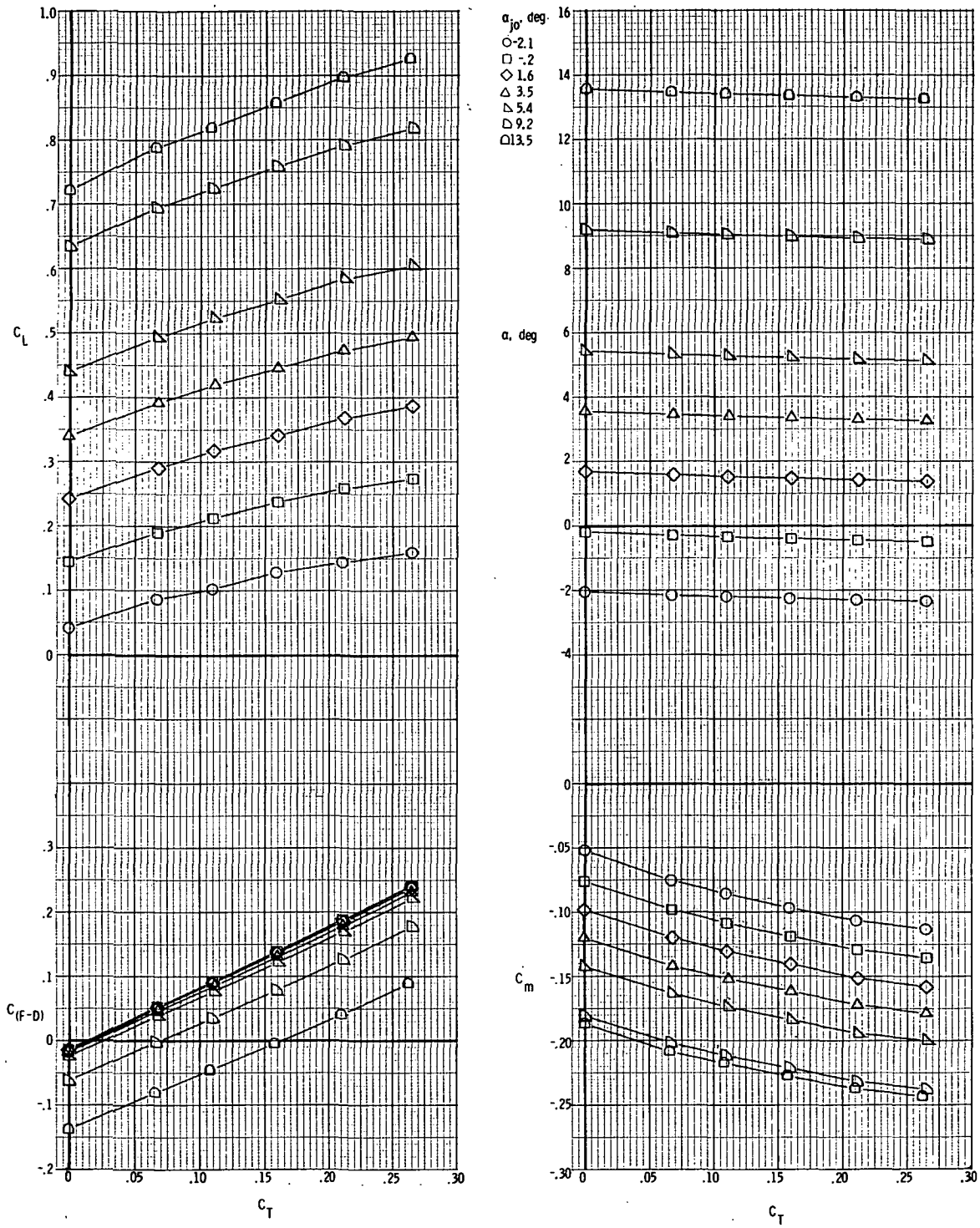

(a) M = 0.70.

Figure 12.- Basic aerodynamic characteristics for model with rectangular exits; $x_e/c_r = 0.14$; $\delta_d = 30^{\circ}$.

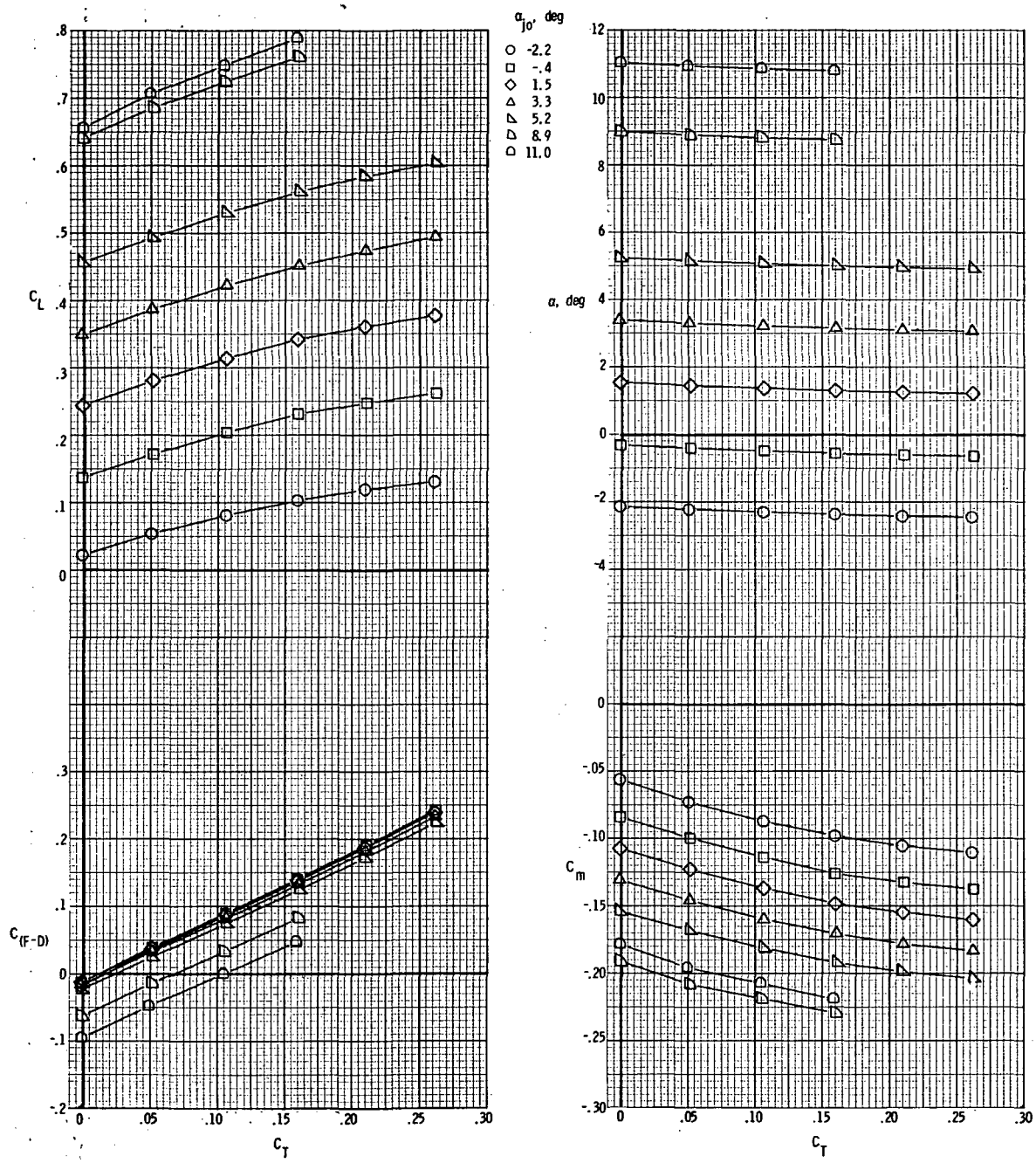

(b) M = 0.80.

Figure 12.- Continued.

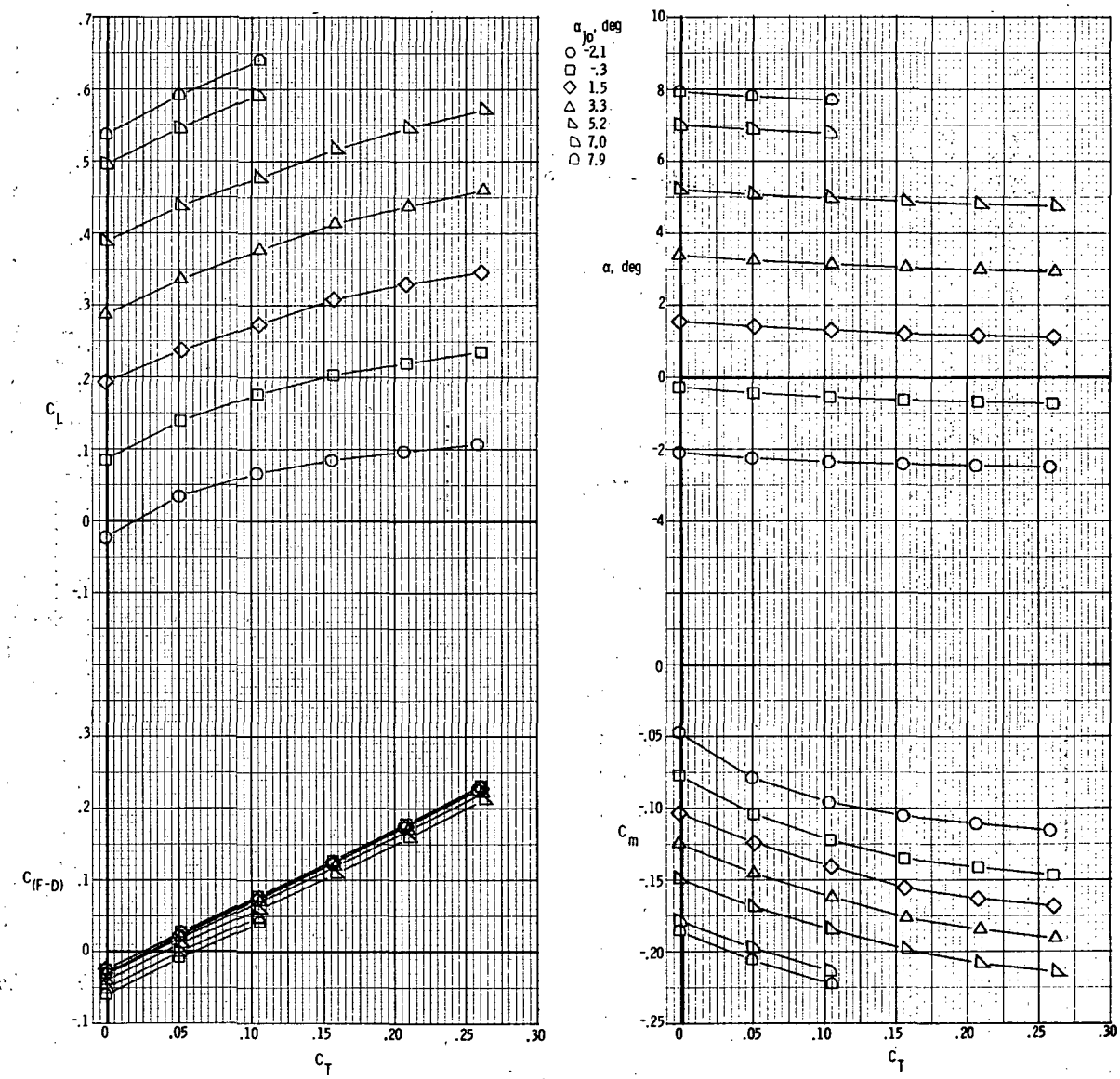

(c) M = 0.90.

Figure 12.- Continued.

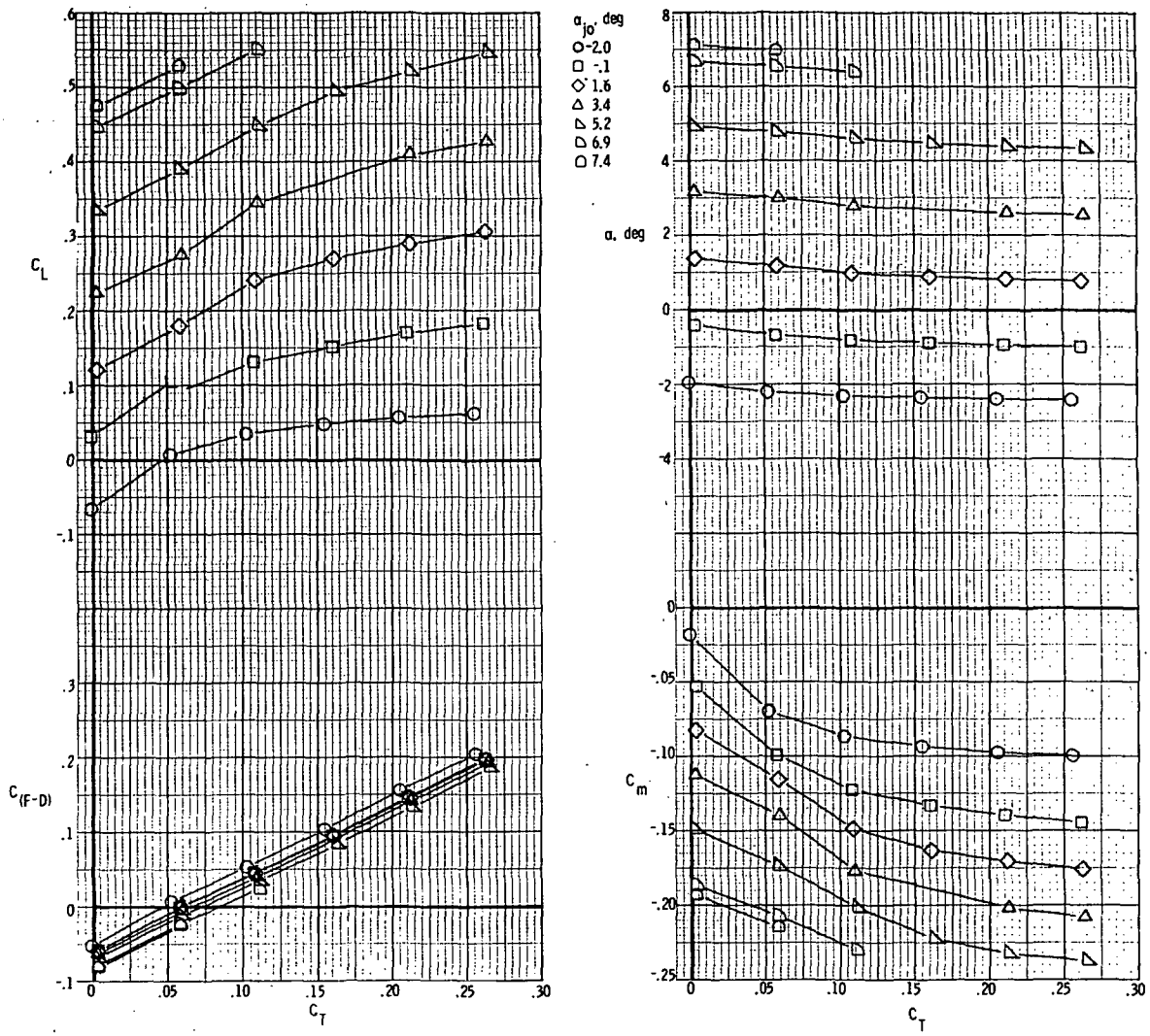

(d) M = 0.95.

Figure 12.- Continued.

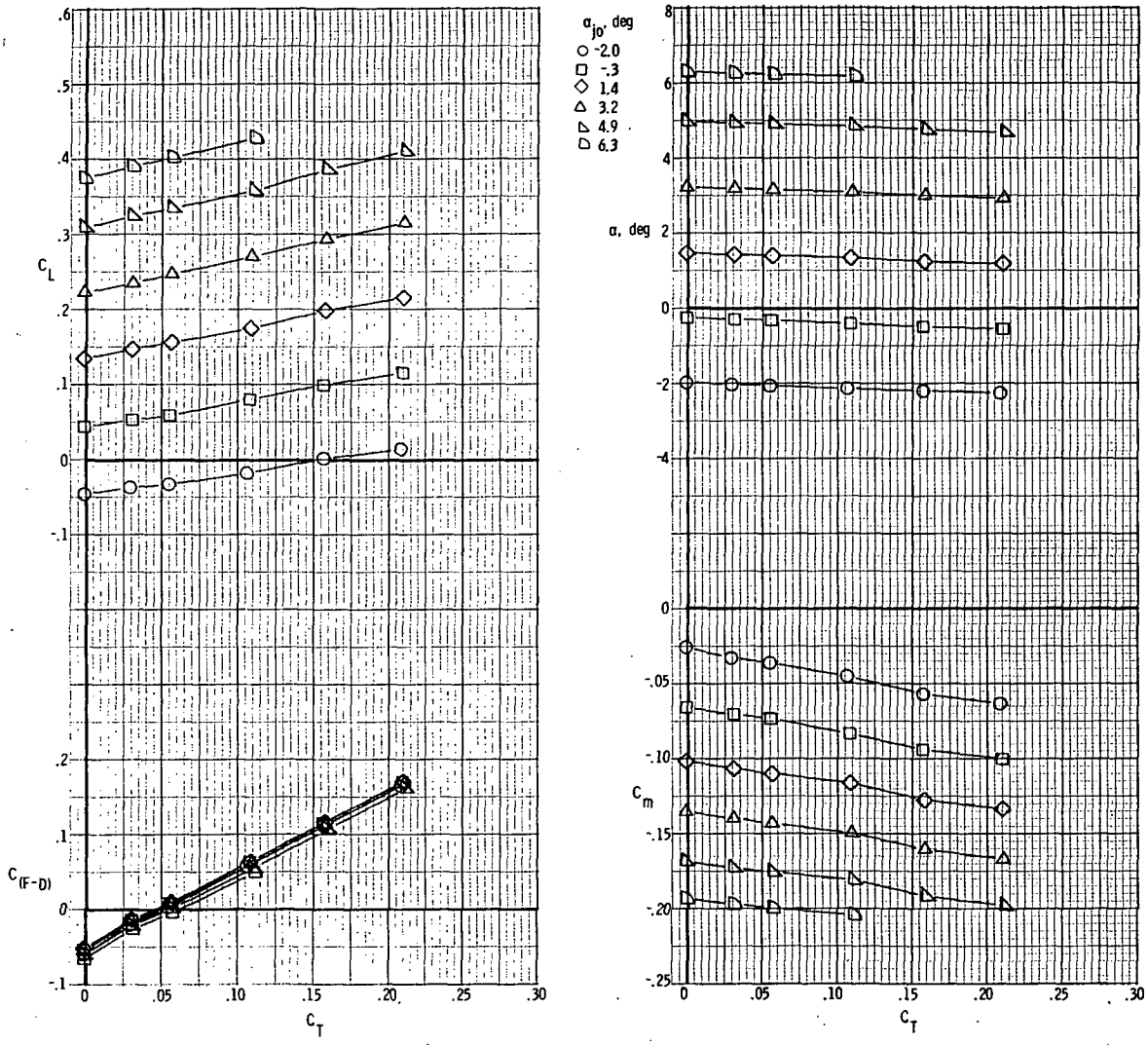

(e) M = 1.20.

Figure 12.- Concluded.

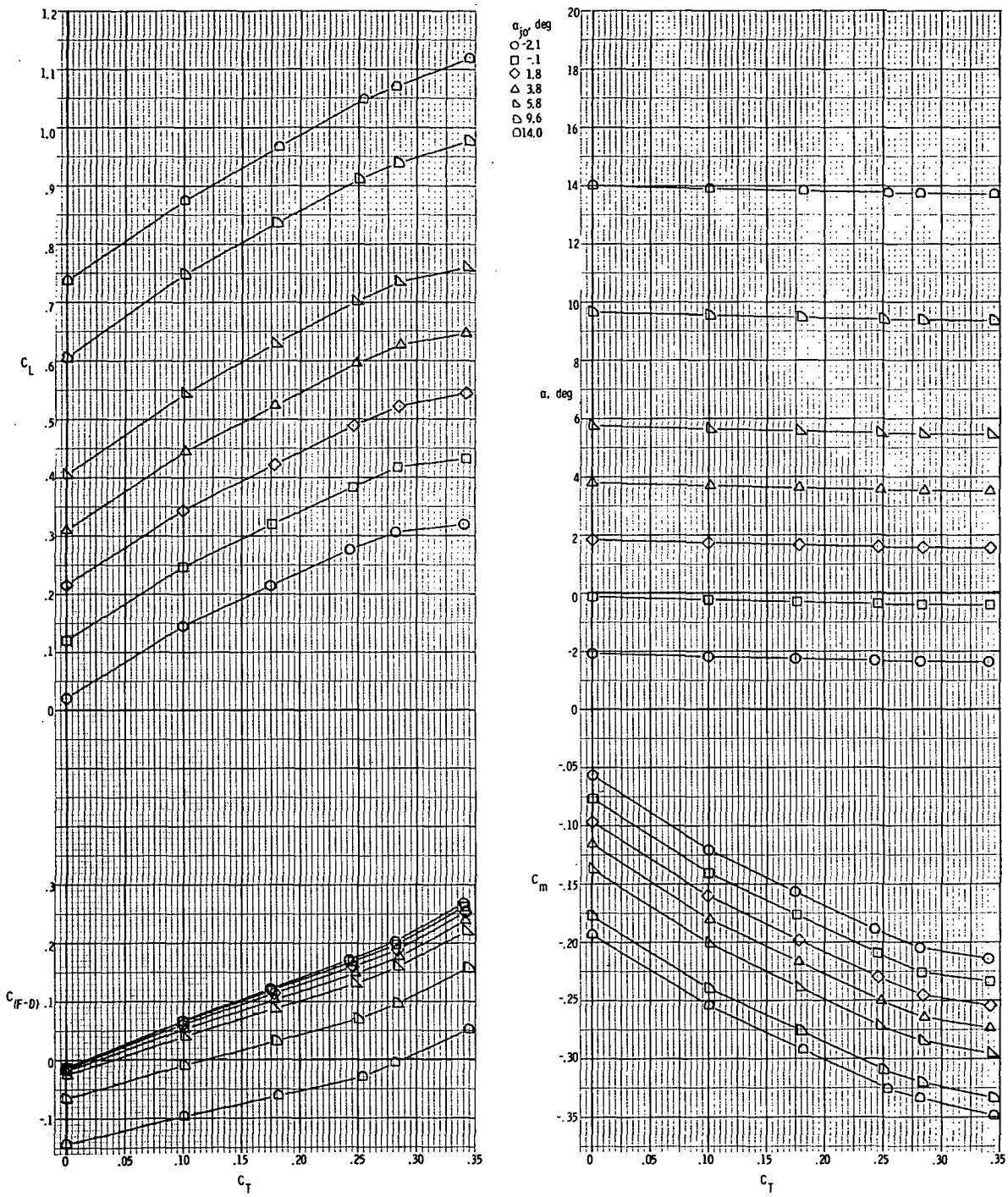

(a) M = 0.40.

Figure 13.- Basic aerodynamic characteristics for model with rectangular exits; $x_e/c_r = 0.14$; $\delta_d = 45^{\circ}$.

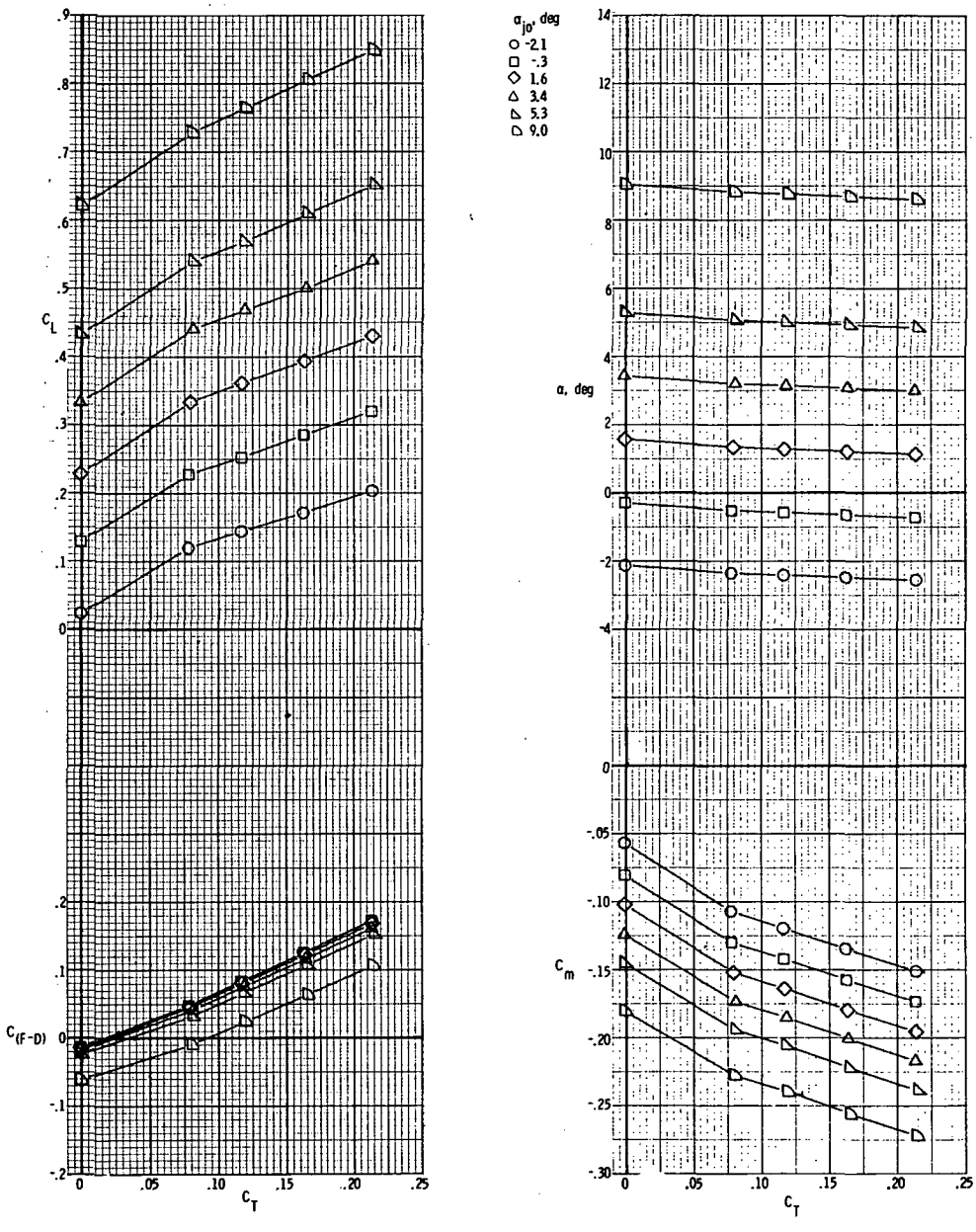

(b) M = 0.70.

Figure 13.- Continued.

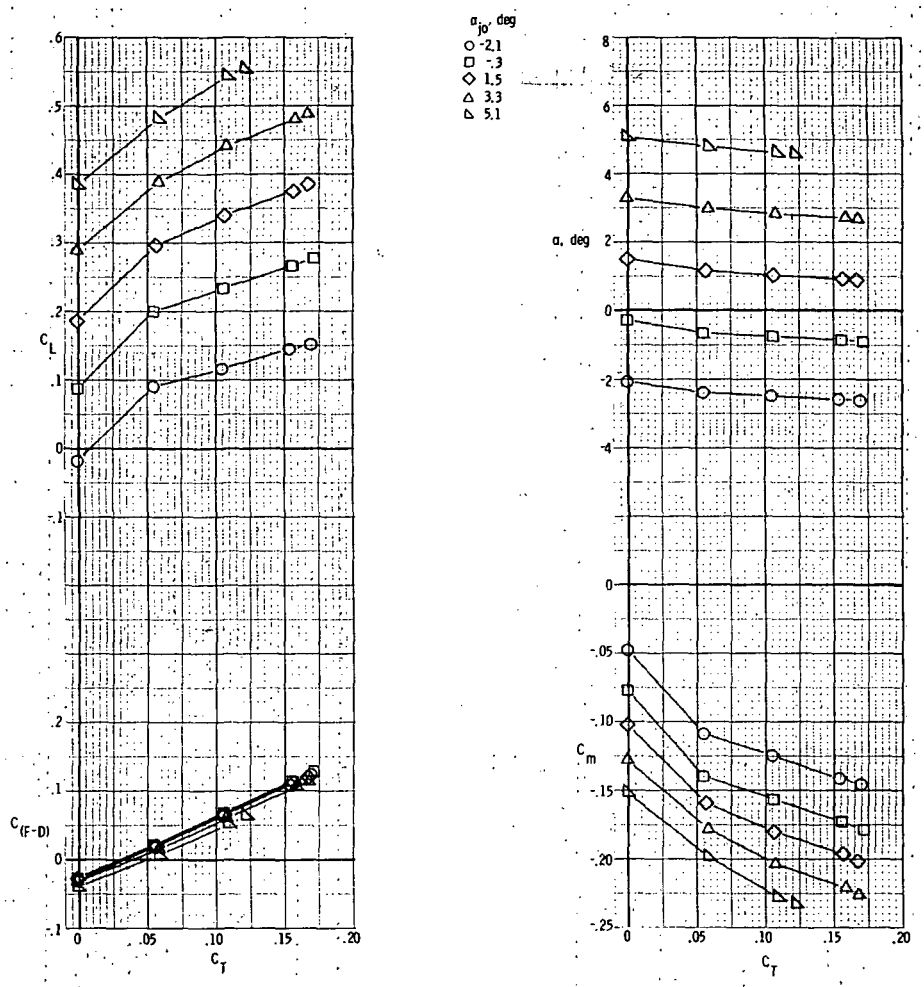

(c) M = 0.90.

Figure 13.- Concluded.

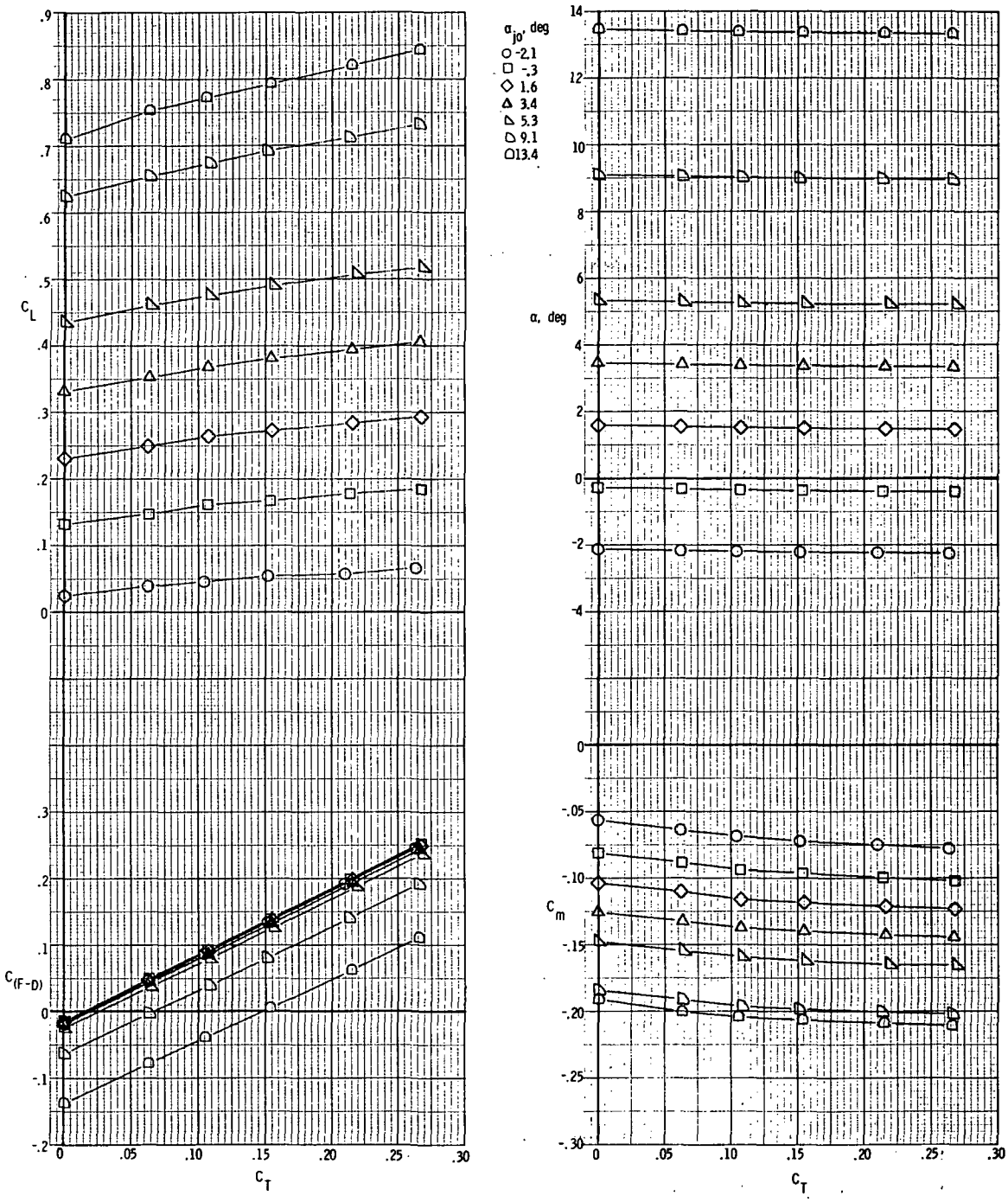

(a) M = 0.70.

Figure 14.- Basic aerodynamic characteristics for model with rectangular exits; $x_e/c_r = 0.21$; $\delta_d = 15^{\circ}$.

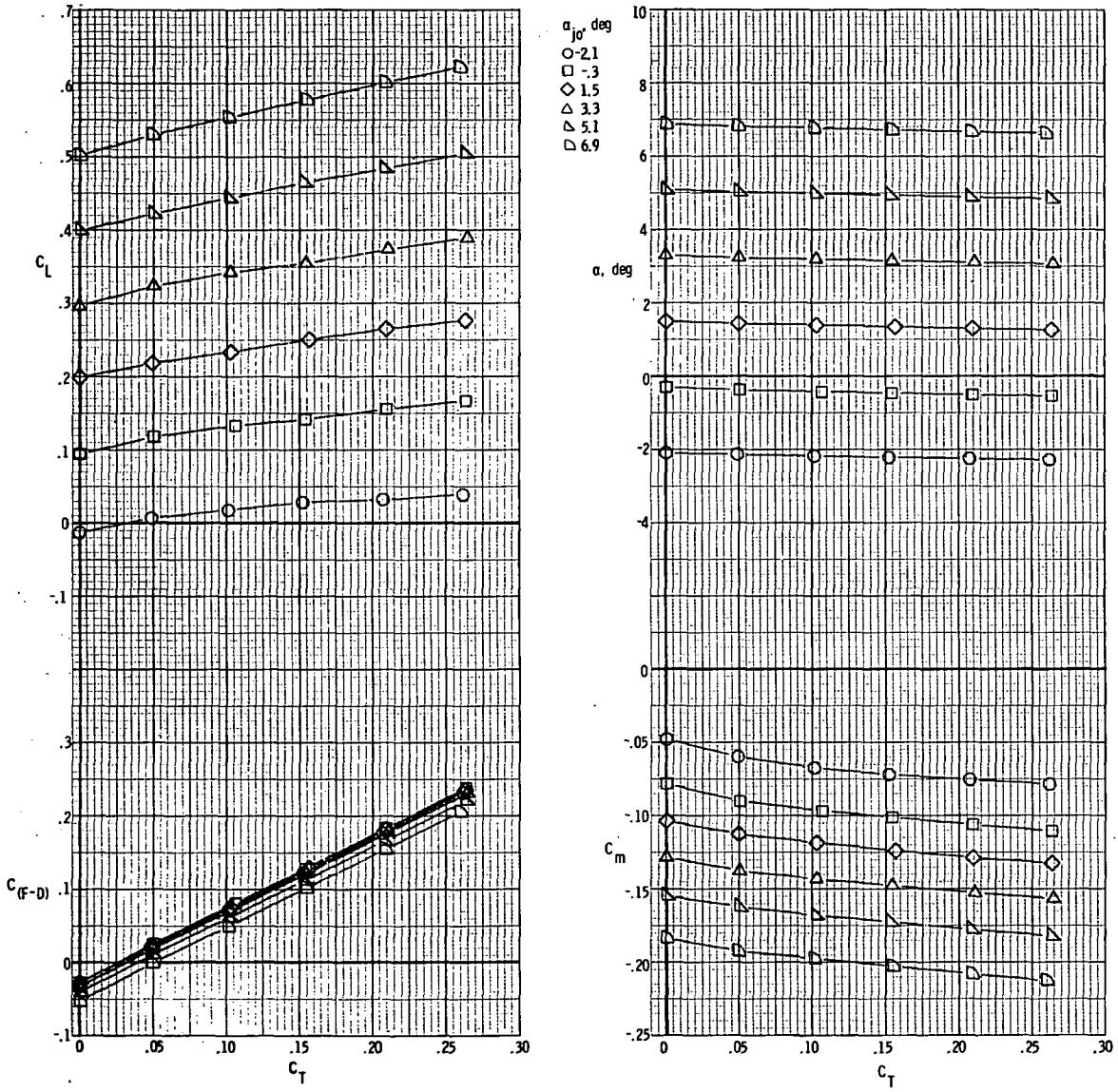

(b) M = 0.90.

Figure 14.- Concluded.

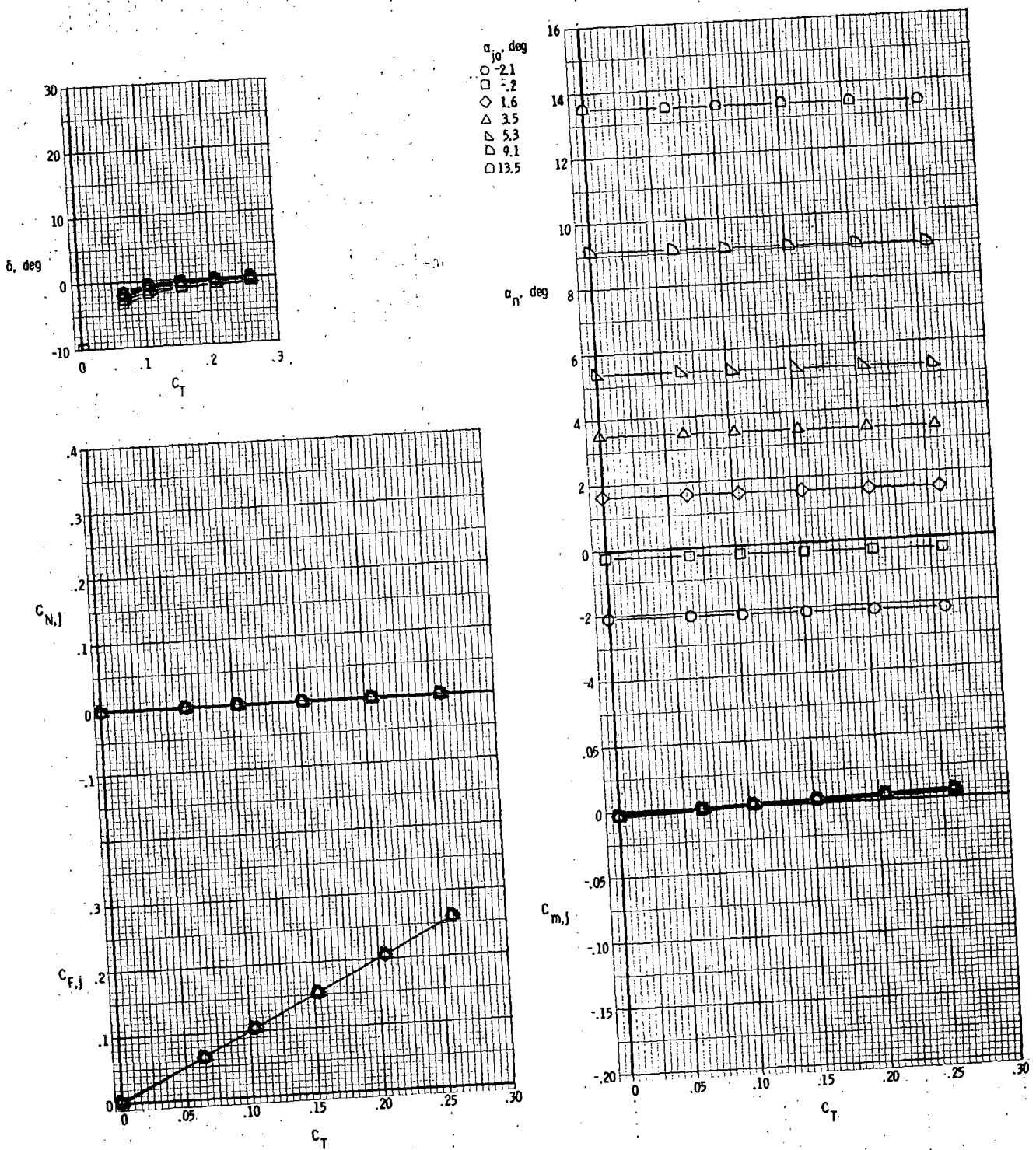

(a) M = 0.70.

Figure 15.- Basic nozzle thrust characteristics for model with rectangular exits; $x_e/c_r = 0.14$; $\delta_d = 0^o$.

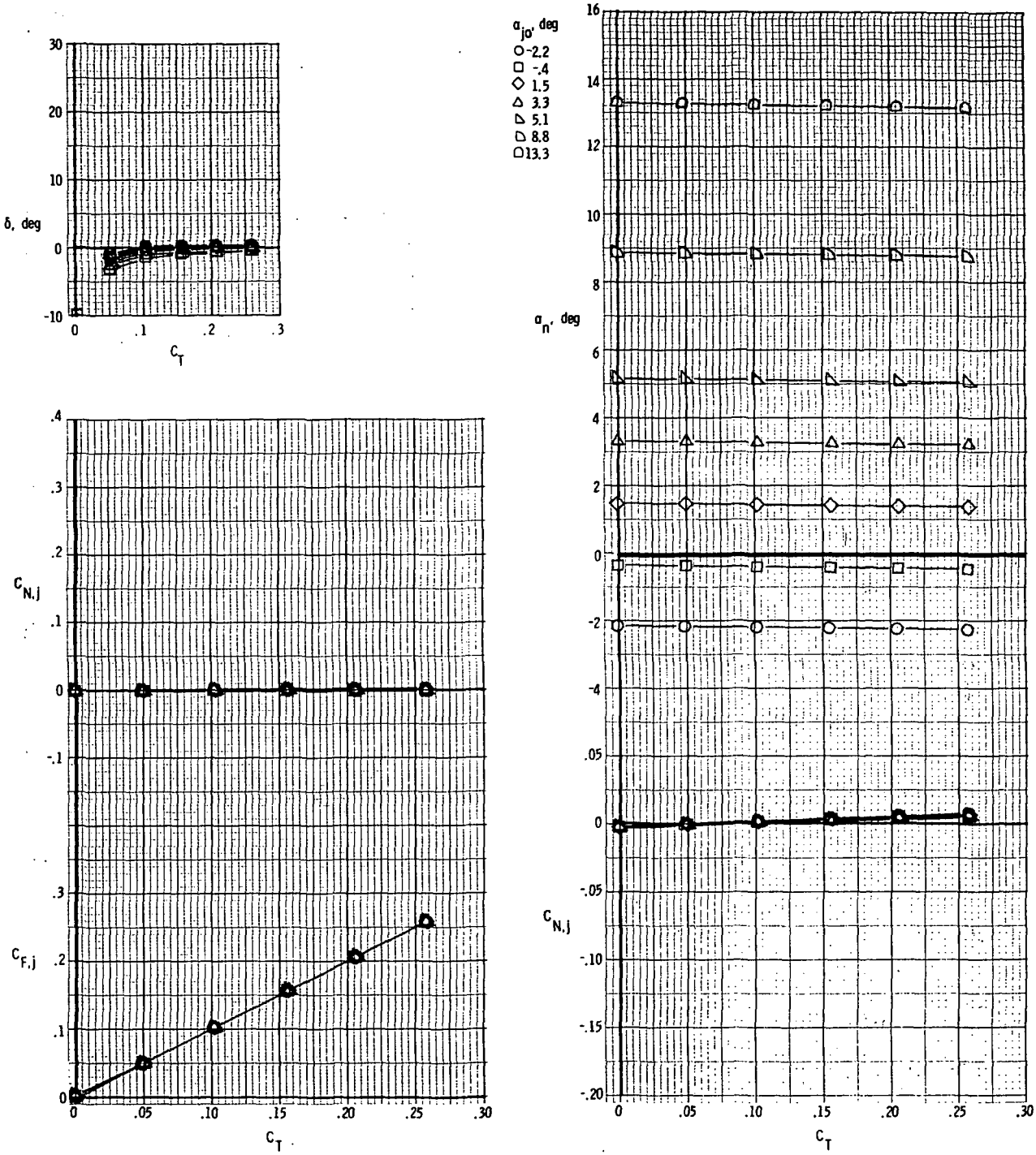

(b) M = 0.80.

Figure 15.- Continued.

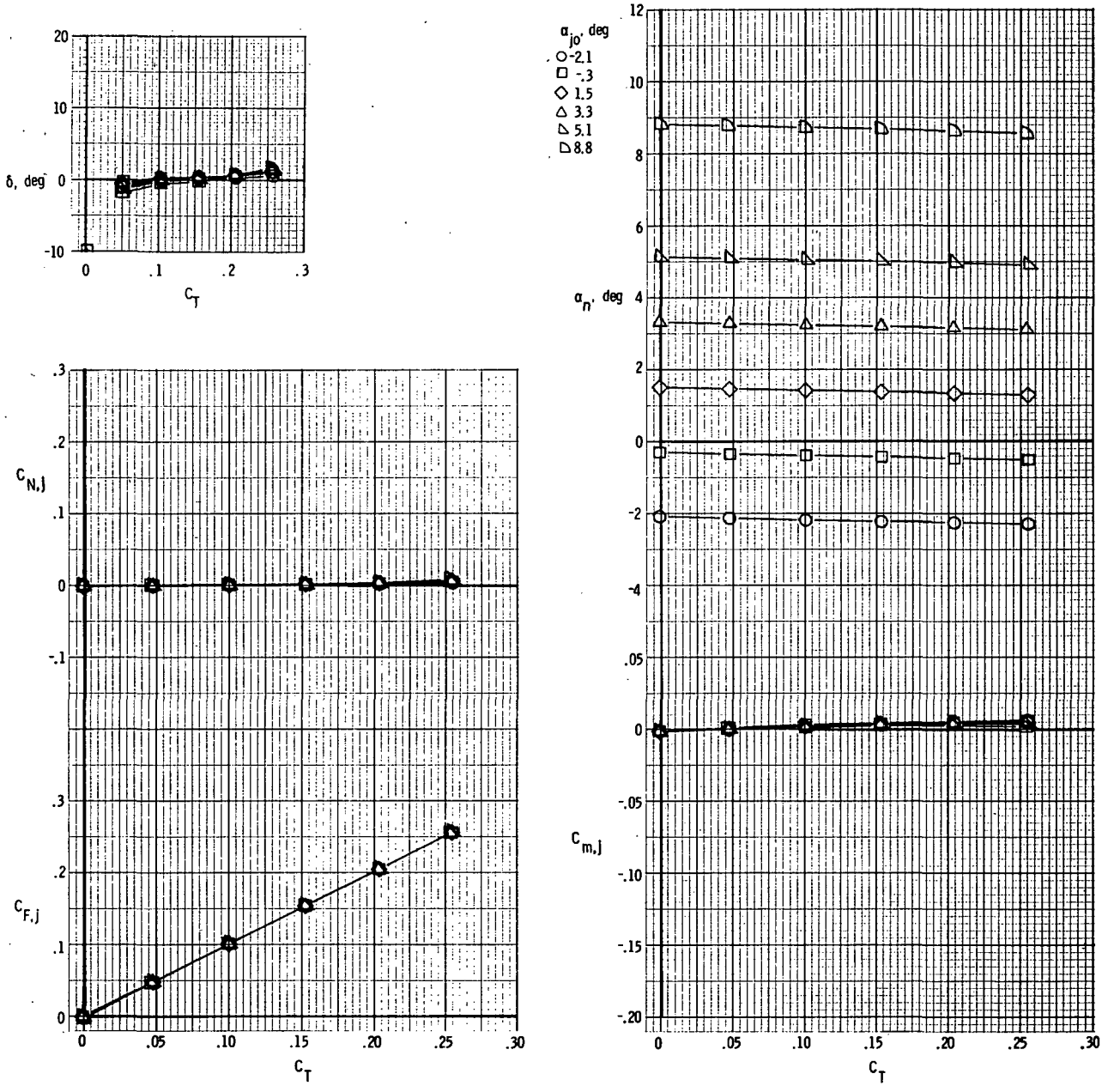

(c) M = 0.90.

Figure 15.- Continued.

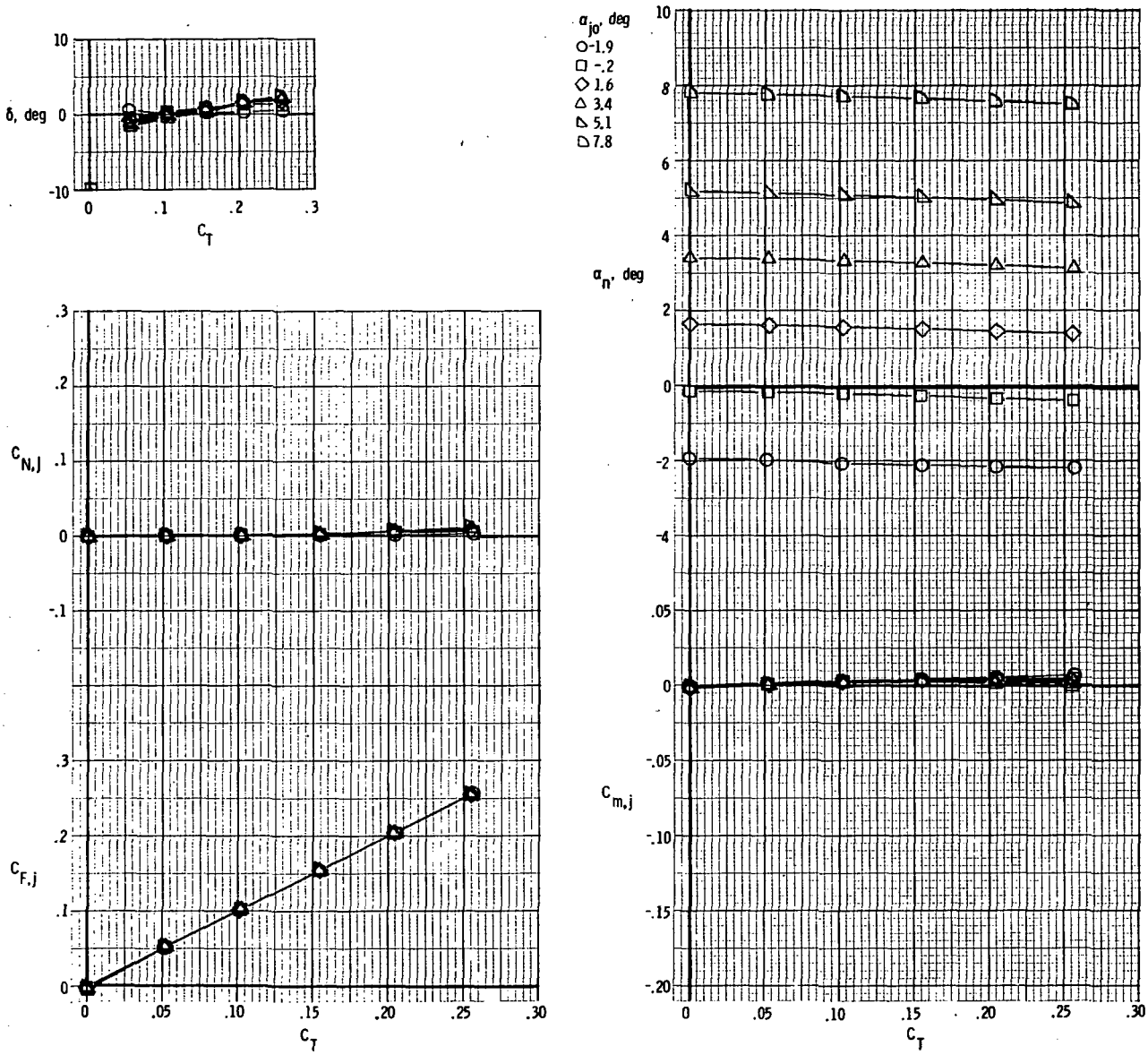

(d) M = 0.95.

Figure 15.- Continued.

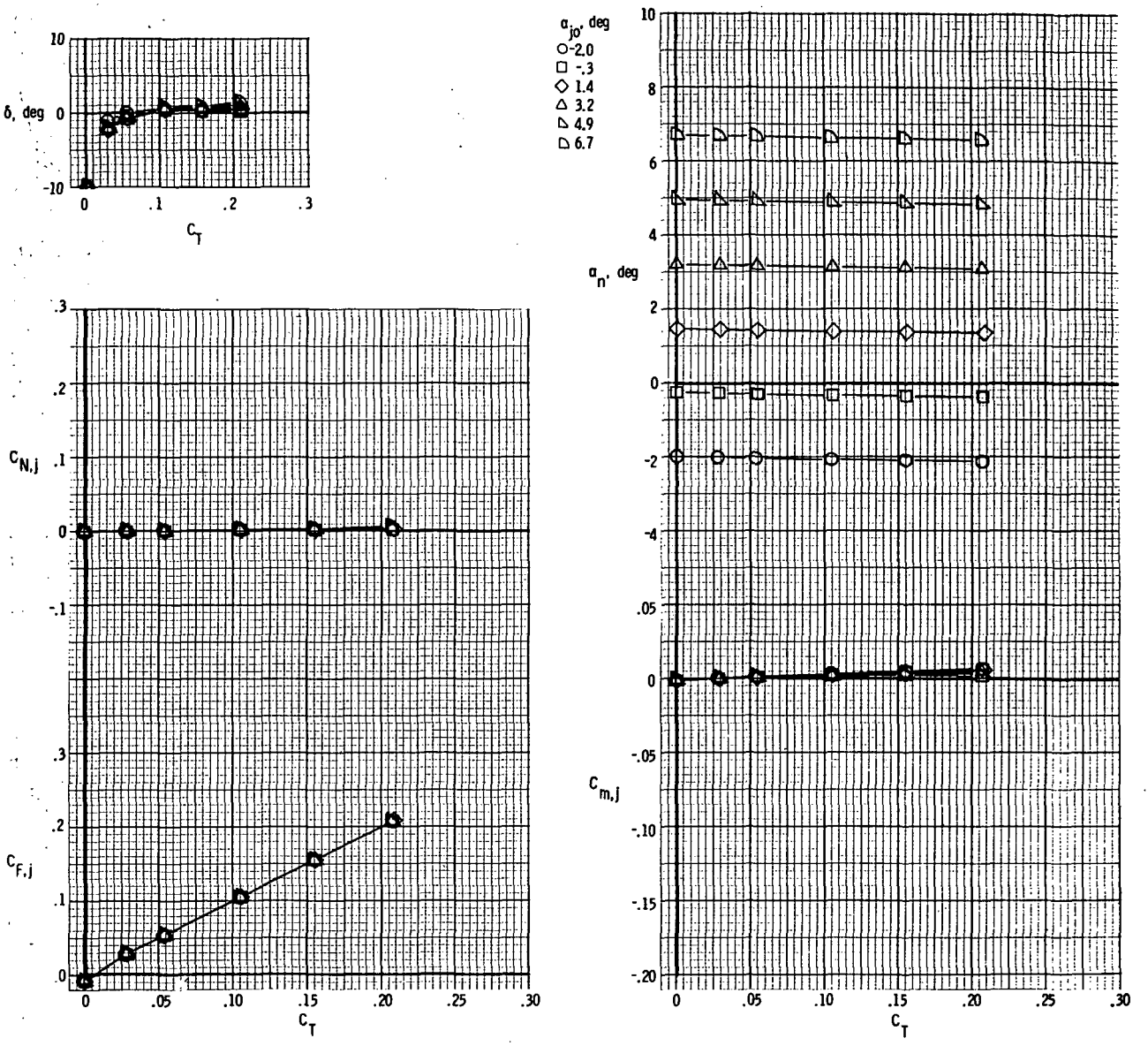

(e) M = 1.20.

Figure 15.- Concluded.

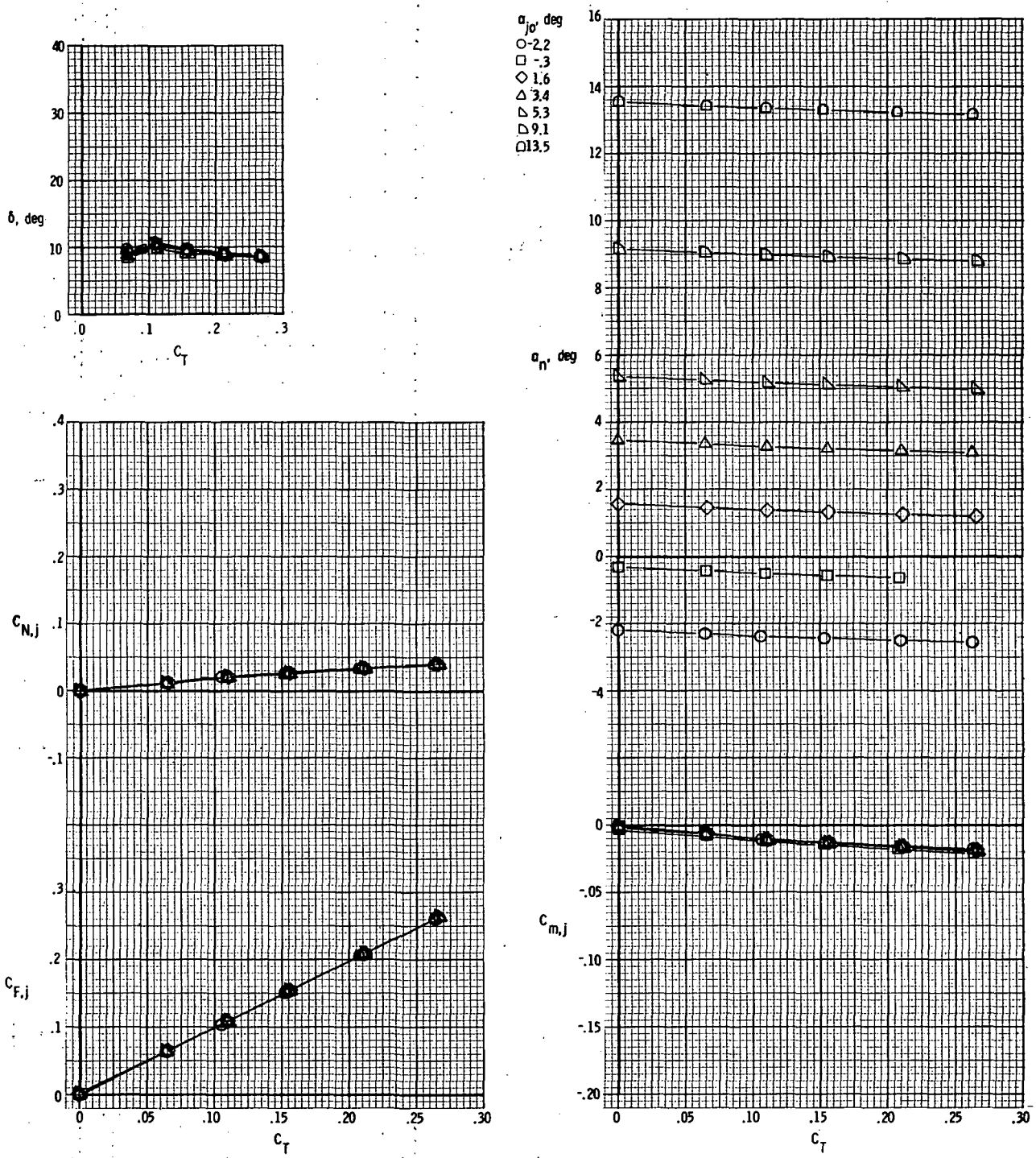

(a) M = 0.70.

Figure 16.- Basic nozzle thrust characteristics for model with rectangular exits; $x_e/c_r = 0.14$; $\delta_d = 15^{\circ}$.

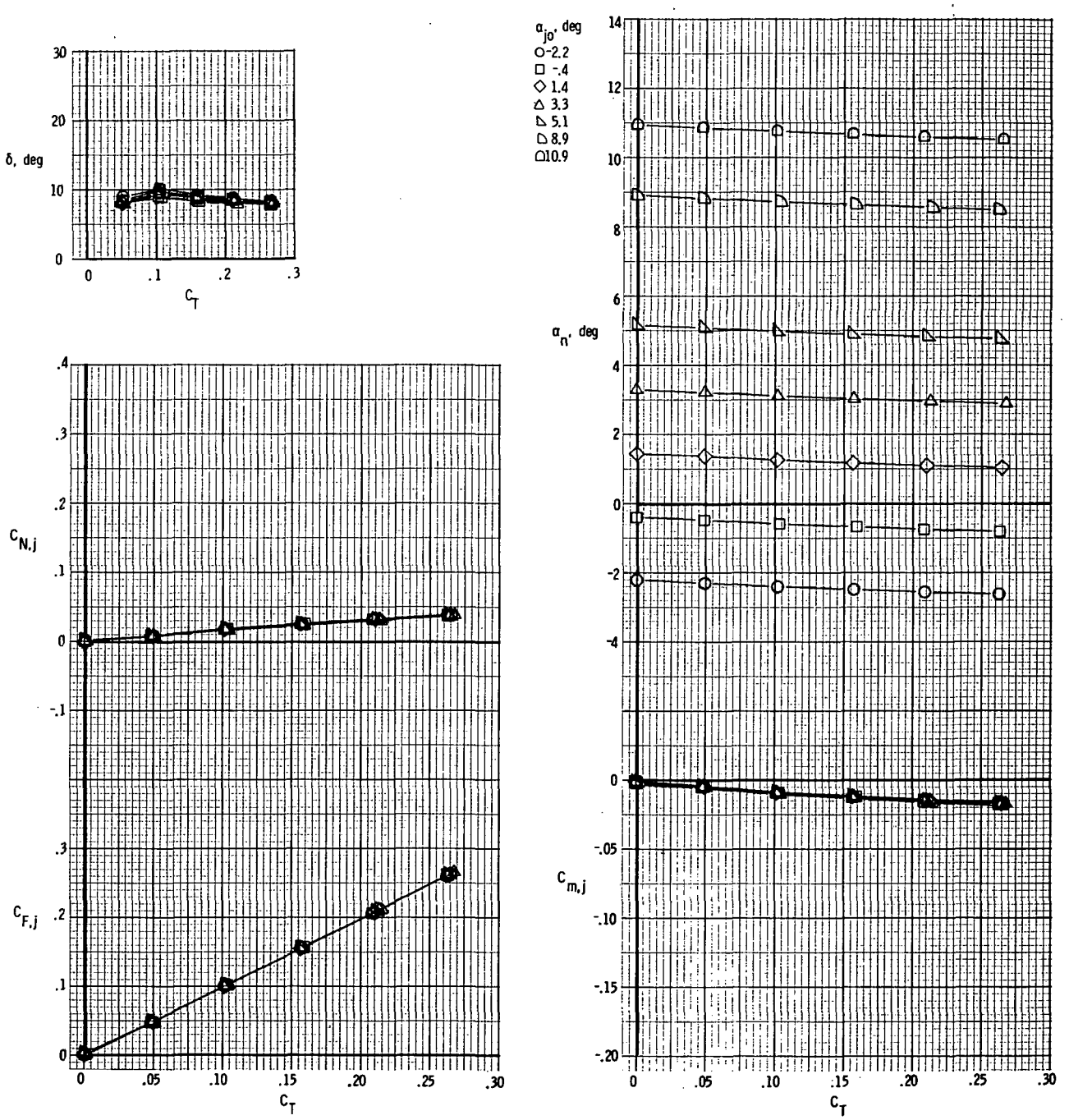

(b) M = 0.80.

Figure 16.- Continued.

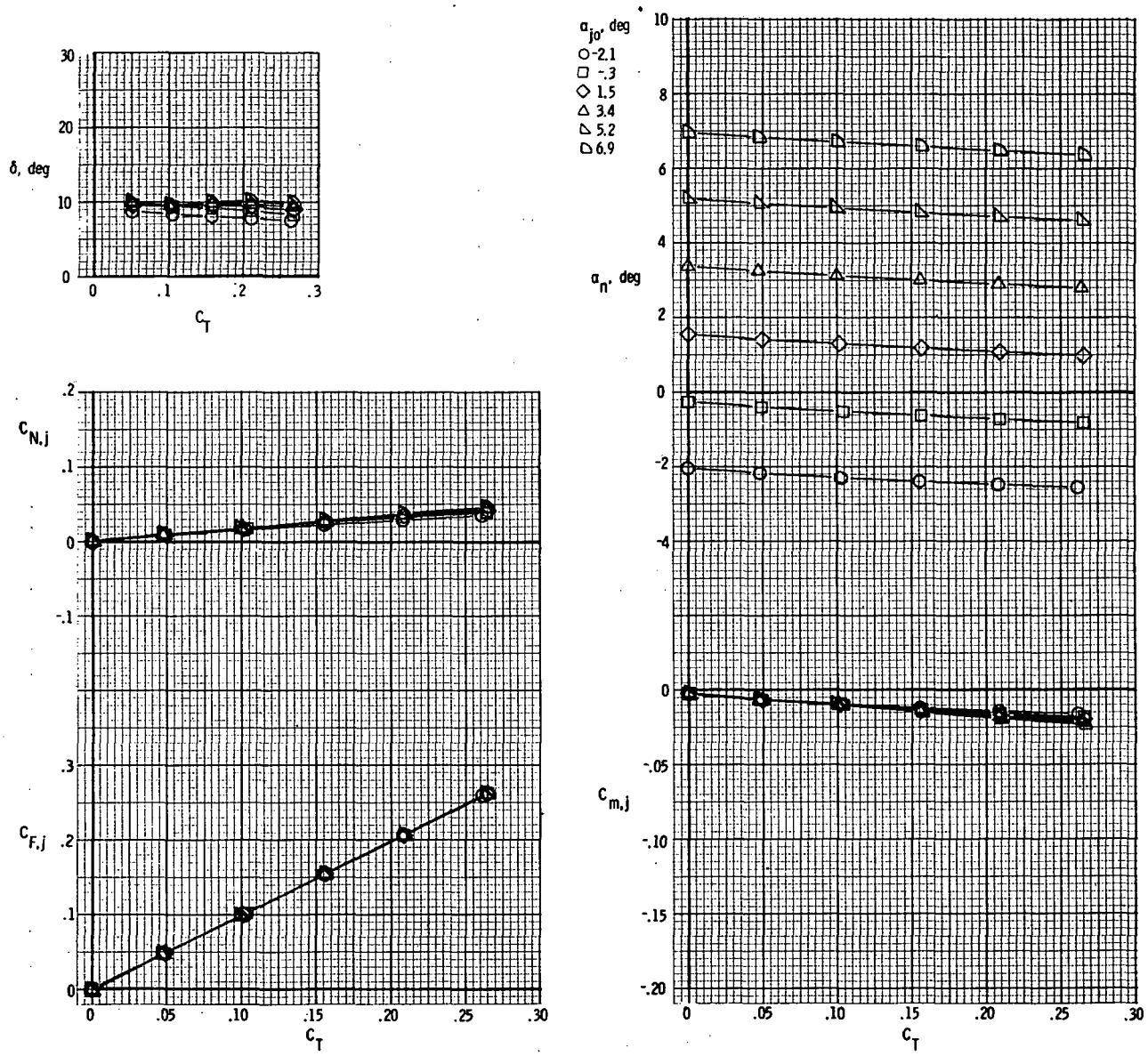

(c) M = 0.90.

Figure 16.- Continued.

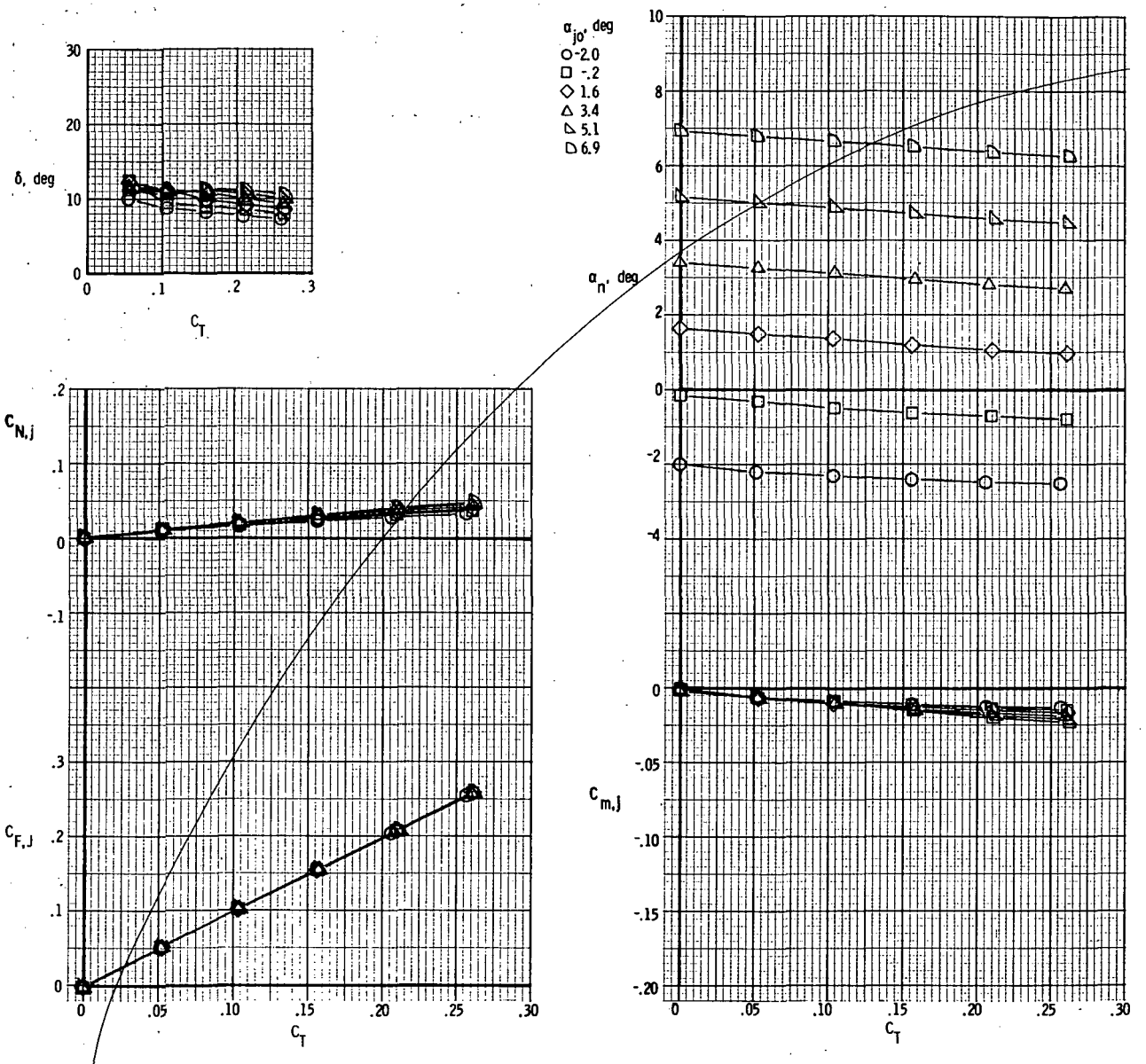

(d) M = 0.95.

Figure 16.- Concluded.

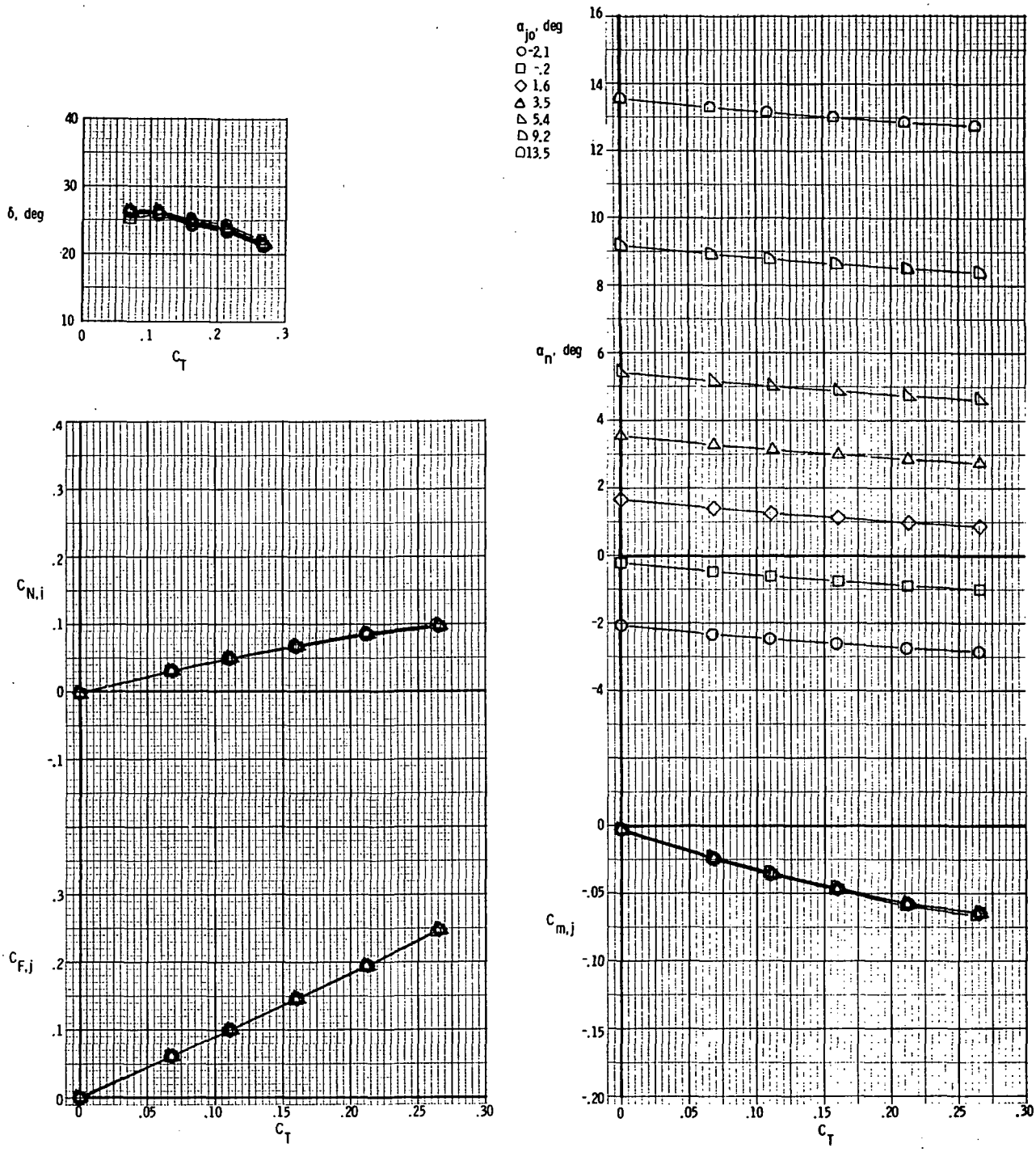

(a) M = 0.70.

Figure 17.- Basic nozzle thrust characteristics for model with rectangular exits; $x_e/c_r = 0.14$; $\delta_d = 30^o$.

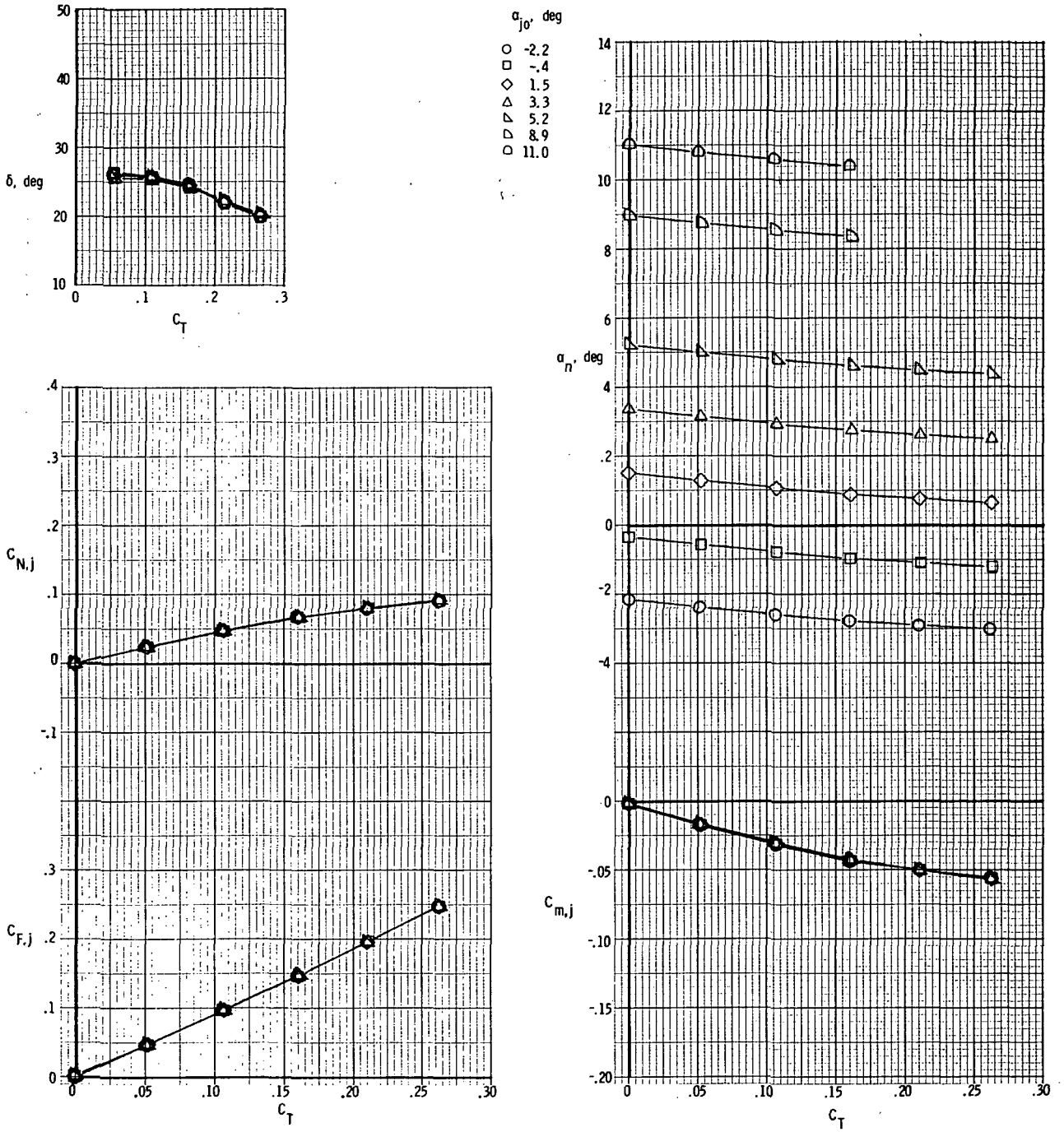

(b) M = 0.80.

Figure 17.- Continued.

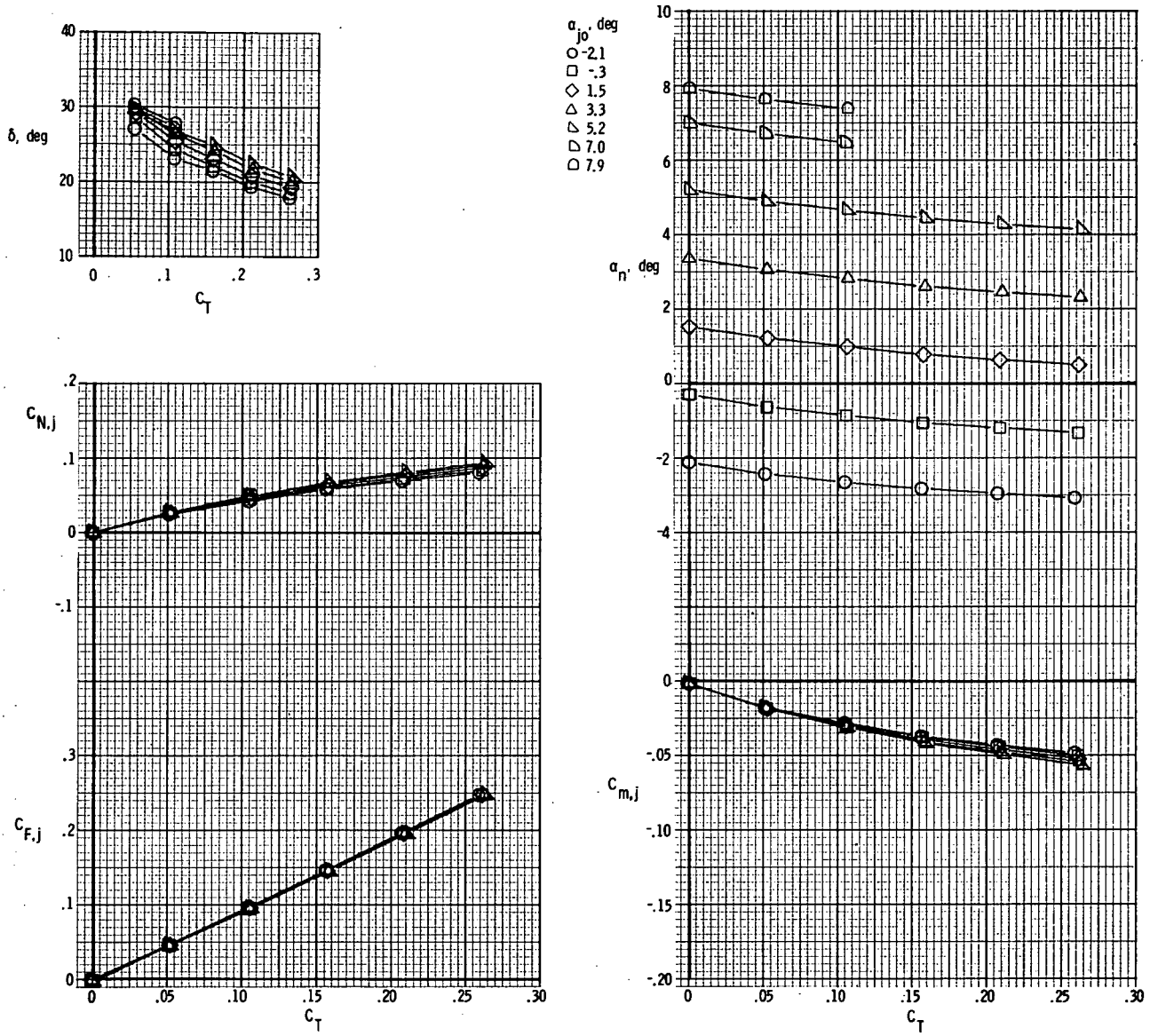

(c) M = 0.90.

Figure 17.- Continued.

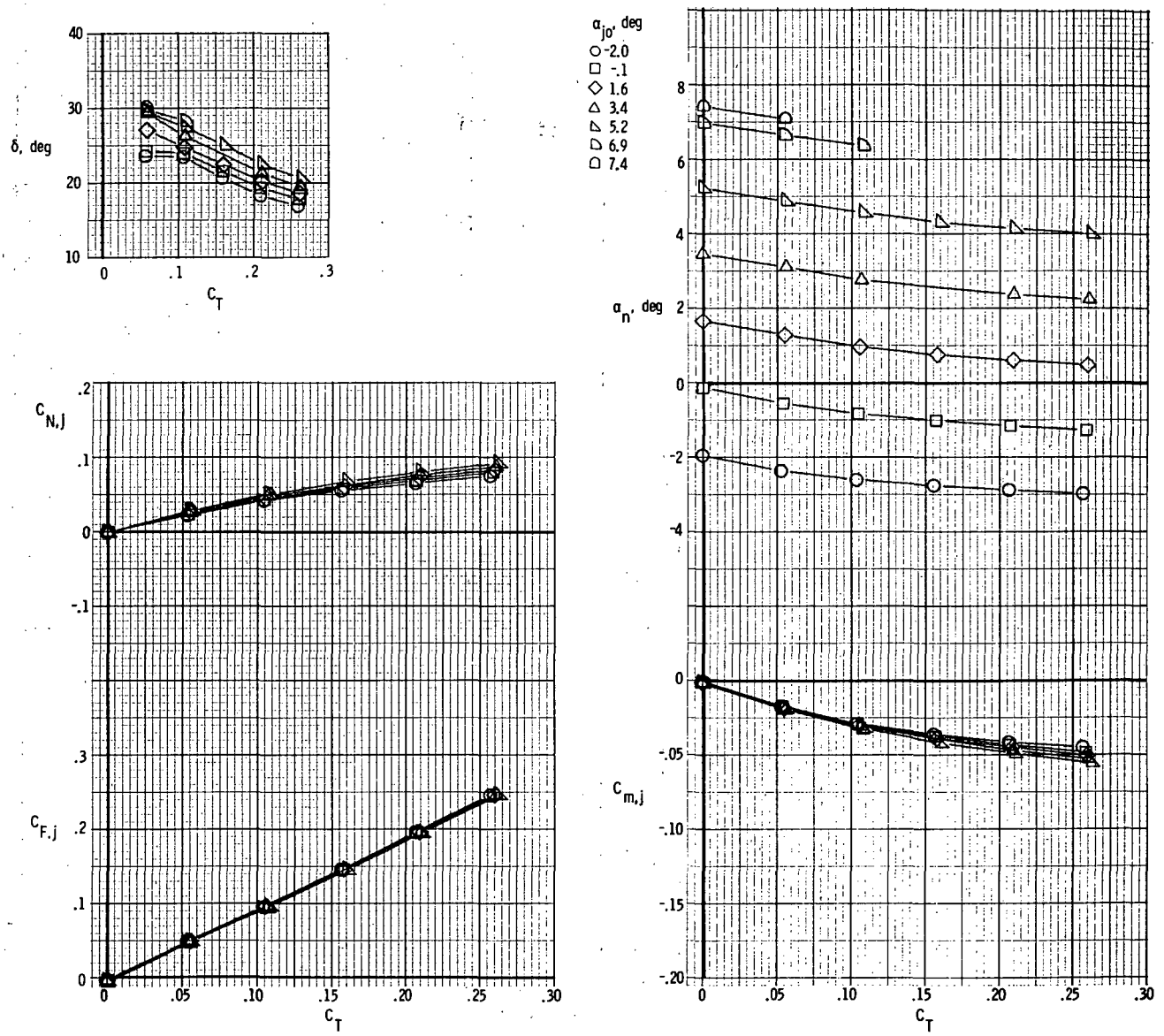

(d) M = 0.95.

Figure 17.- Continued.

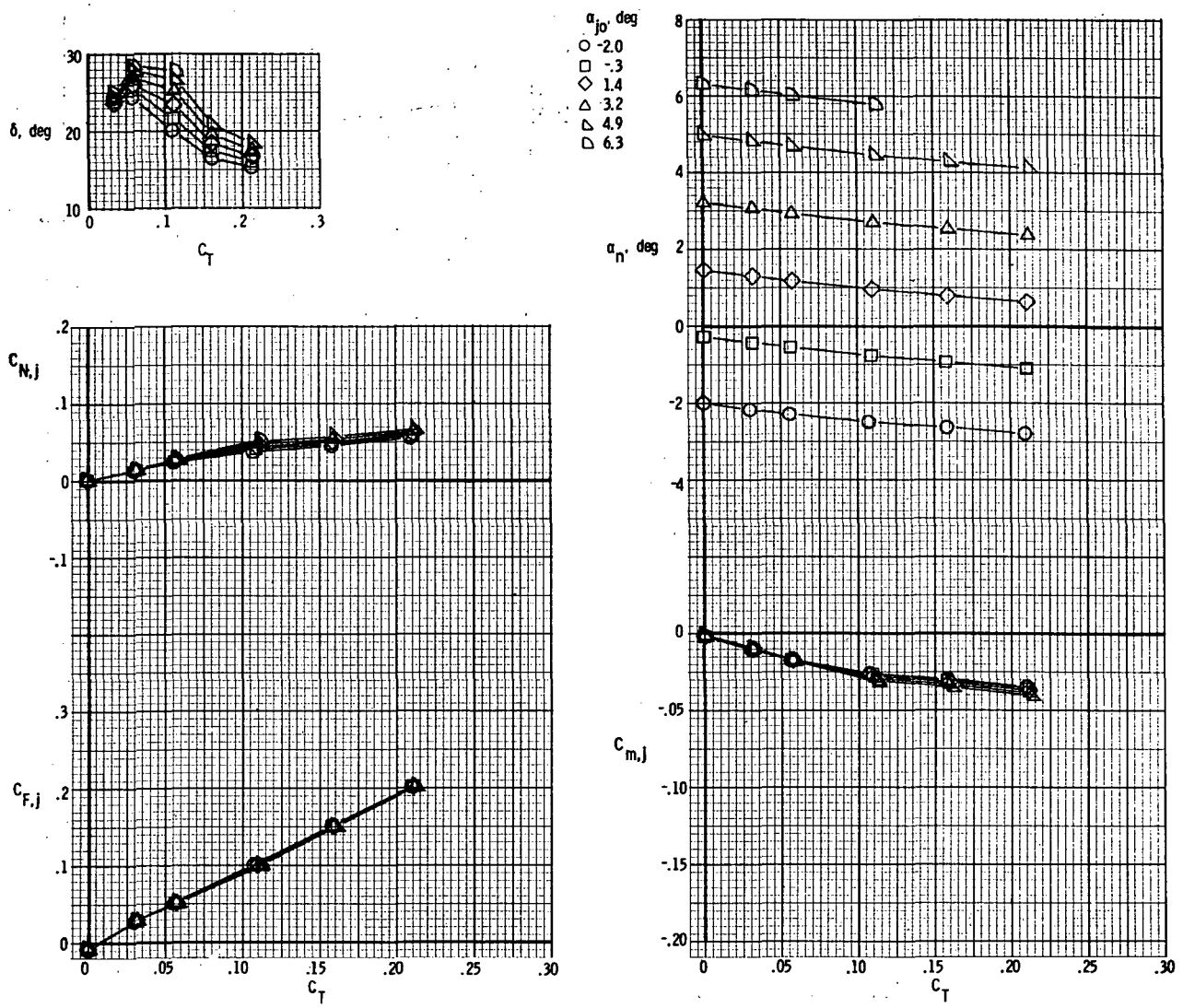

(e) M = 1.20.

Figure 17.- Concluded.

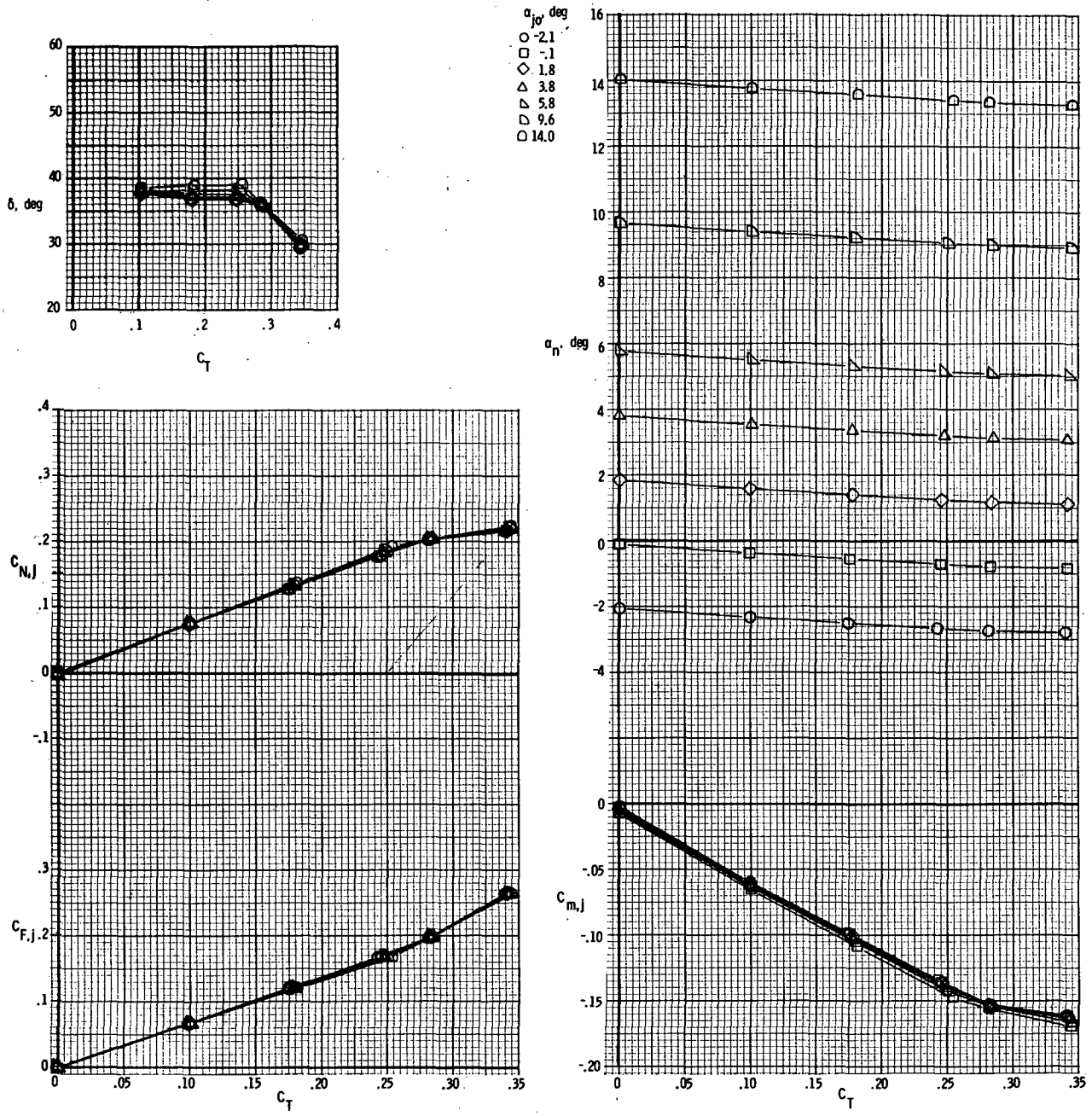

(a) M = 0.40.

Figure 18.- Basic nozzle thrust characteristics for model with rectangular exits; $x_e/c_r = 0.14$; $\delta_d = 45^{\circ}$.

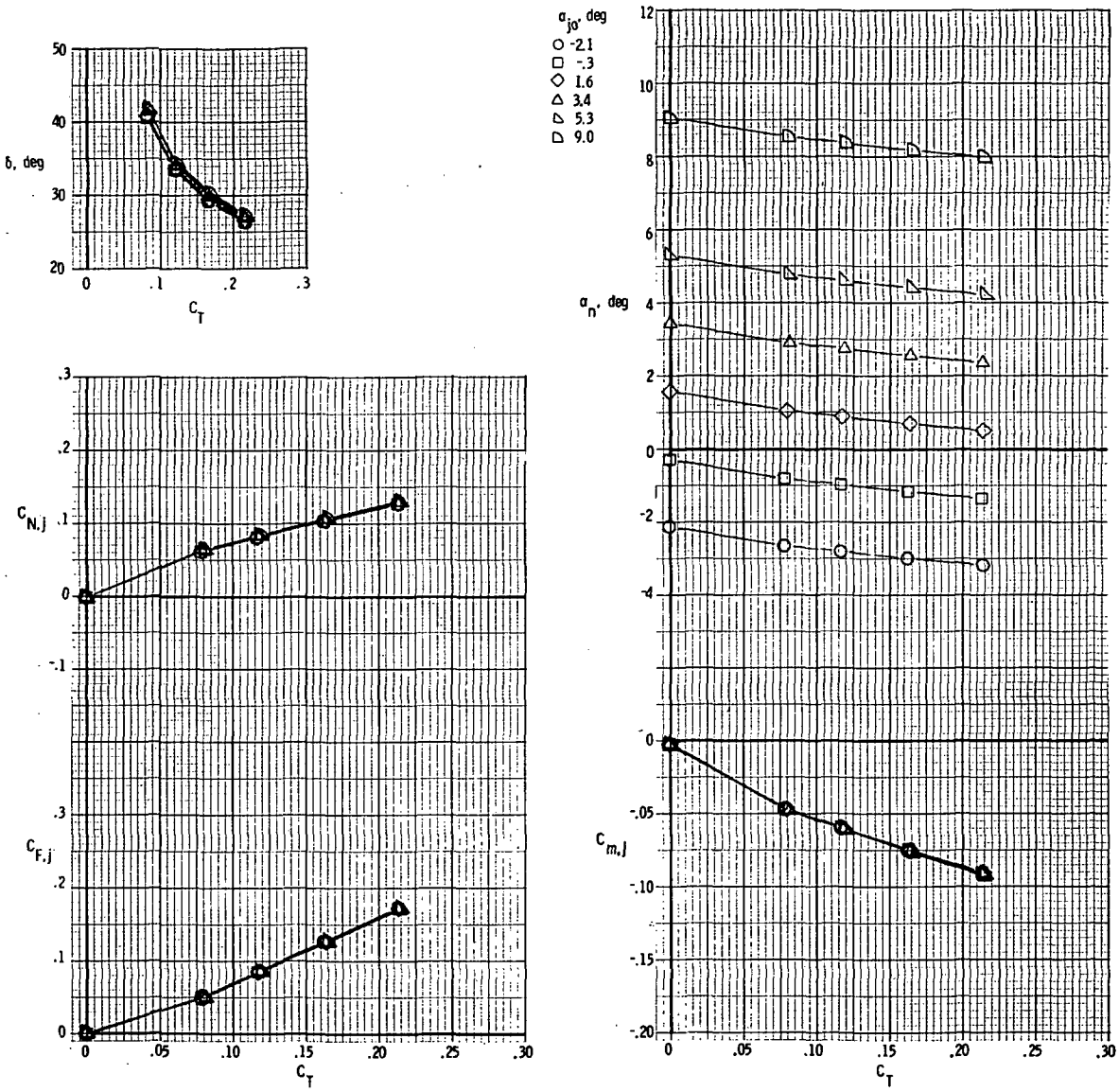

(b) M = 0.70.

Figure 18.- Continued.

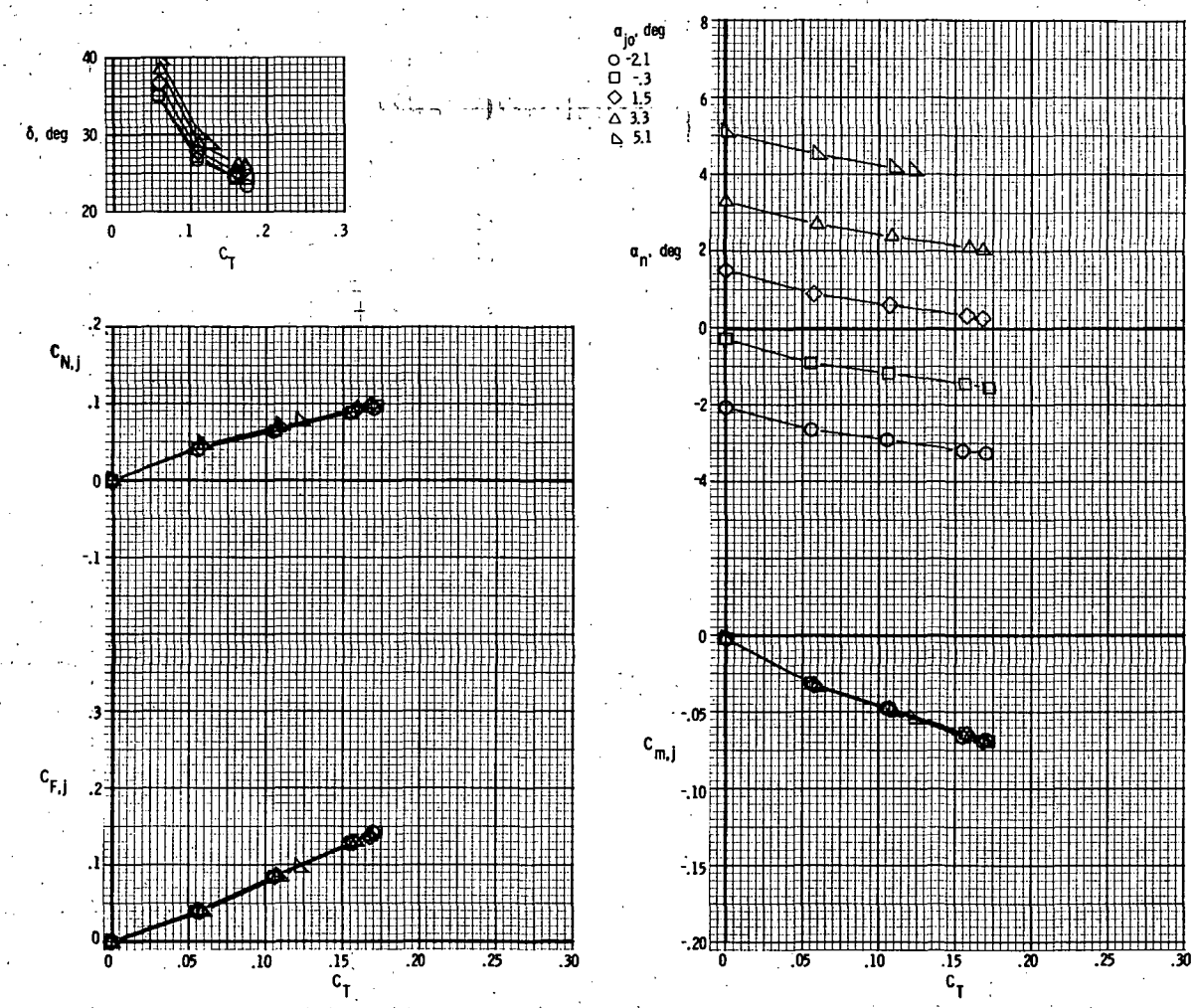

(c) M = 0.90.

Figure 18.- Concluded.

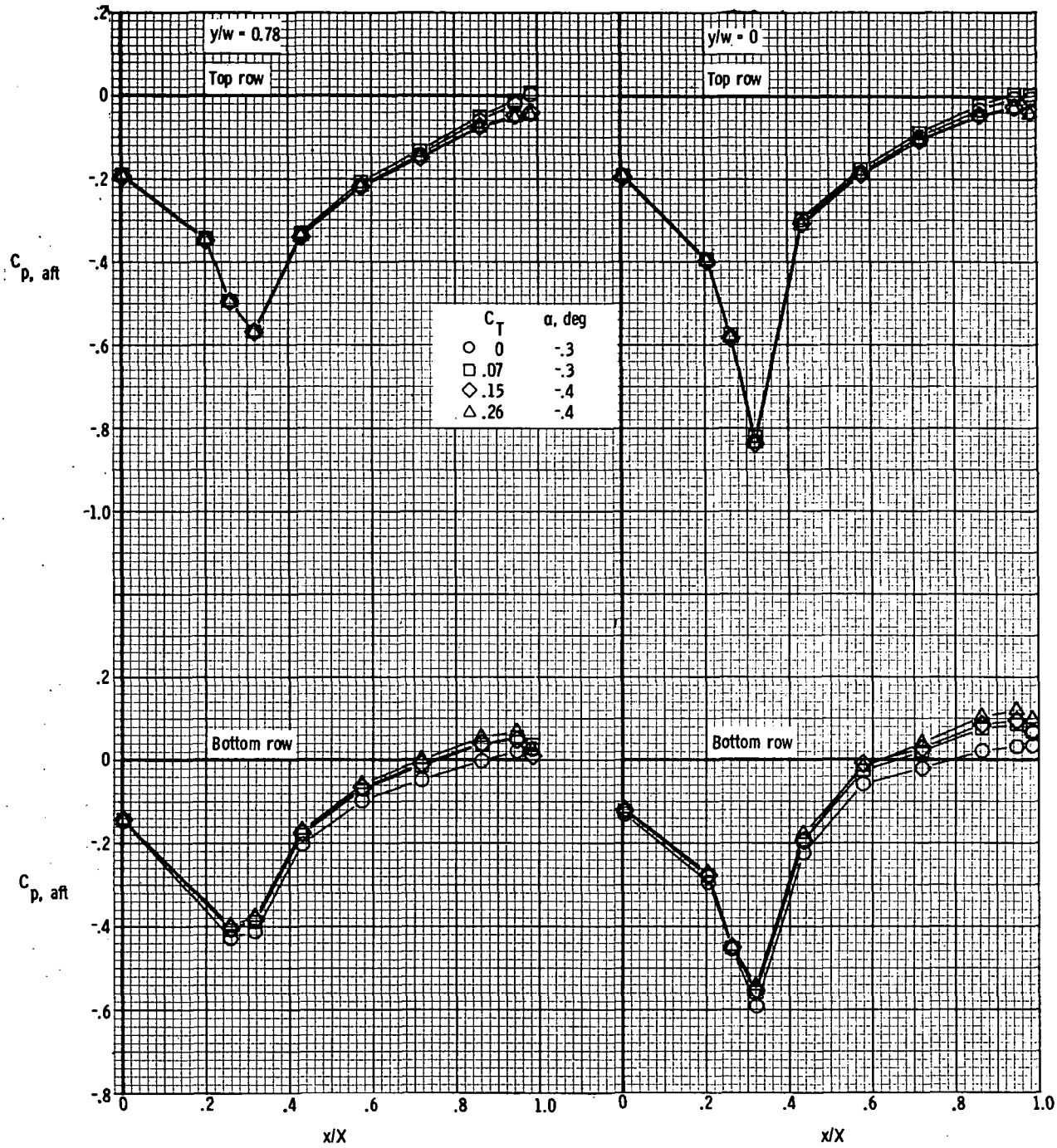

(a) M = 0.70; $\alpha \approx -0.3^{\circ}$.

Figure 19.- Afterbody pressure distributions for model with rectangular exits; $x_e/c_r = 0.70$; $\delta_d = 15^{\circ}$.

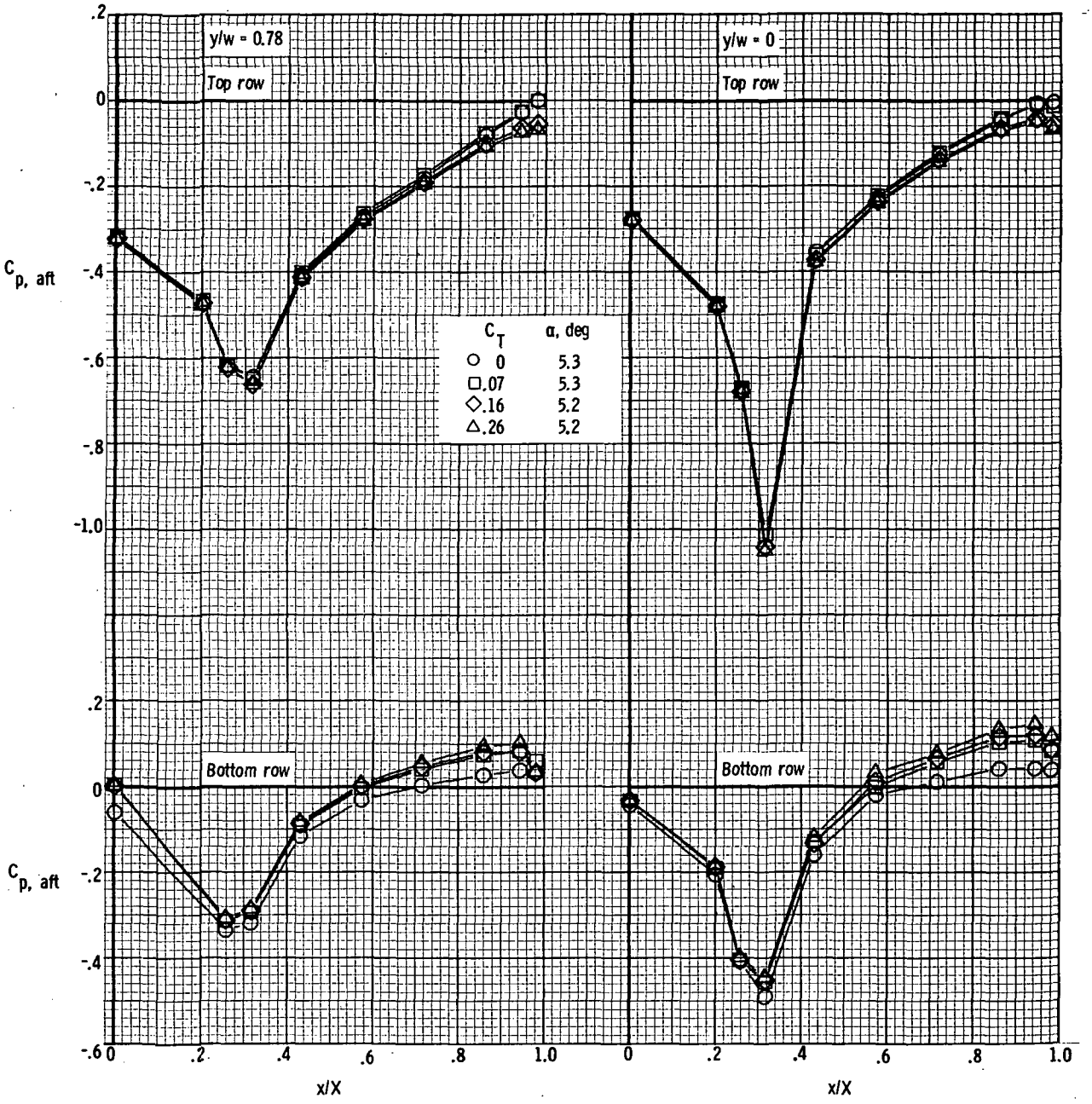

(b) M = 0.70; $\alpha \approx 5.3^{\circ}$.

Figure 19.- Continued.

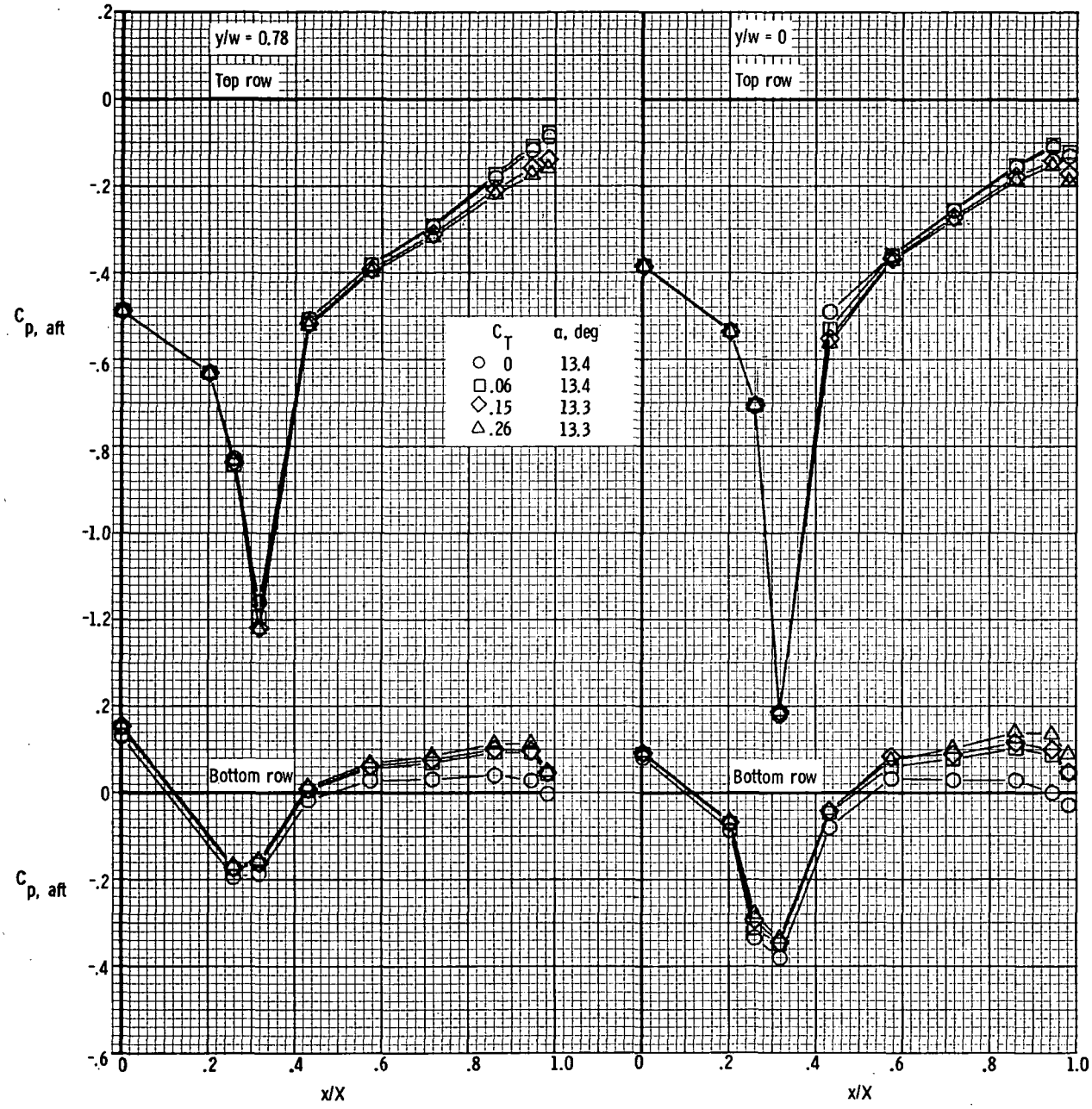

(c) M = 0.70; $\alpha \approx 13.4^{\circ}$.

Figure 19.- Continued.

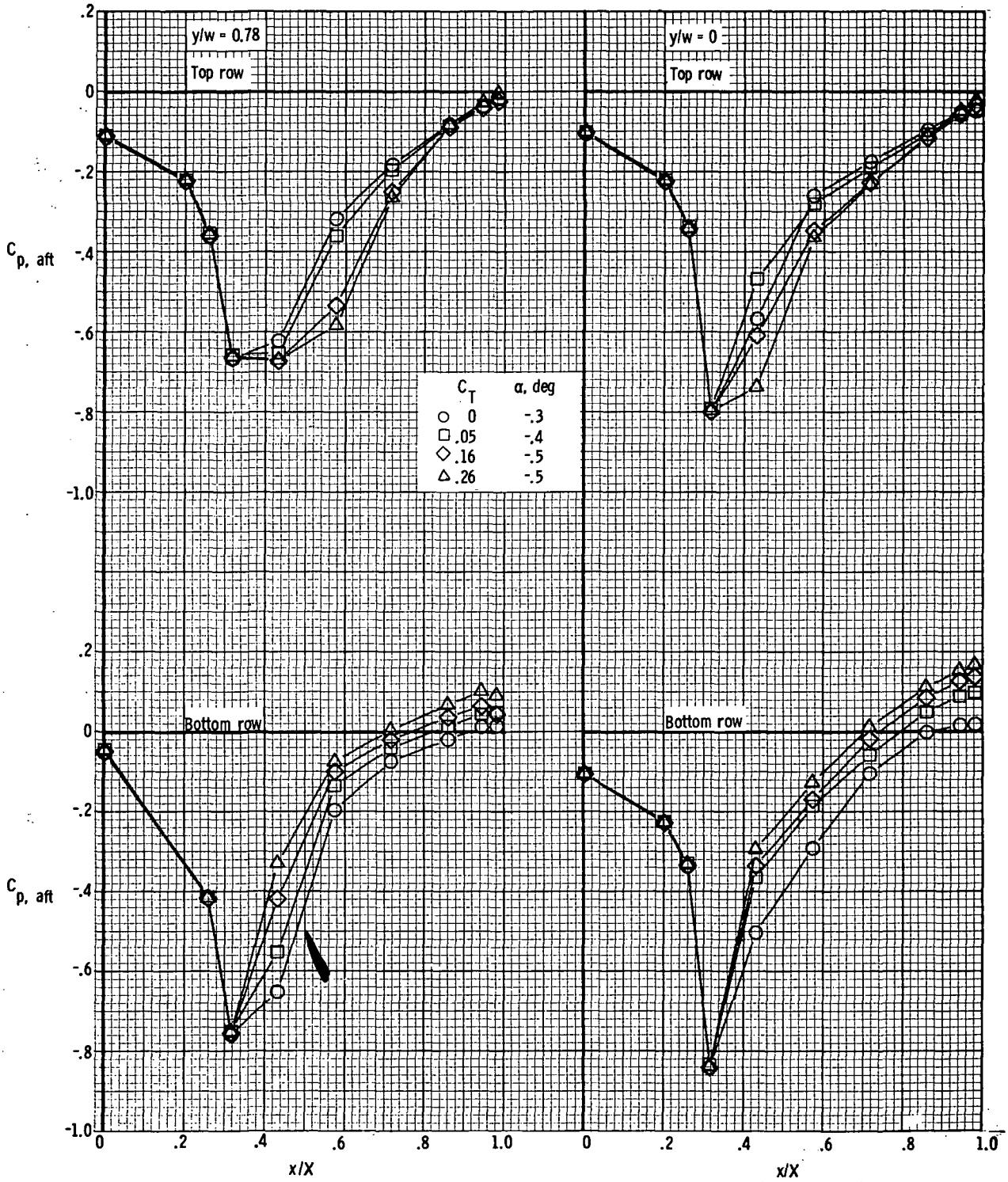

(d) M = 0.90; $\alpha \approx -0.3^{\circ}$.

Figure 19.- Continued.

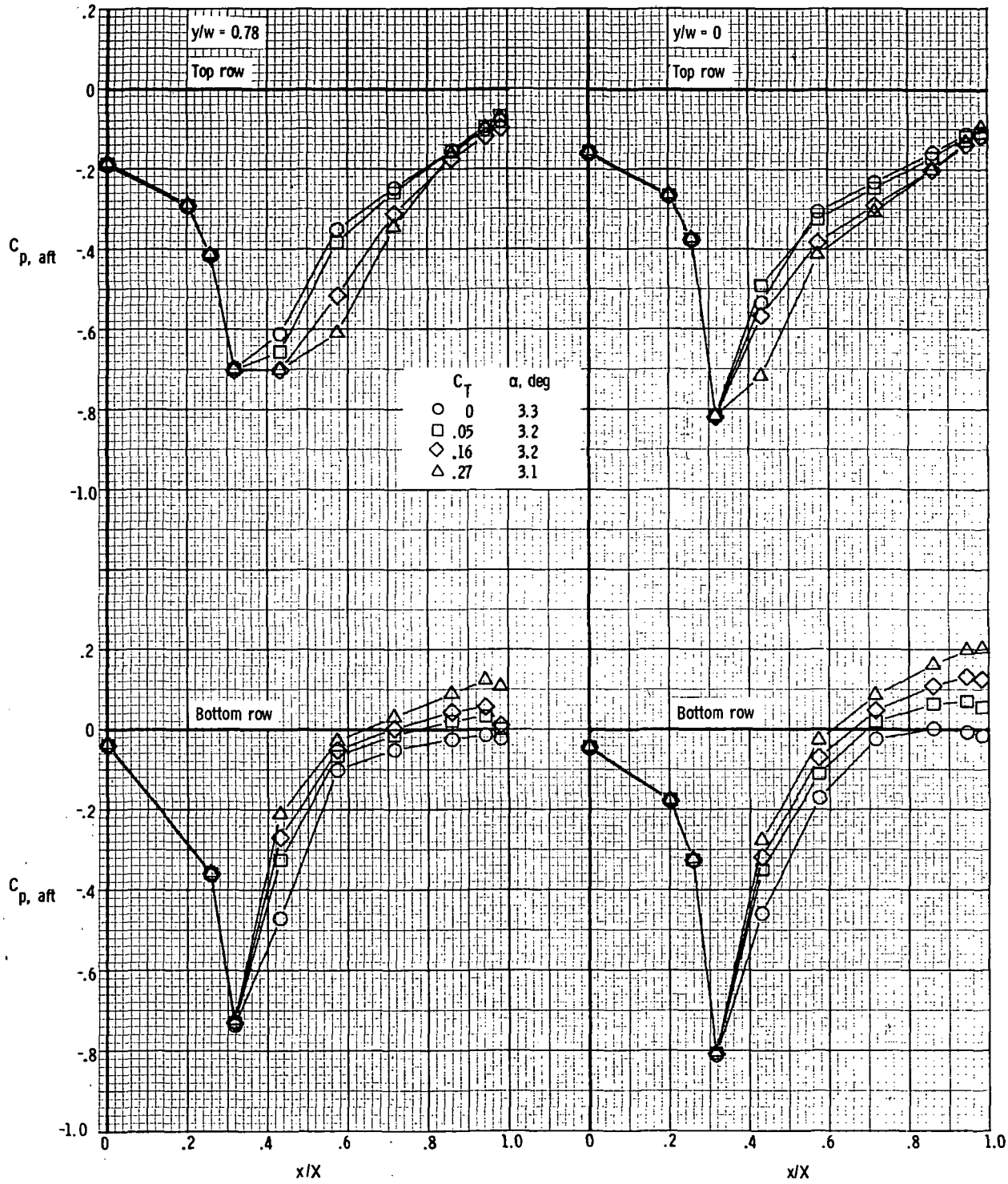

(e) M = 0.90; $\alpha \approx 3.2^{\circ}$.

Figure 19.- Continued.

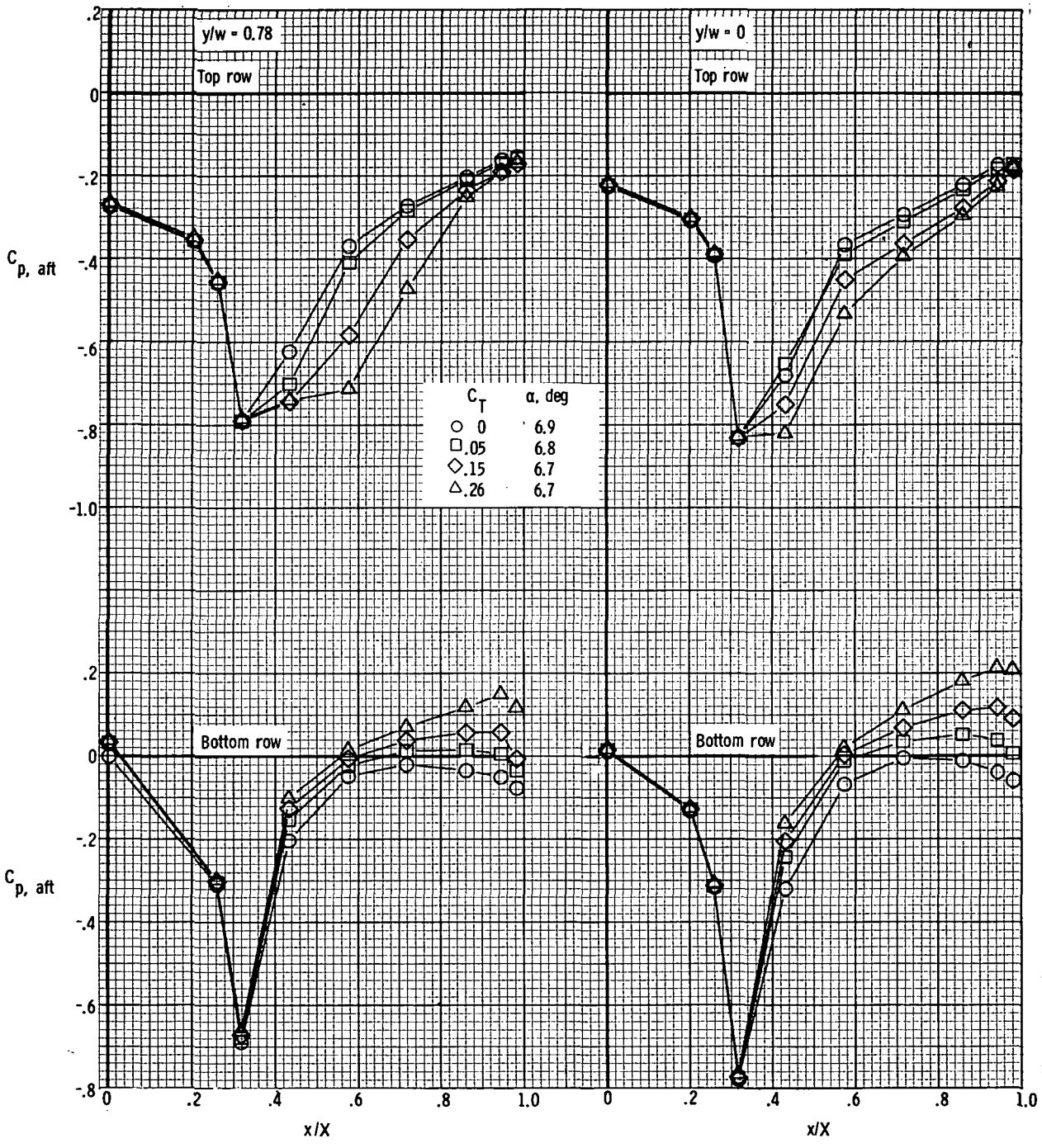

(f) M = 0.90; $\alpha \approx 6.8^{\circ}$.

Figure 19.- Concluded.

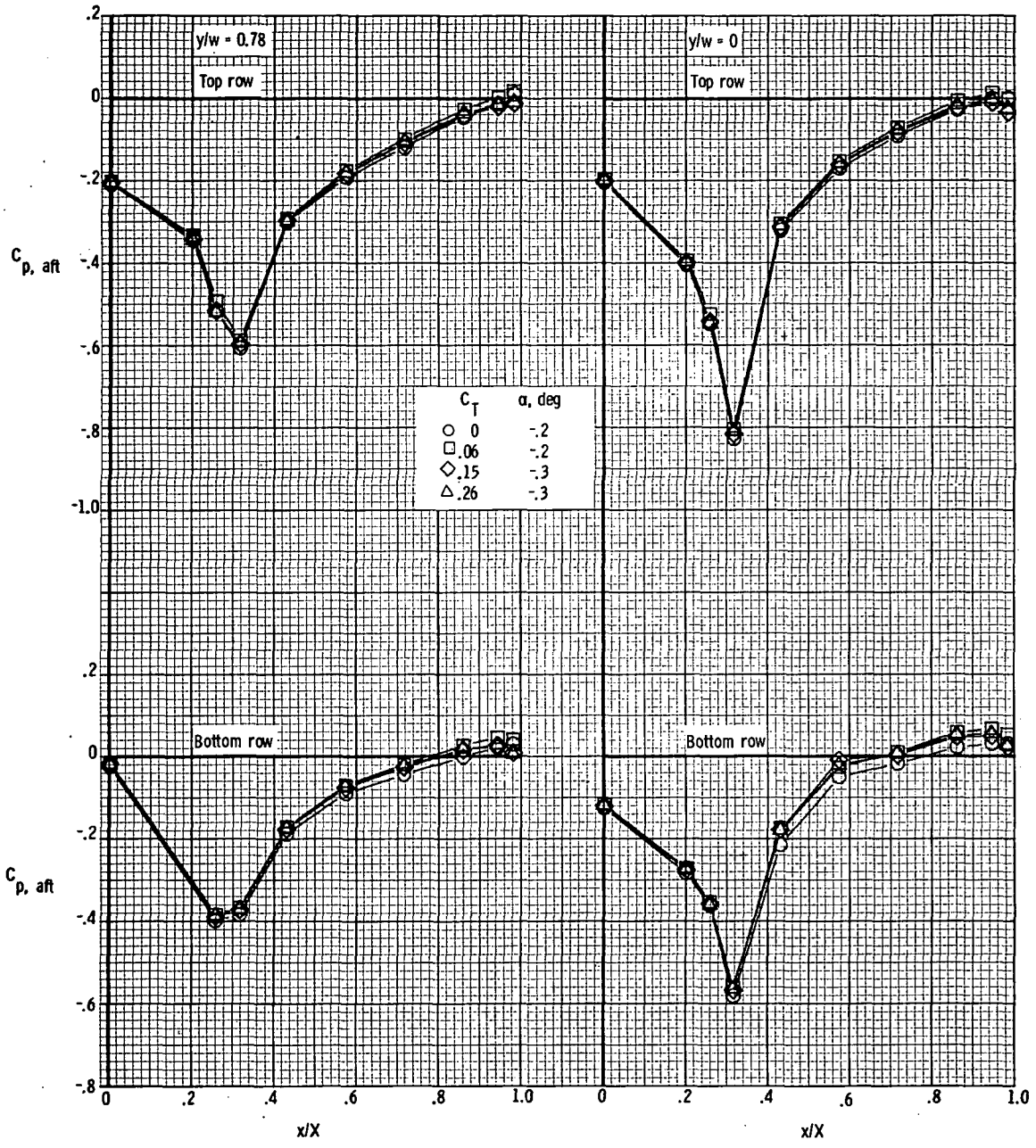

(a) M = 0.70; $\alpha \approx -0.2^{\circ}$.

Figure 20.- Afterbody pressure distributions for model with rectangular exits; $x_e/c_r = 0.14$; $\delta_d = 0^{\circ}$.

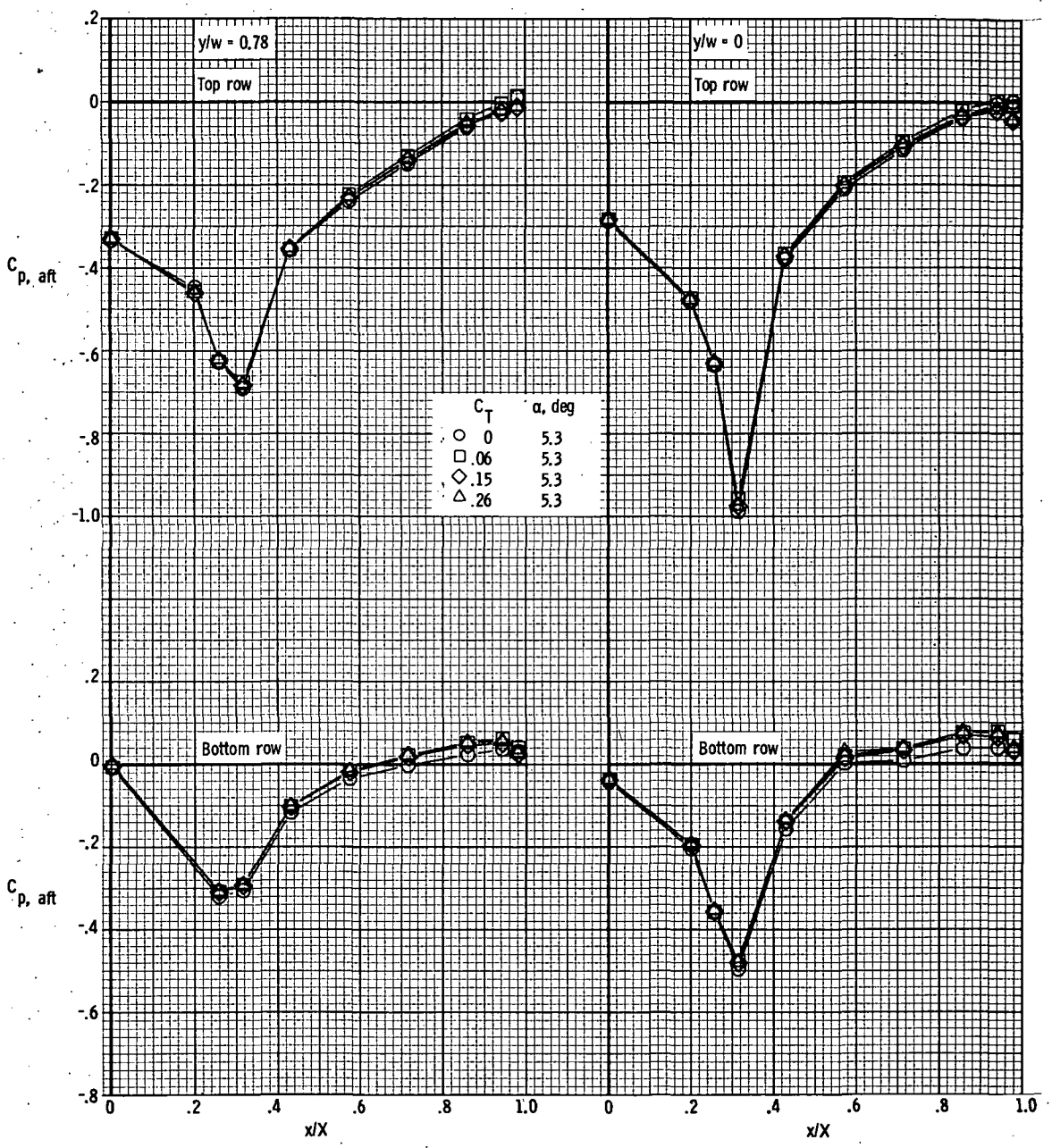

(b) M = 0.70; $\alpha \approx 5.3^{\circ}$.

Figure 20.- Continued.

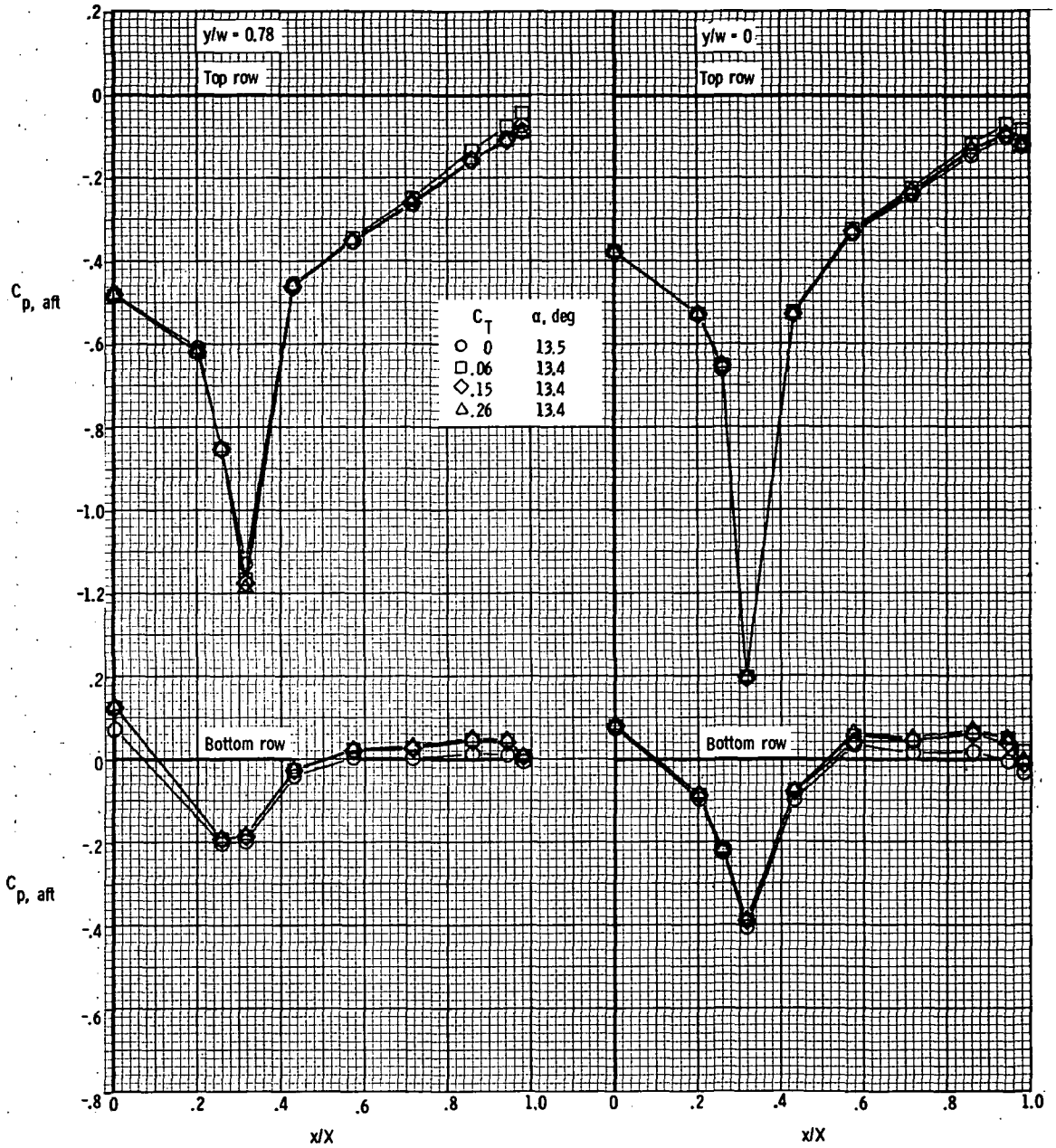

(c) M = 0.70; $\alpha \approx 13.4^{\circ}$.

Figure 20.- Continued.

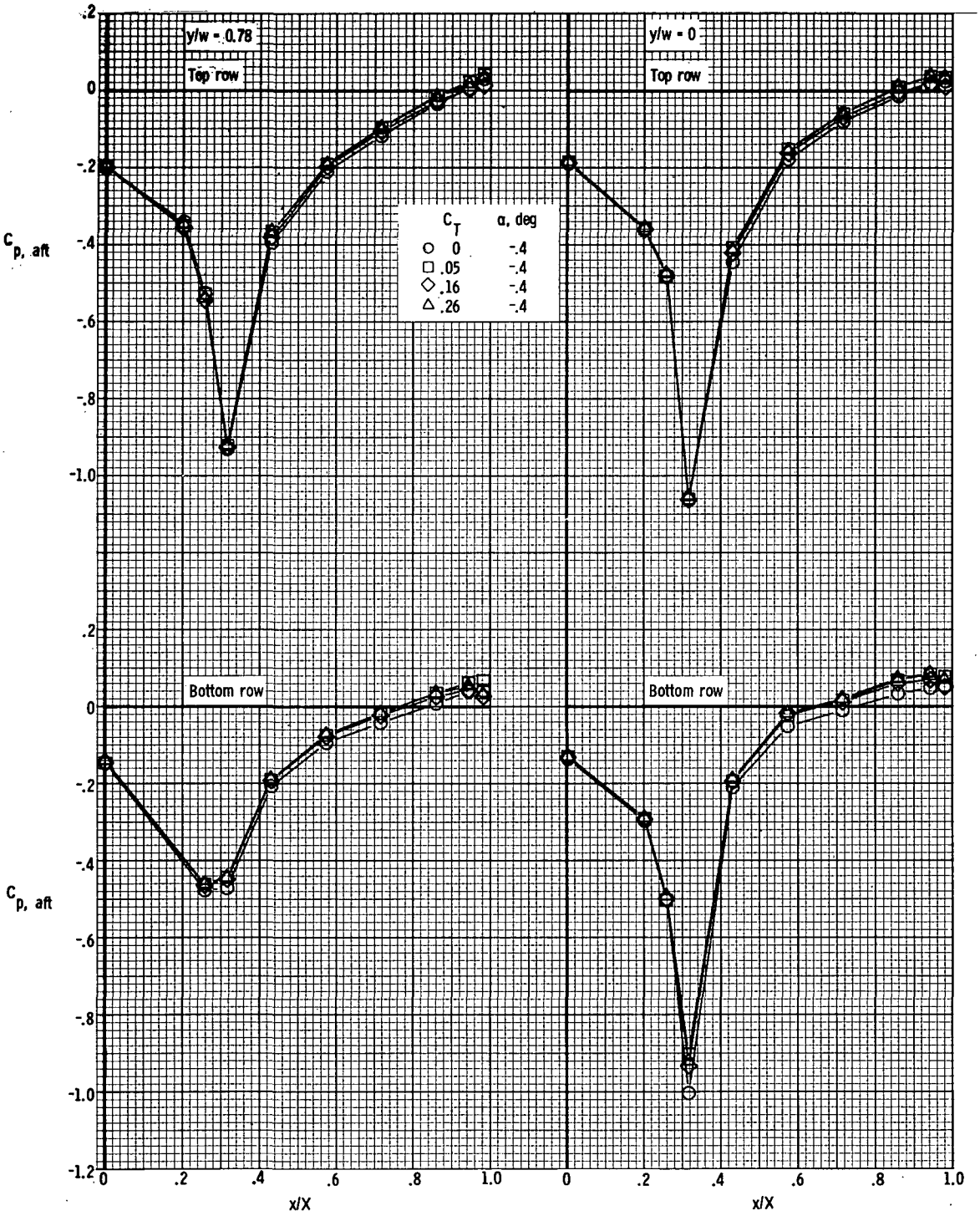

(d) M = 0.80; $\alpha \approx -0.4^{\circ}$.

Figure 20.- Continued.

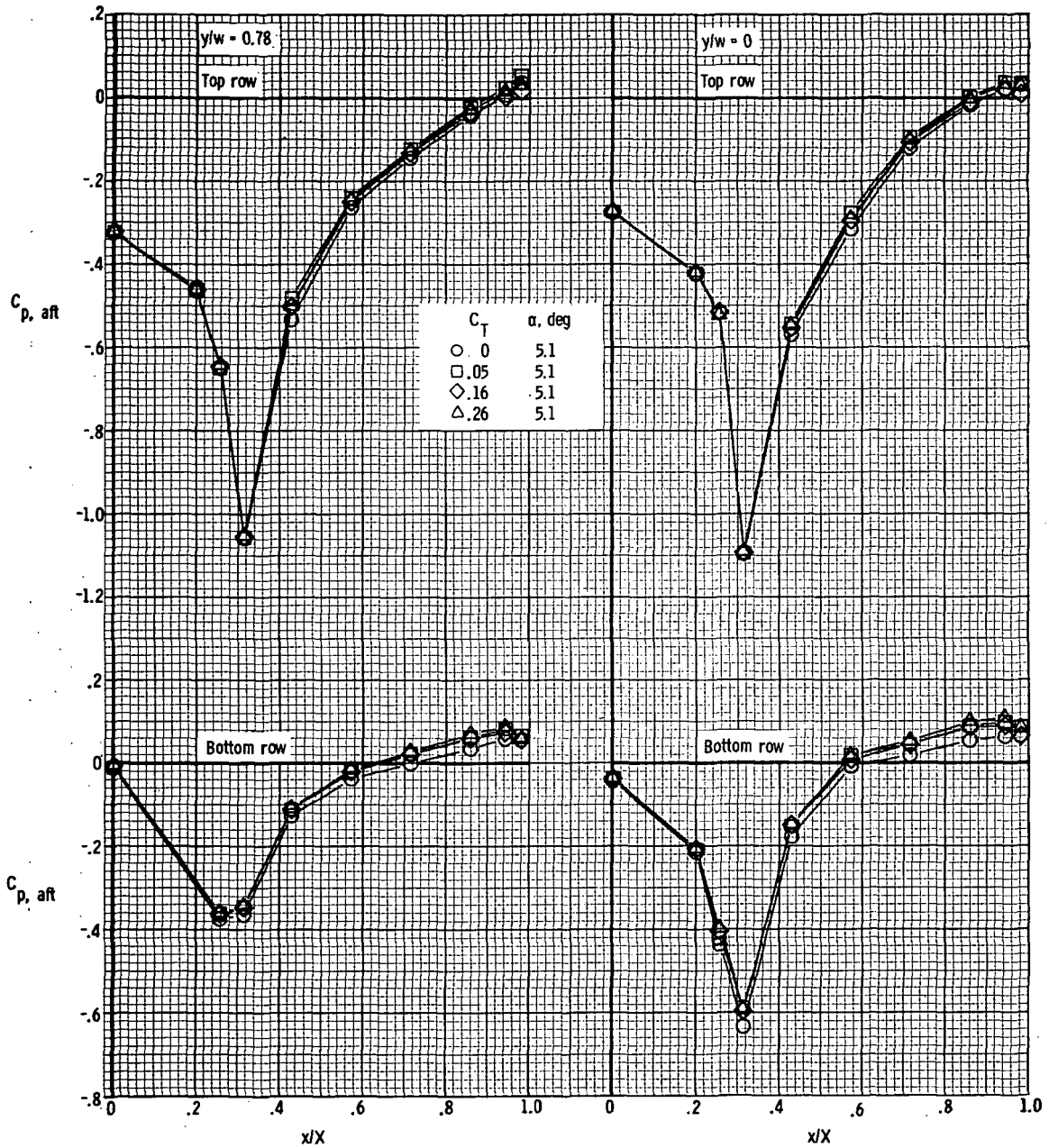

(e) M = 0.80; $\alpha \approx 5.1^{\circ}$.

Figure 20.- Continued.

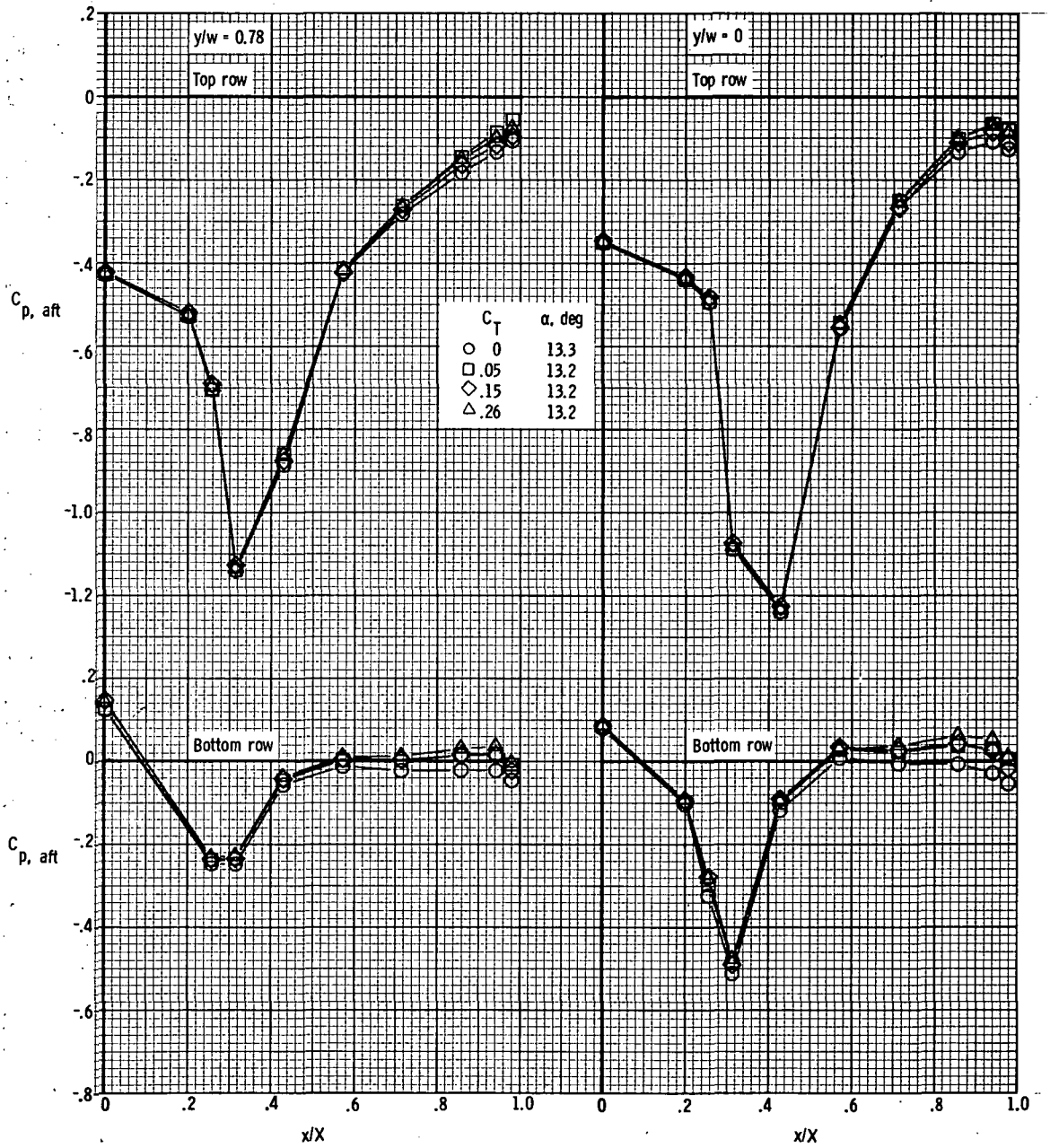

(f) M = 0.80; $\alpha \approx 13.2^{\circ}$.

Figure 20.- Continued.

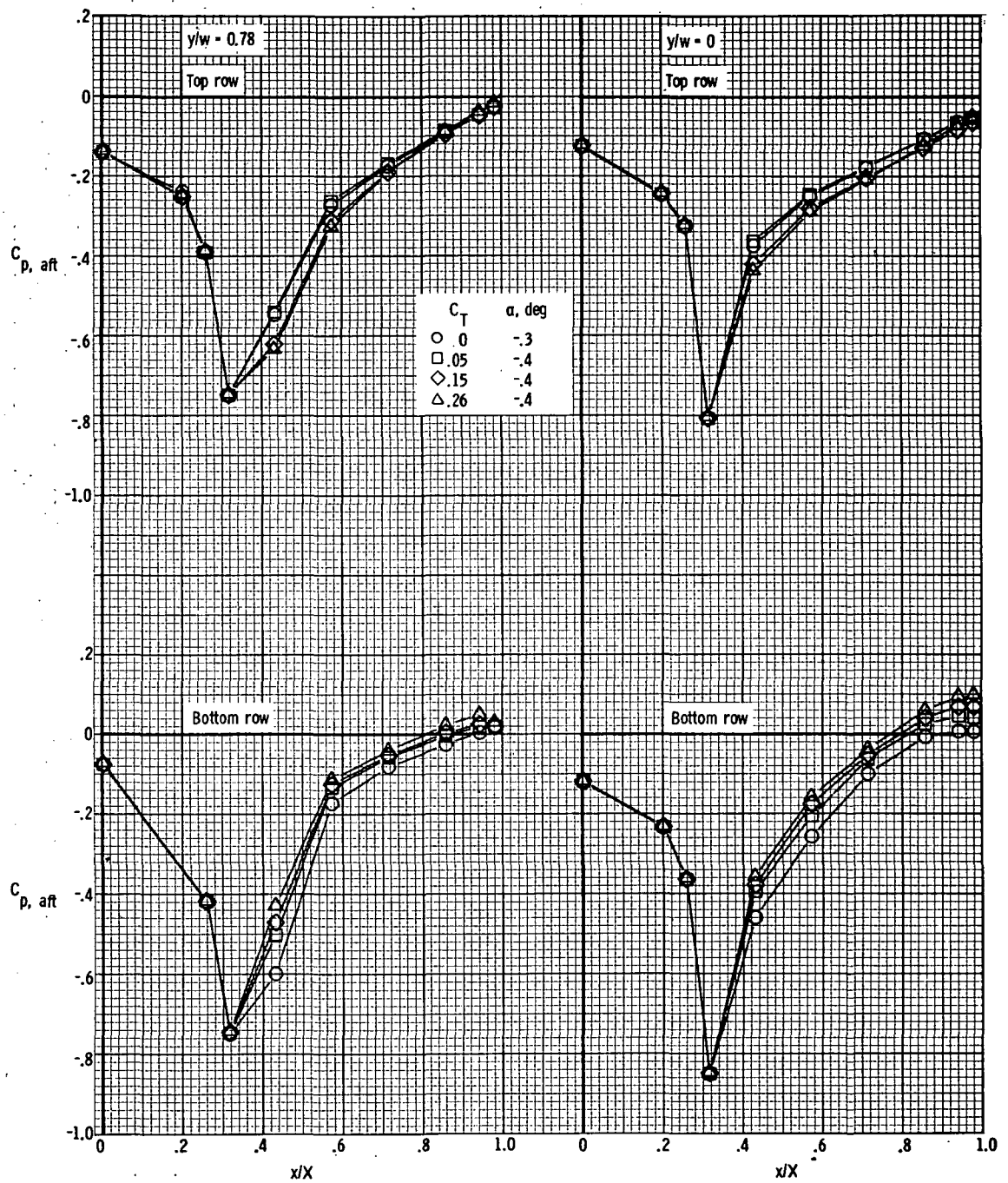

(g) M = 0.90; $\alpha \approx -0.4^{\circ}$.

Figure 20. - Continued.

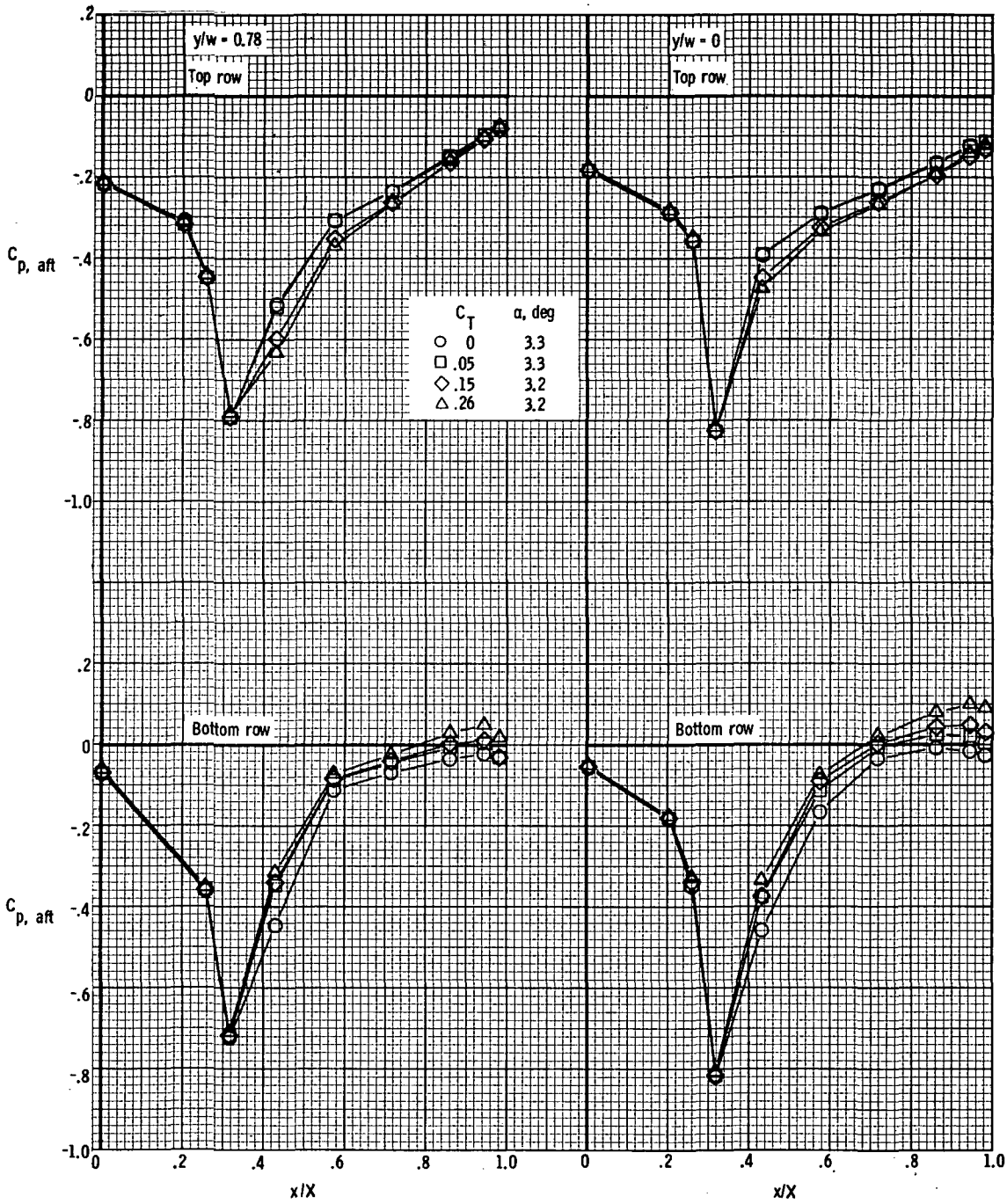

(h) M = 0.90; $\alpha \approx 3.3^{\circ}$.

Figure 20.- Continued.

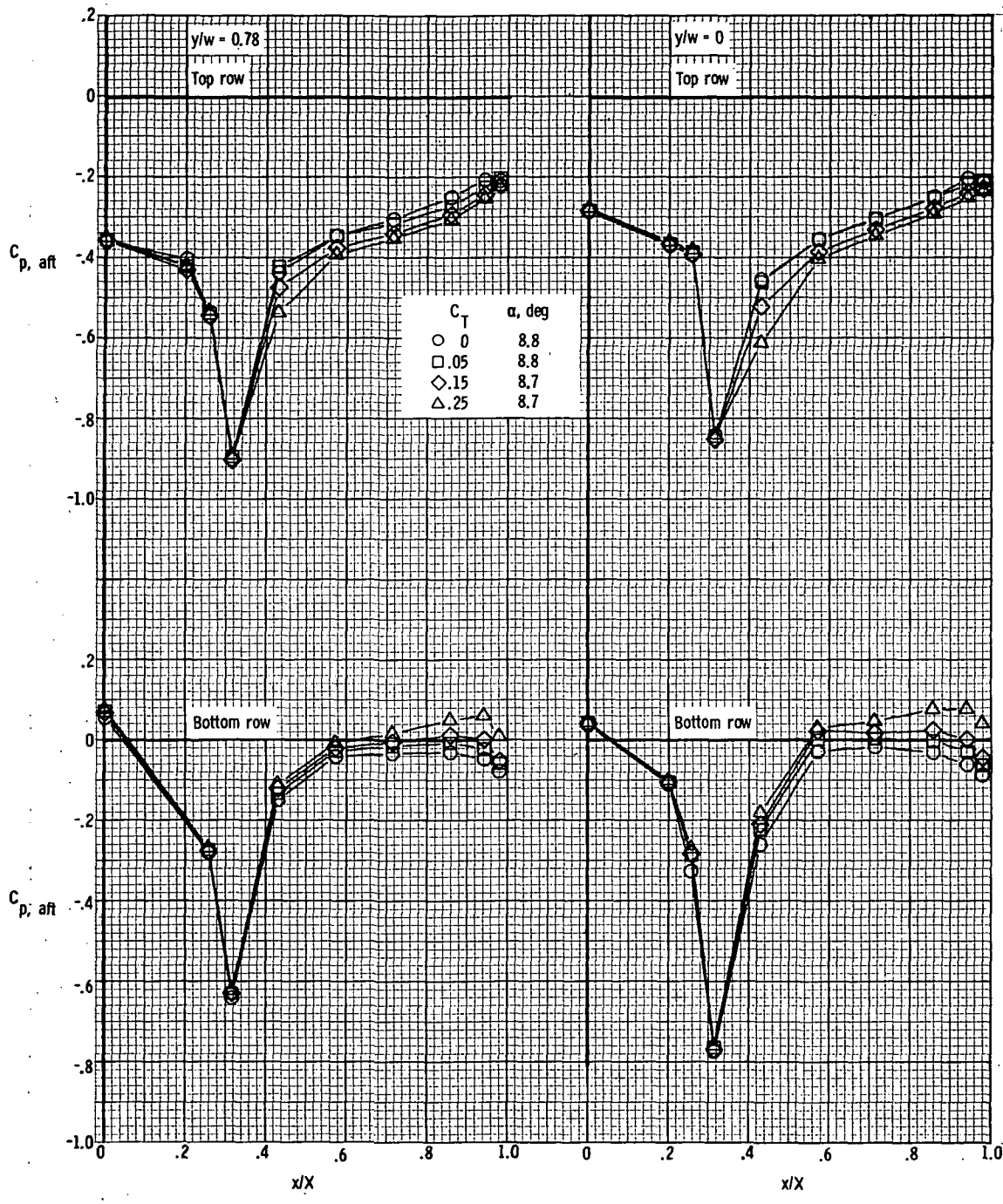

(i) M = 0.90; $\alpha \approx 8.8^{\circ}$.

Figure 20.- Continued.

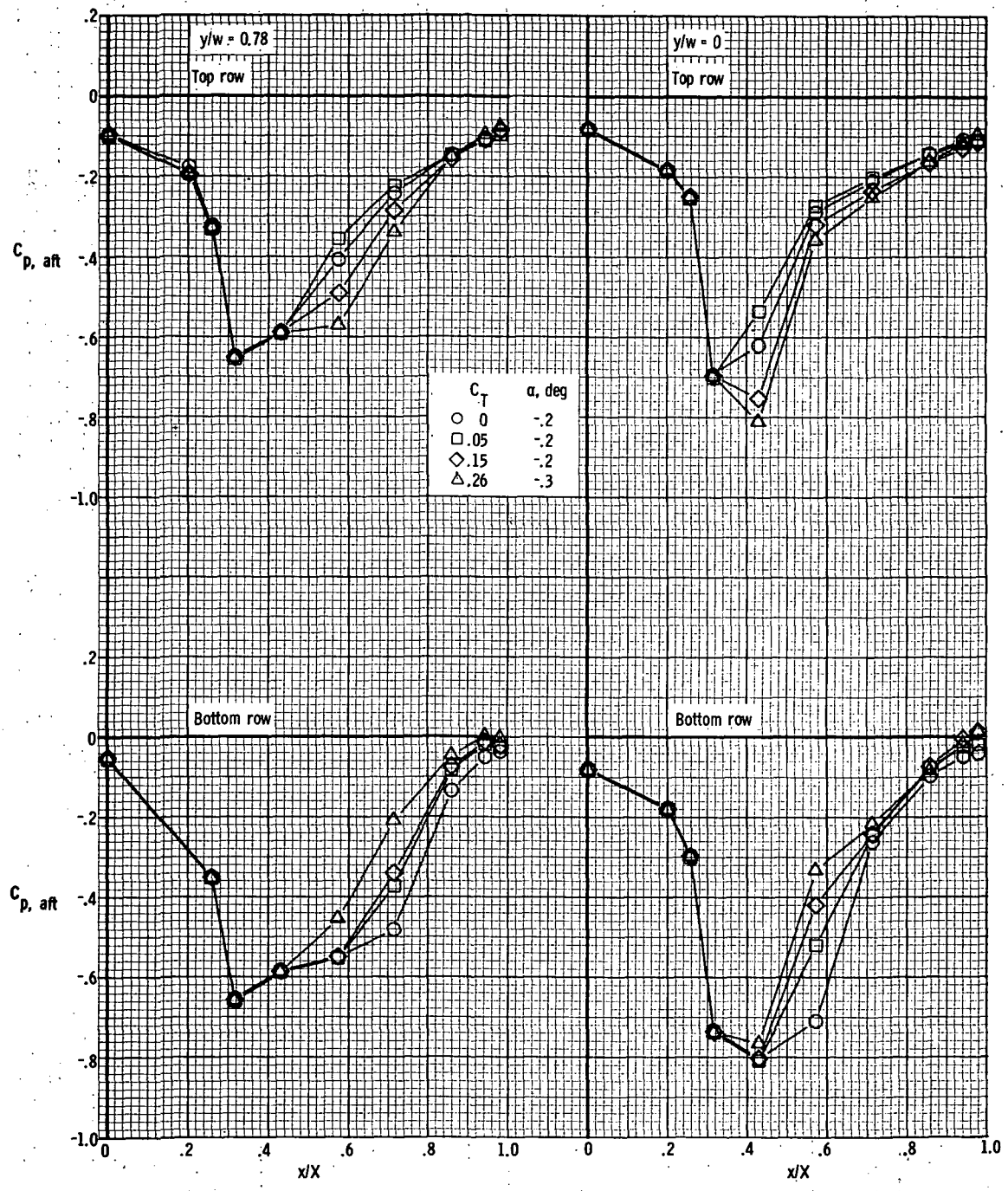

(j) M = 0.95; $\alpha \approx -0.2^{\circ}$.

Figure 20.- Continued.

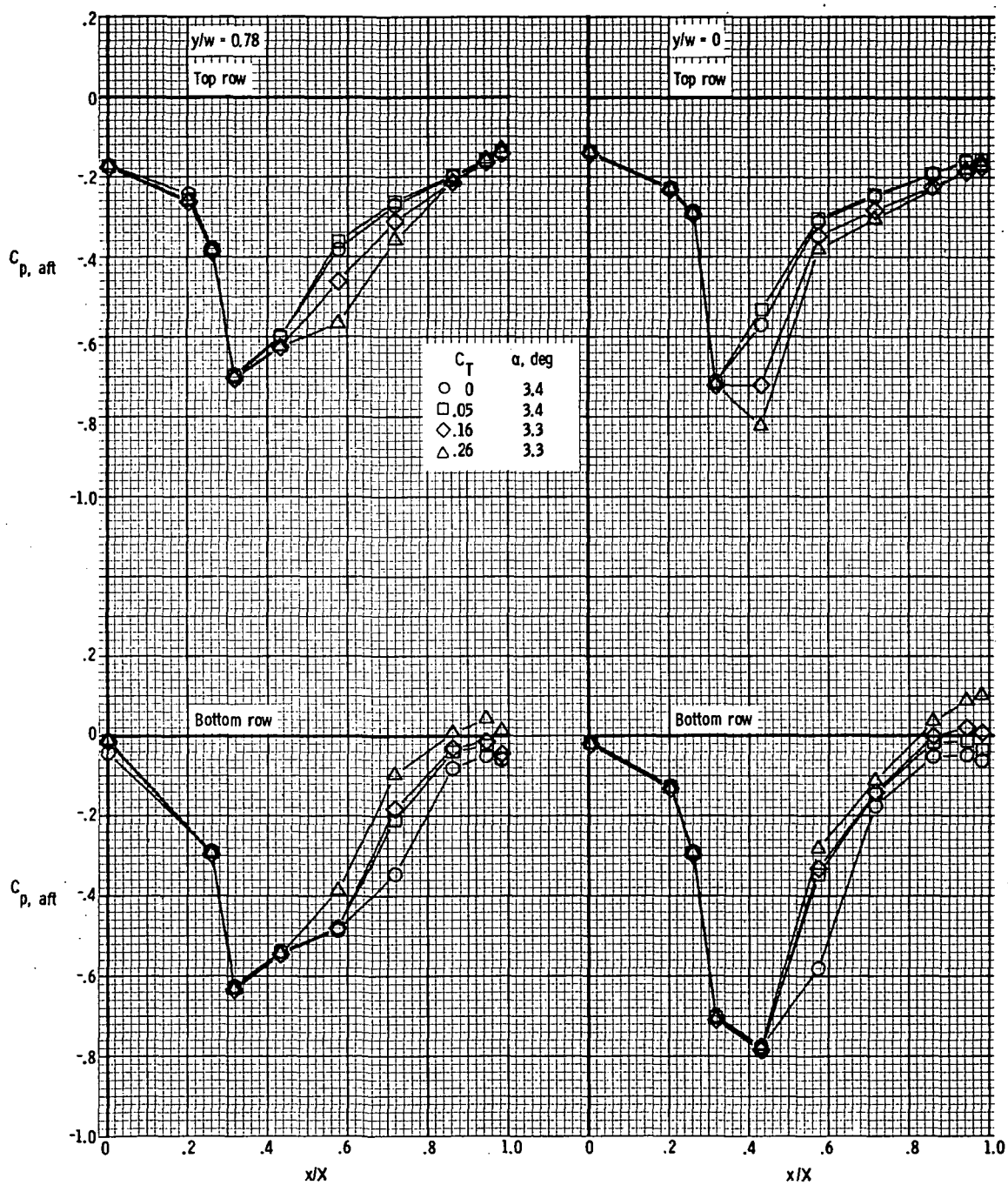

(k) M = 0.95; $\alpha \approx 3.4^{\circ}$.

Figure 20.- Continued.

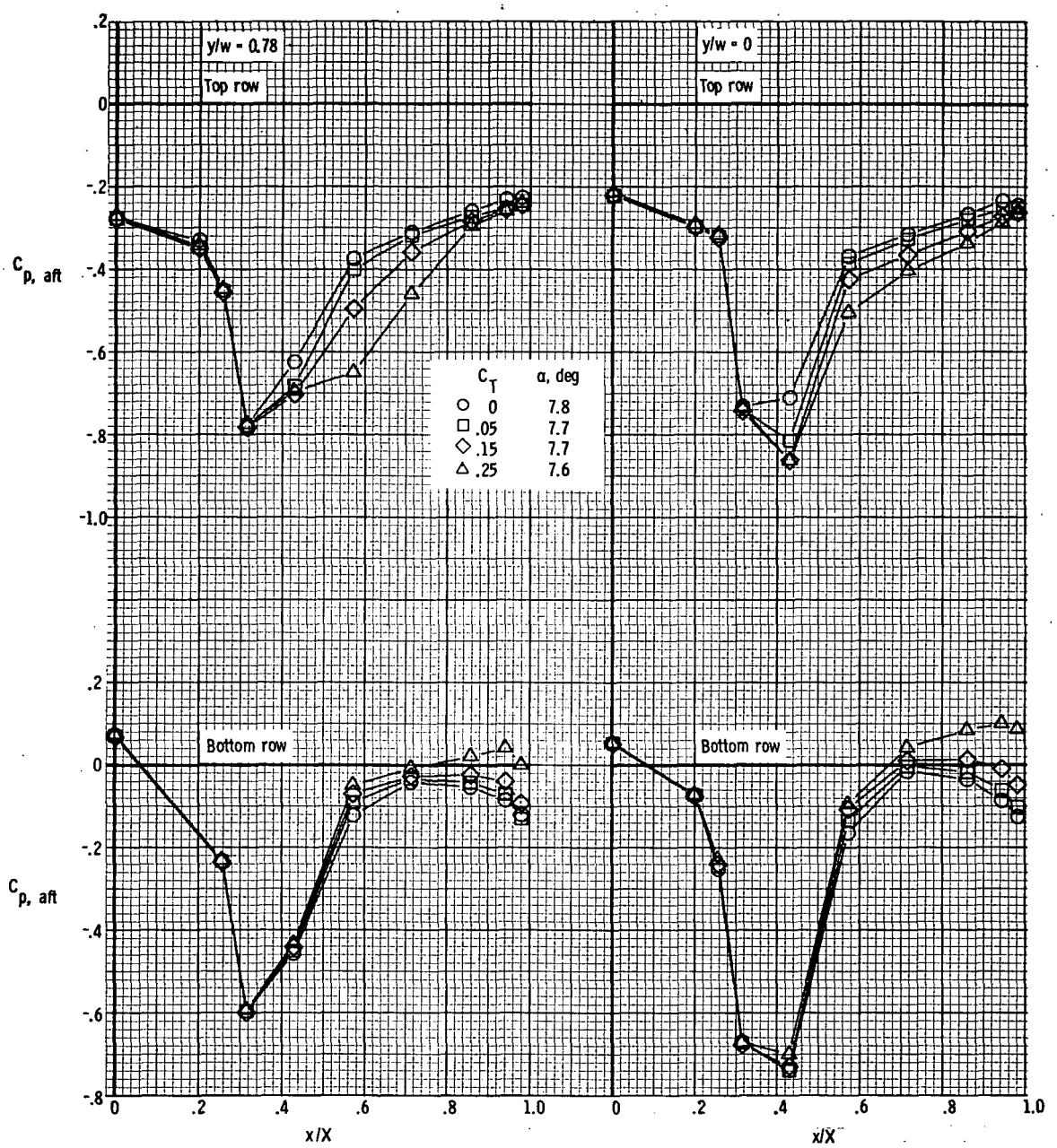

(l) M = 0.95; $\alpha \approx 7.7^{\circ}$.

Figure 20.- Continued.

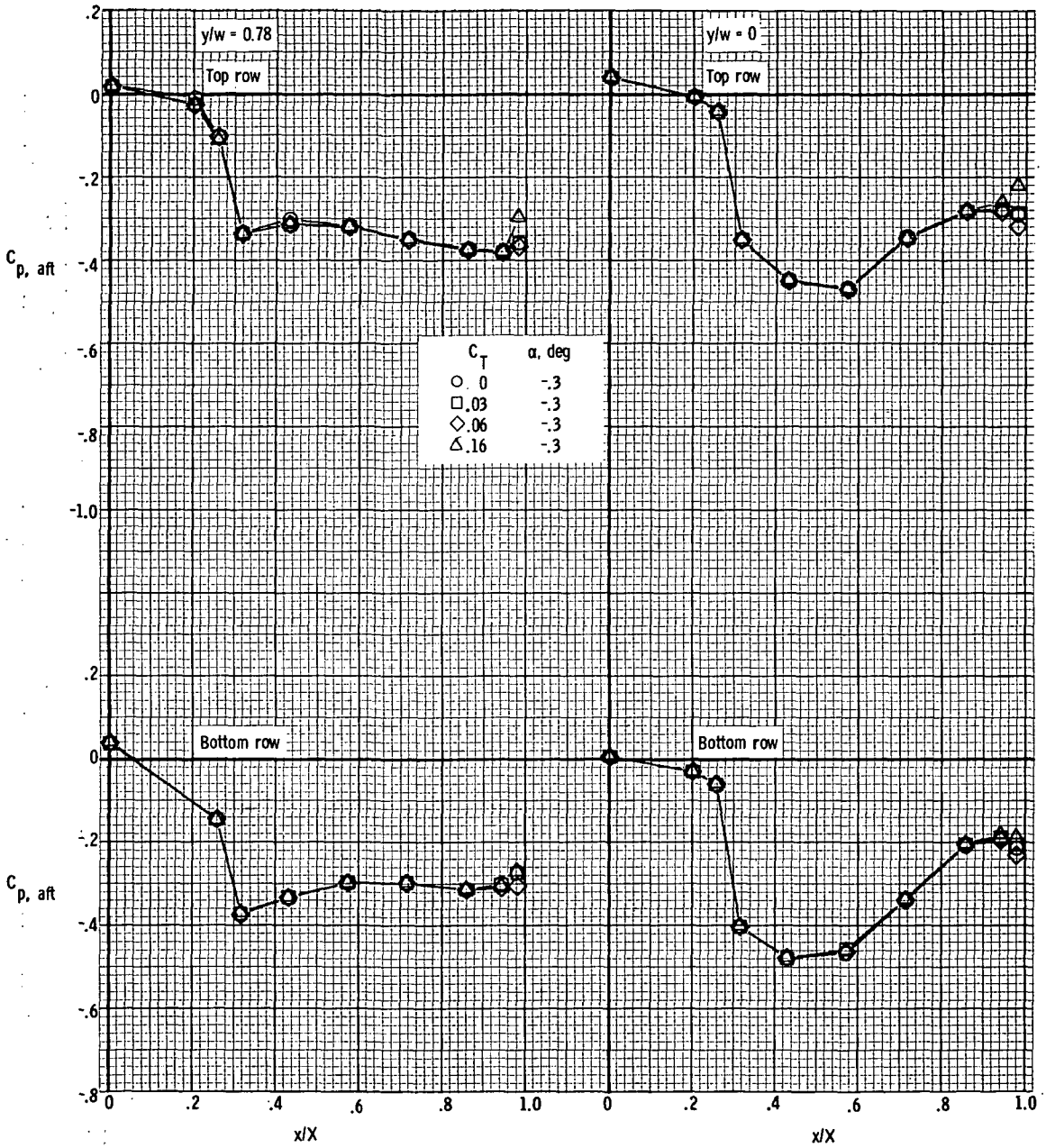

(m) M = 1.20; $\alpha \approx -0.3^{\circ}$.

Figure 20.- Continued.

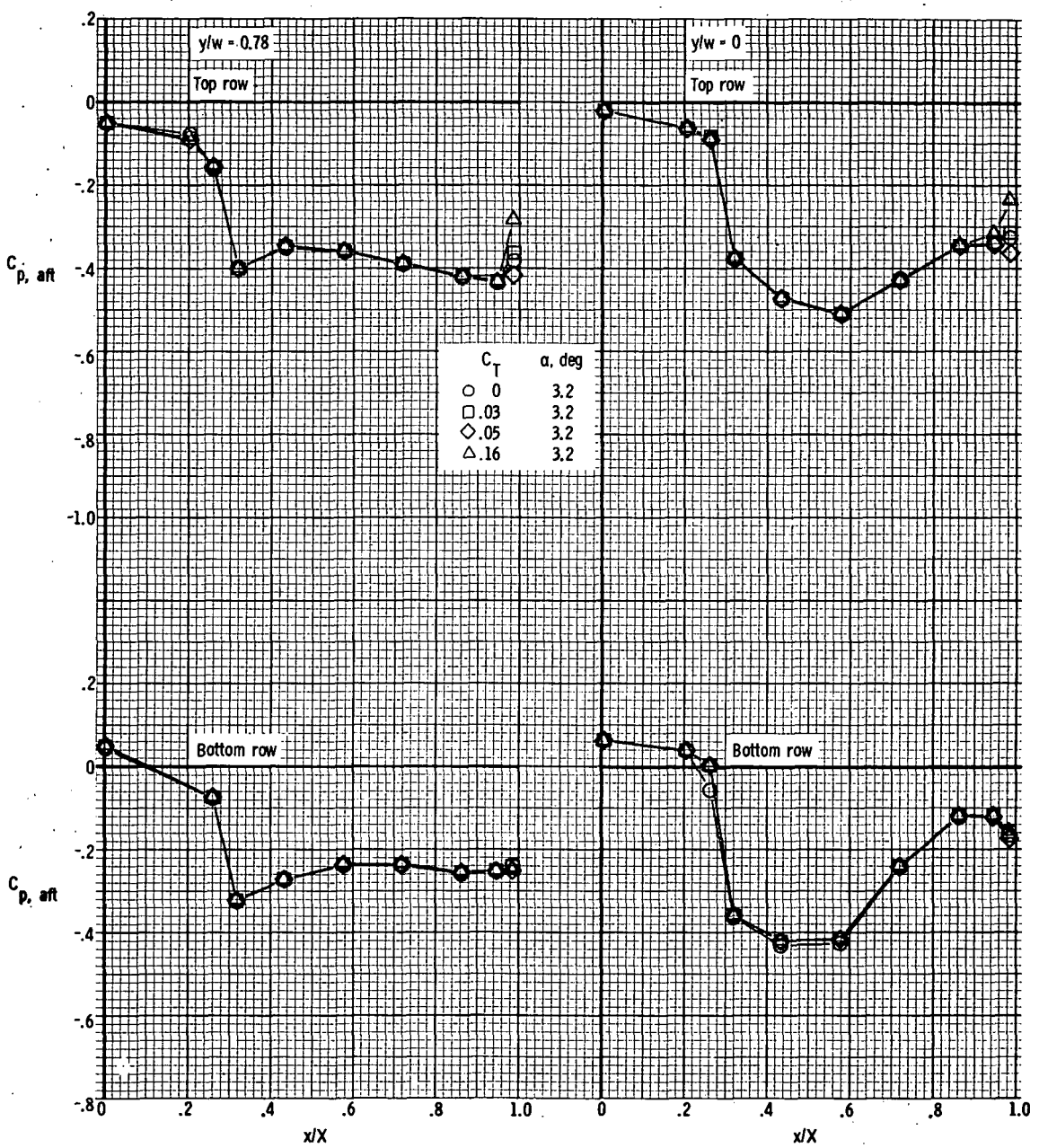

(n) M = 1.20; $\alpha \approx 3.2^{\circ}$.

Figure 20. - Continued.

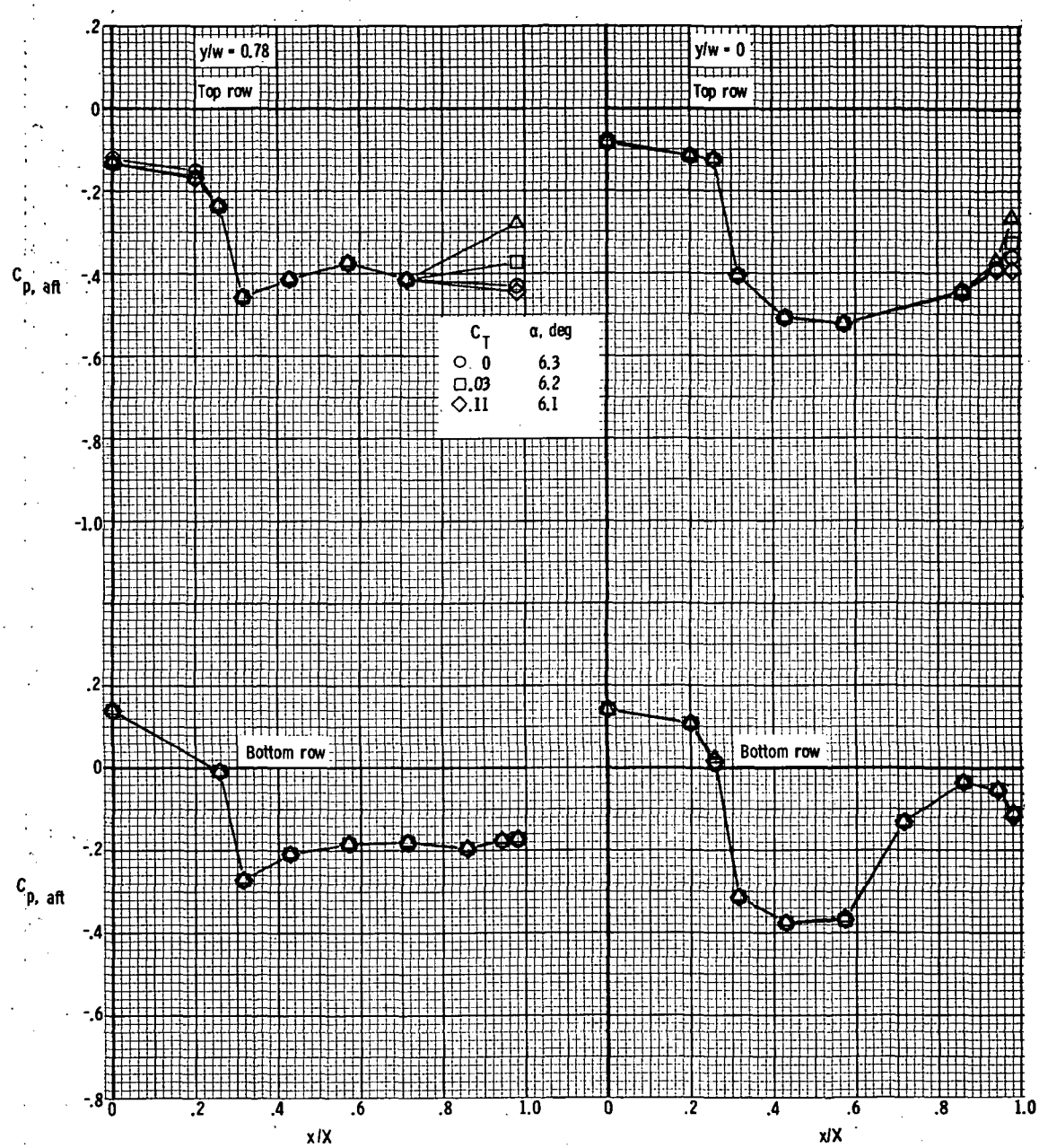

(o) M = 1.20; $\alpha \approx 6.3^{\circ}$.

Figure 20.- Concluded.

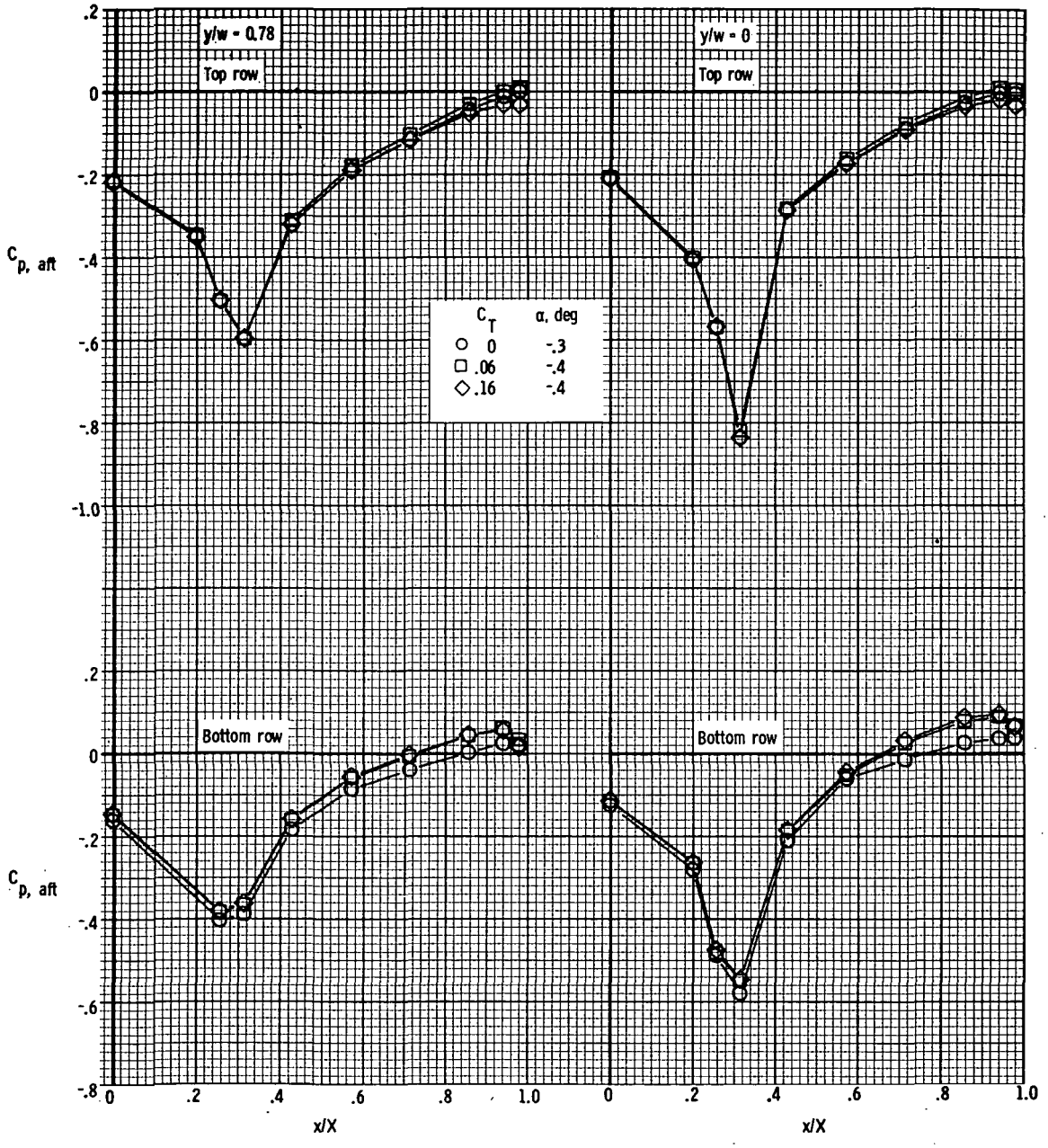

(a) M = 0.70; $\alpha \approx -0.4^{\circ}$.

Figure 21.- Afterbody pressure distributions for model with rectangular exits; $x_e/c_r = 0.14$; $\delta_d = 15^{\circ}$.

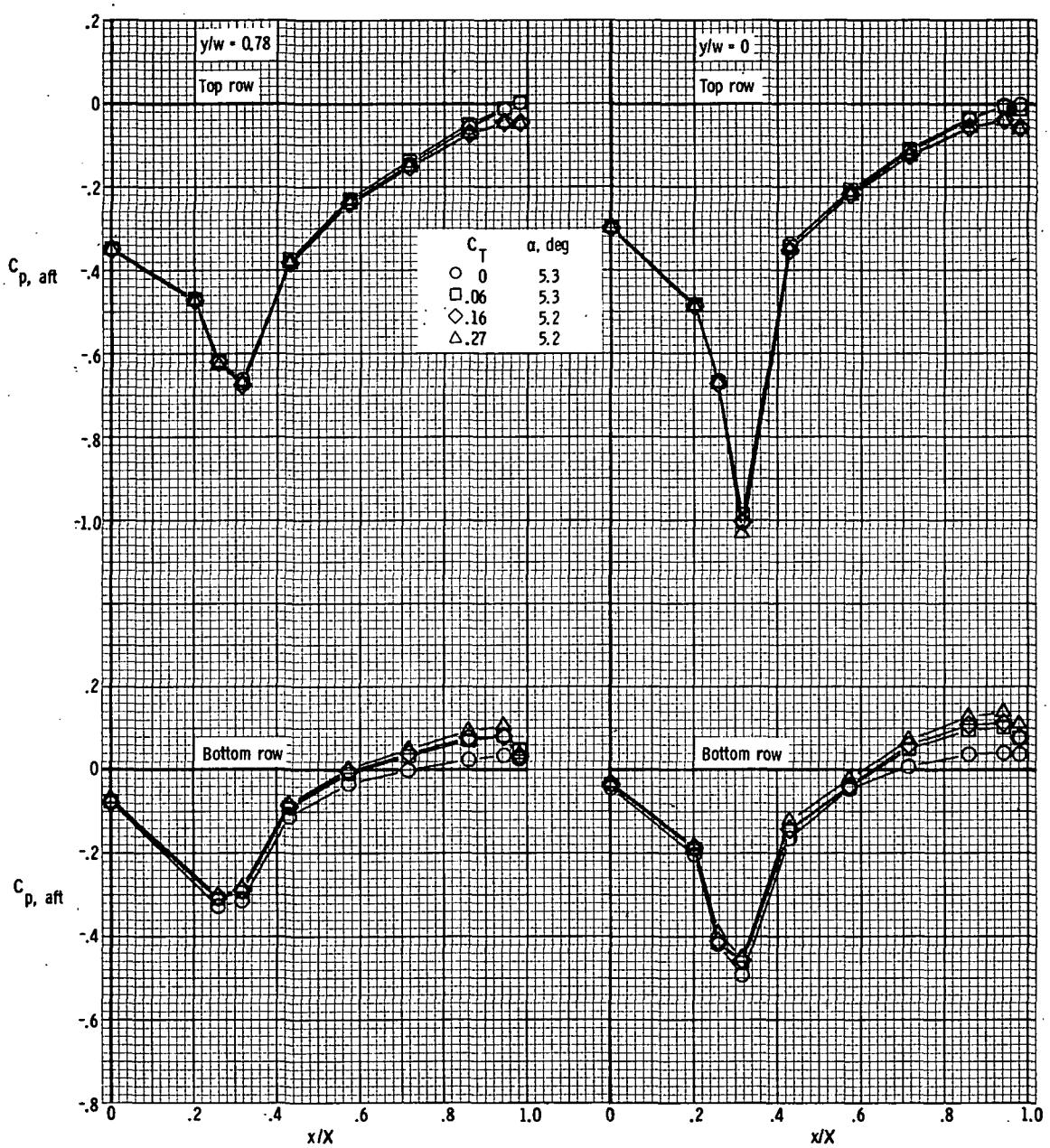

(b) M = 0.70; $\alpha \approx 5.3^{\circ}$.

Figure 21.- Continued.

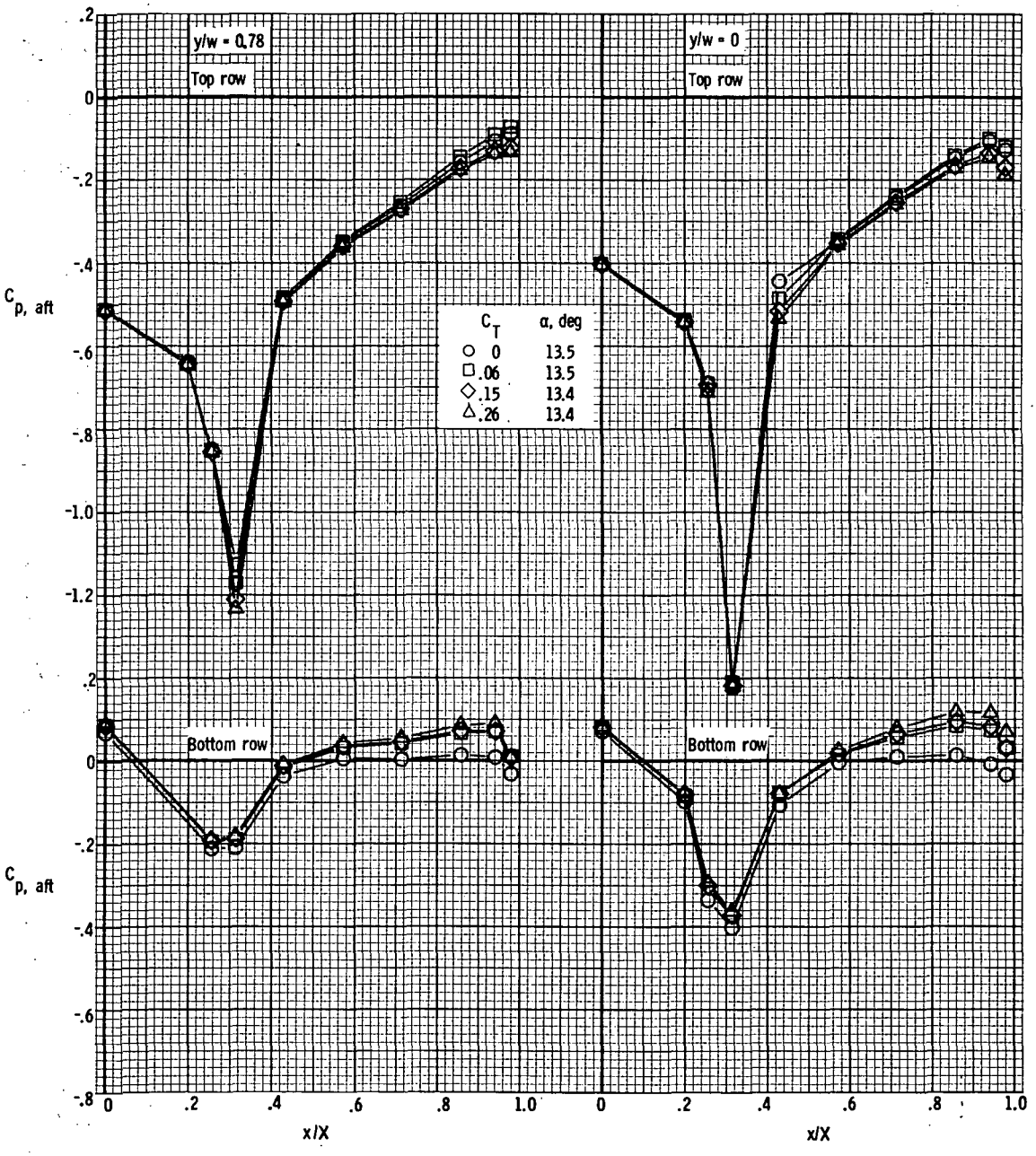

(c) M = 0.70; $\alpha \approx 13.5^{\circ}$.

Figure 21.- Continued.

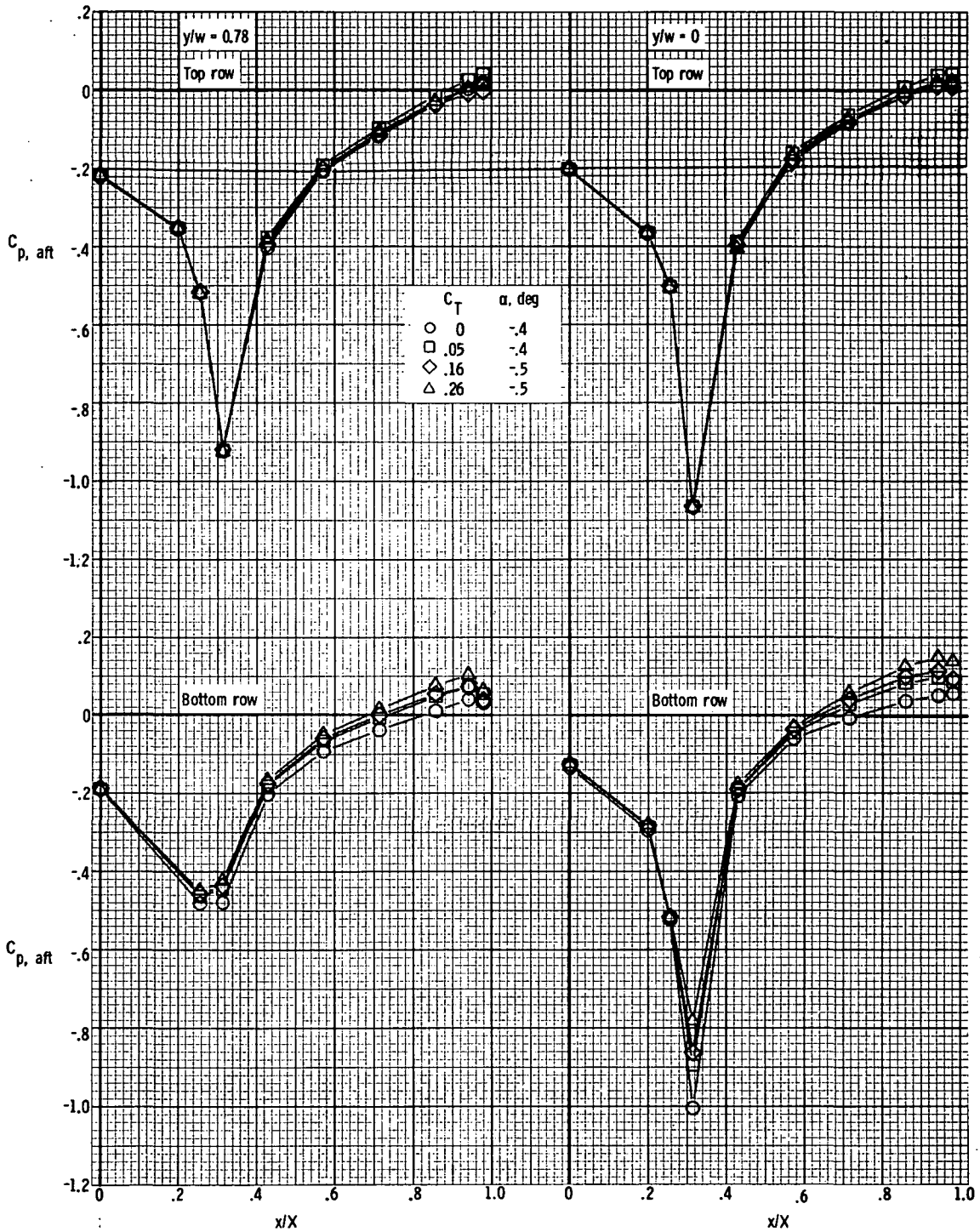

(d) M = 0.80; $\alpha \approx -0.4^{\circ}$.

Figure 21.- Continued.

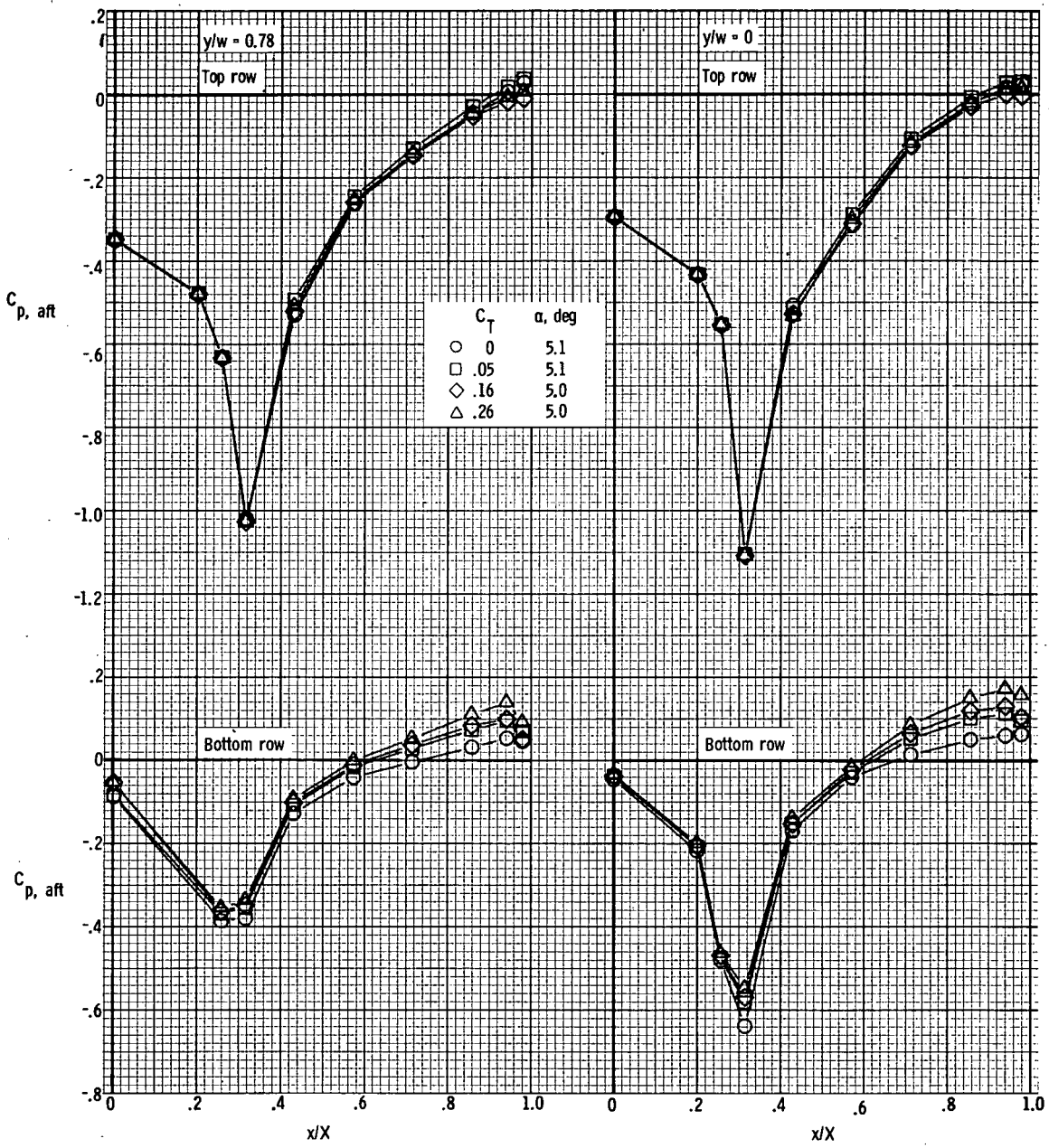

(e) M = 0.80; $\alpha \approx 5.1^{\circ}$.

Figure 21.- Continued.

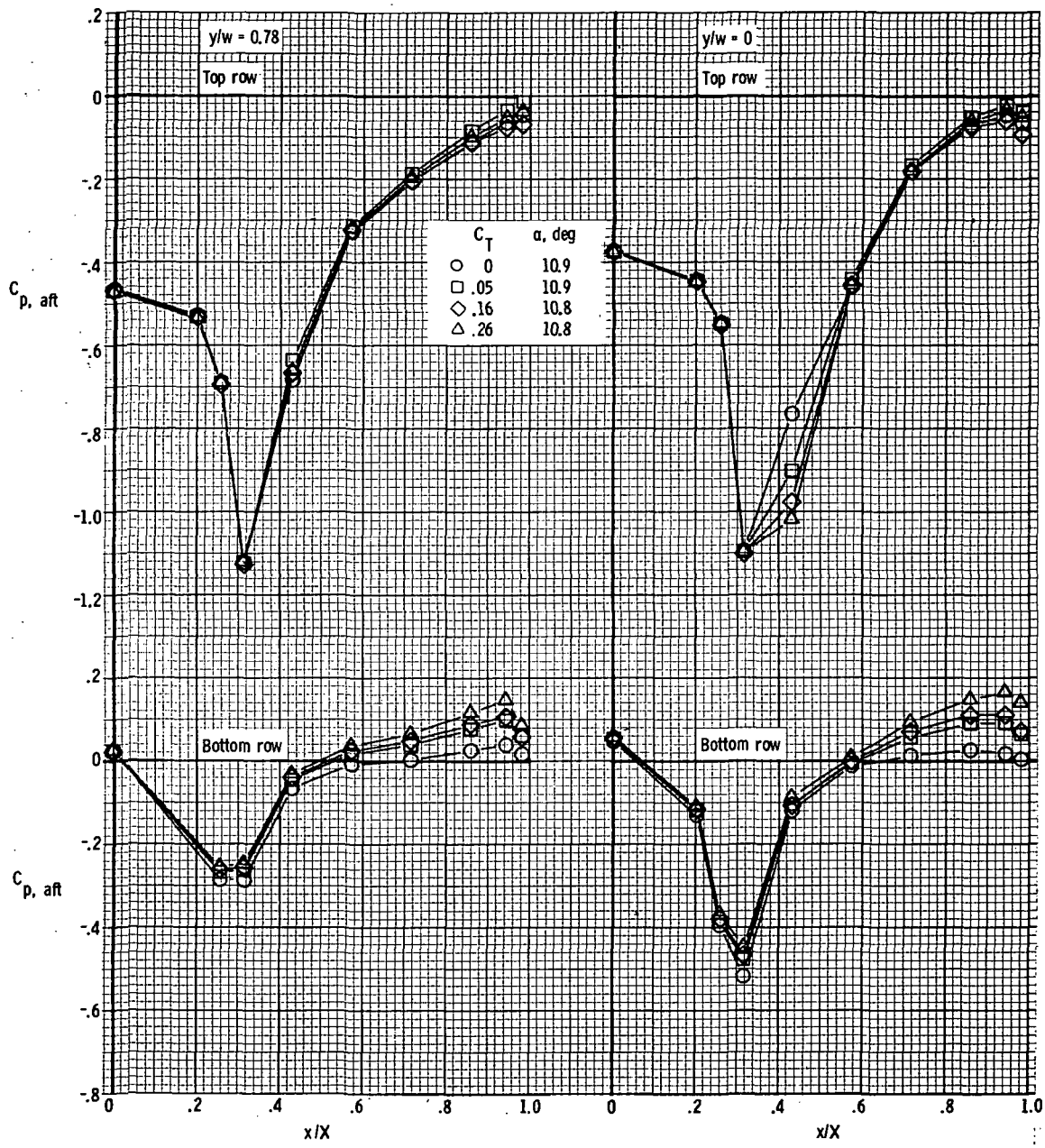

(f) M = 0.80; $\alpha \approx 10.9^{\circ}$.

Figure 21.- Continued.

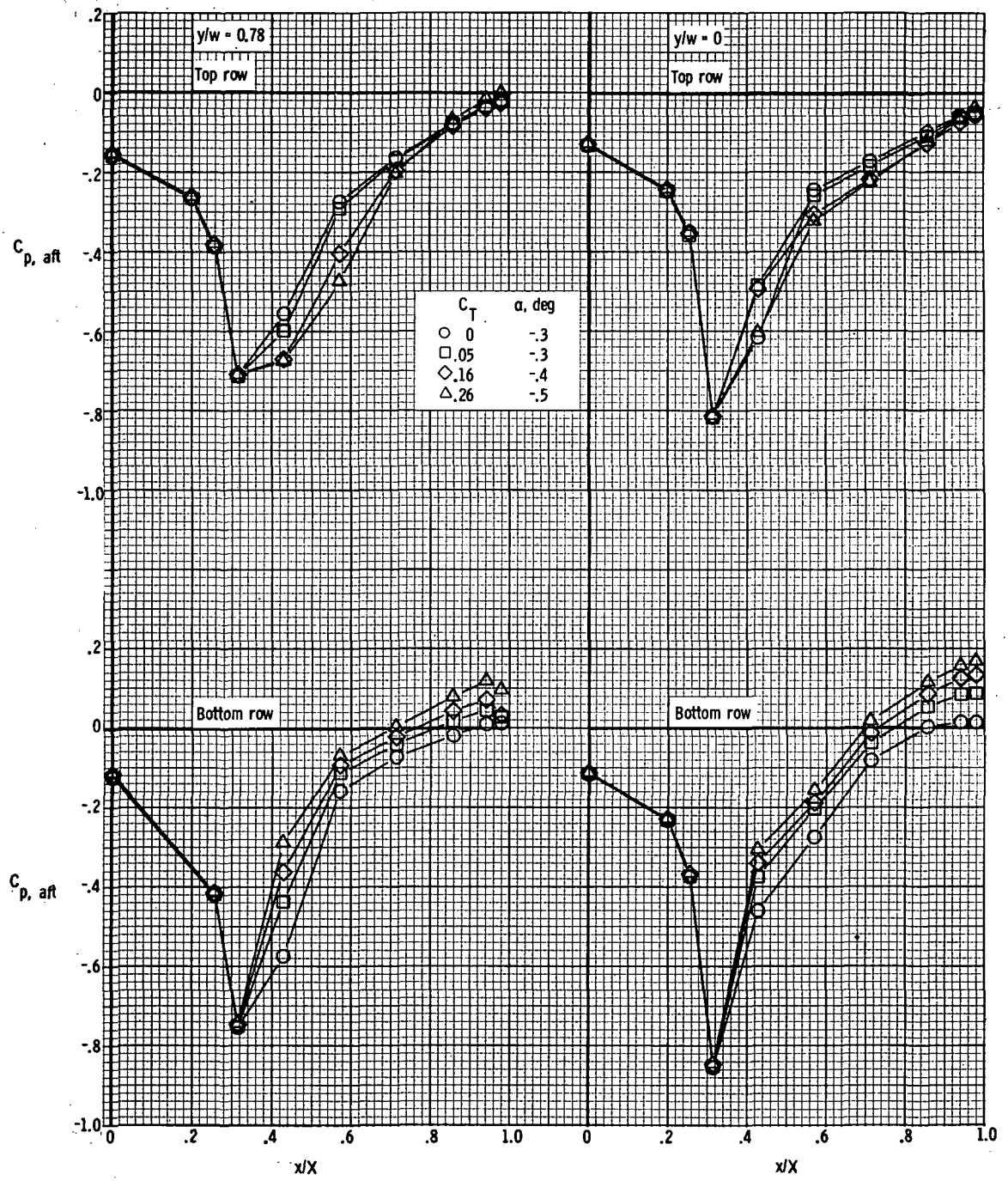

(g) M = 0.90; $\alpha \approx -0.3^{\circ}$.

Figure 21.- Continued.

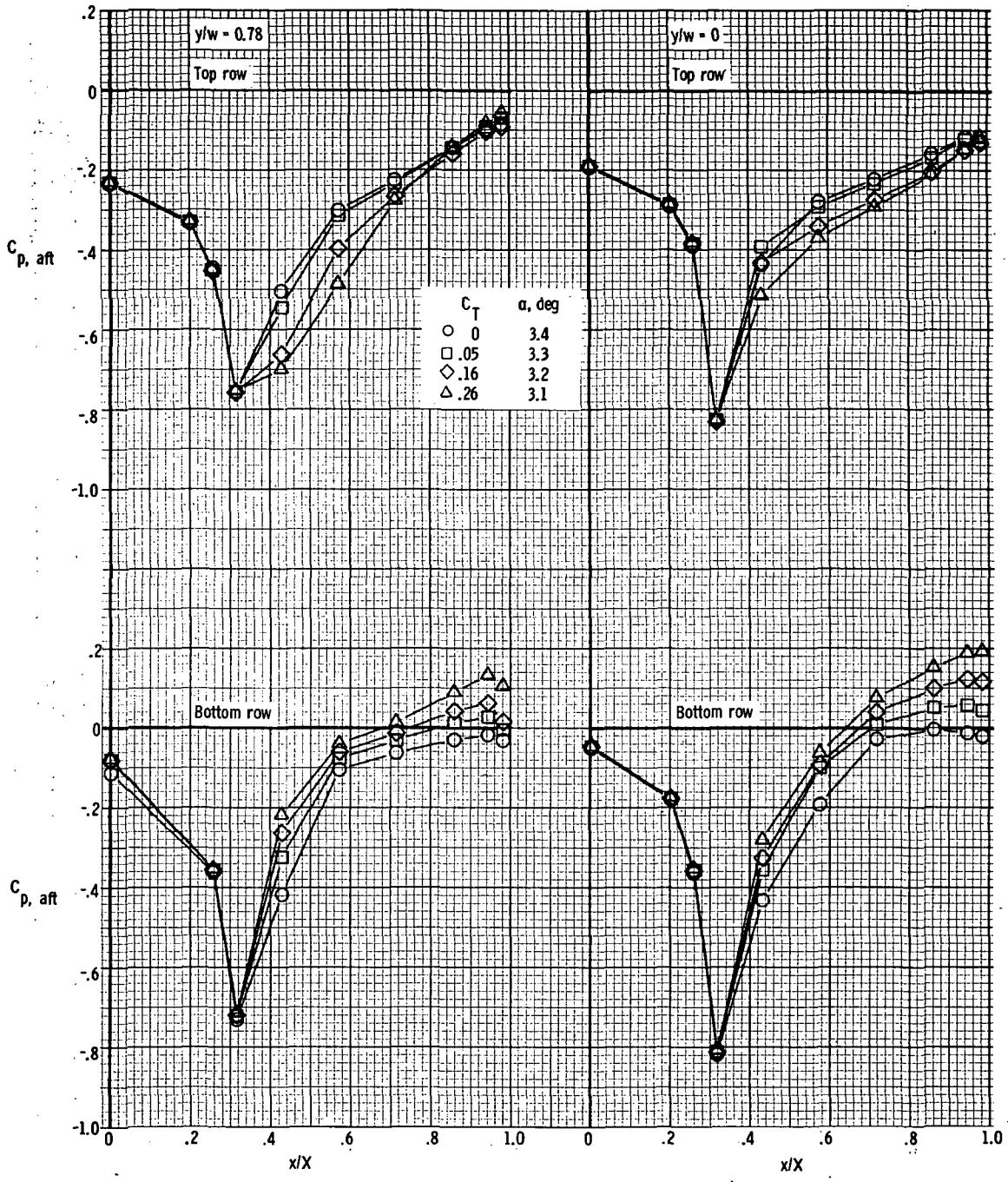

(h) M = 0.90; $\alpha \approx 3.3^{\circ}$.

Figure 21.- Continued.

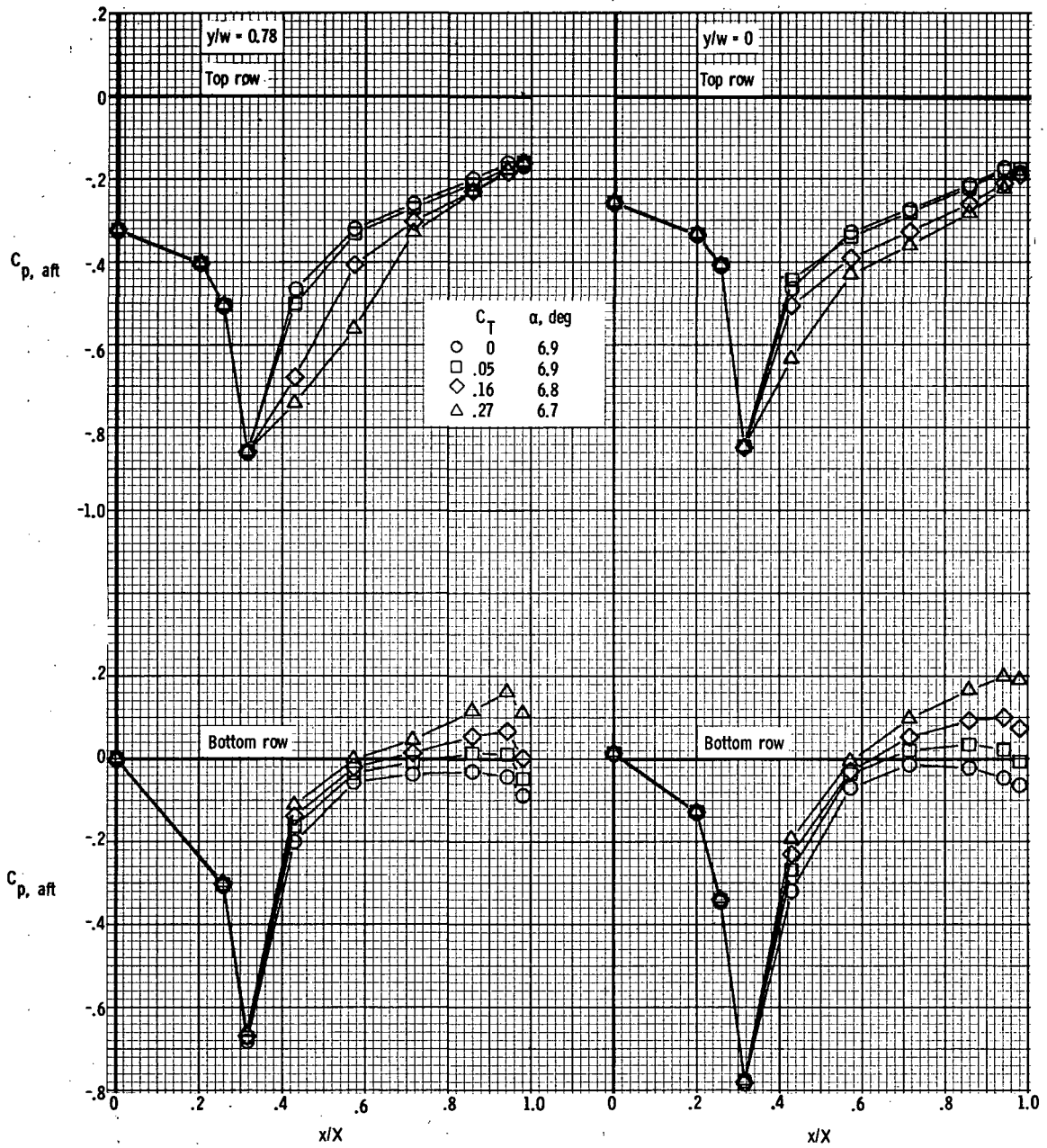

(i) M = 0.90; $\alpha \approx 6.9^{\circ}$.

Figure 21.- Continued.

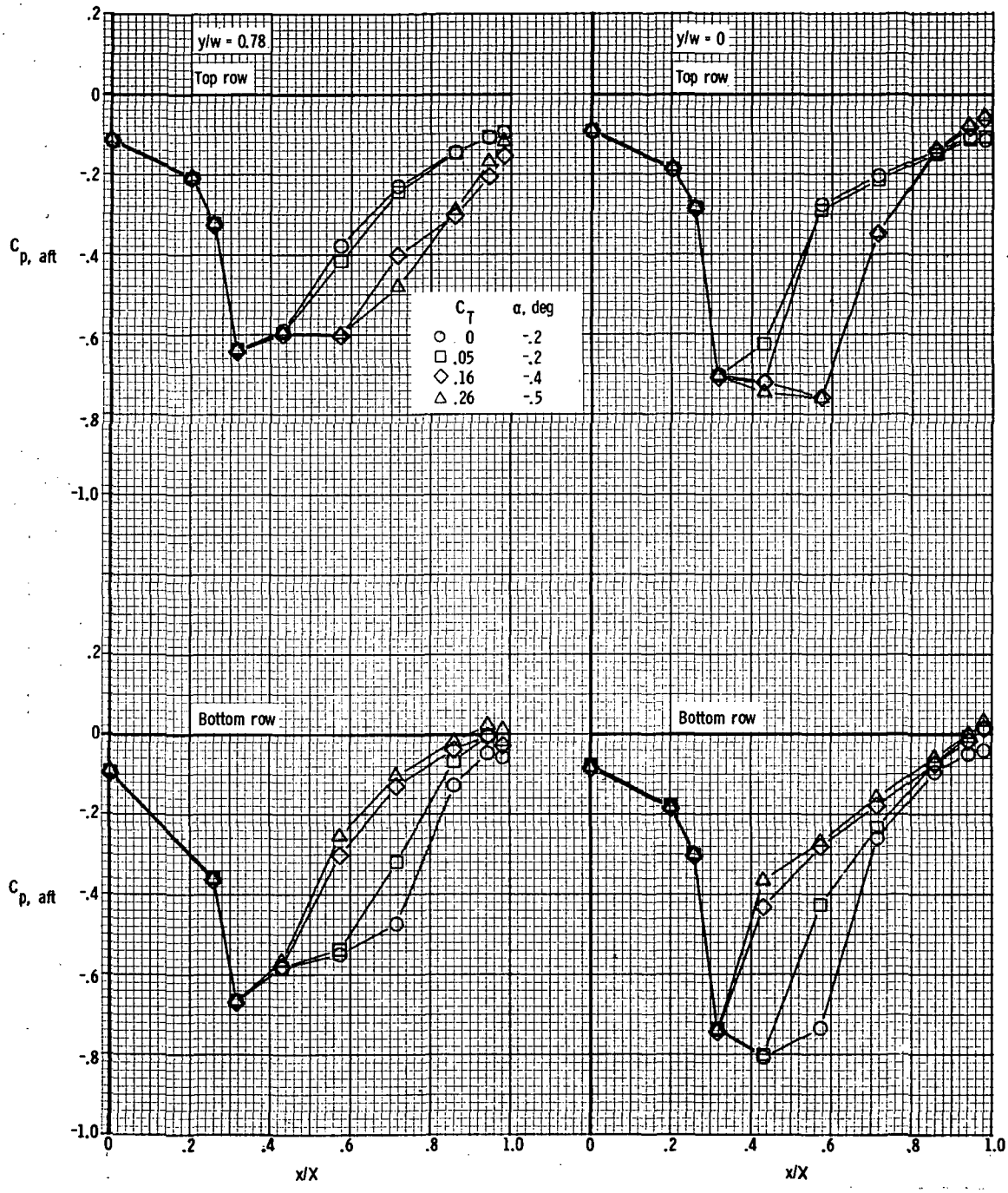

(j) M = 0.95; $\alpha \approx -0.2^{\circ}$.

Figure 21.- Continued.

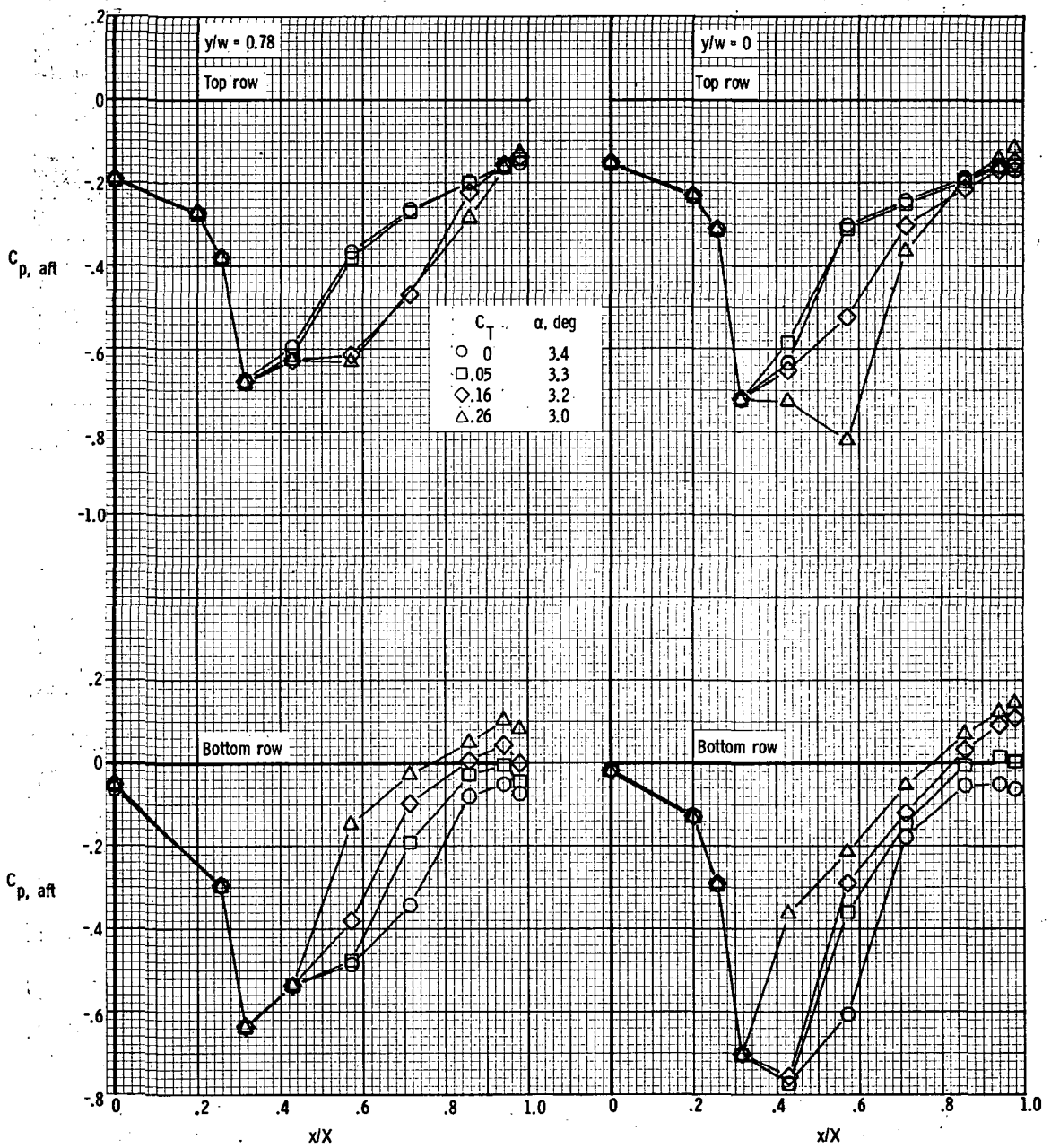

(k) M = 0.95; $\alpha \approx 3.3^{\circ}$.

Figure 21. - Continued.

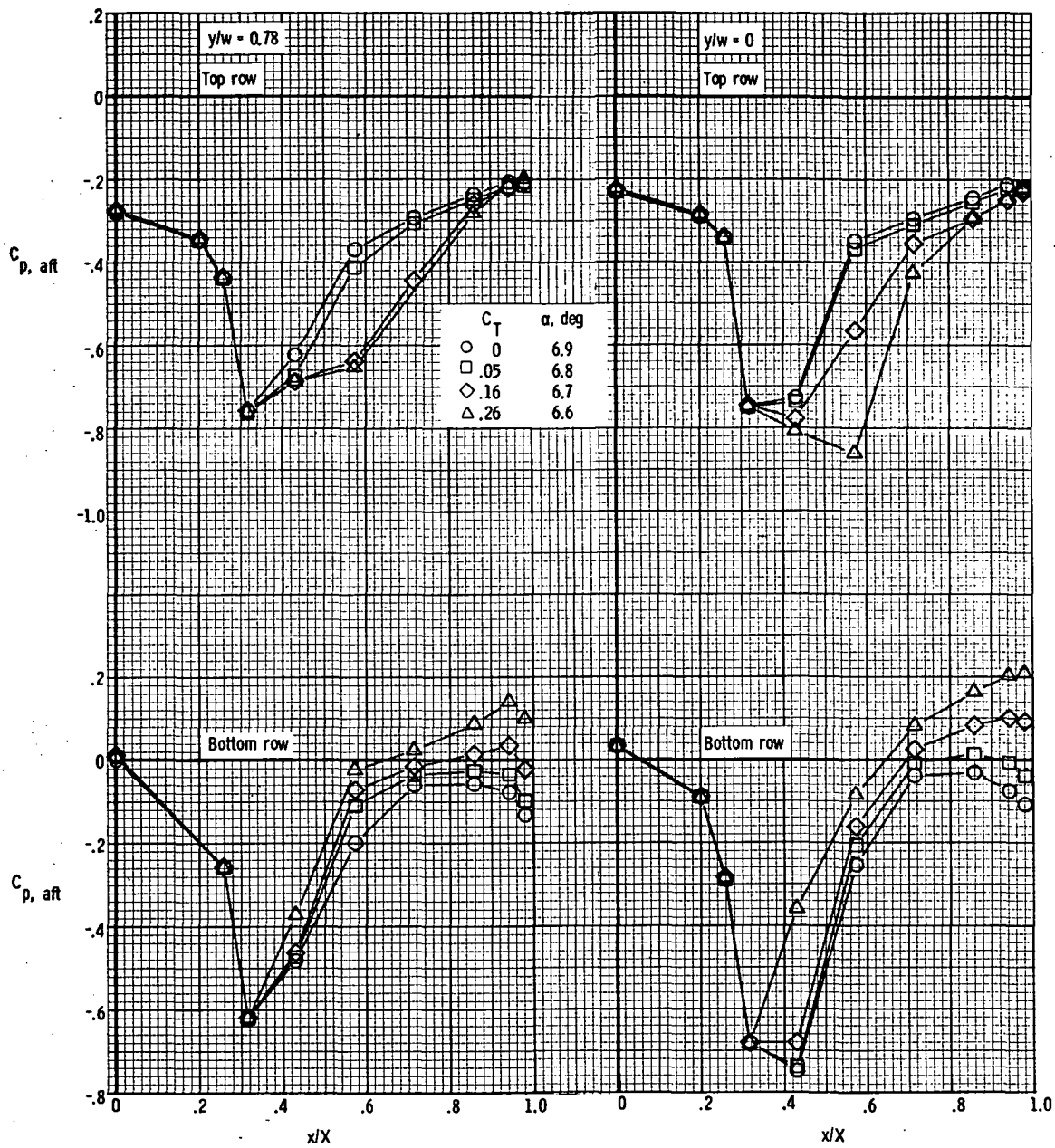

(l) M = 0.95; $\alpha \approx 6.8^{\circ}$.

Figure 21.- Concluded.

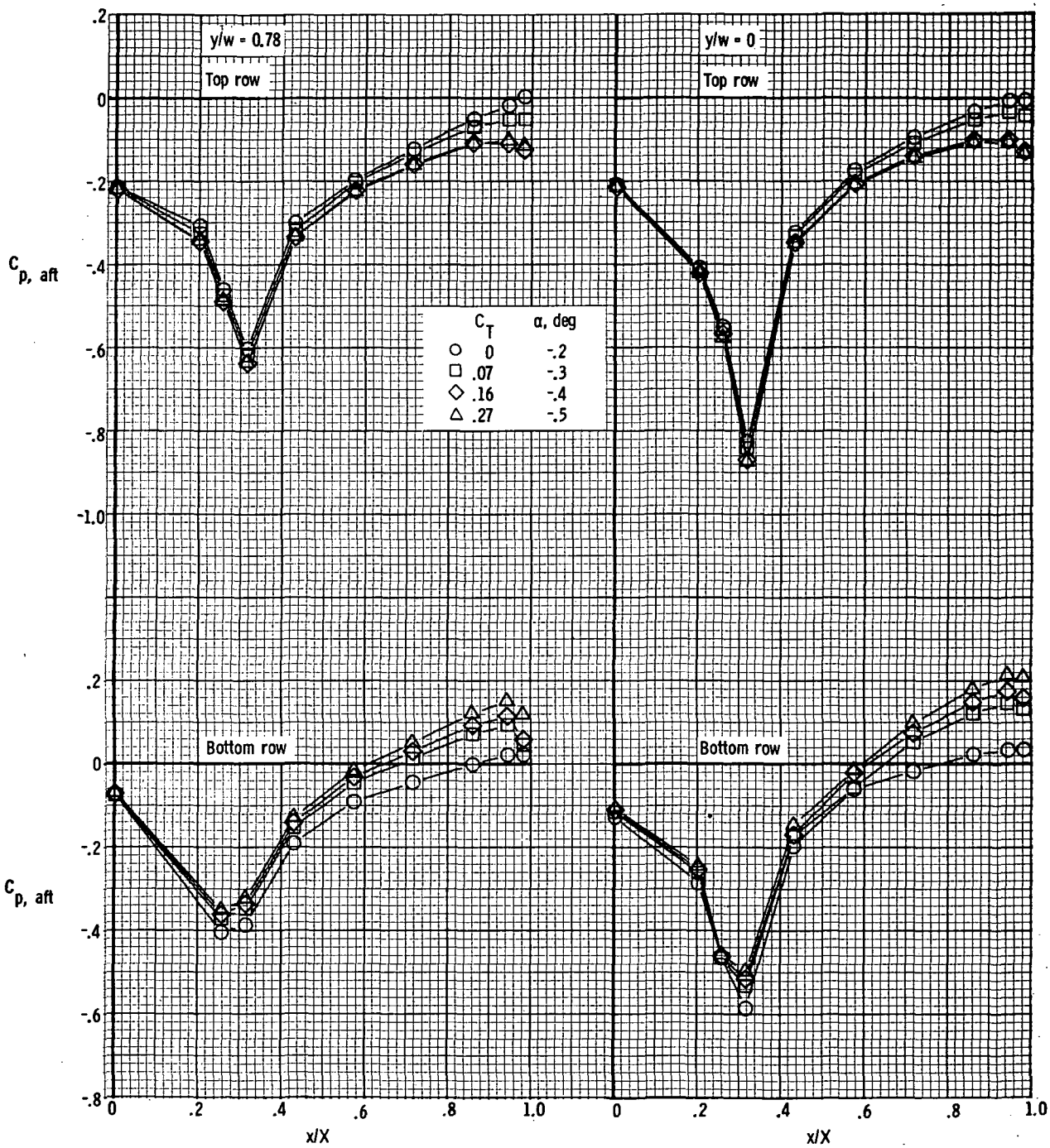

(a) M = 0.70; $\alpha \approx -0.3^{\circ}$.

Figure 22.- Afterbody pressure distributions for model with rectangular exits; $x_e/c_r = 0.14$; $\delta_d = 30^{\circ}$.

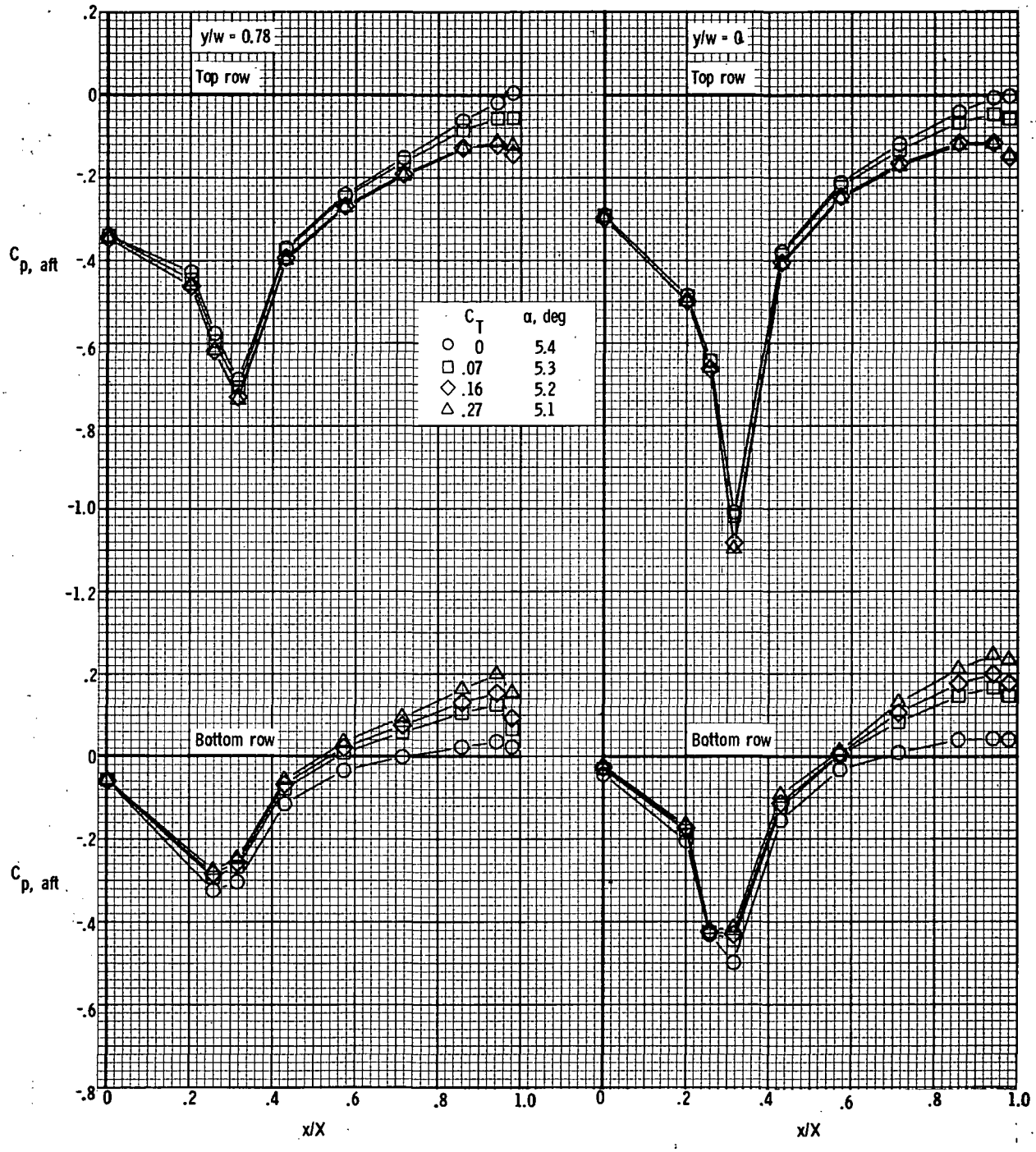

(b) M = 0.70; $\alpha \approx 5.3^{\circ}$.

Figure 22.- Continued.

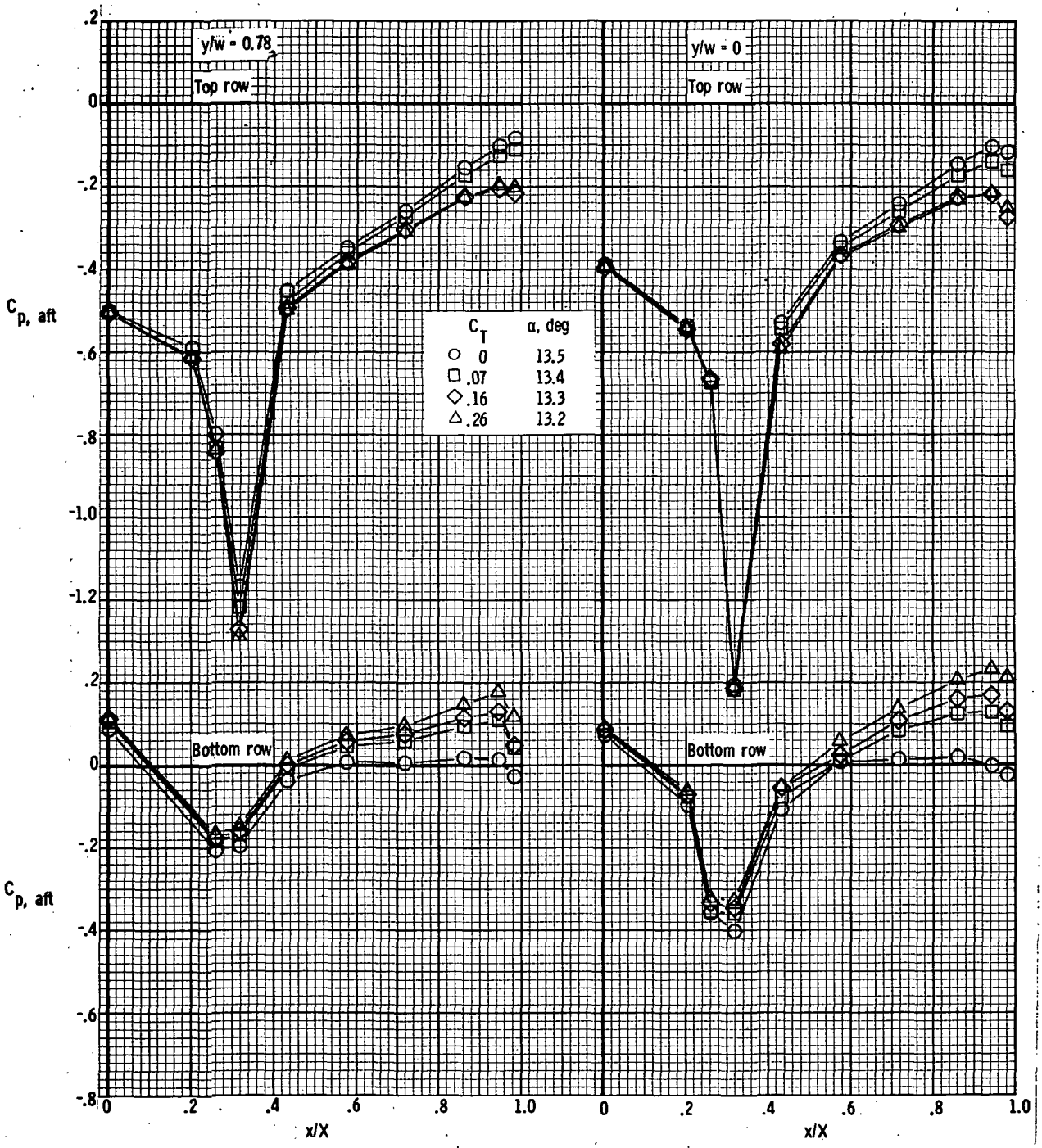

(c) M = 0.70; $\alpha \approx 13.4^{\circ}$.

Figure 22.- Continued.

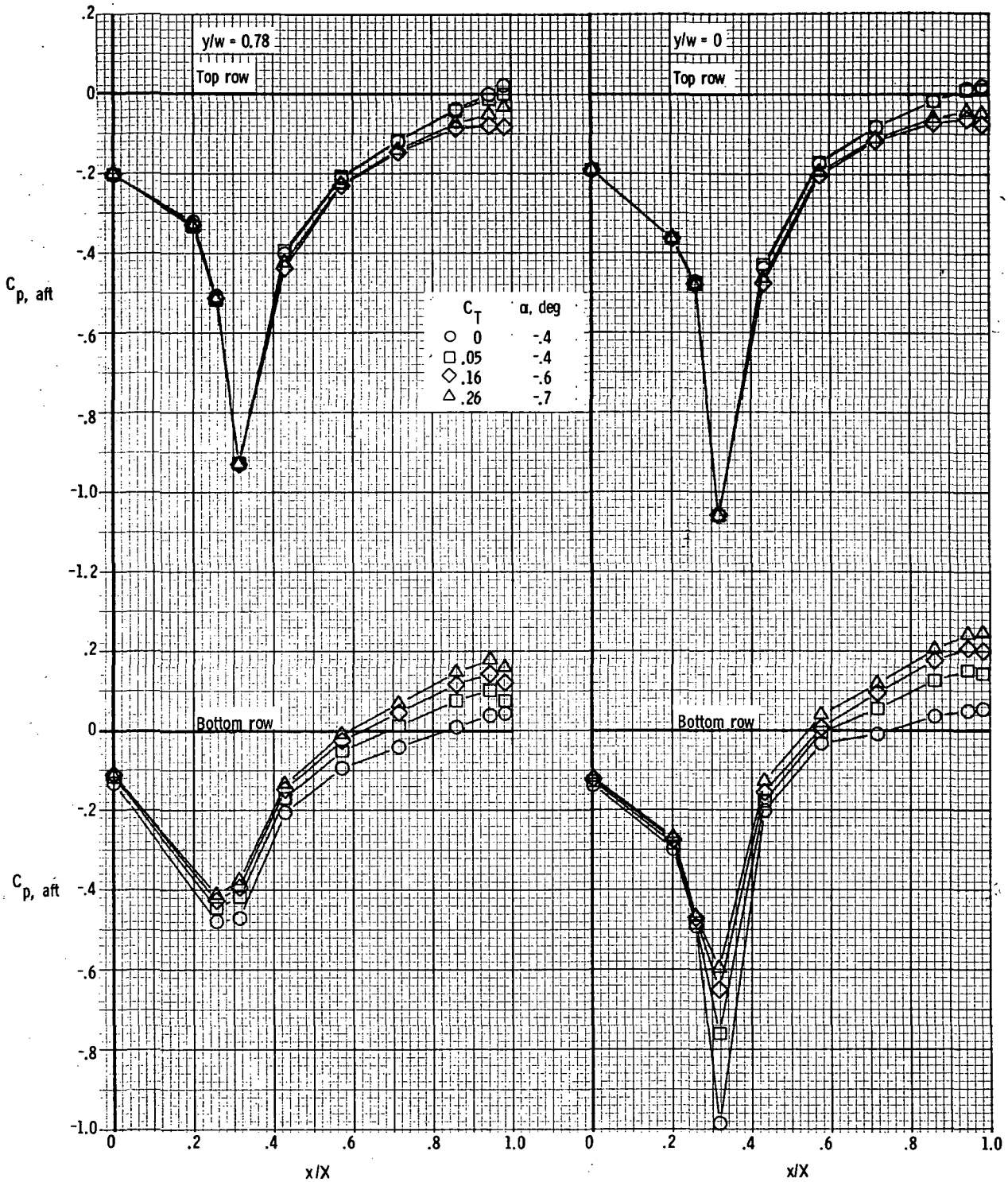

(d) M = 0.80; $\alpha \approx -0.4^{\circ}$.

Figure 22.- Continued.

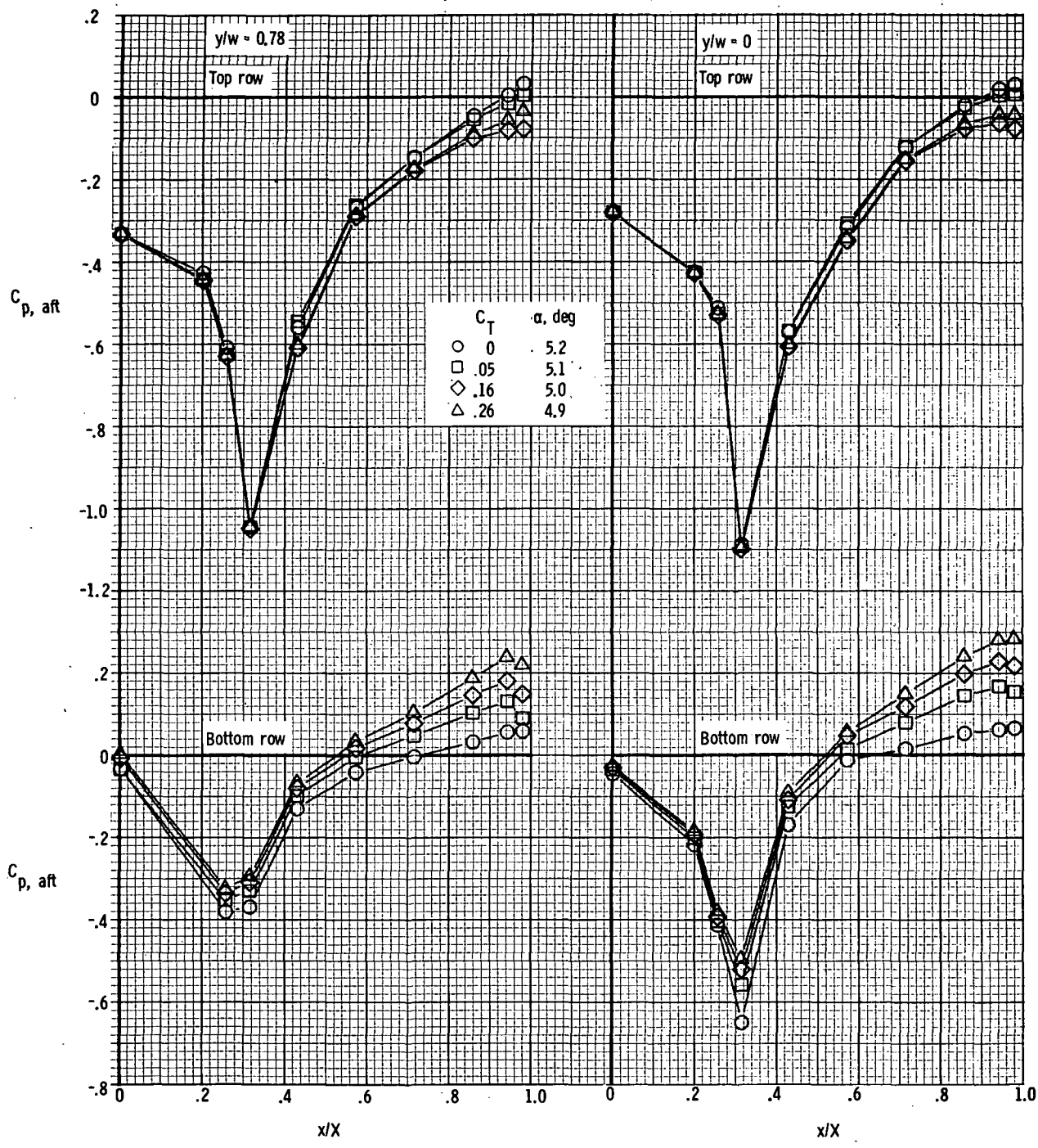

(e) M = 0.80; $\alpha \approx 5.1^{\circ}$.

Figure 22.- Continued.

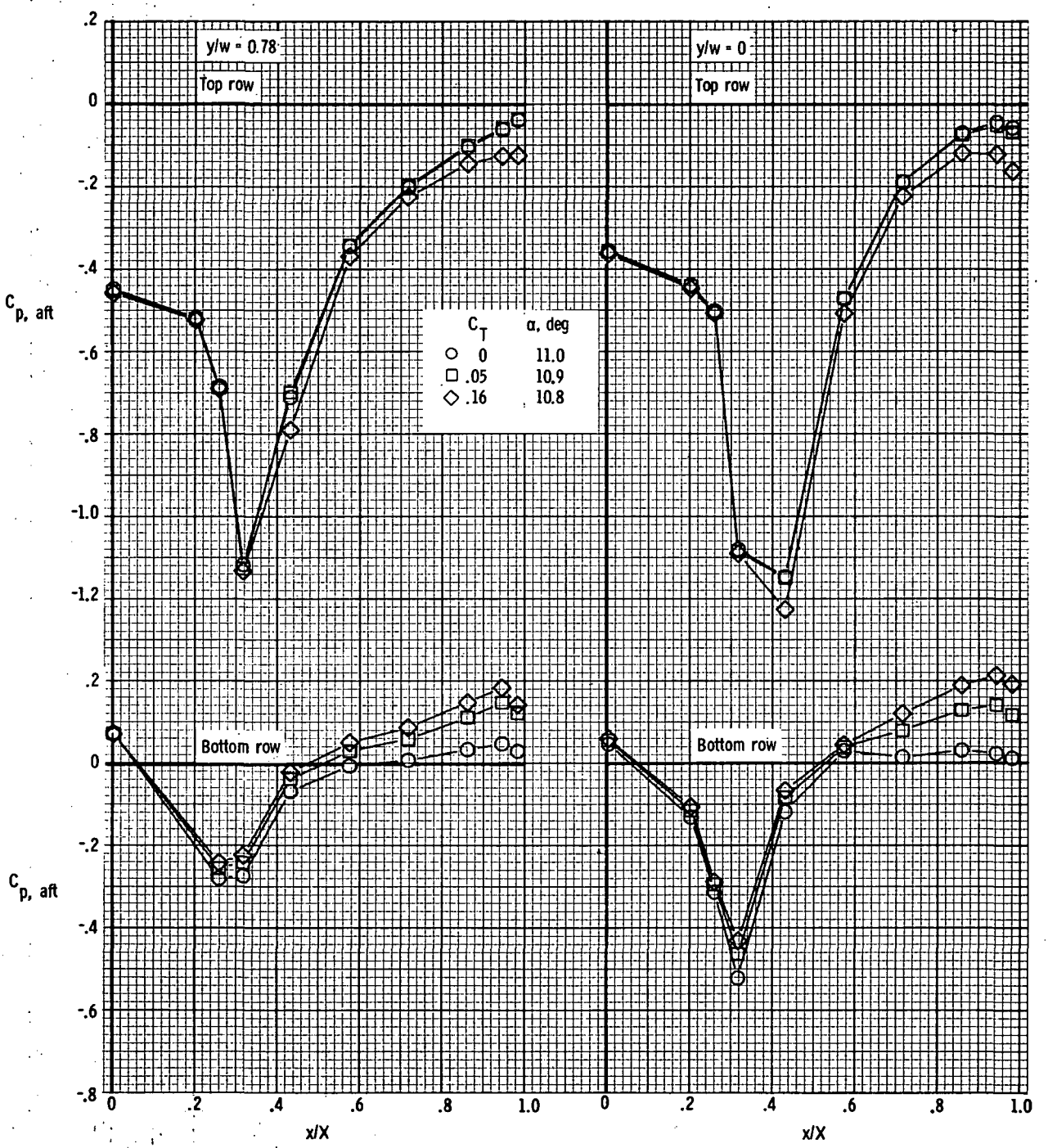

(f) M = 0.80; $\alpha \approx 10.9^{\circ}$.

Figure 22.- Continued.

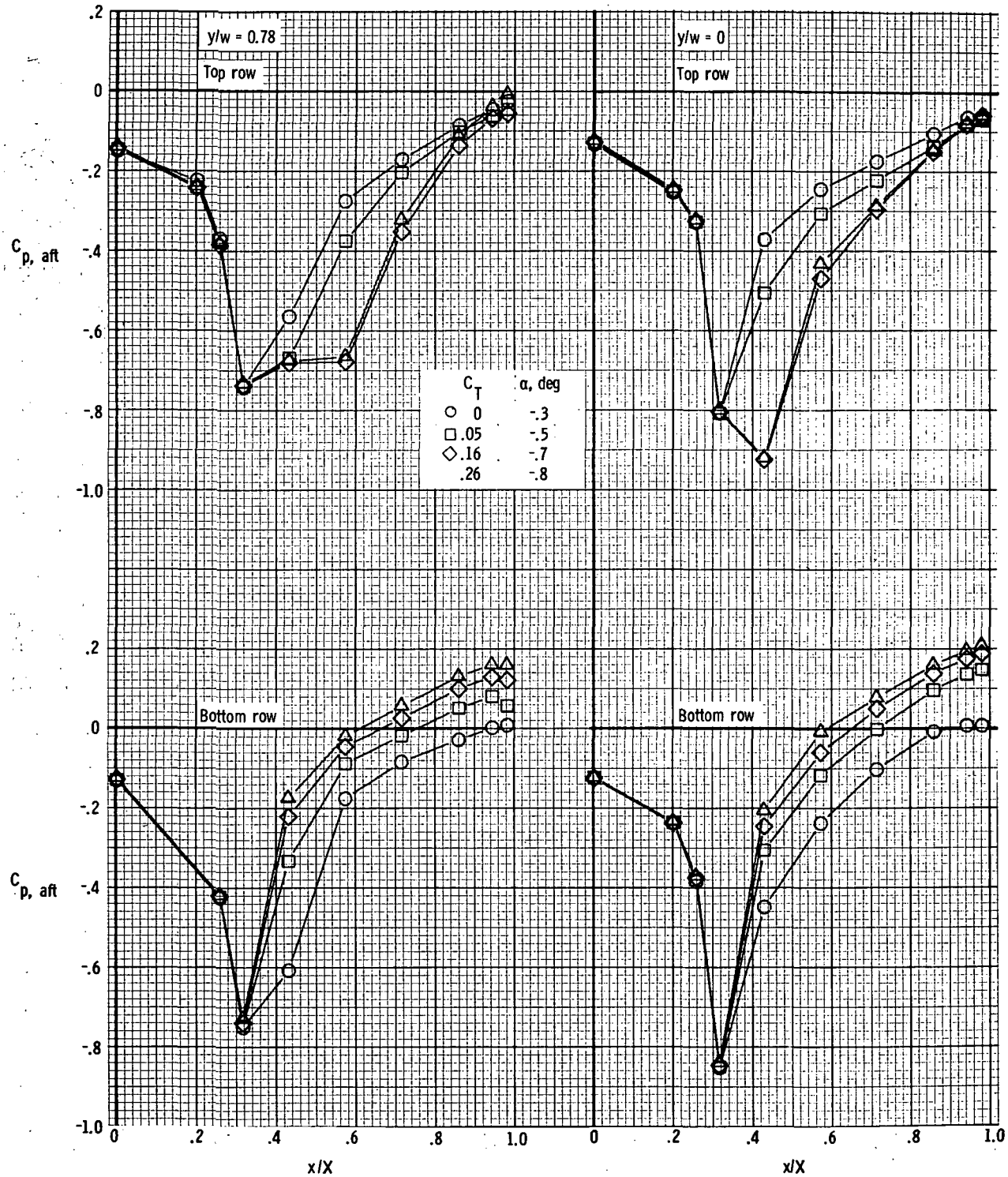

(g) M = 0.90; $\alpha \approx -0.5^{\circ}$.

Figure 22.- Continued.

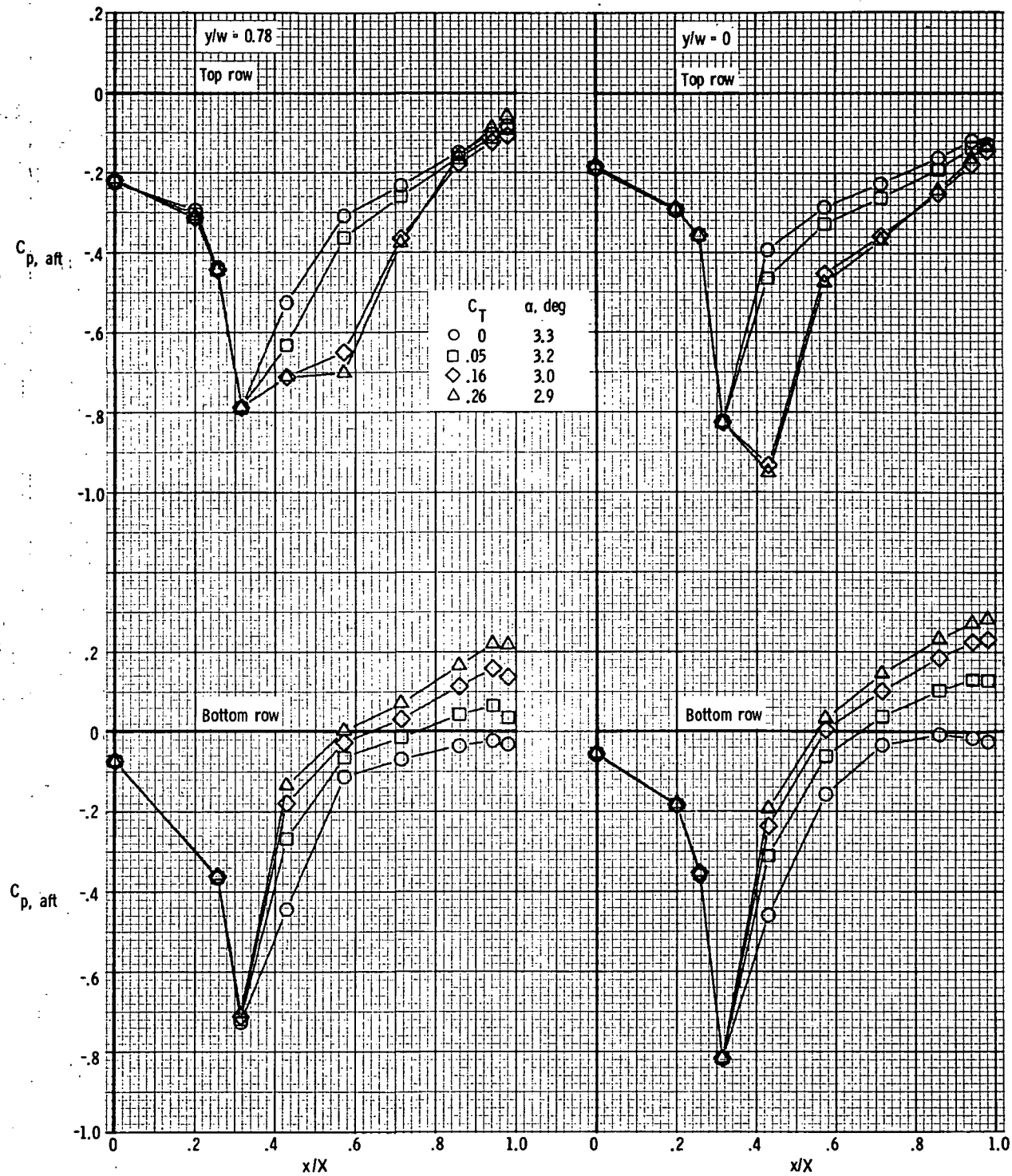

(h) M = 0.90; $\alpha \approx 3.2^{\circ}$.

Figure 22. - Continued.

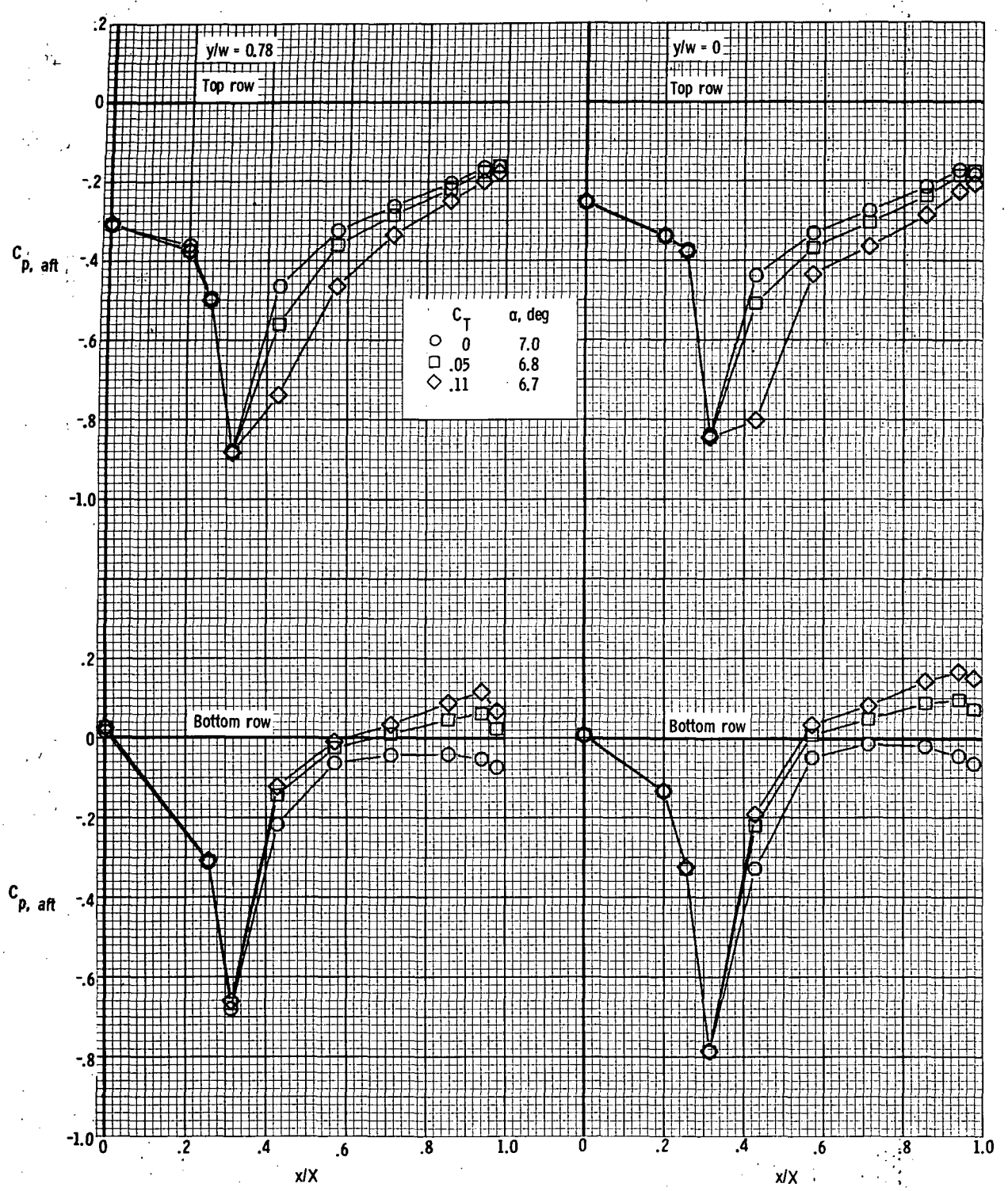

(i) M = 0.90; $\alpha \approx 6.8^{\circ}$.

Figure 22.- Continued.

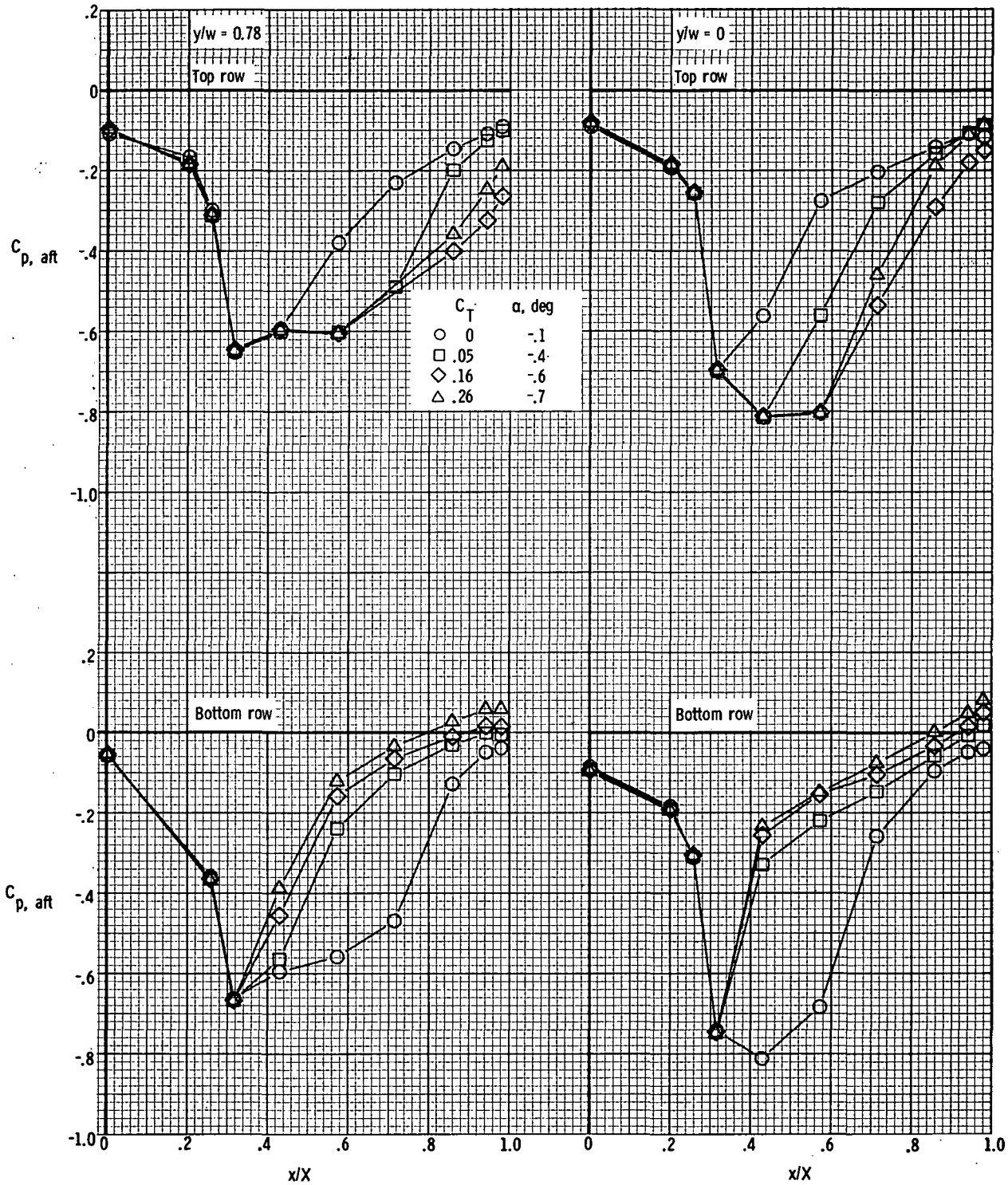

(j) M = 0.95; $\alpha \approx -0.4^{\circ}$.

Figure 22.- Continued.

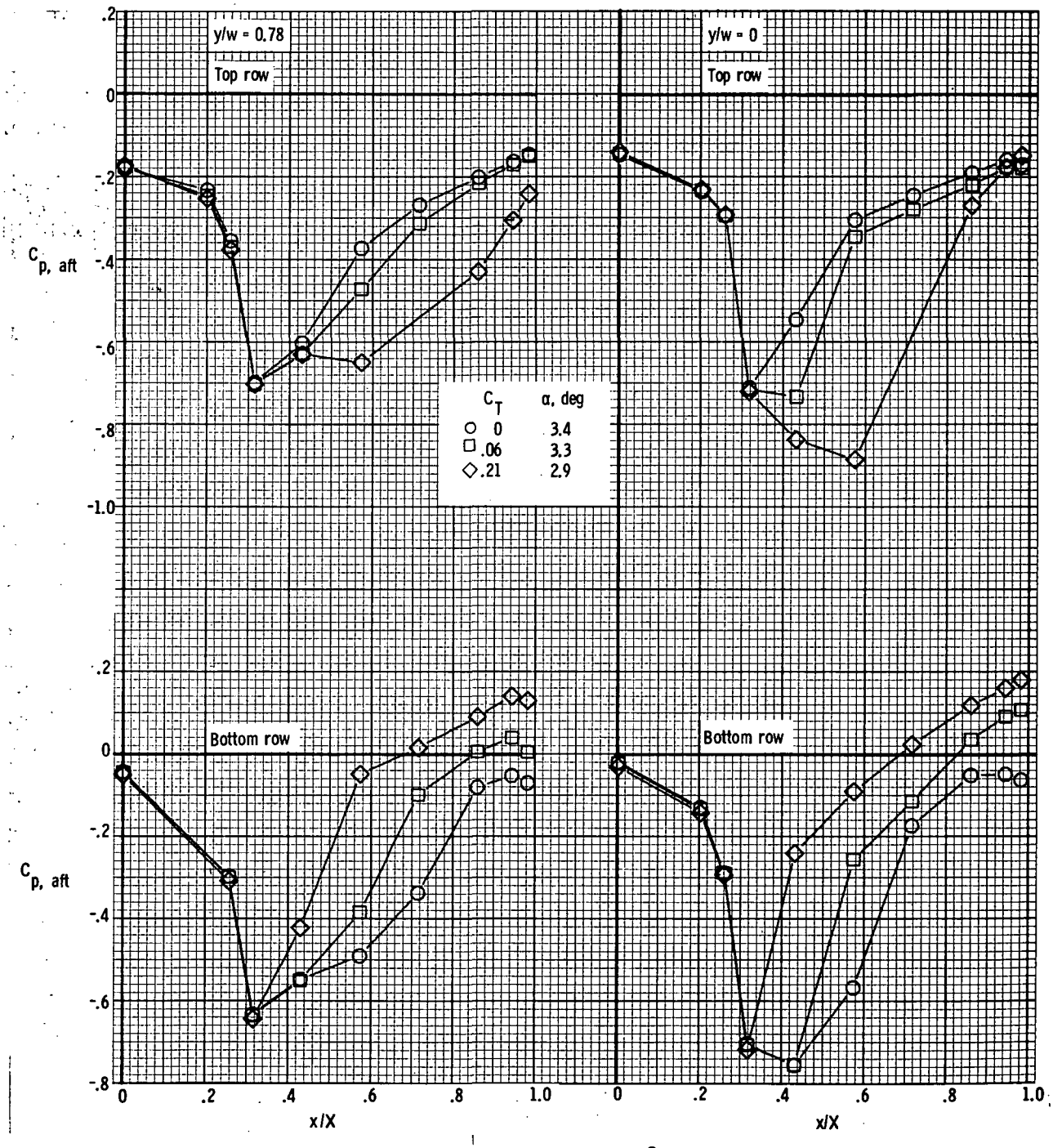

(k) M = 0.95; $\alpha \approx 3.3^{\circ}$.

Figure 22.- Continued.

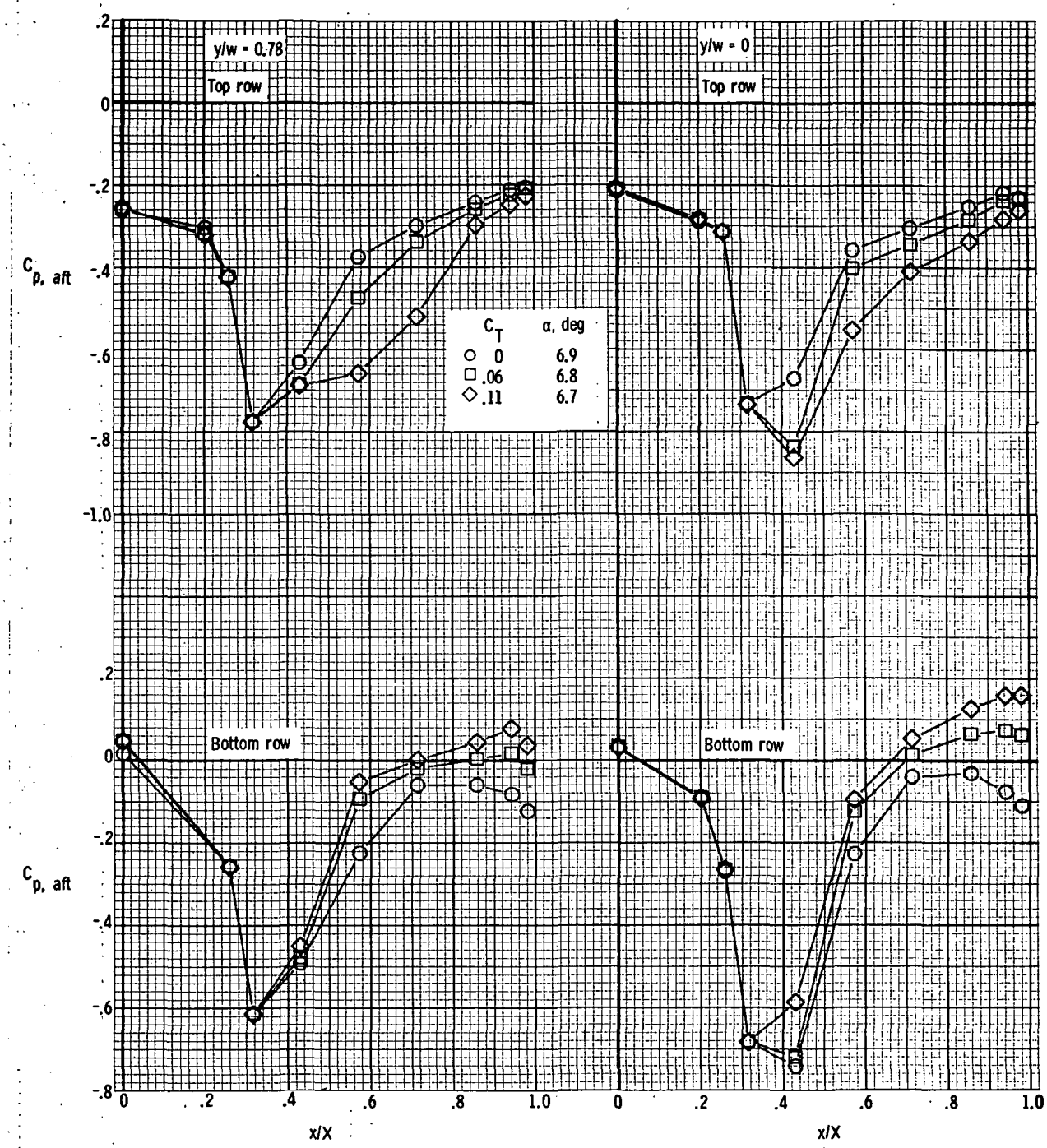

(l) M = 0.95; $\alpha \approx 6.8^{\circ}$.

Figure 22.- Continued.

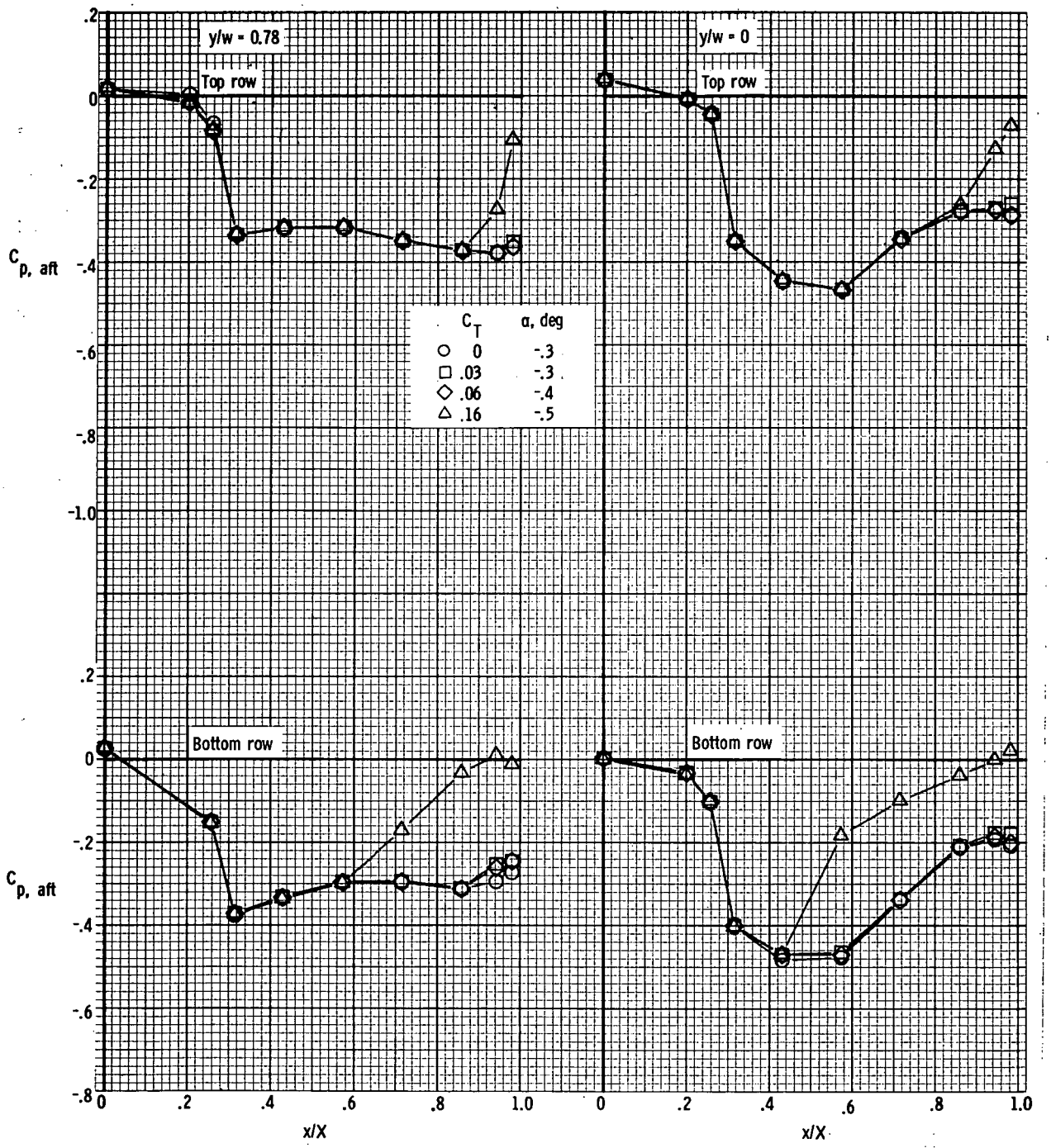

(m) M = 1.20; $\alpha \approx -0.3^{\circ}$.

Figure 22.- Continued.

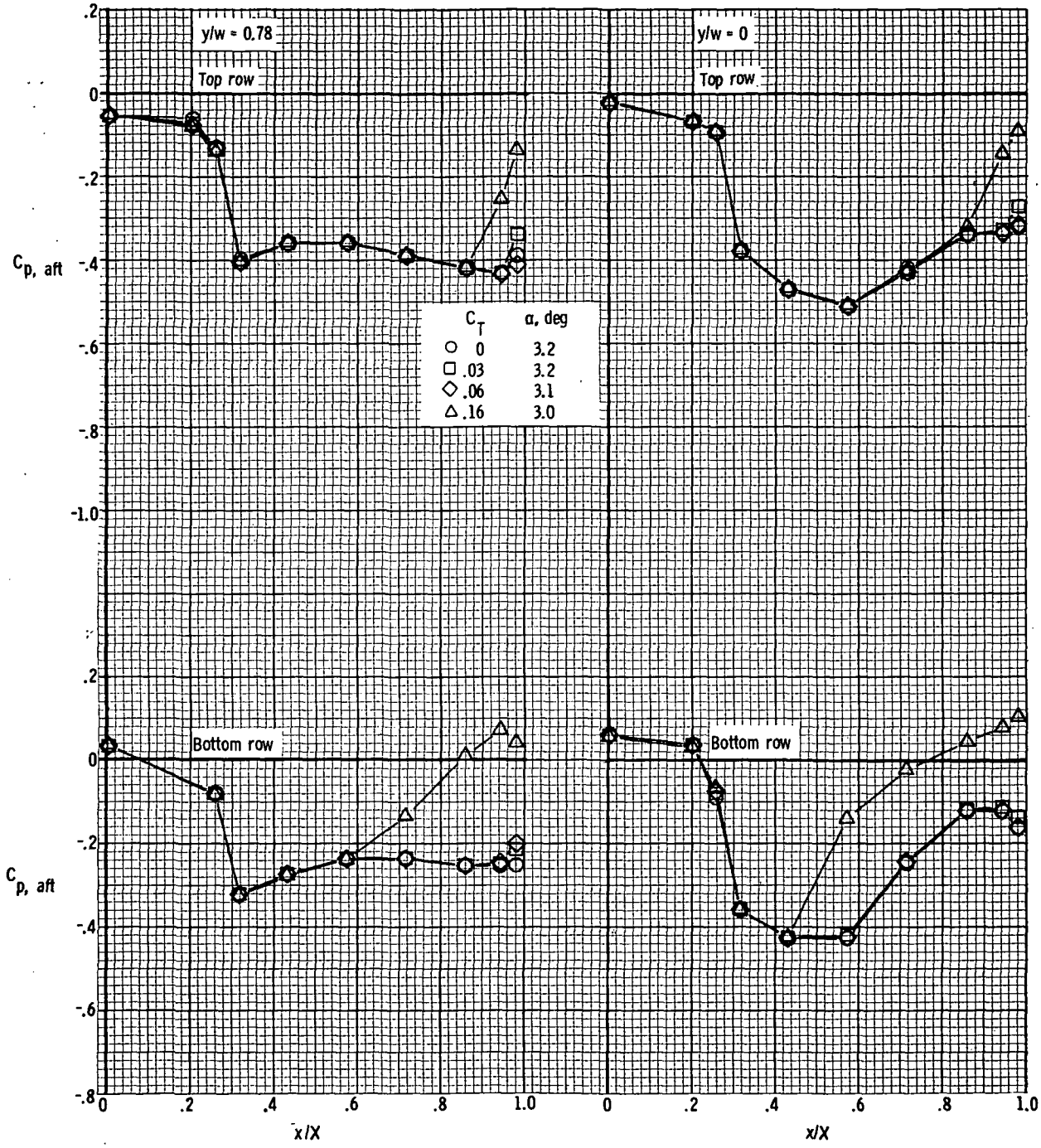

(n) $M = 1.20$; $\alpha \approx 3.2^{\circ}$.

Figure 22.- Continued.

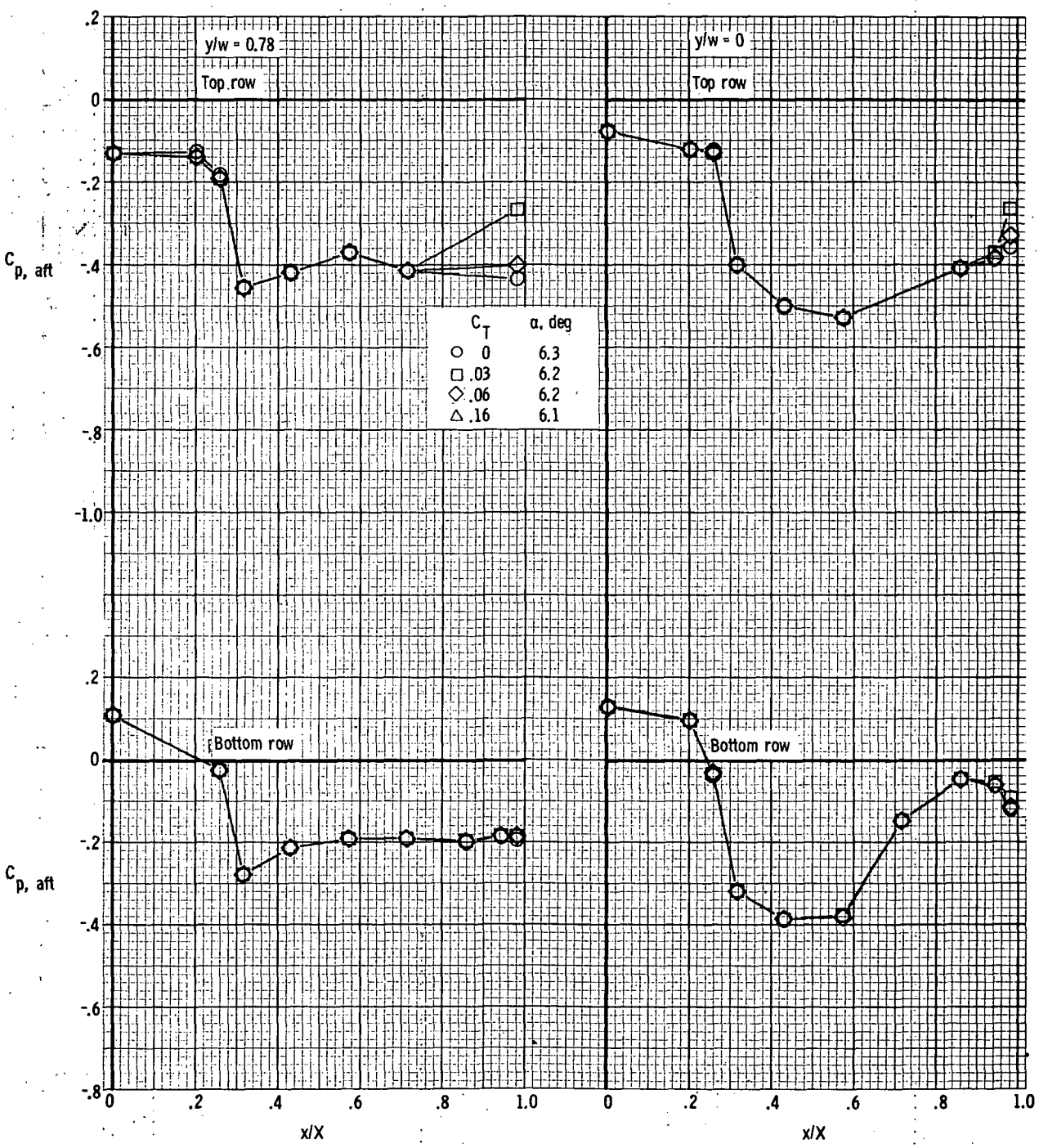

(o) M = 1.20; $\alpha \approx 6.2^{\circ}$.

Figure 22.- Concluded.

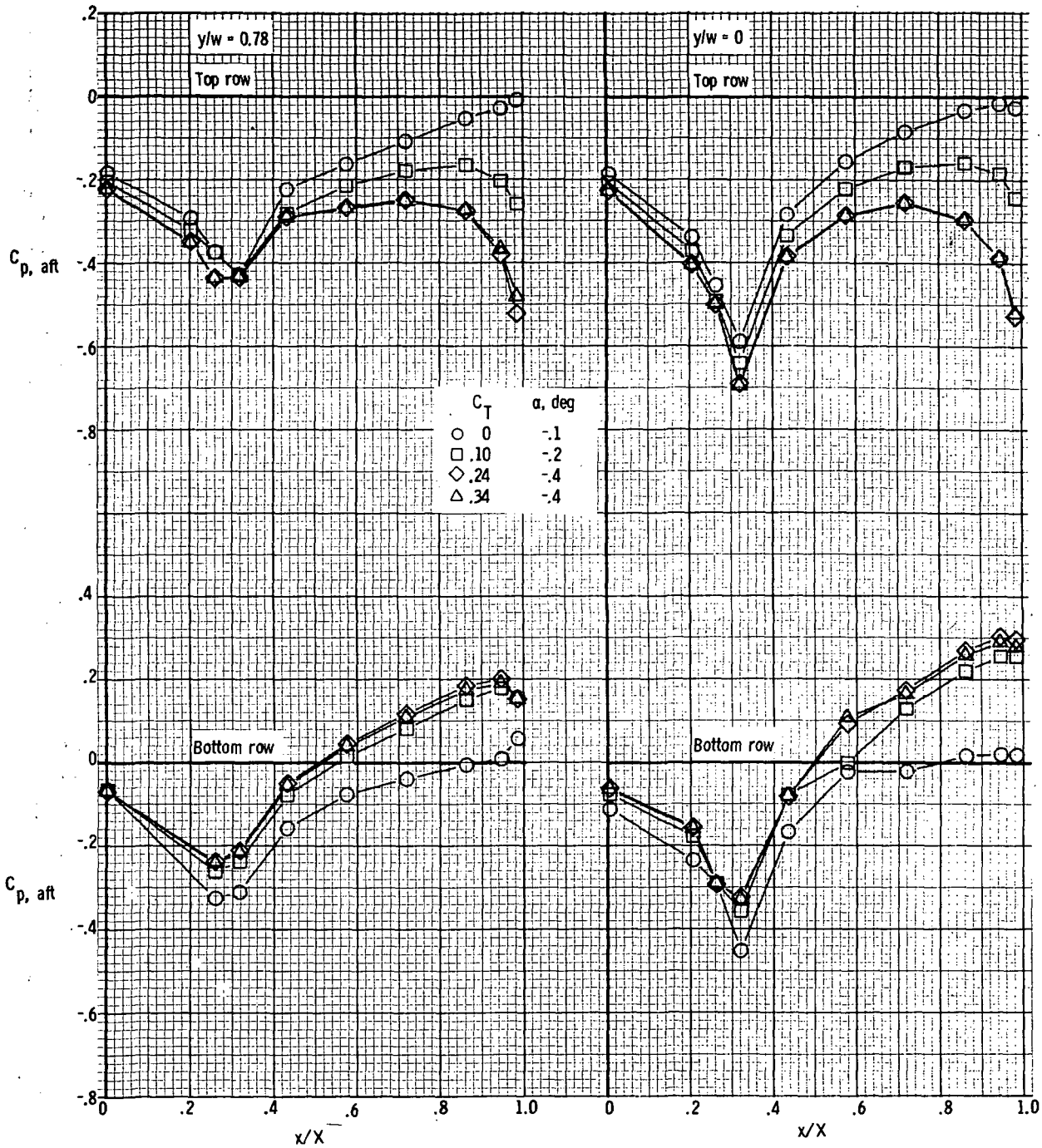

(a) M = 0.40; $\alpha \approx -0.2^{\circ}$.

Figure 23. - Afterbody pressure distributions for model with rectangular exits; $x_e/c_r = 0.14$; $\delta_d = 45^{\circ}$.

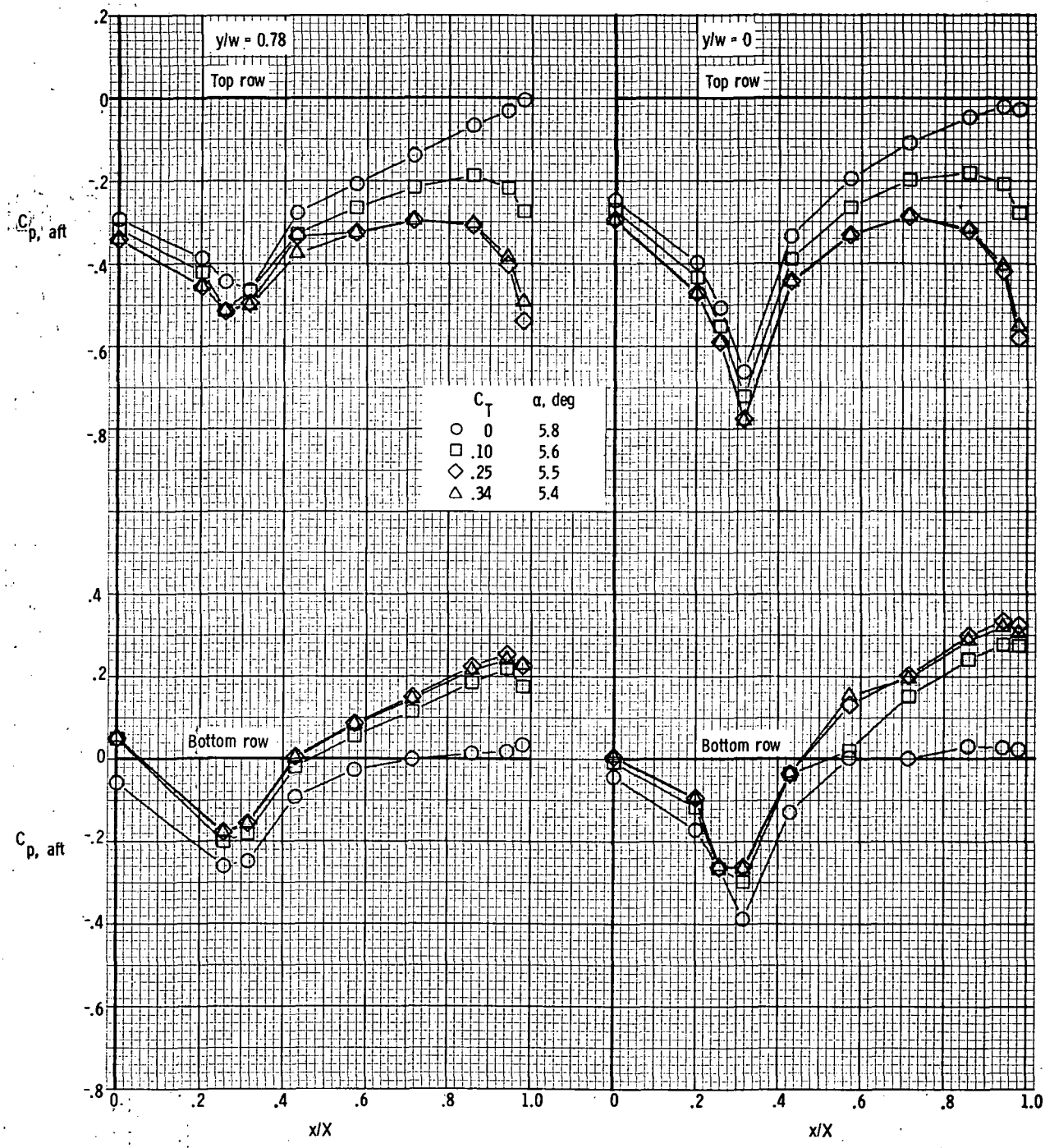

(b) M = 0.40; $\alpha \approx 5.6^{\circ}$.

Figure 23.- Continued.

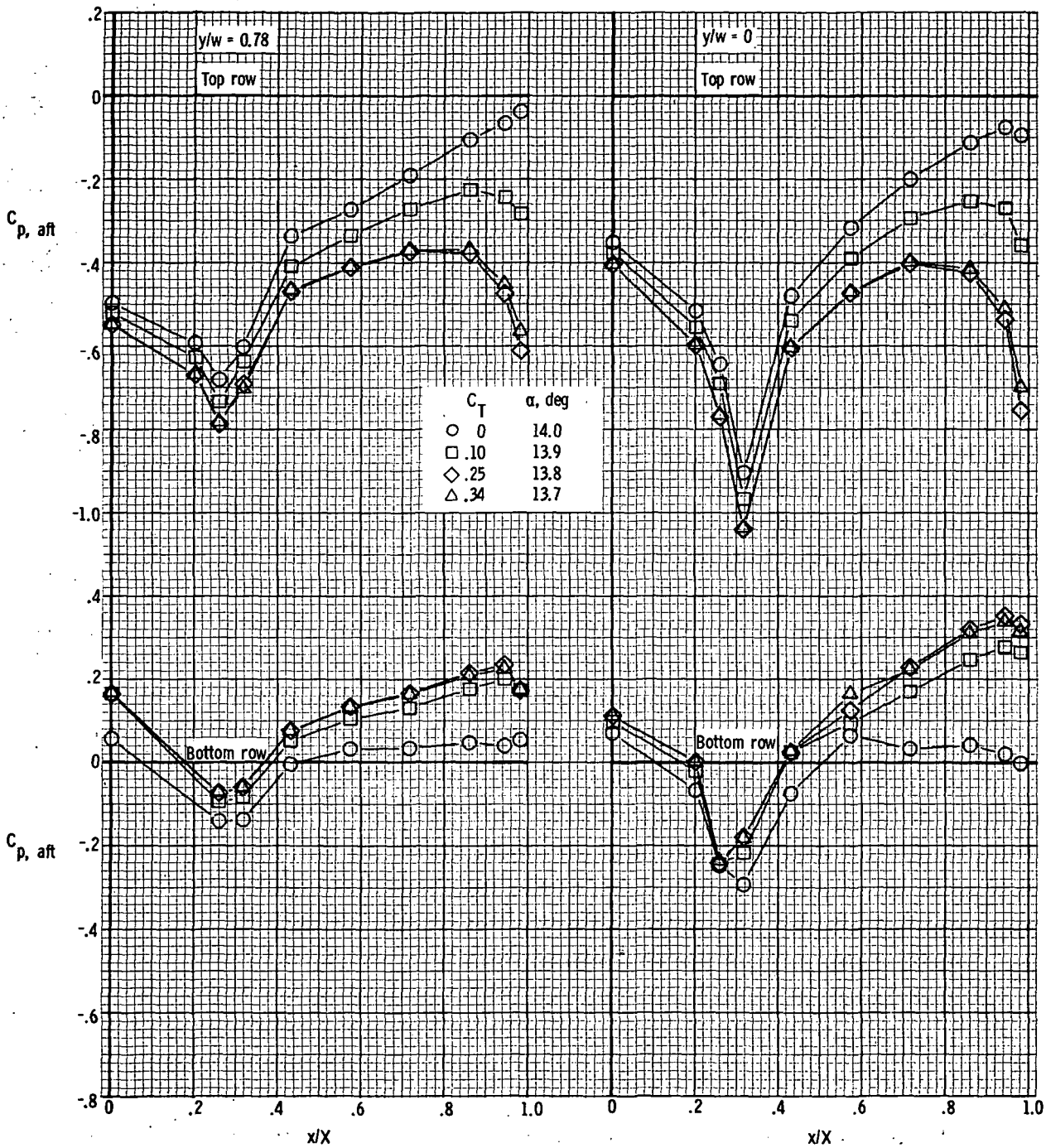

(c) M = 0.40; $\alpha \approx 13.9^{\circ}$.

Figure 23.- Continued.

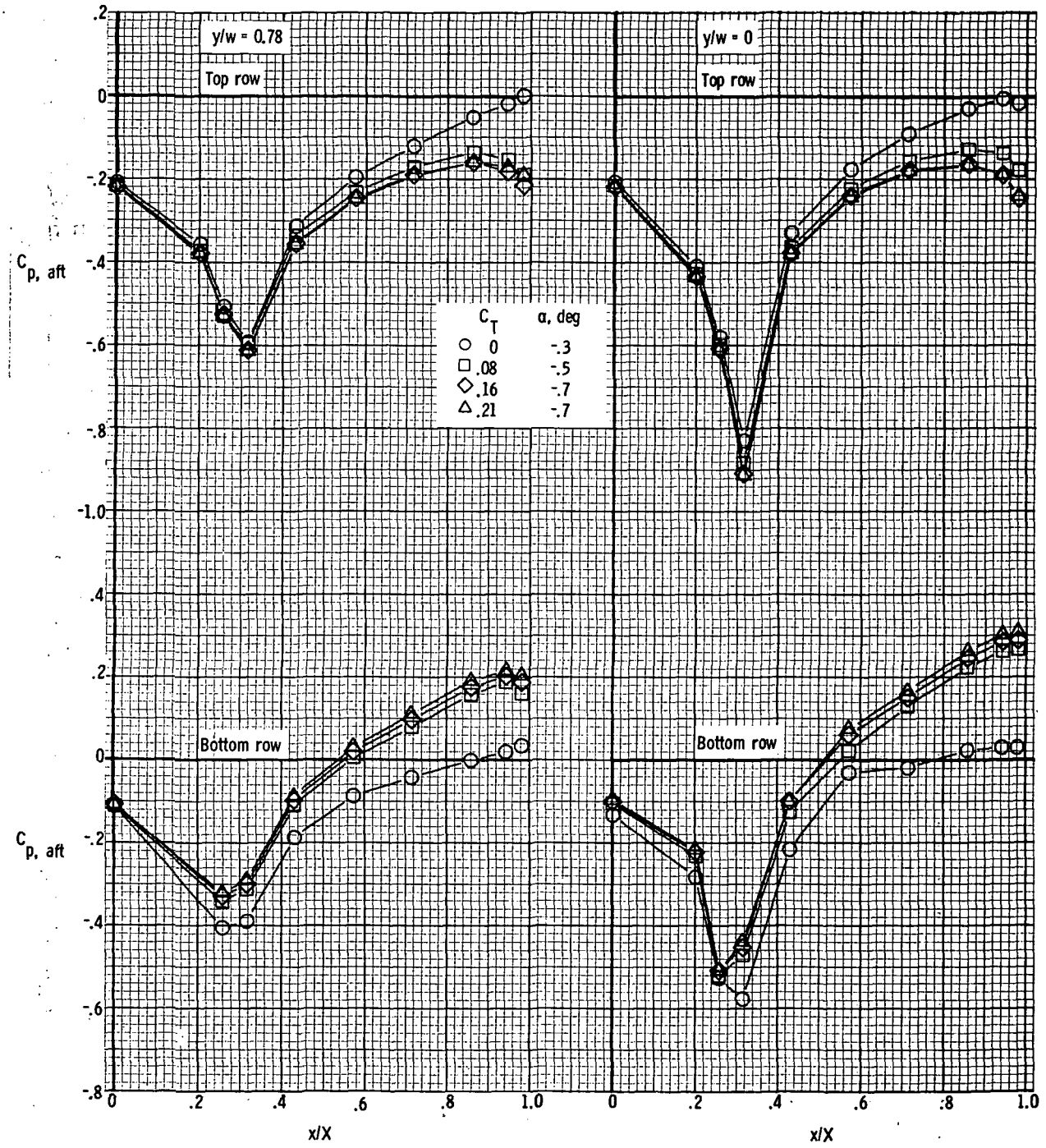

(d) M = 0.70; $\alpha \approx -0.5^{\circ}$.

Figure 23.- Continued.

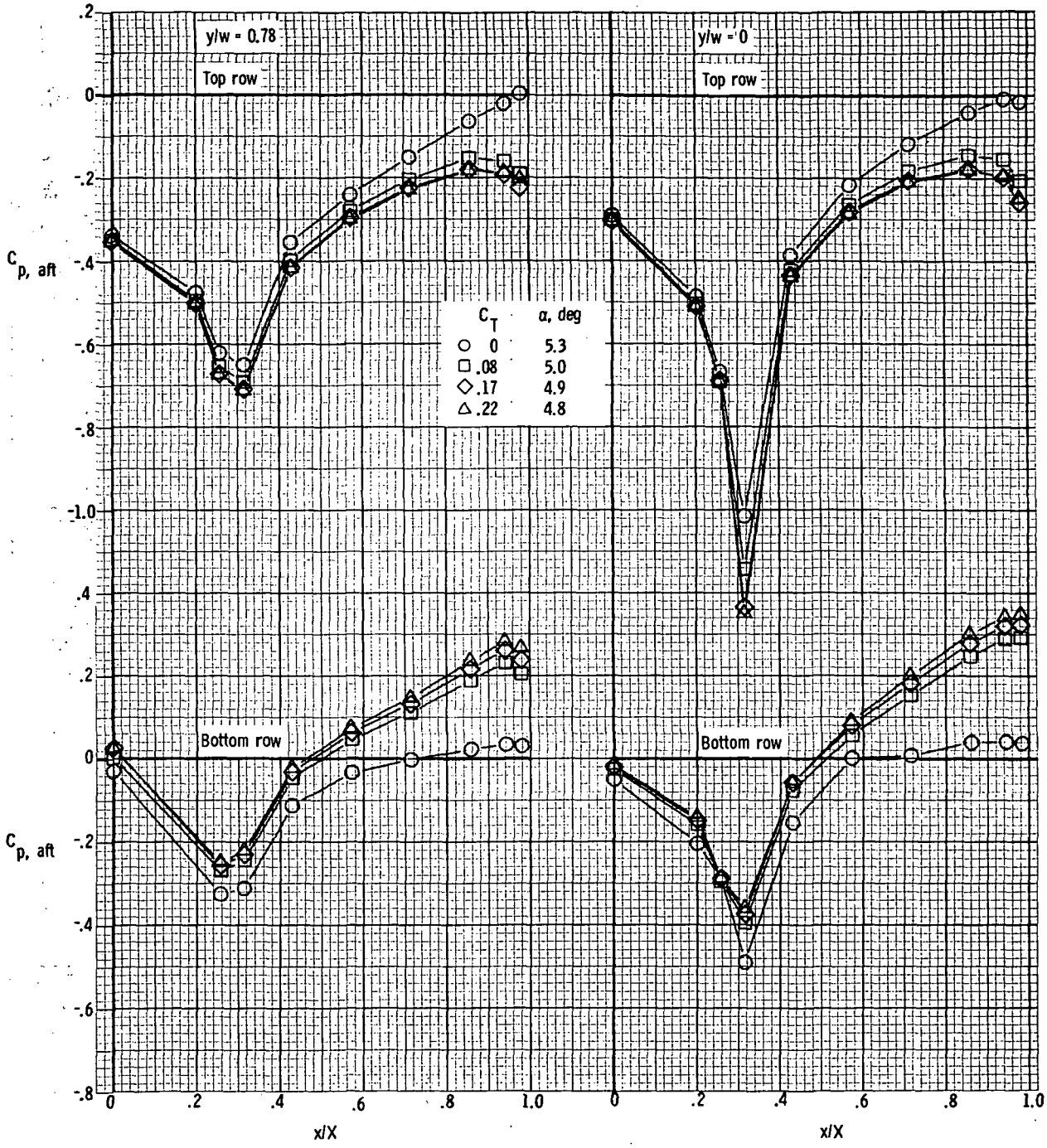

(e) M = 0.70; $\alpha \approx 5.0^{\circ}$.

Figure 23.- Continued.

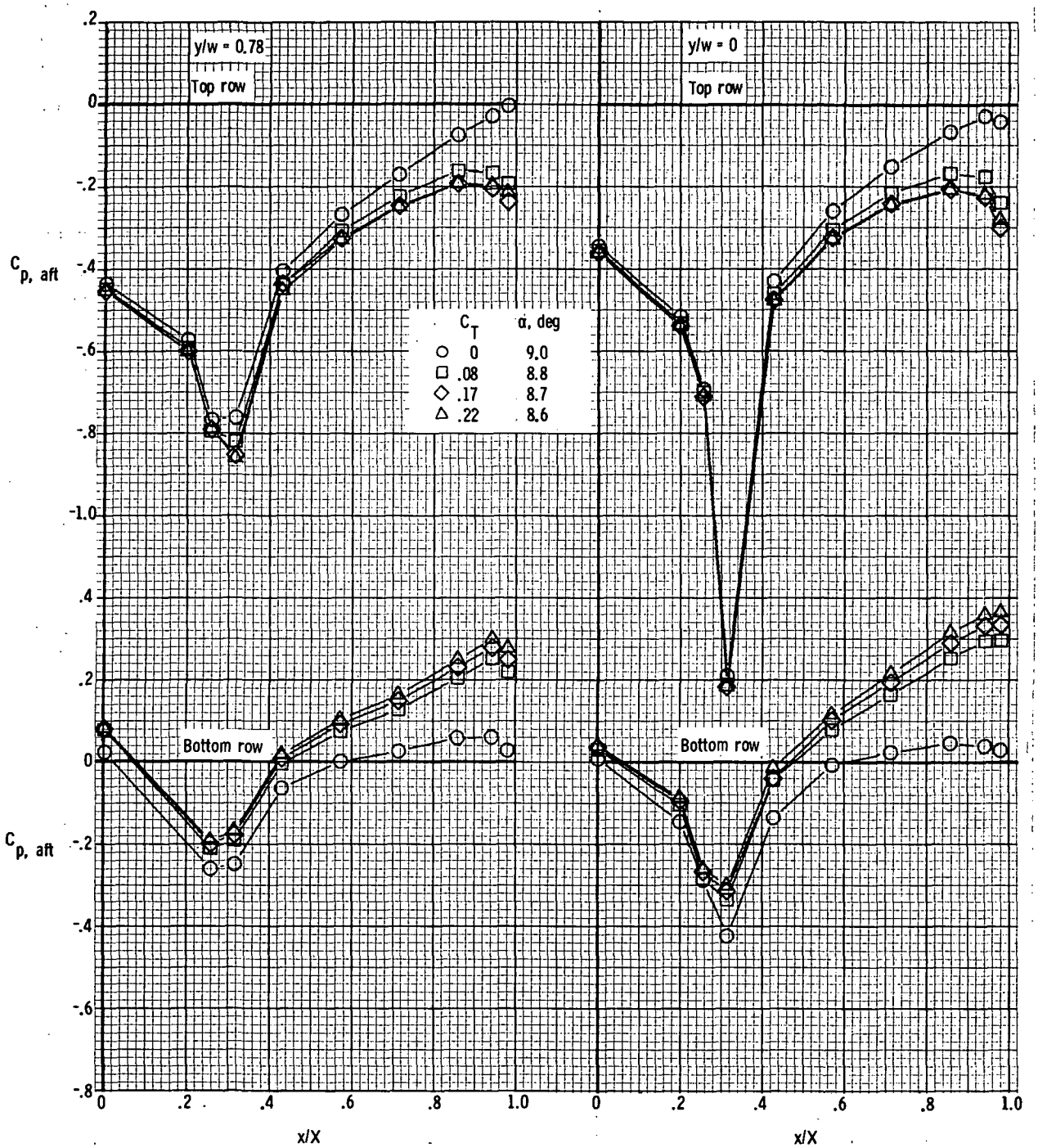

(f) M = 0.70; $\alpha \approx 8.8^{\circ}$.

Figure 23.- Continued.

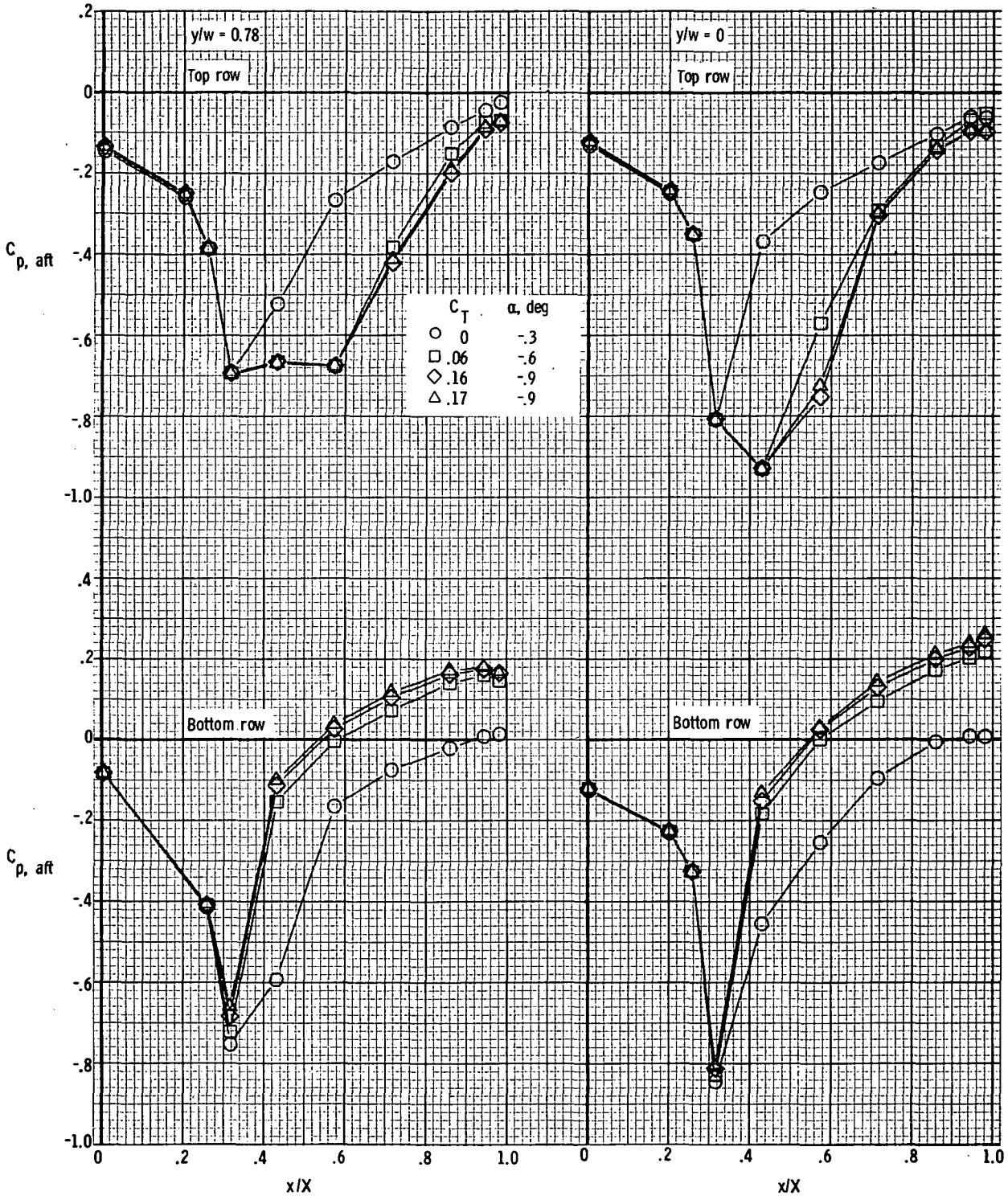

(g) M = 0.90; $\alpha \approx -0.6^{\circ}$.

Figure 23.- Continued.

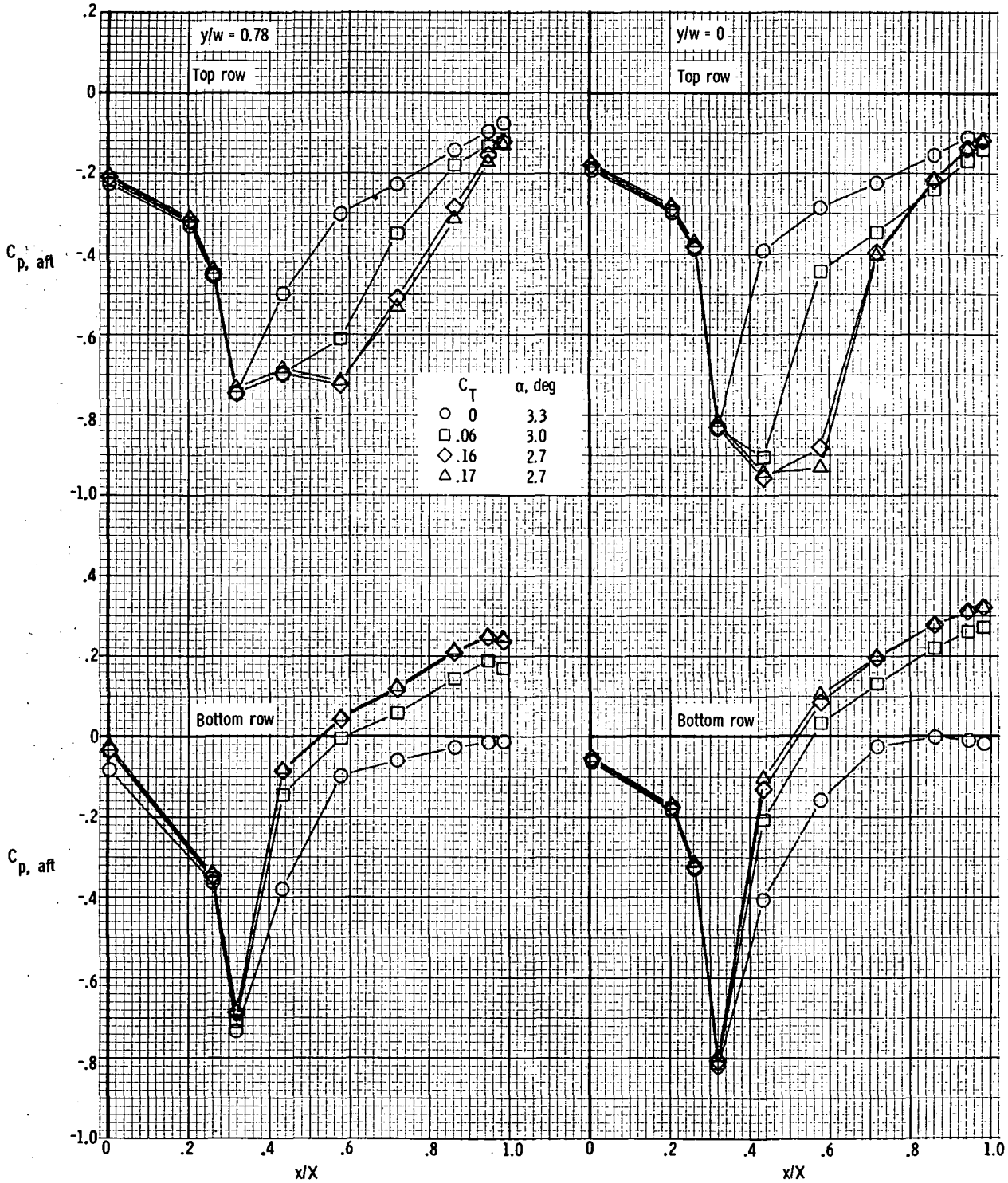

(h) M = 0.90; $\alpha \approx 3.0^{\circ}$.

Figure 23.- Continued.

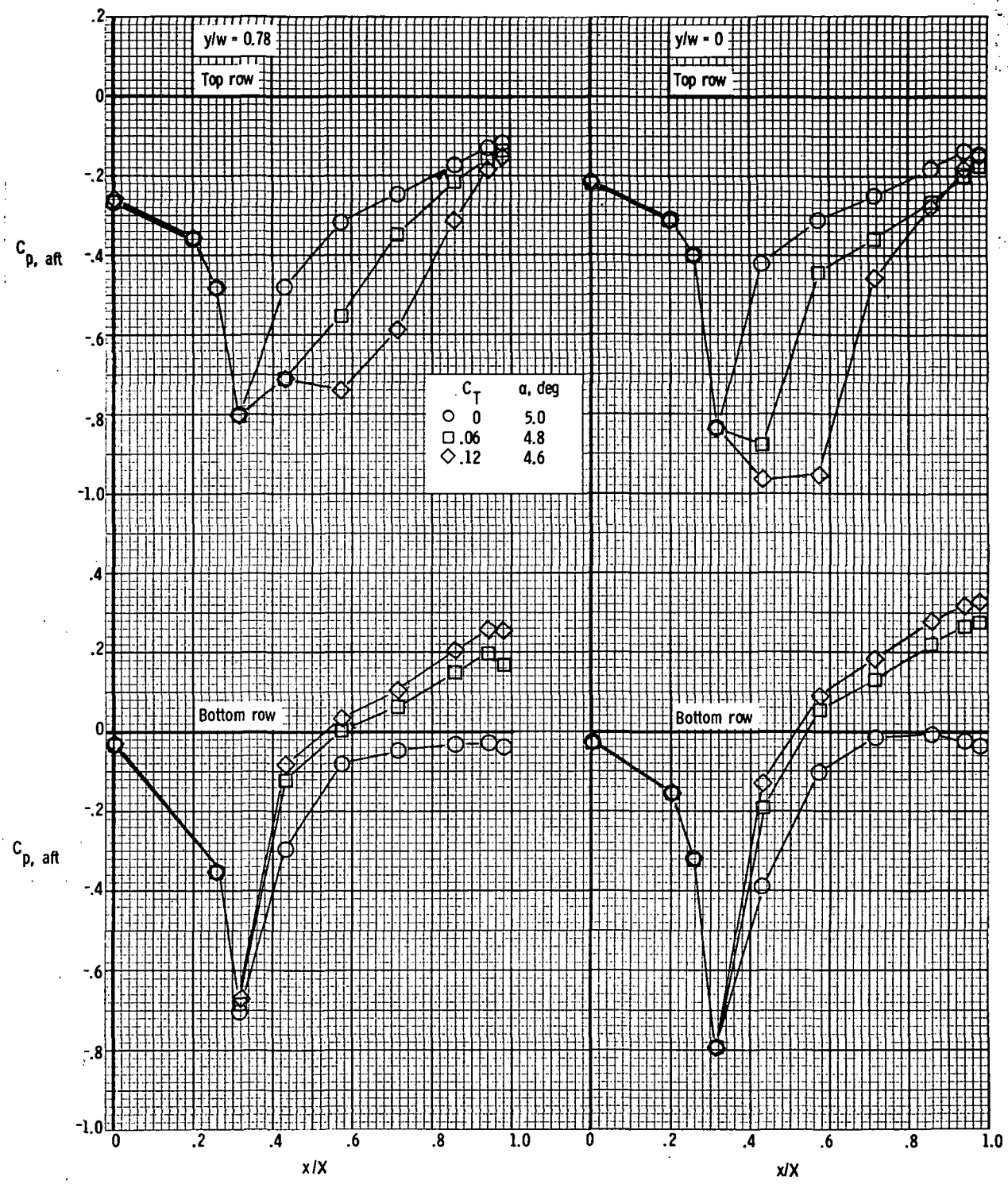

(i) M = 0.90; $\alpha \approx 4.8^{\circ}$.

Figure 23.- Concluded.

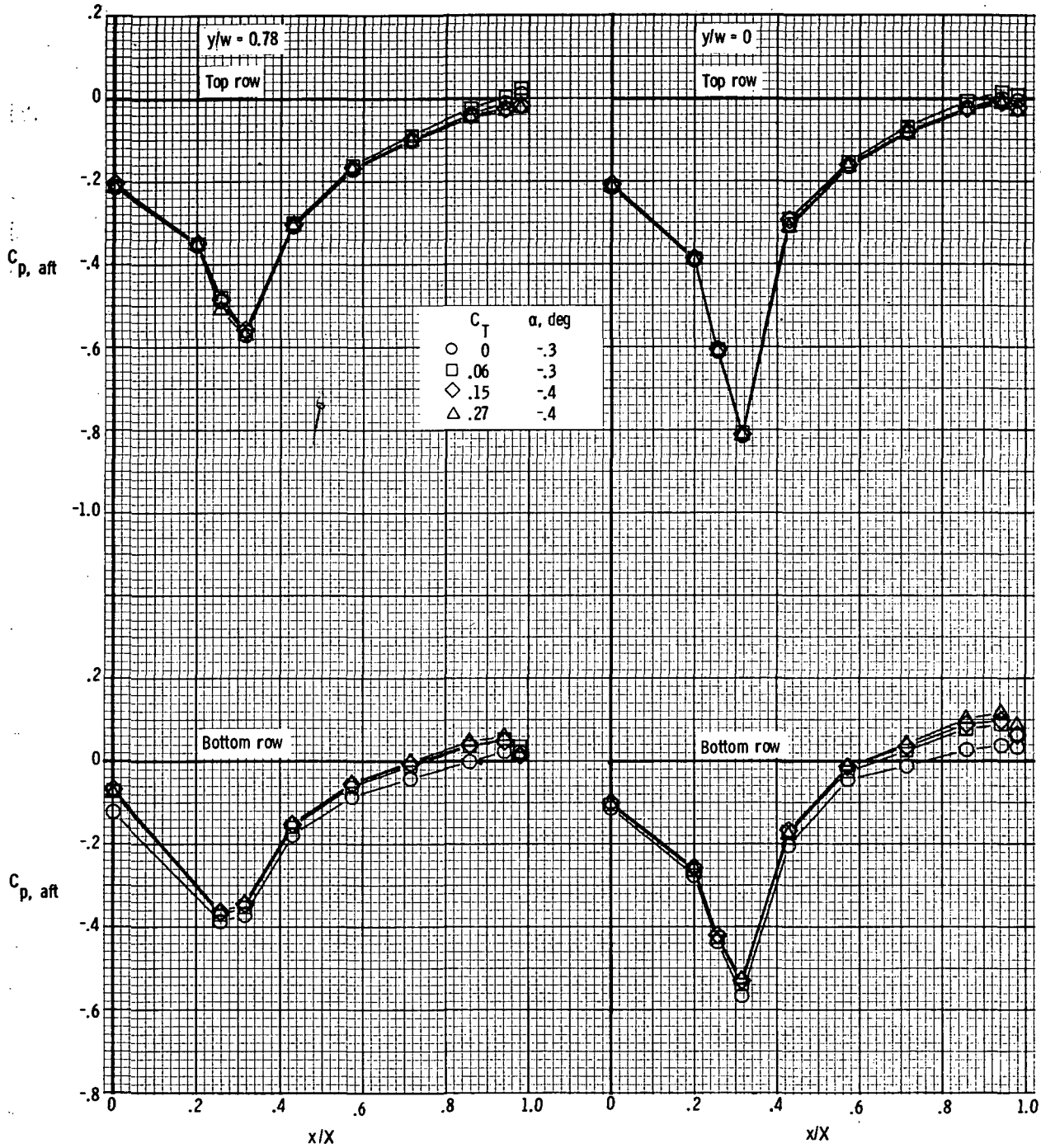

(a) M = 0.70; $\alpha \approx -0.3^{\circ}$.

Figure 24.- Afterbody pressure distributions for model with rectangular exits; $x_e/c_r = 0.21$; $\delta_d = 15^{\circ}$.

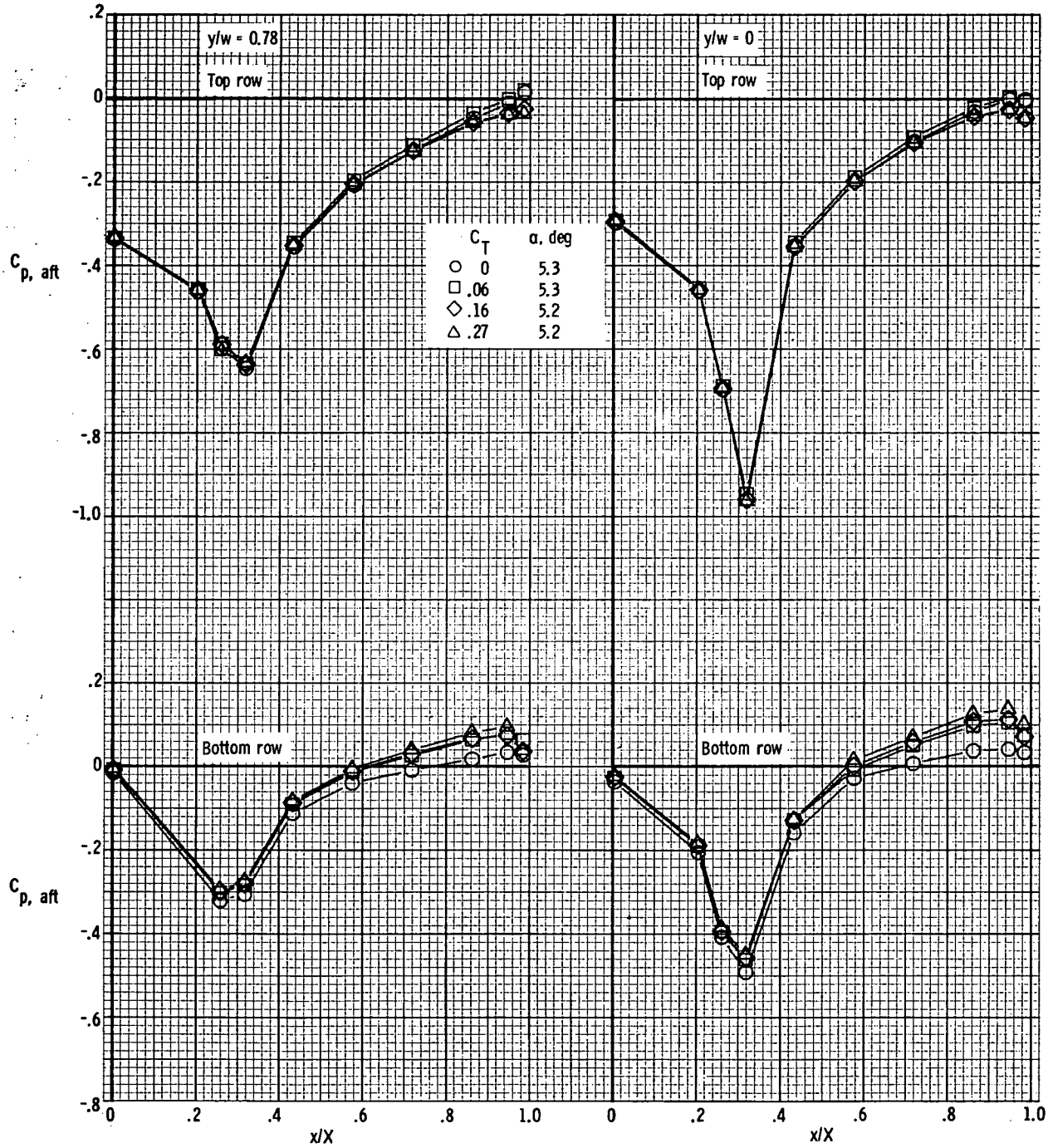

(b) M = 0.70; $\alpha \approx 5.3^{\circ}$.

Figure 24.- Continued.

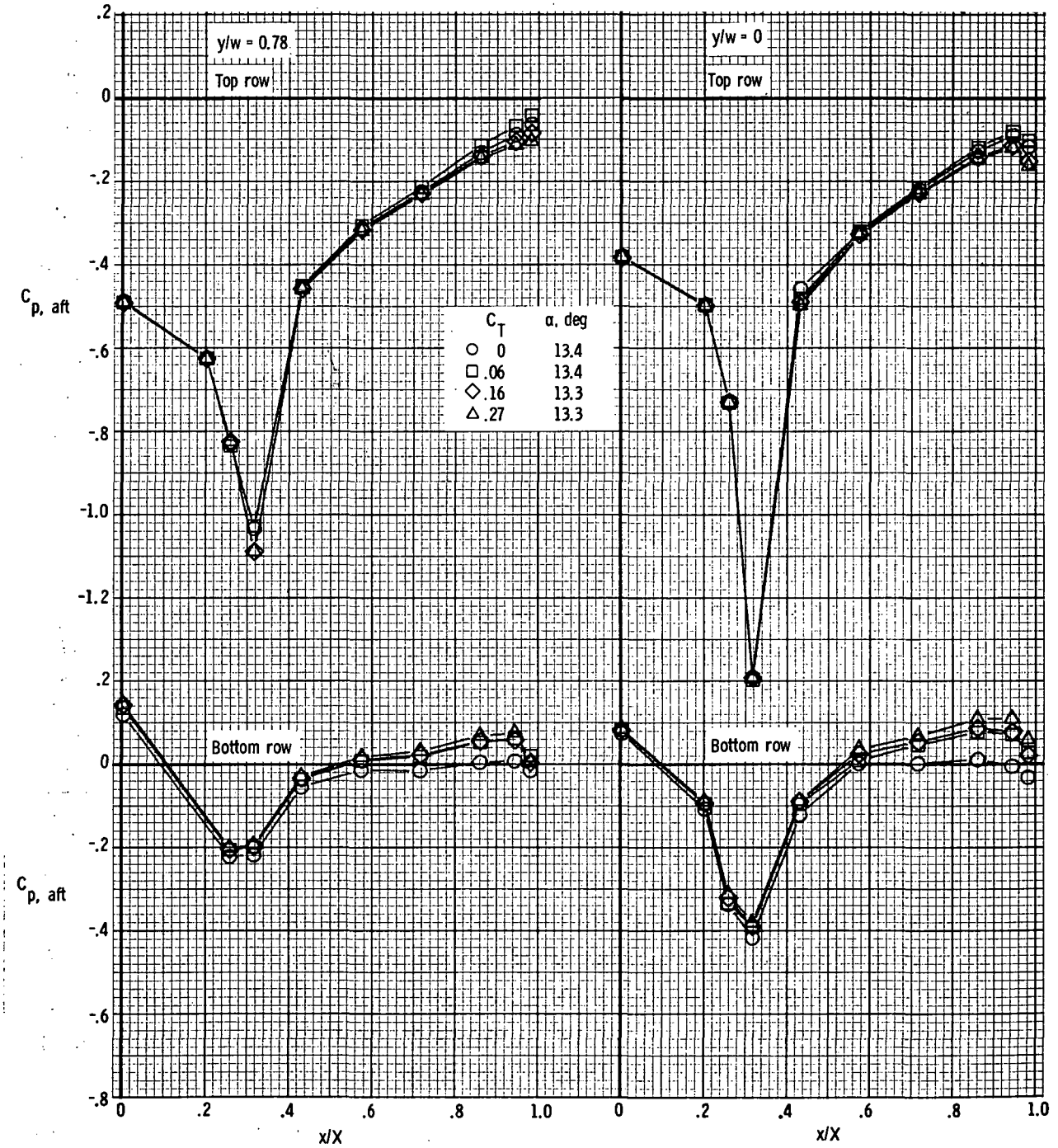

(c) M = 0.70; $\alpha \approx 13.4^{\circ}$.

Figure 24. - Continued.

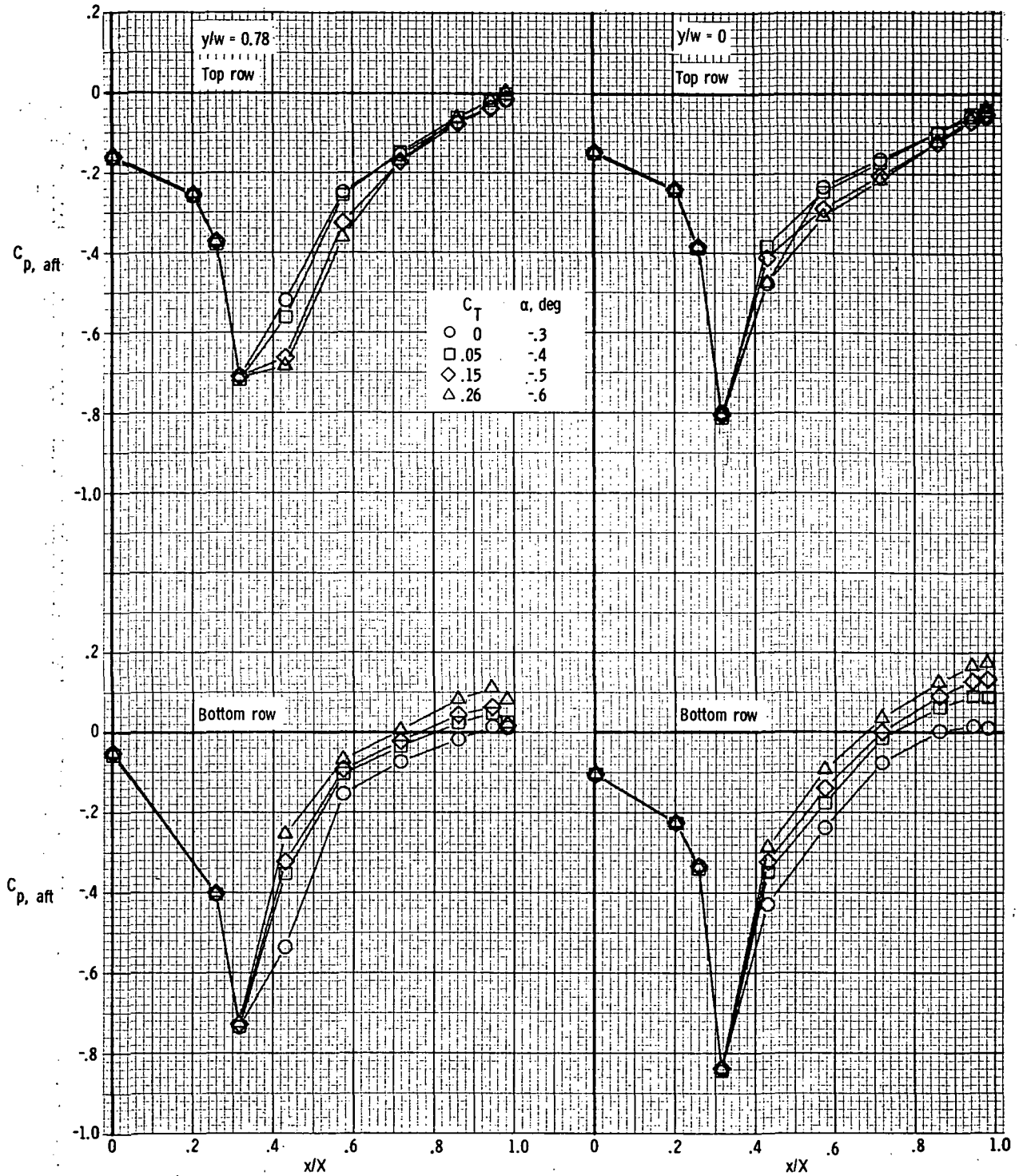

(d) M = 0.90; $\alpha \approx -0.4^{\circ}$.

Figure 24.- Continued.

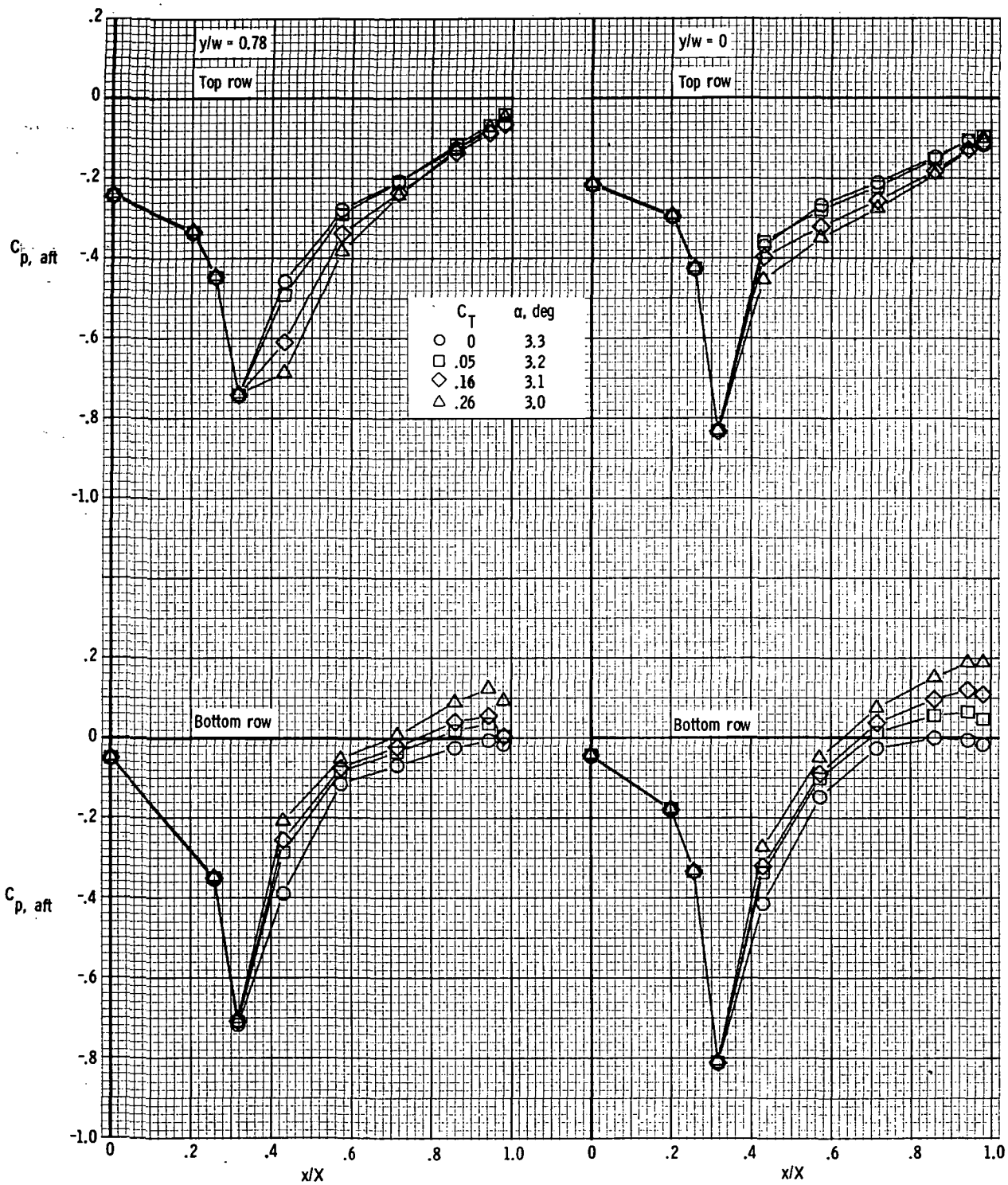

(e) M = 0.90; $\alpha \approx 3.2^{\circ}$.

Figure 24.- Continued.

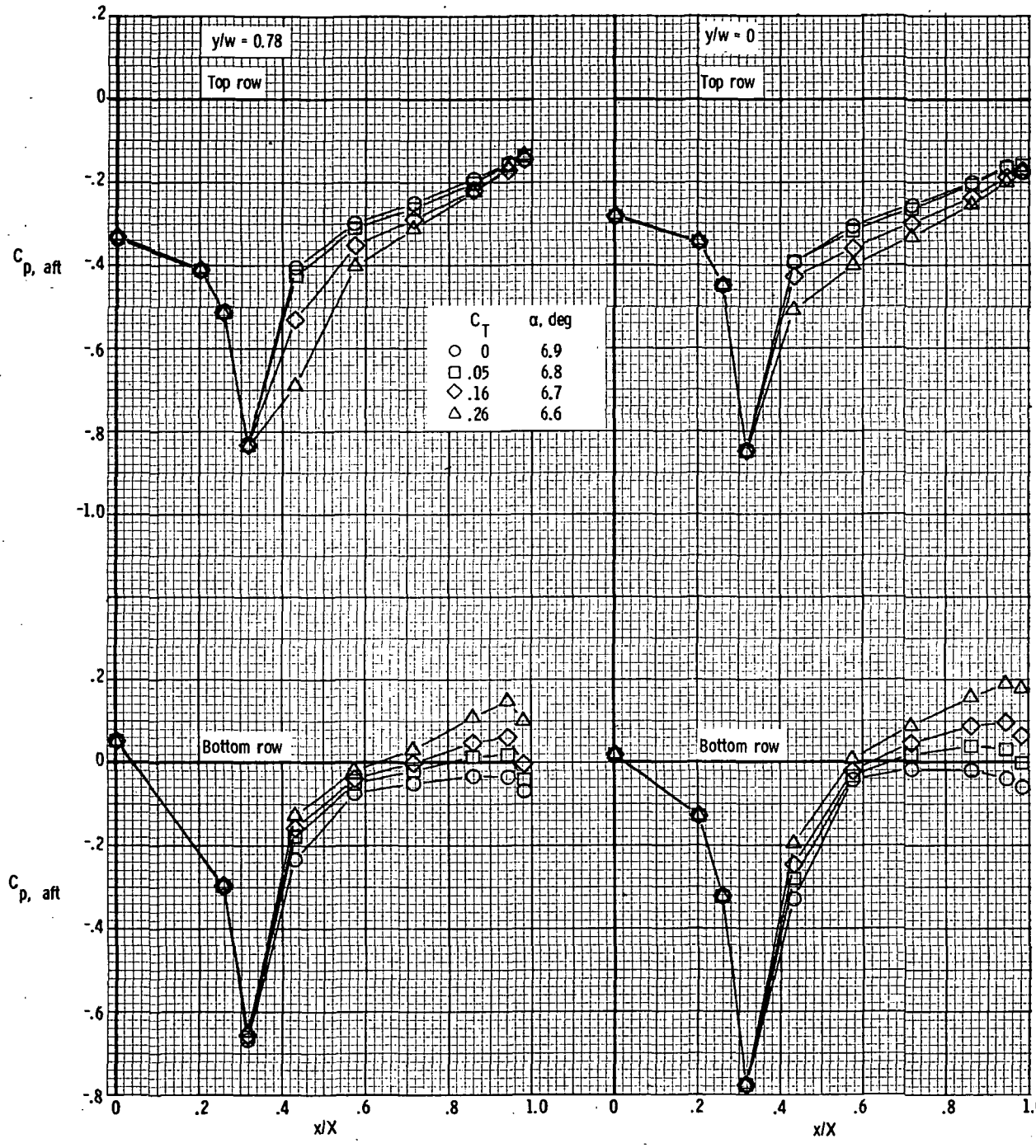

(f) M = 0.90; $\alpha \approx 6.8^{\circ}$.

Figure 24.- Concluded.

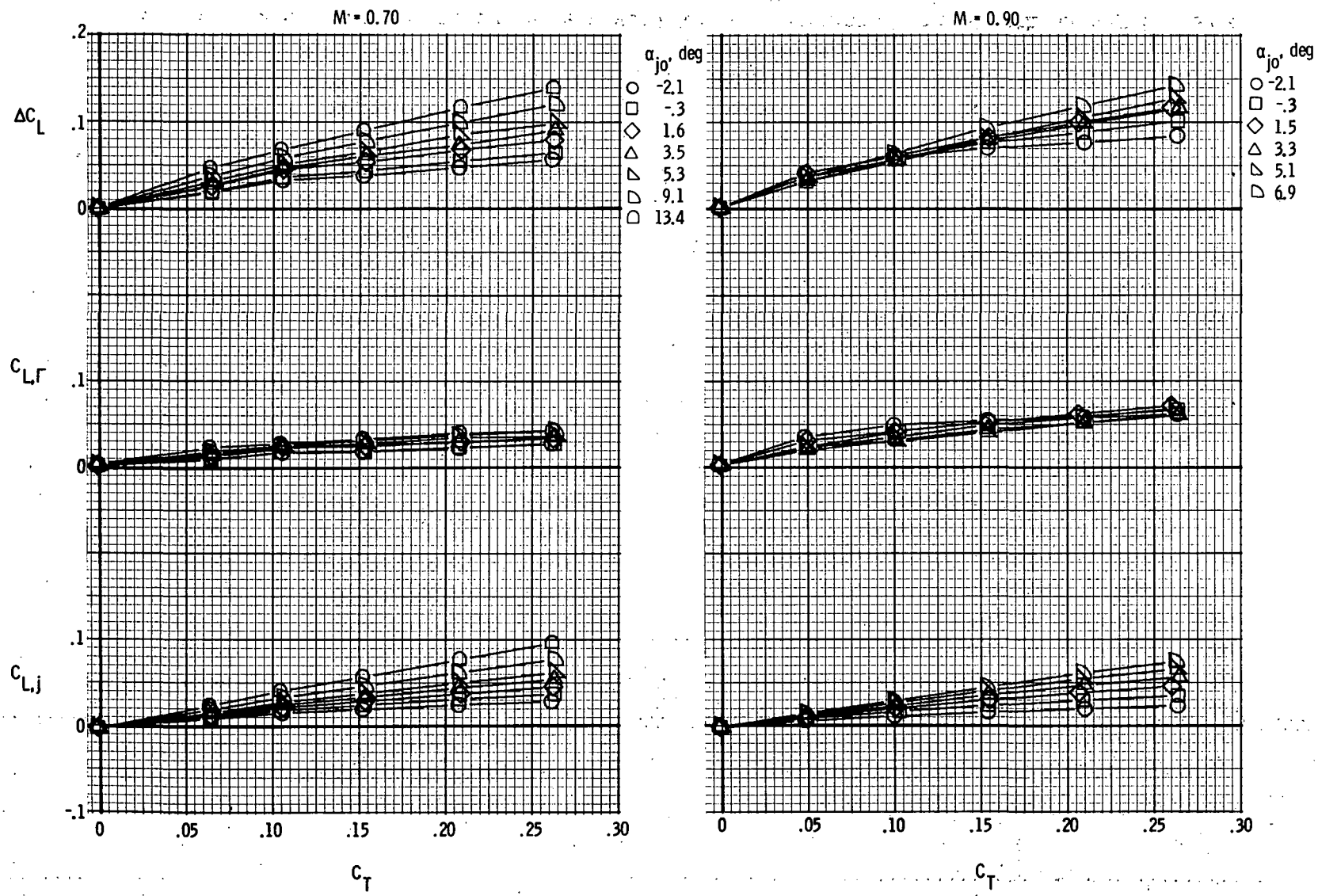

Figure 25.- Jet lift, induced lift, and incremental lift characteristics for model with rectangular exits; $x_e/c_r = 0.07$; $\delta_d = 15^o$; M = 0.70 and 0.90.

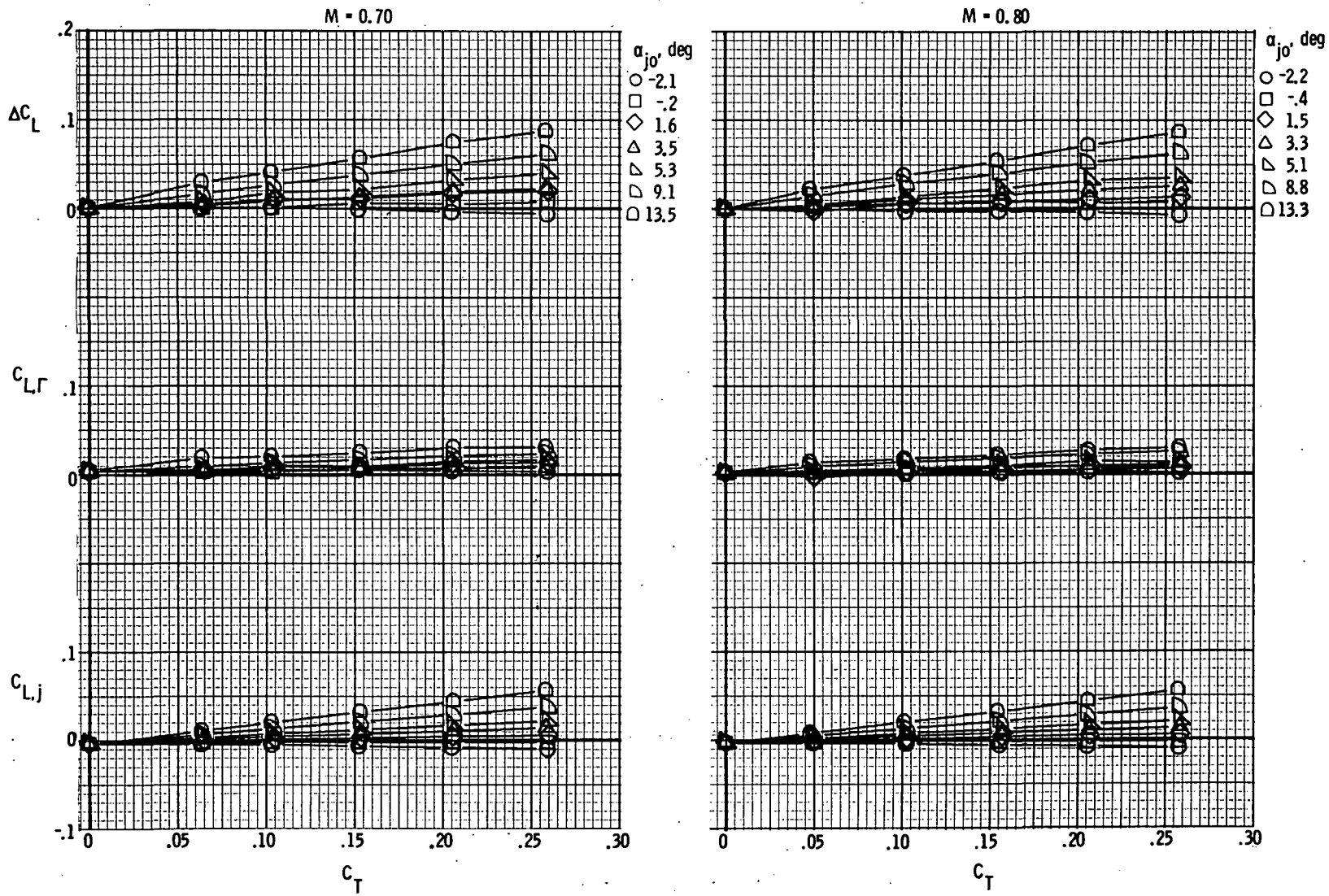

(a) M = 0.70 and 0.80.

Figure 26.- Jet lift, induced lift, and incremental lift characteristics for model with rectangular exits; $x_e/c_r = 0.14$; $\delta_d = 0^o$.

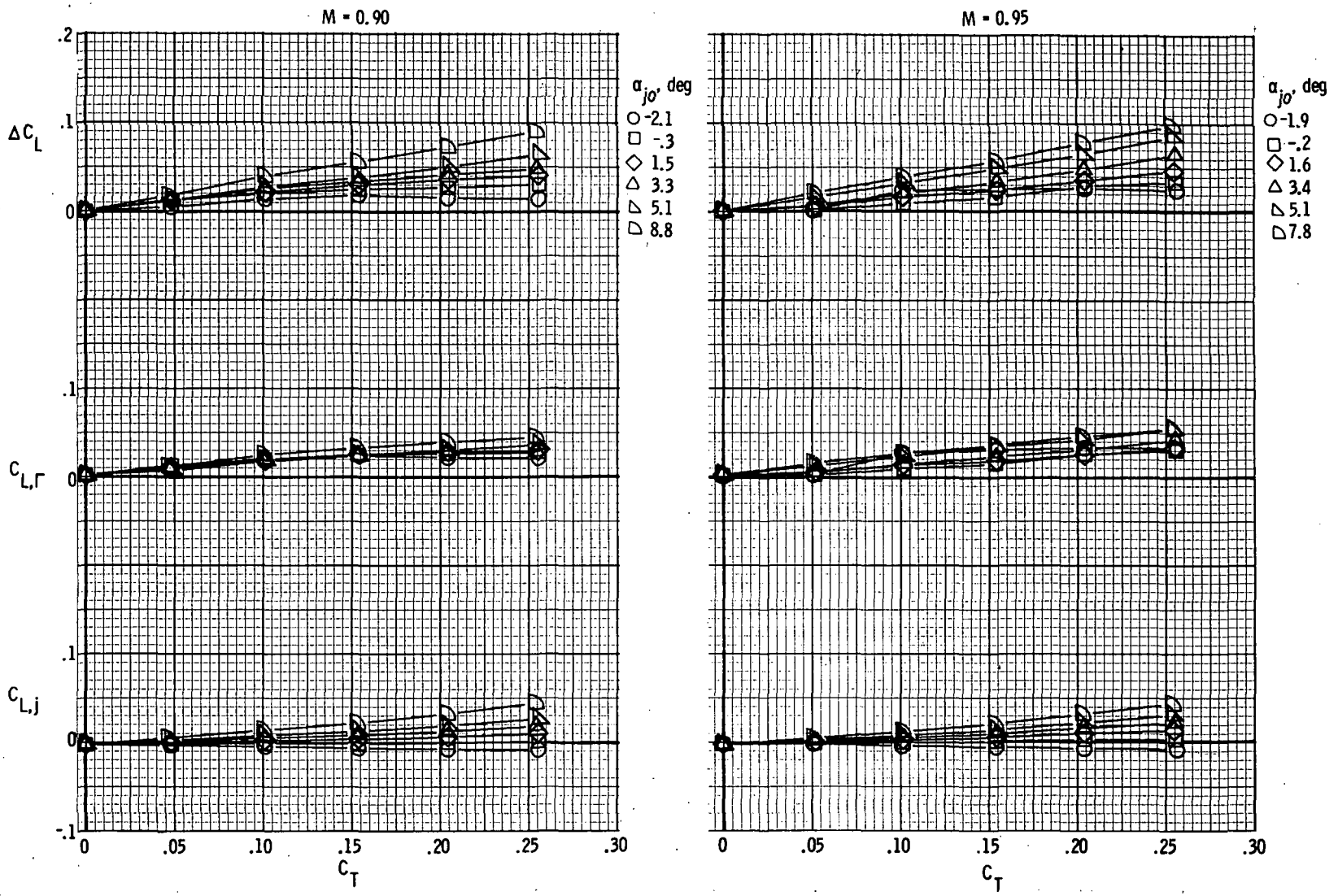

(b) M = 0.90 and 0.95.

Figure 26.- Continued.

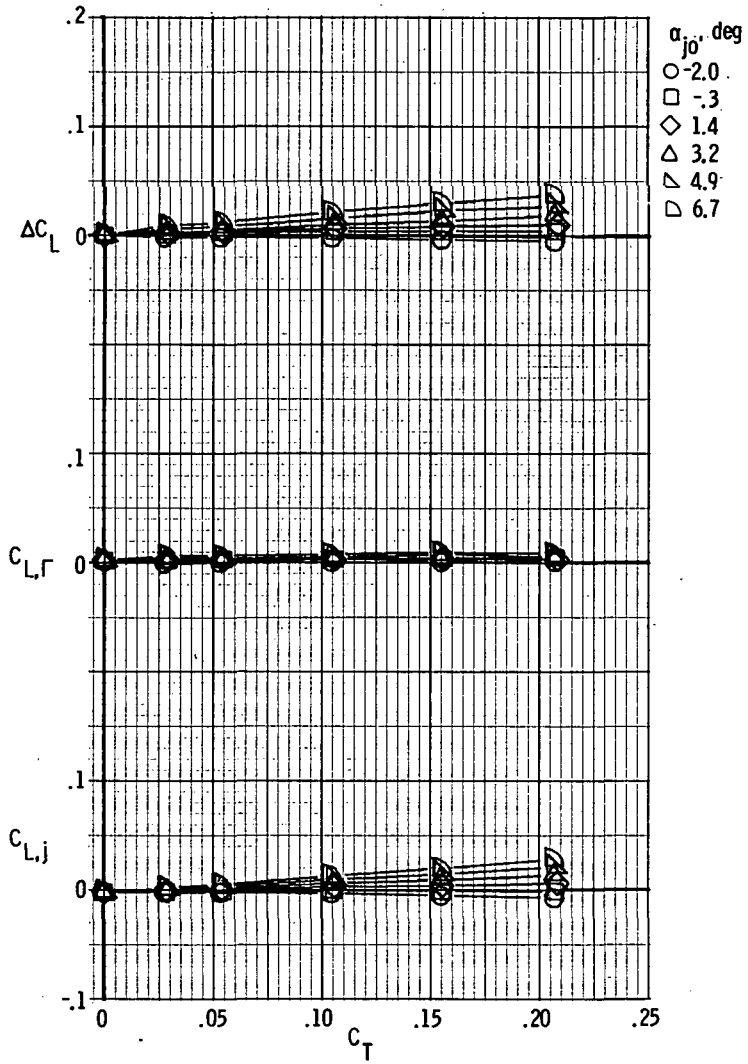

(c) M = 1.20.

Figure 26.- Concluded.

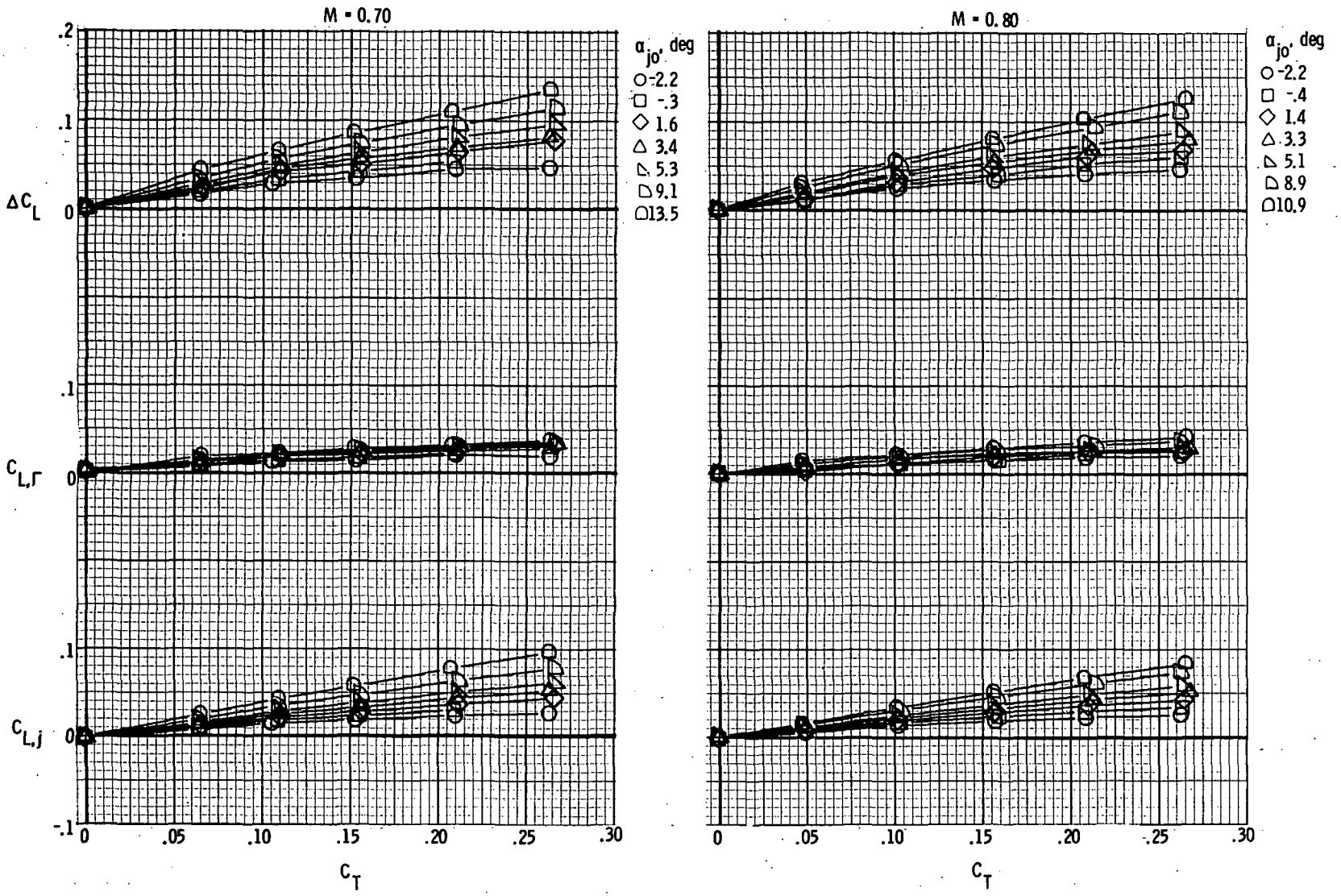

(a) M = 0.70 and 0.80.

Figure 27.- Jet lift, induced lift, and incremental lift characteristics for model with rectangular exits; $x_e/c_r = 0.14$; $\delta_d = 15^o$.

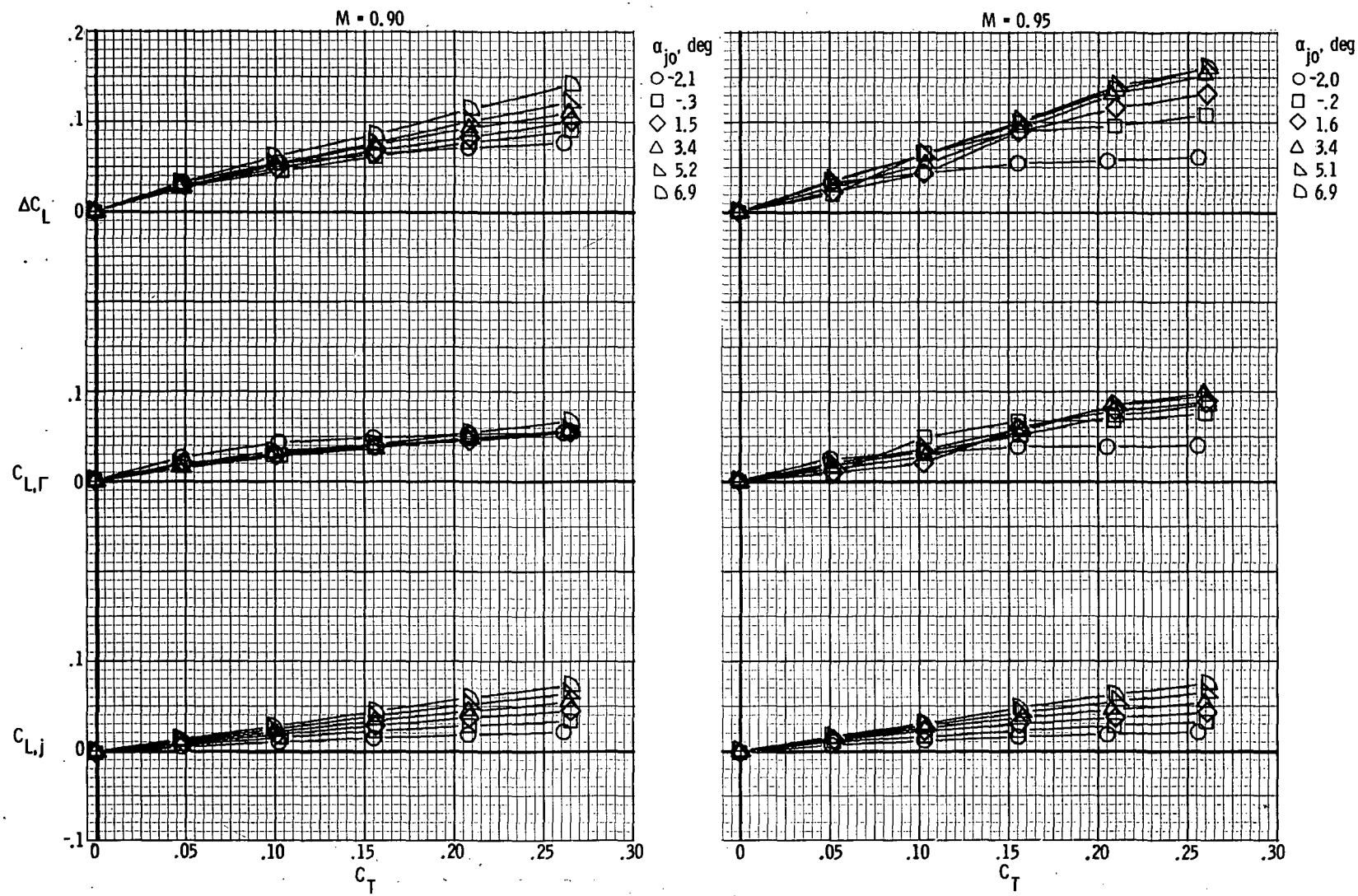

(b) M = 0.90 and 0.95.

Figure 27.- Concluded.

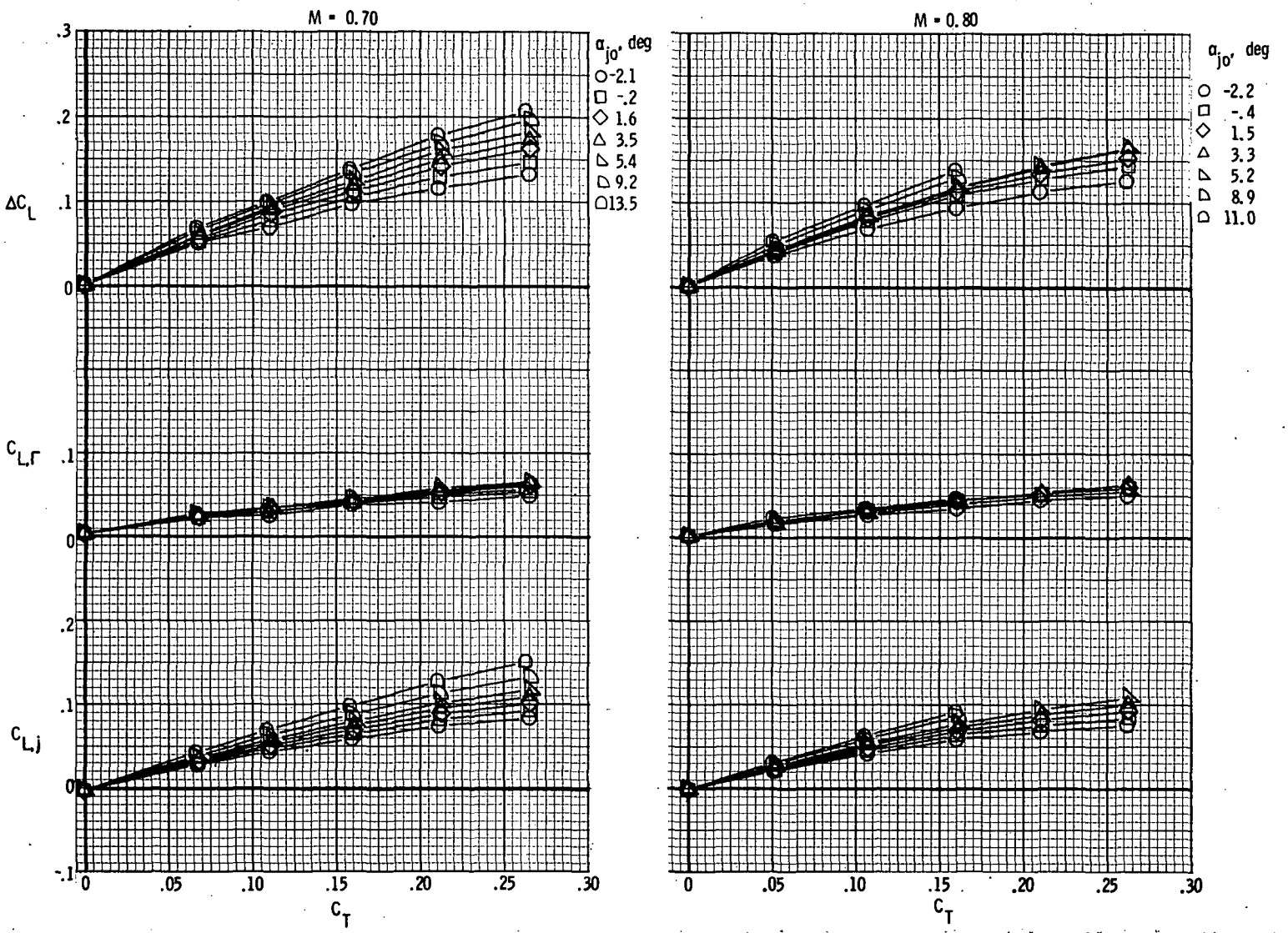

(a) M = 0.70 and 0.80.

Figure 28.- Jet lift, induced lift, and incremental lift characteristics for model with rectangular exits; $x_e/c_r = 0.14$; $\delta_d = 30^{\circ}$.

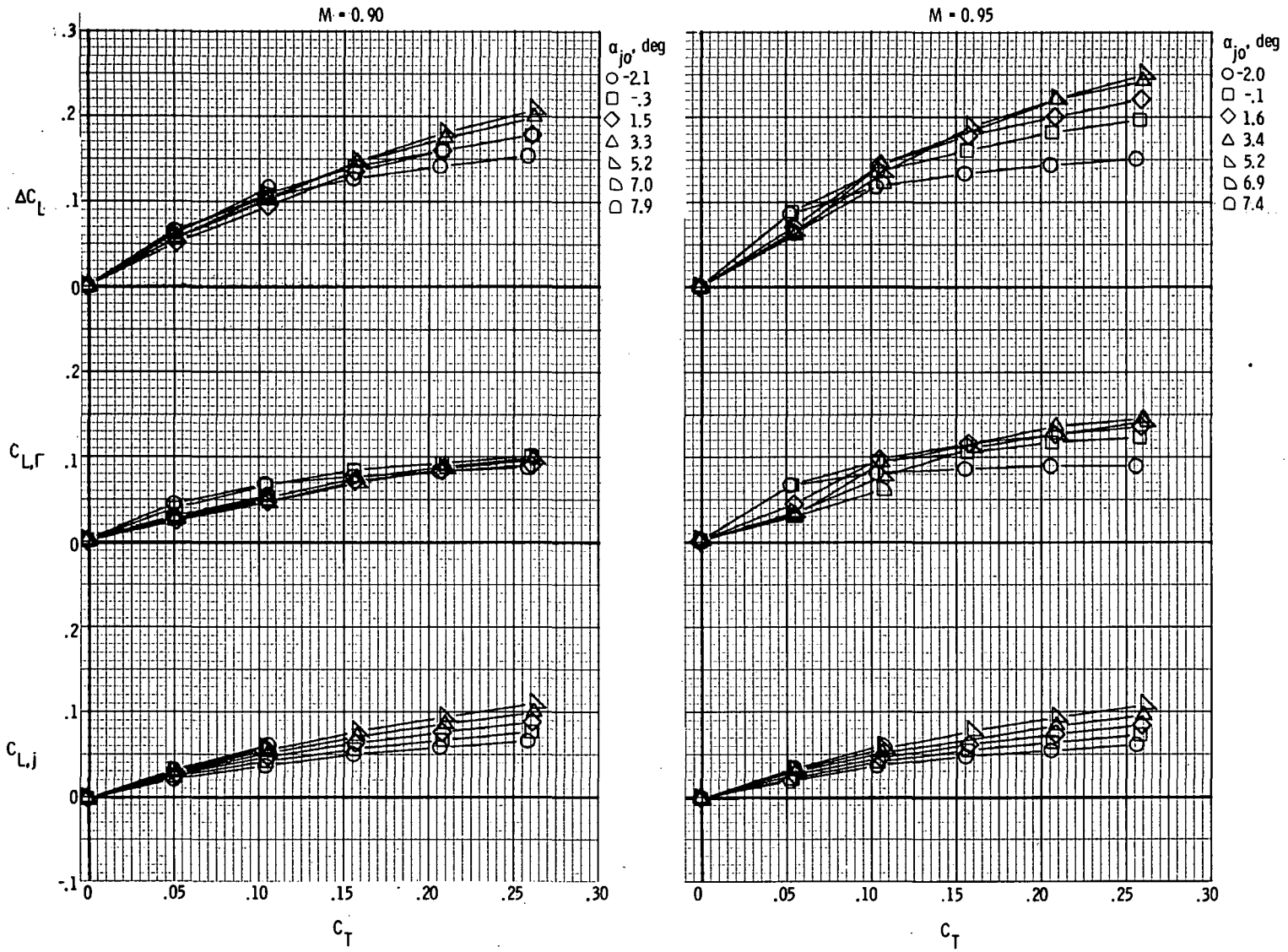

(b) M = 0.90 and 0.95.

Figure 28.- Continued.

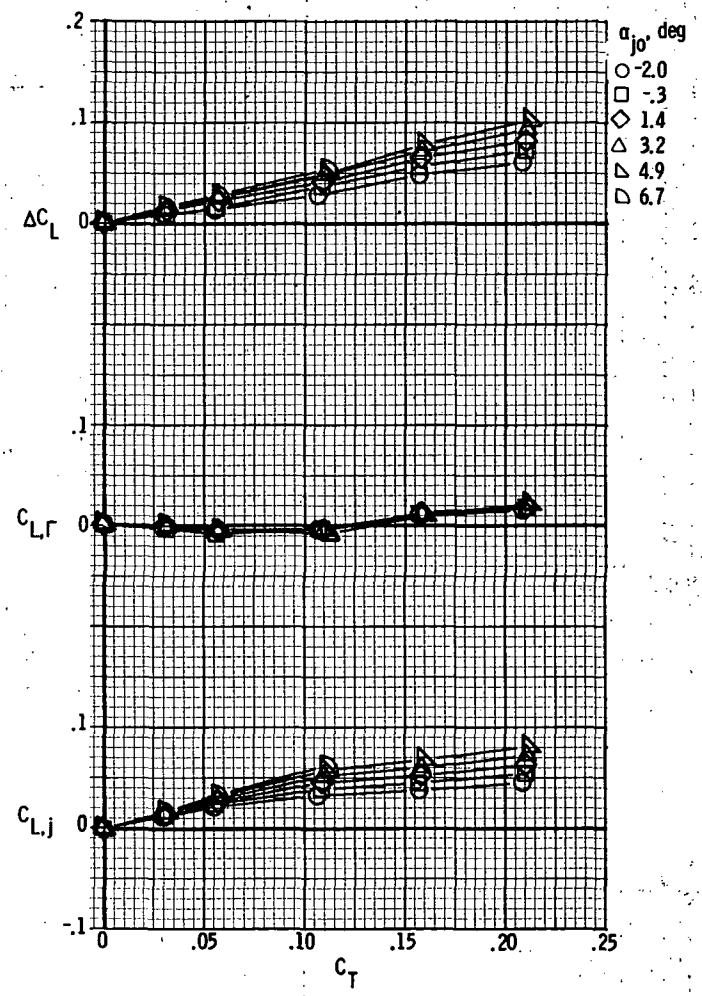

(c) M = 1.20.

Figure 28.- Concluded.

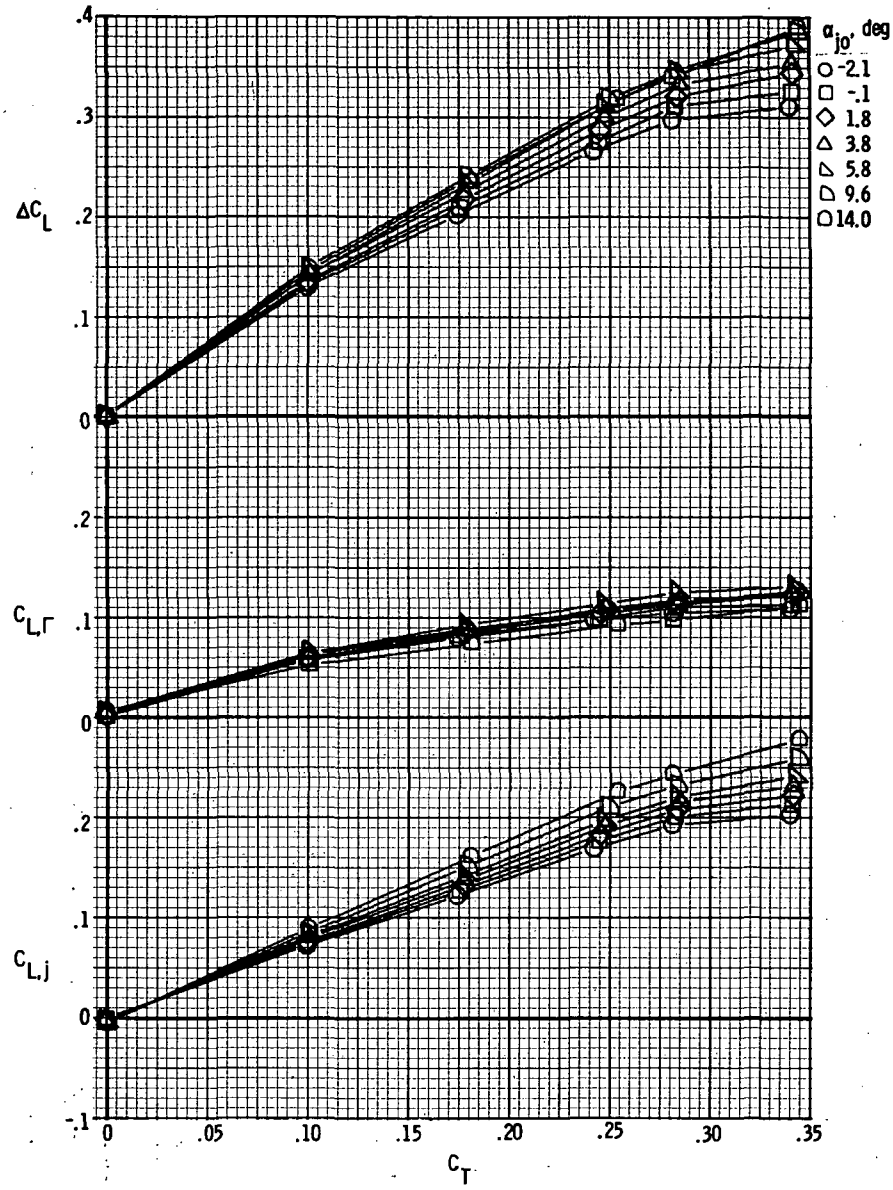

(a) M = 0.40.

Figure 29.- Jet lift, induced lift, and incremental lift characteristics for model with rectangular exits; $x_e/c_r = 0.14$; $\delta_d = 45^{\circ}$.

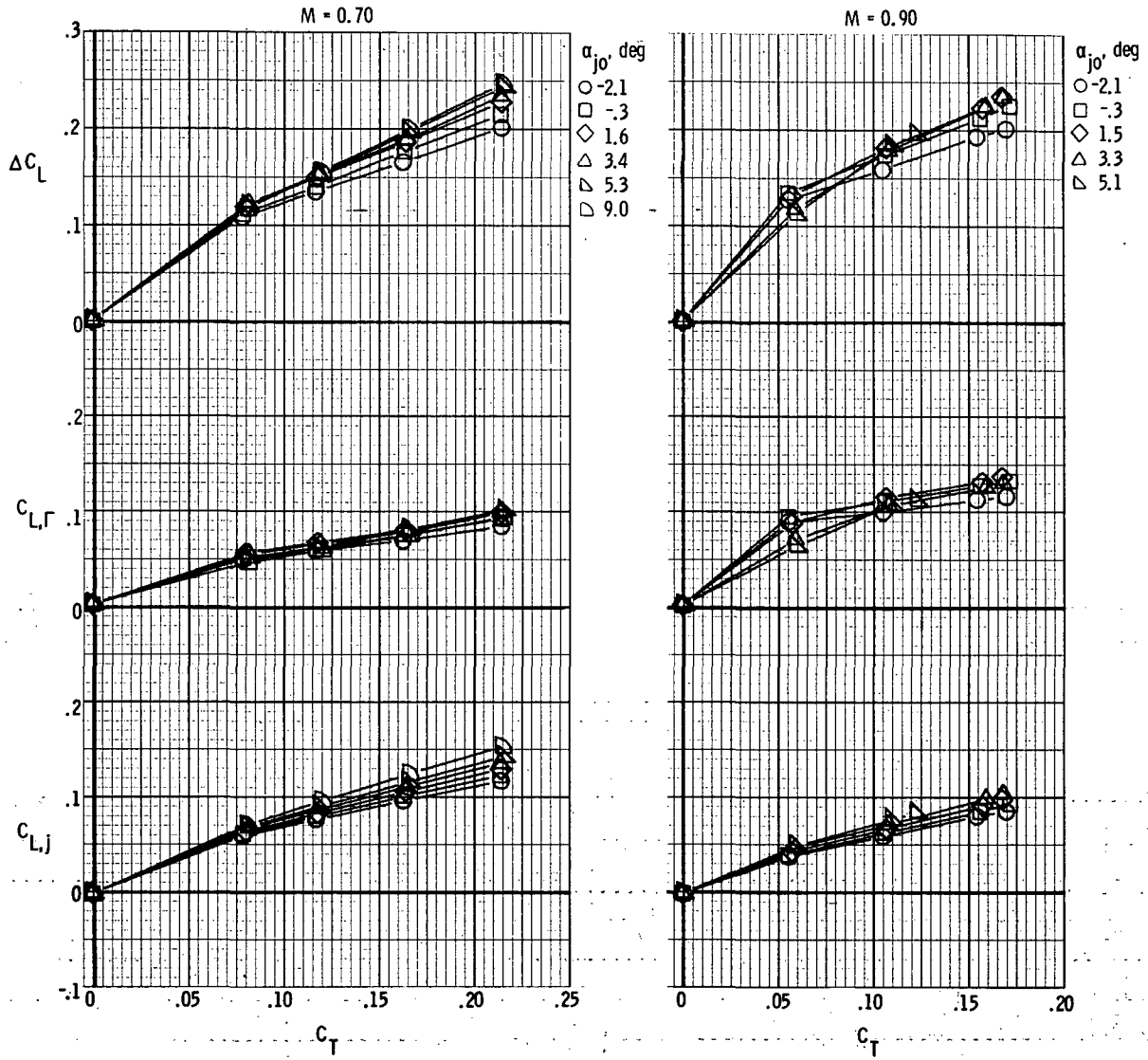

(b) M = 0.70 and 0.90.

Figure 29.- Concluded.

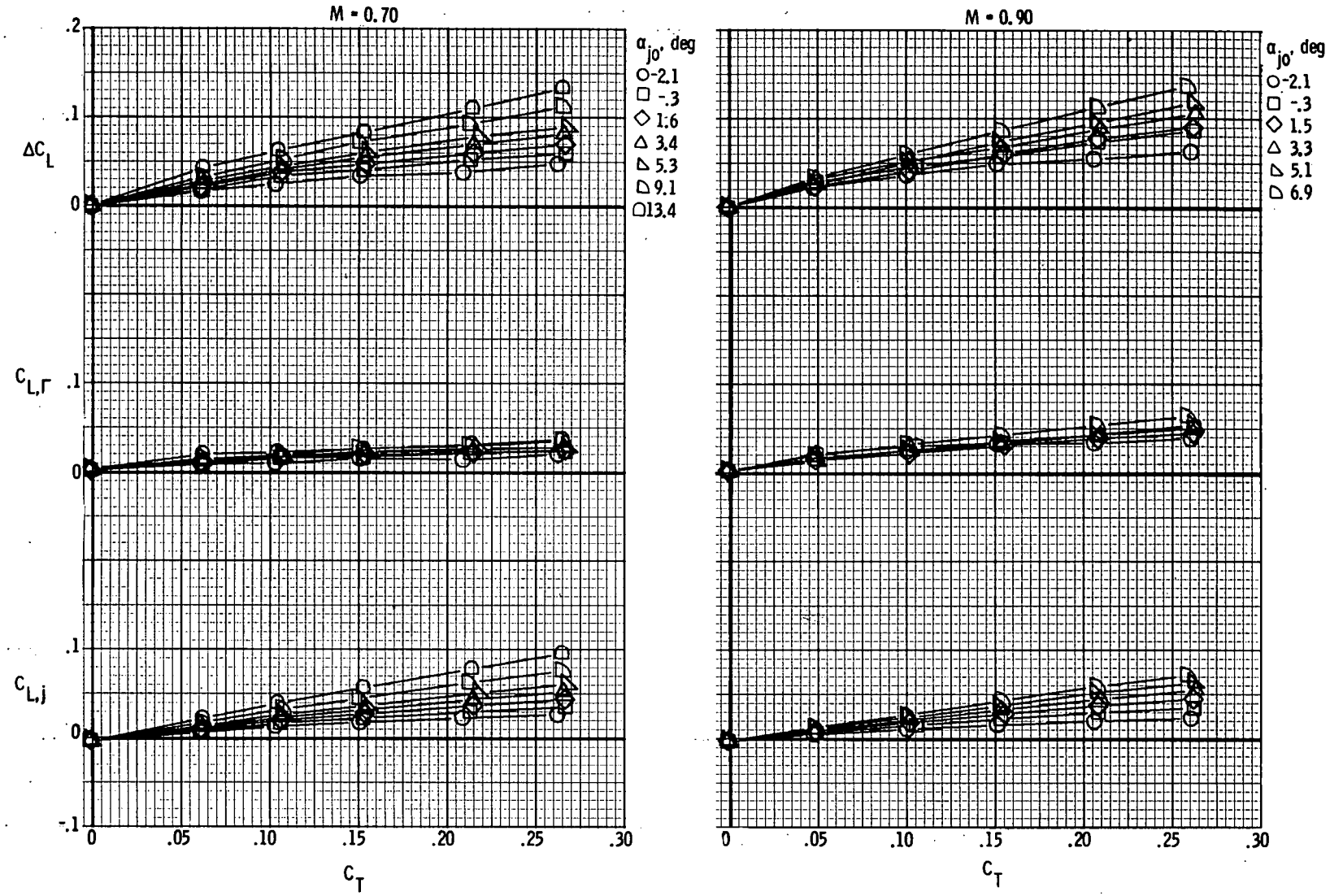

Figure 30.- Jet lift, induced lift, and incremental lift characteristics for model with rectangular exits; $x_e/c_r = 0.21$; $\delta_d = 15^{\circ}$; M = 0.70 and 0.90.

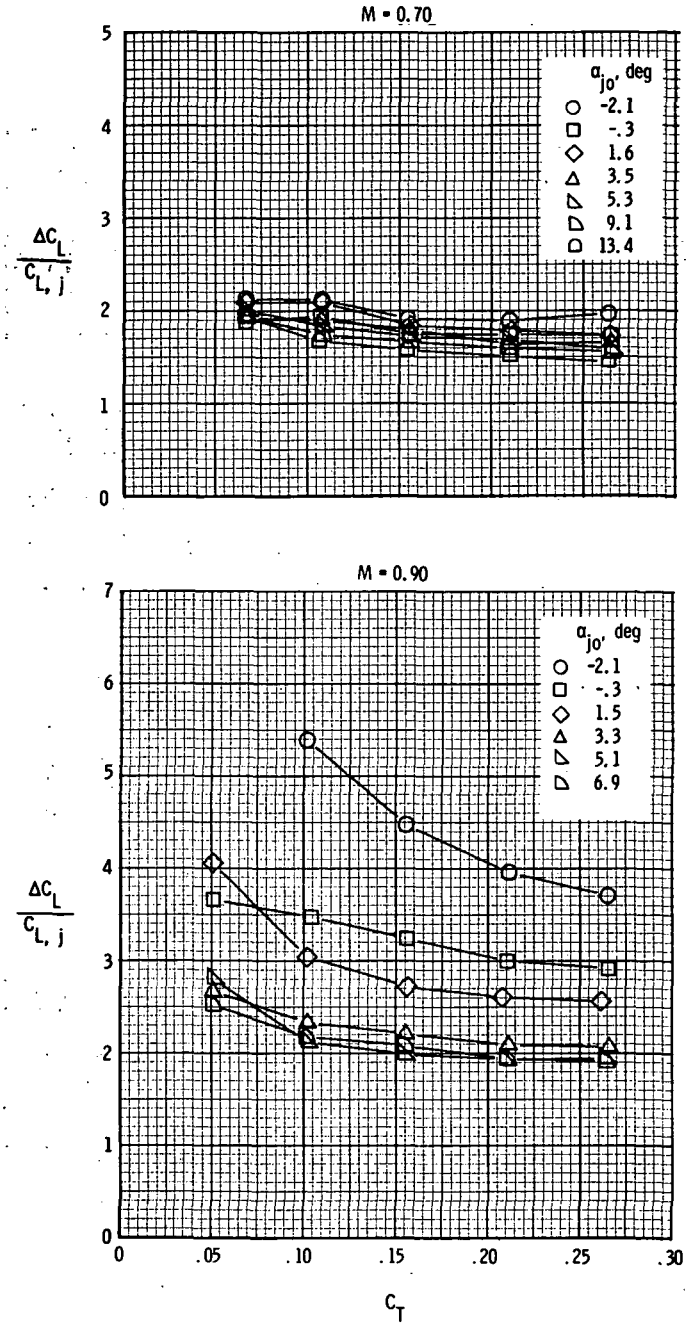

(a) $x_e/c_r = 0.07$; $\delta_d = 15^o$.

Figure 31.- Variation of lift augmentation factor with thrust coefficient for model with rectangular exits.

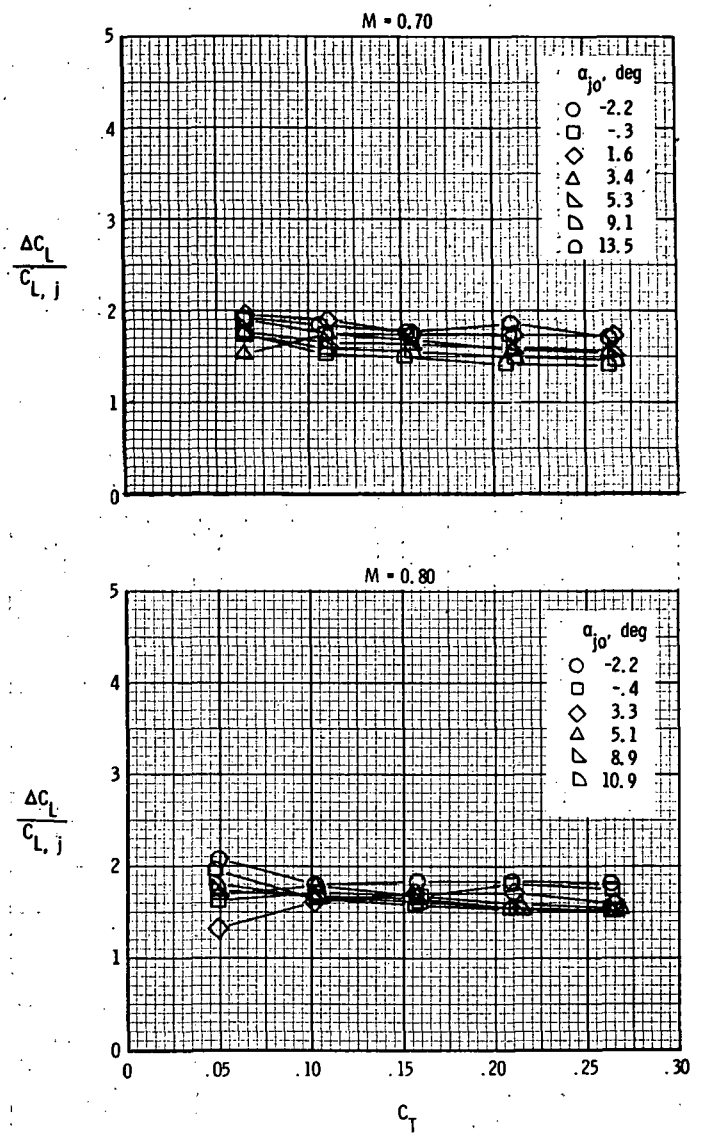

(b) $x_e/c_r = 0.14$; $\delta_d = 15^{\circ}$.

Figure 31.- Continued.

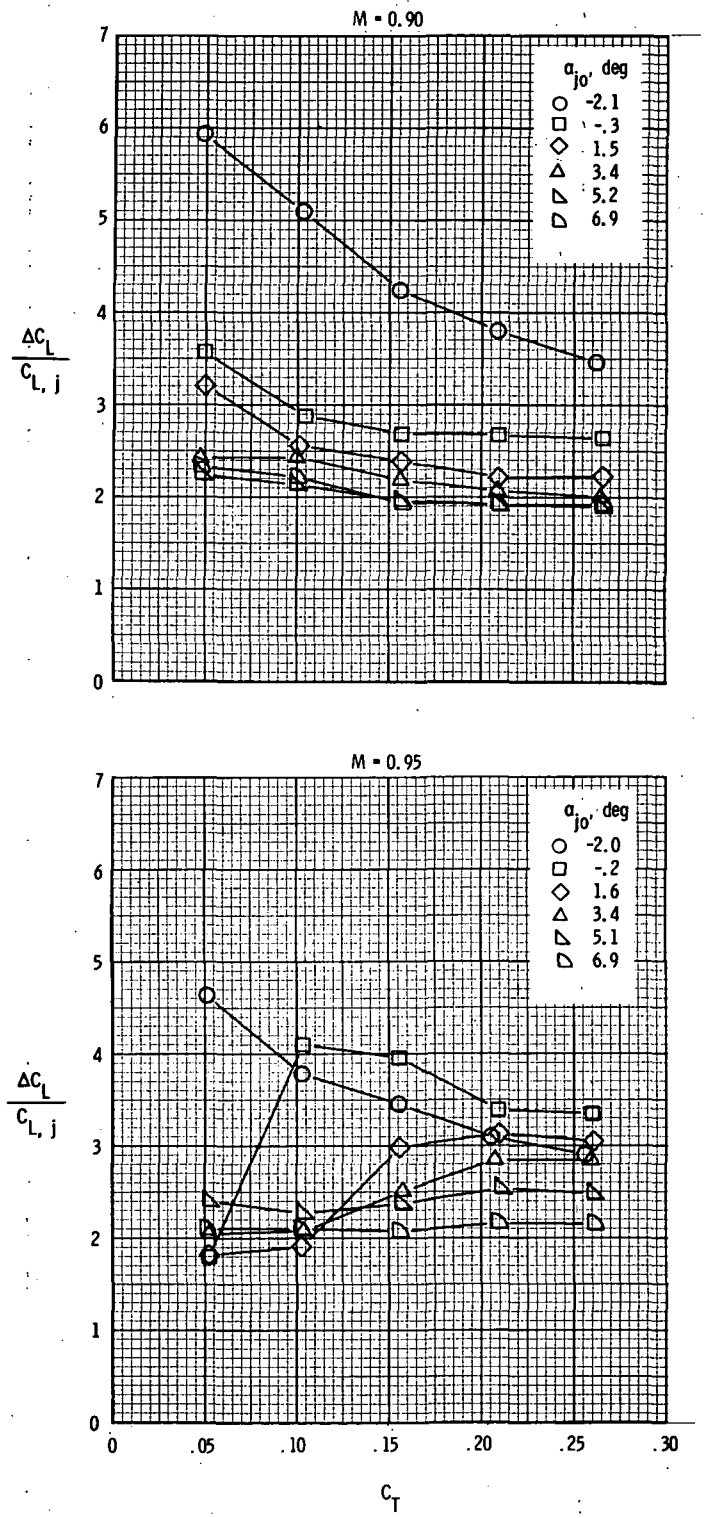

(b) Concluded.

Figure 31.- Continued.

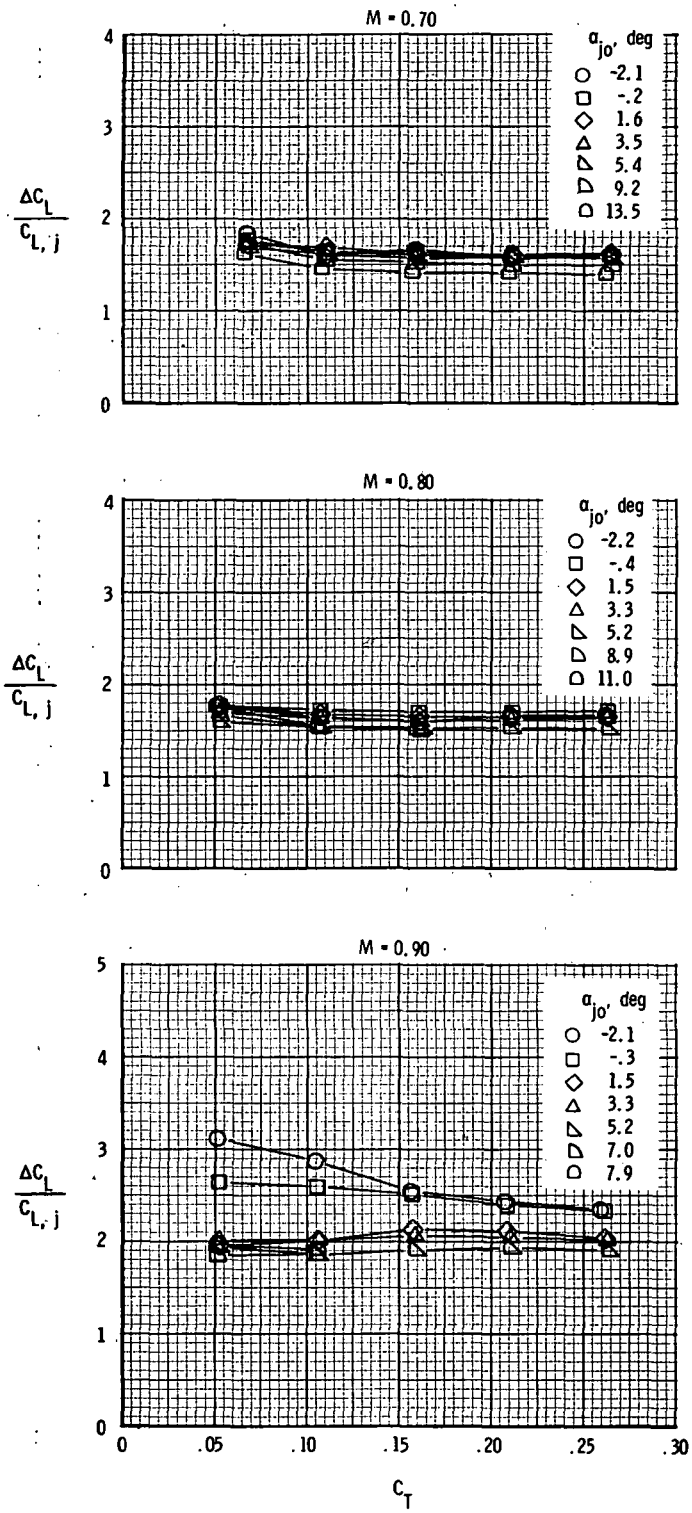

(c) $x_e/c_r = 0.14$; $\delta_d = 30^{\circ}$.

Figure 31.- Continued.

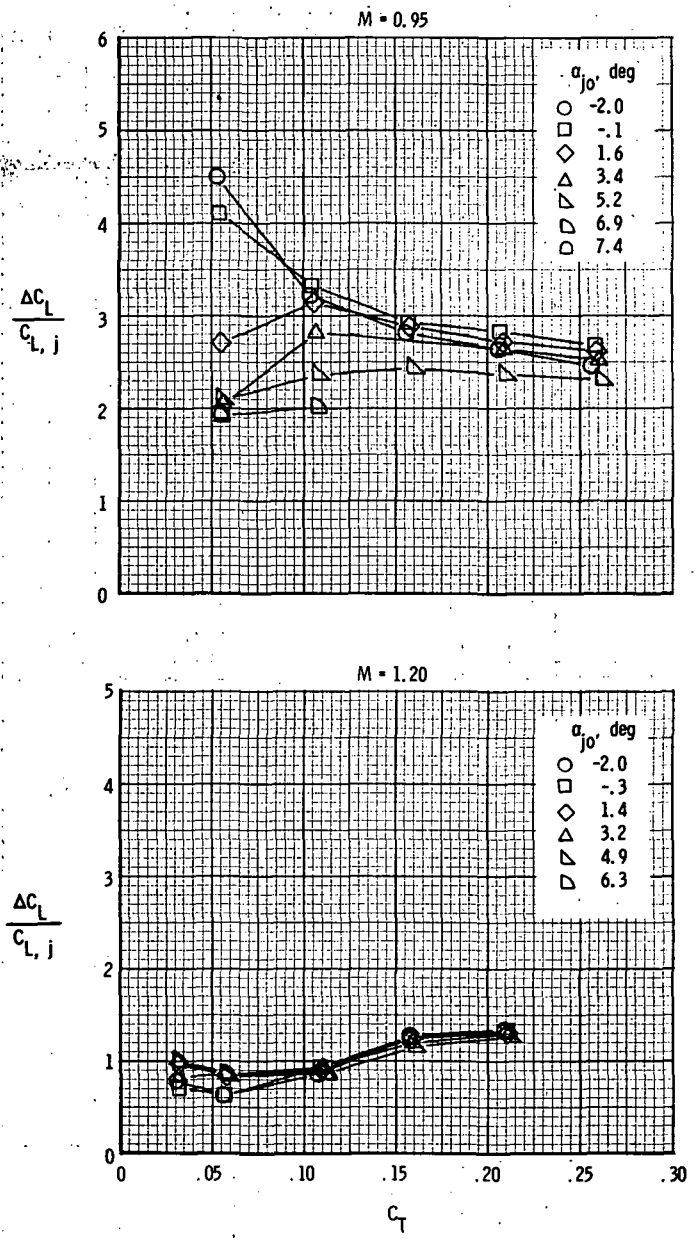

(c) Concluded.

Figure 31.- Continued.

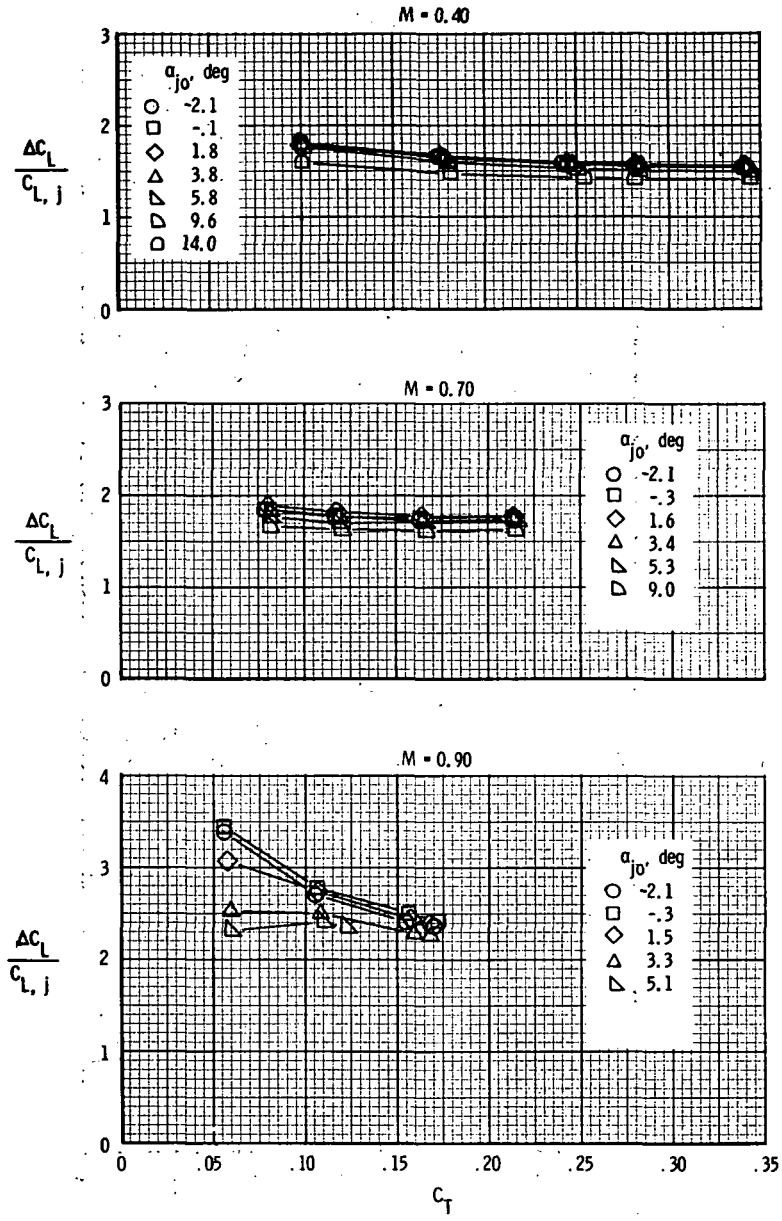

(d) $x_e/c_r = 0.14$; $\delta_d = 45^{\circ}$.

Figure 31.- Continued.

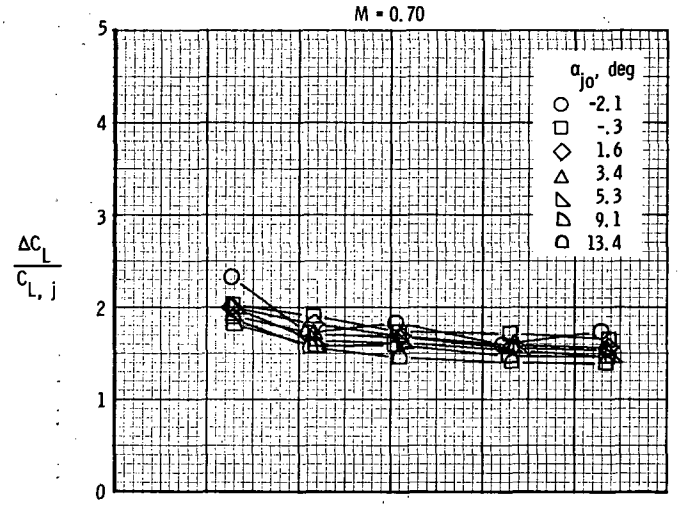

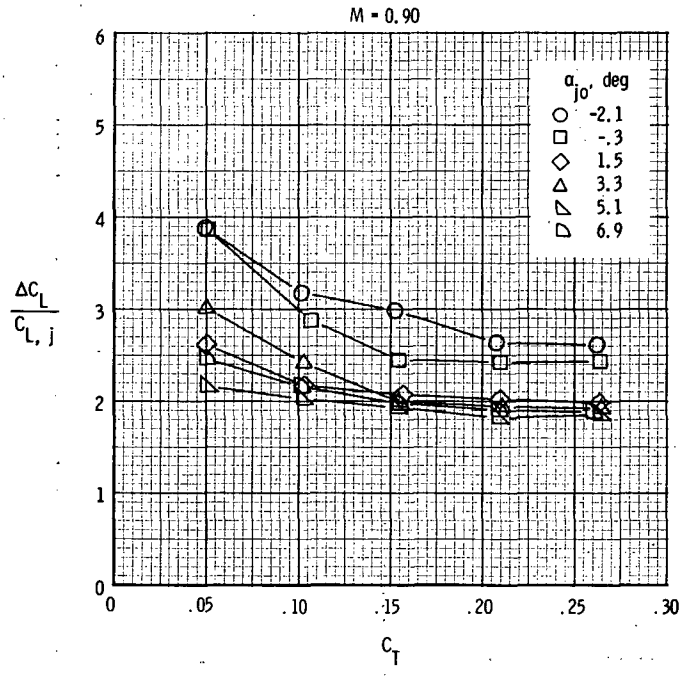

(e) $x_e/c_r = 0.21$; $\delta_d = 15^{\circ}$.

Figure 31.- Concluded.

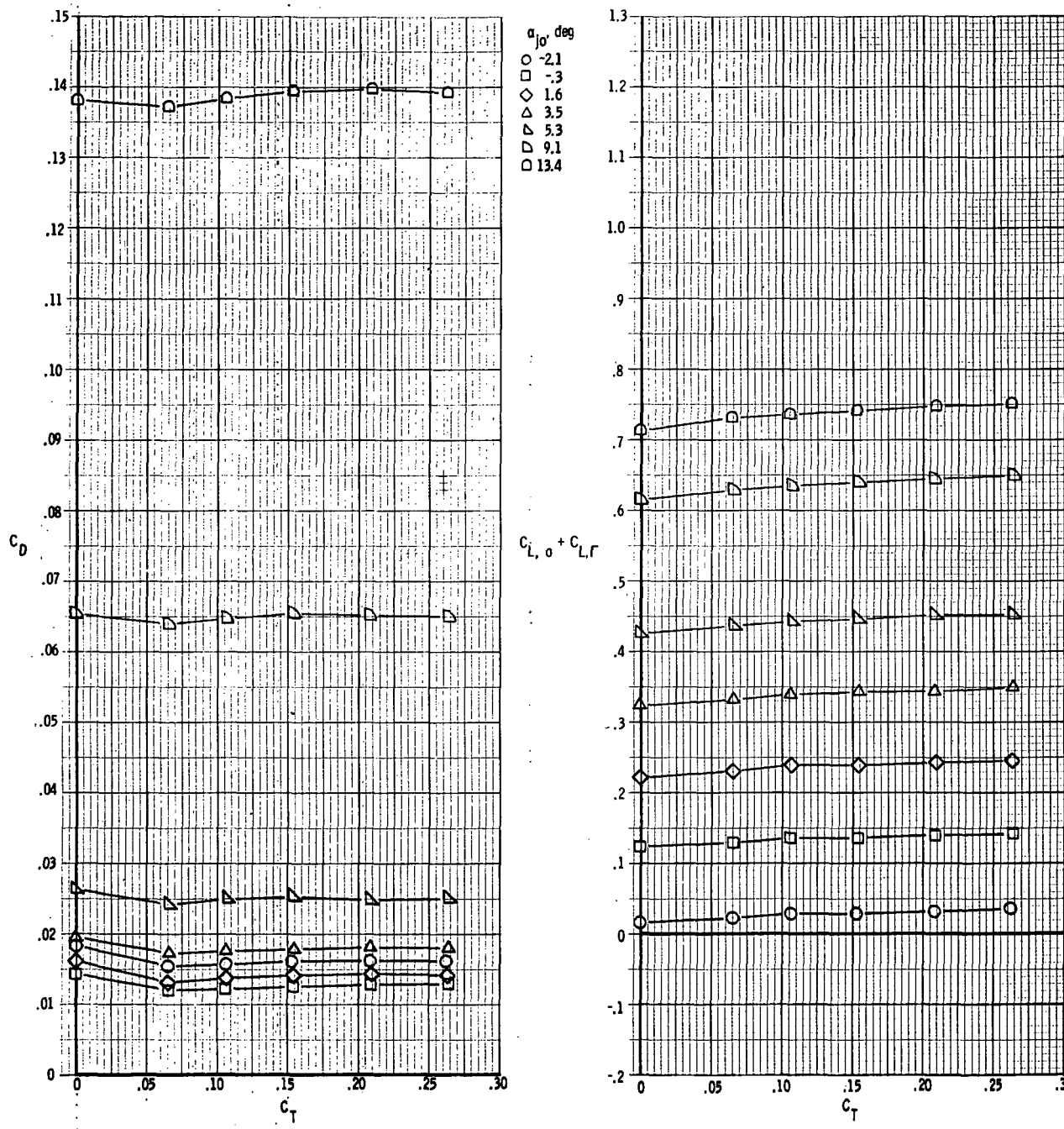

(a) M = 0.70.

Figure 32.- Drag and lift characteristics for model with rectangular exits; $x_e/c_r = 0.07$; $\delta_d = 15^{\circ}$.

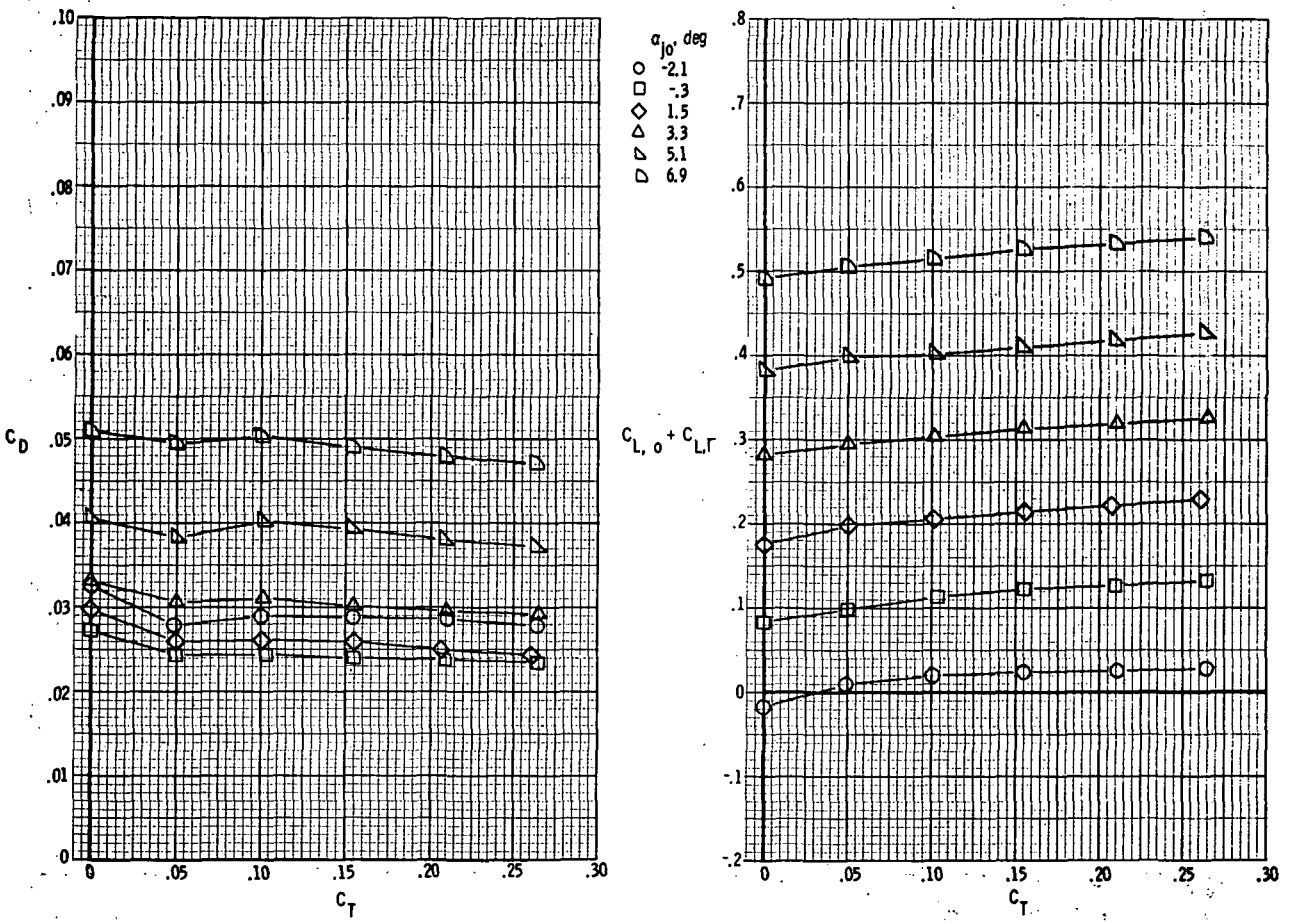

(b) M = 0.90.

Figure 32.- Concluded.

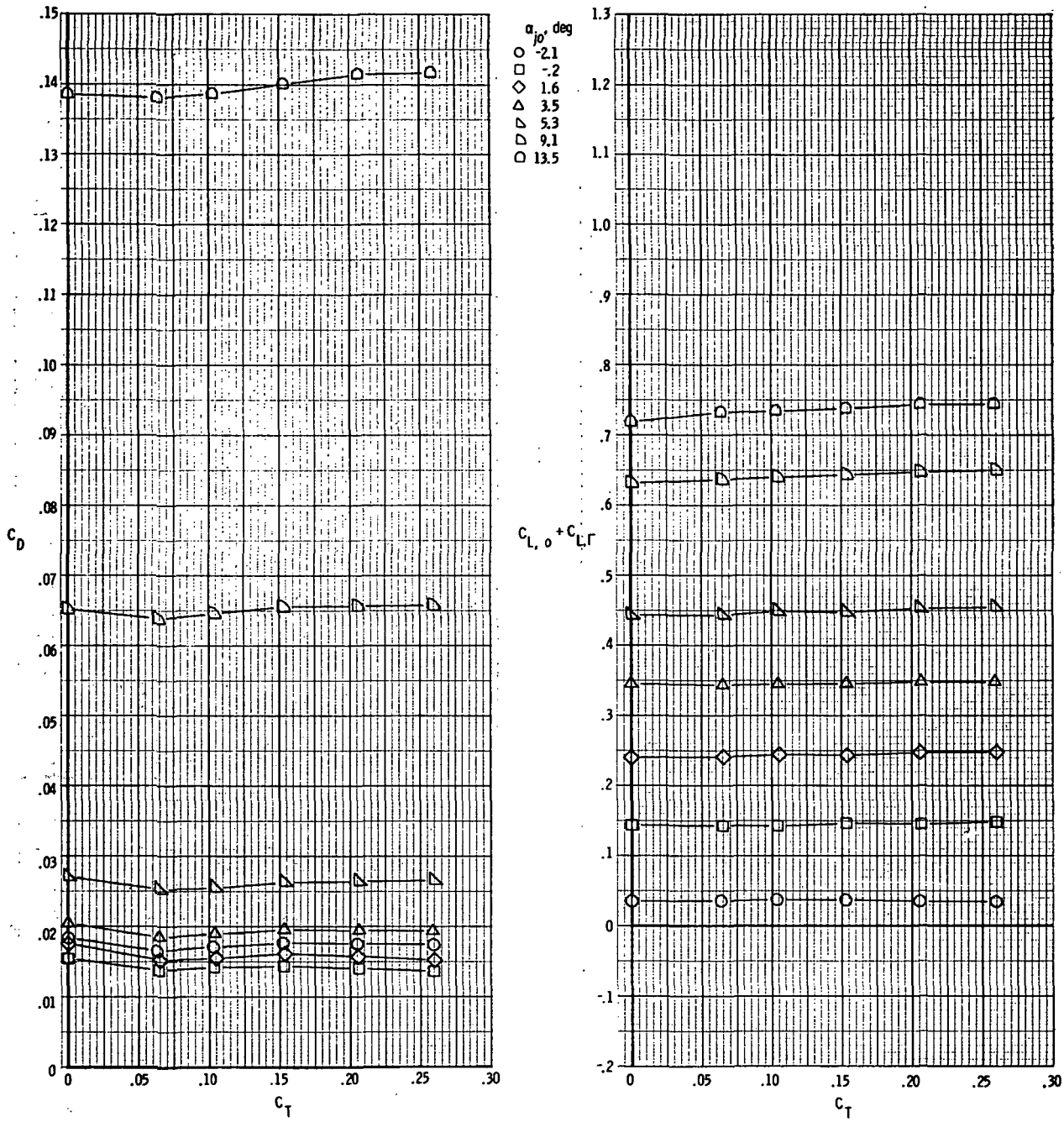

(a) M = 0.70.

Figure 33.- Drag and lift characteristics for model with rectangular exits; $x_e/c_r = 0.14$; $\delta_d = 0^o$.

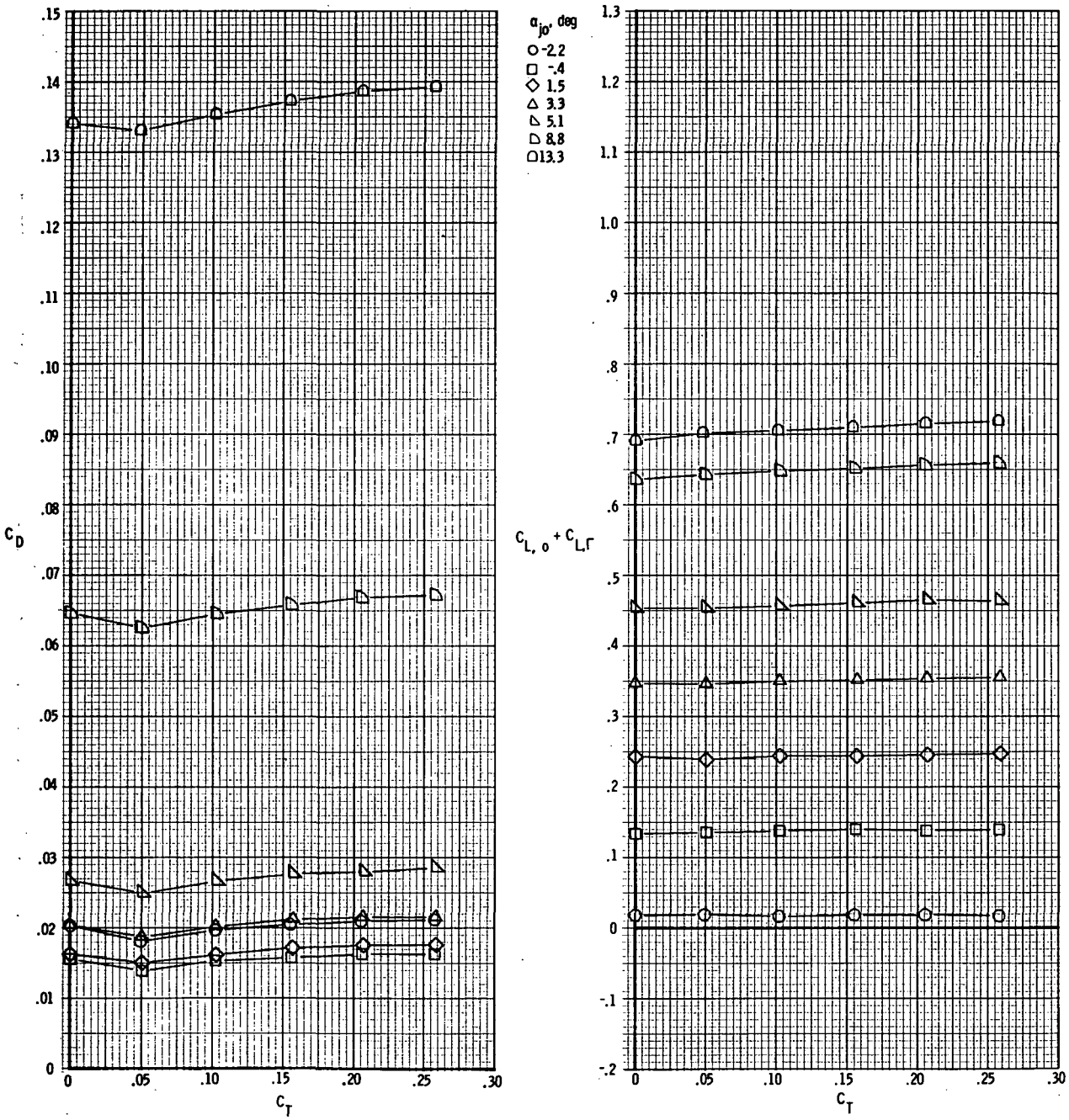

(b) M = 0.80.

Figure 33. - Continued.

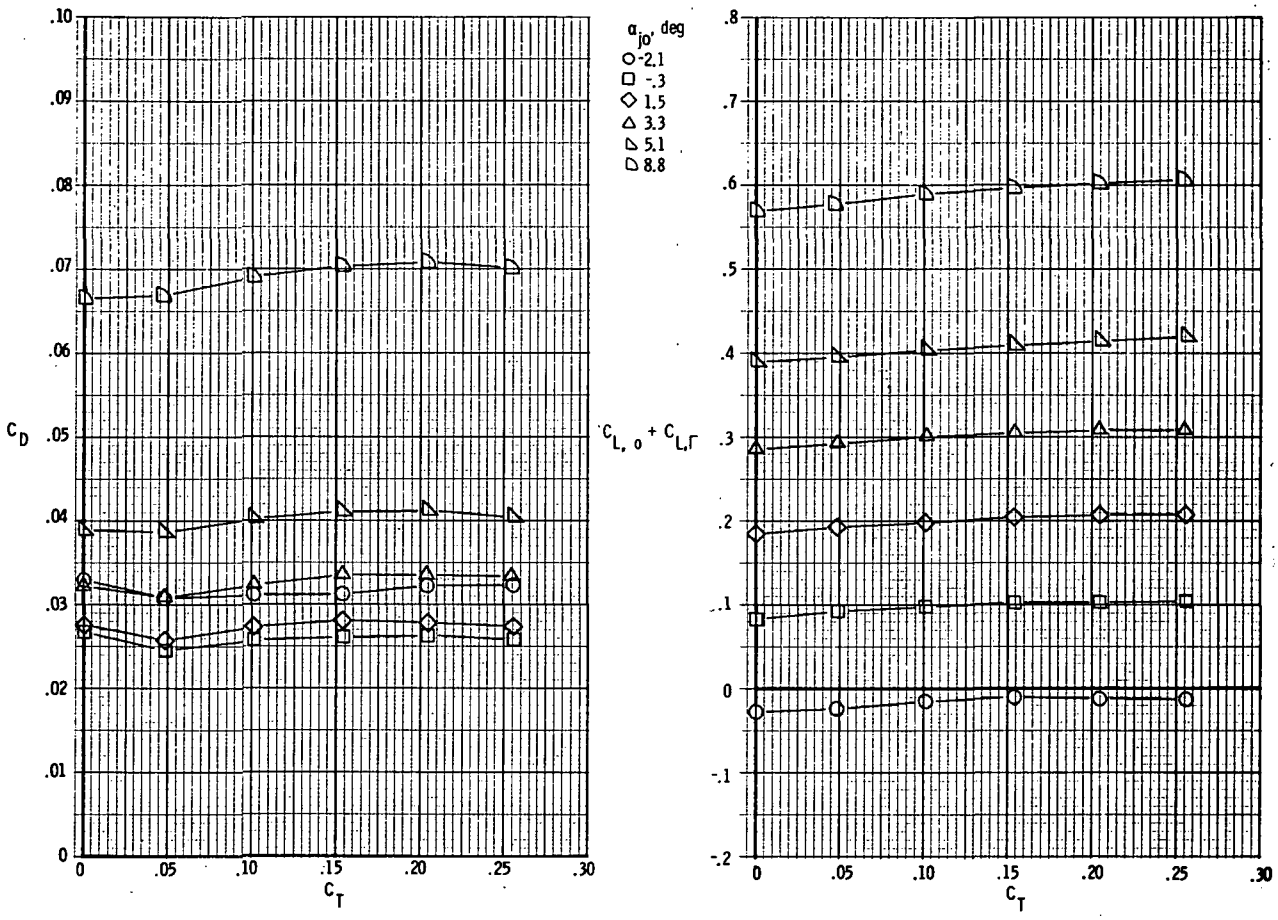

(c) M = 0.90.

Figure 33.- Continued.

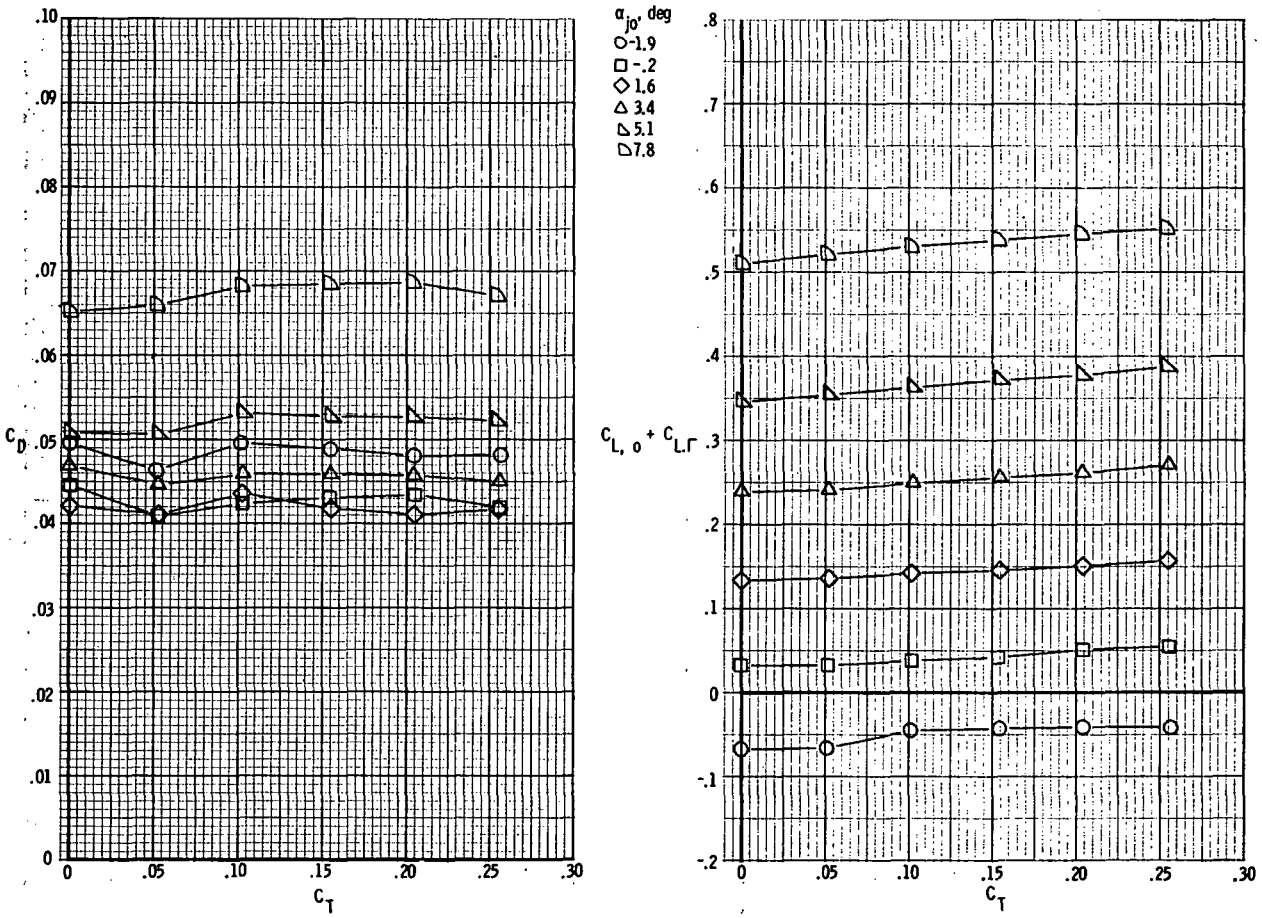

(d) M = 0.95.

Figure 33.- Continued.

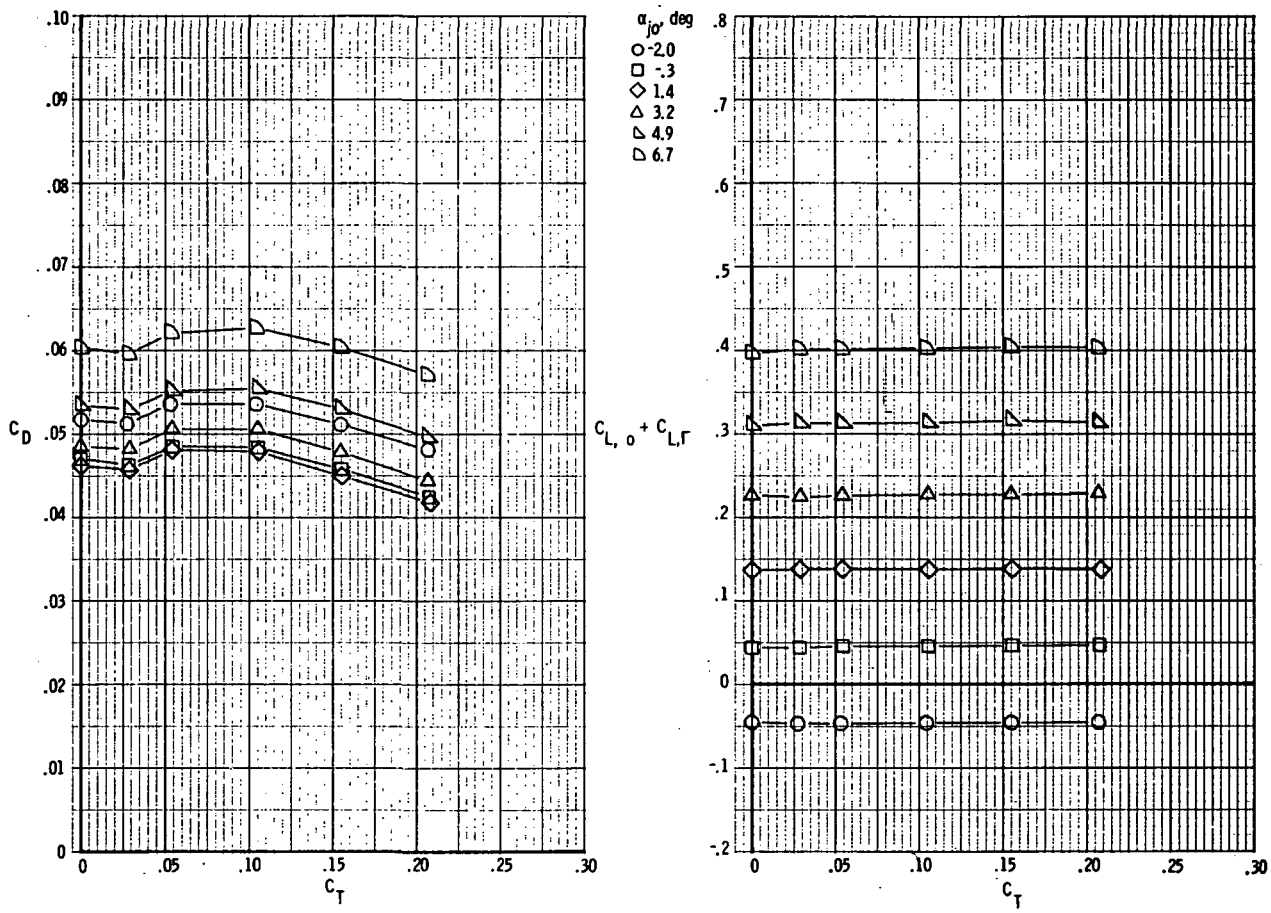

(e) M = 1.20.

Figure 33.- Concluded.

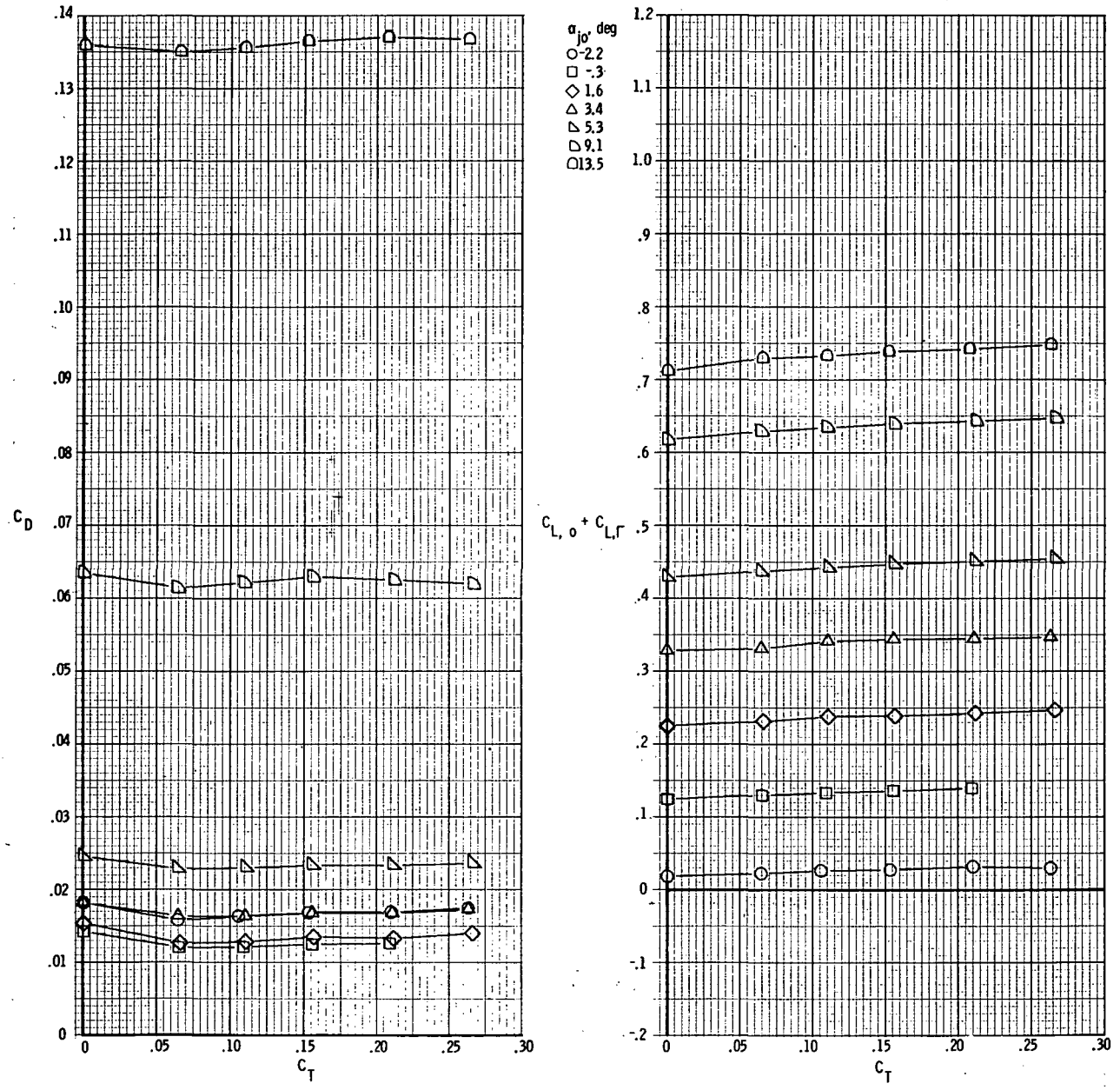

(a) M = 0.70.

Figure 34.- Drag and lift characteristics for model with rectangular exits; $x_e/c_r = 0.14$; $\delta_d = 15^{\circ}$.

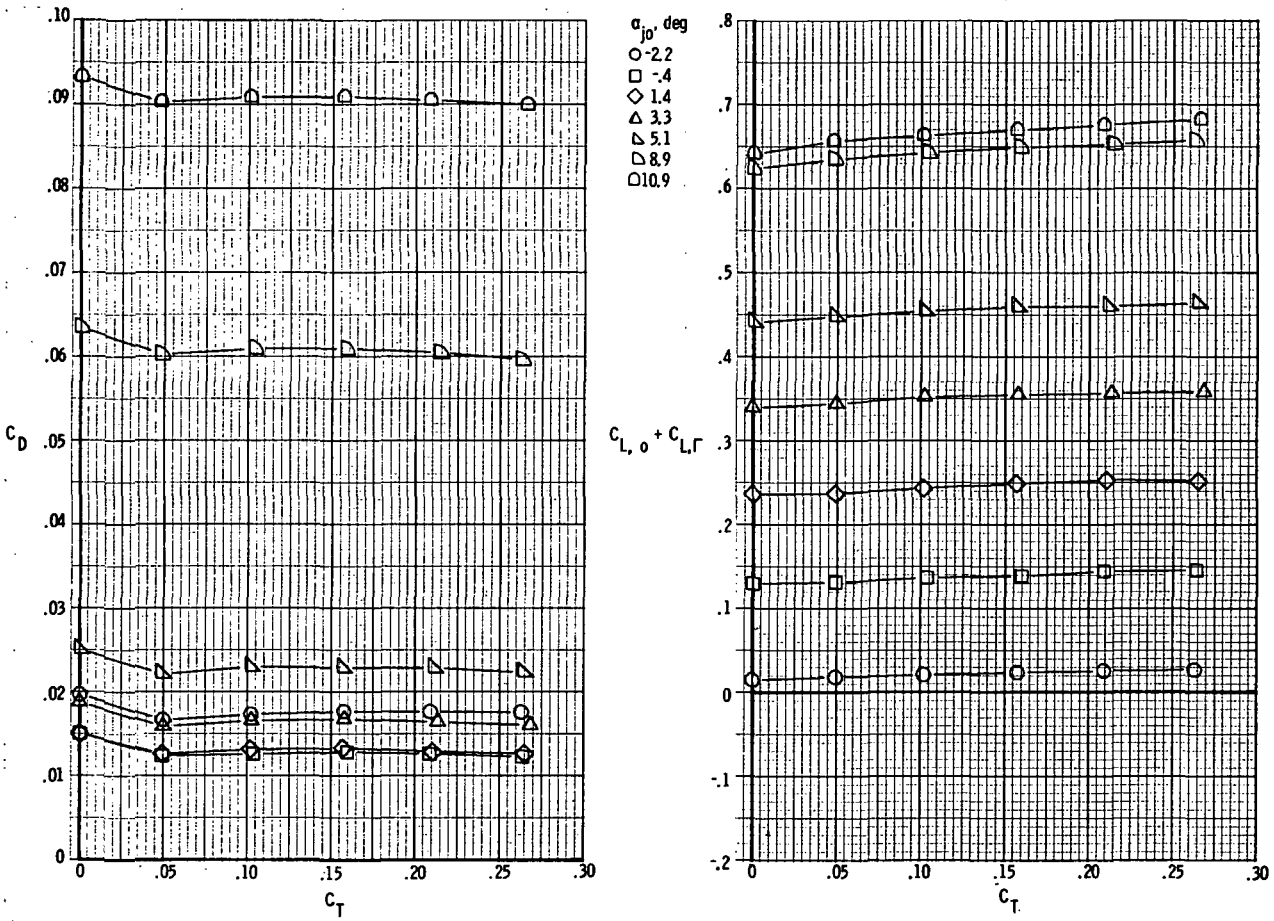

(b) M = 0.80.

Figure 34.- Continued.

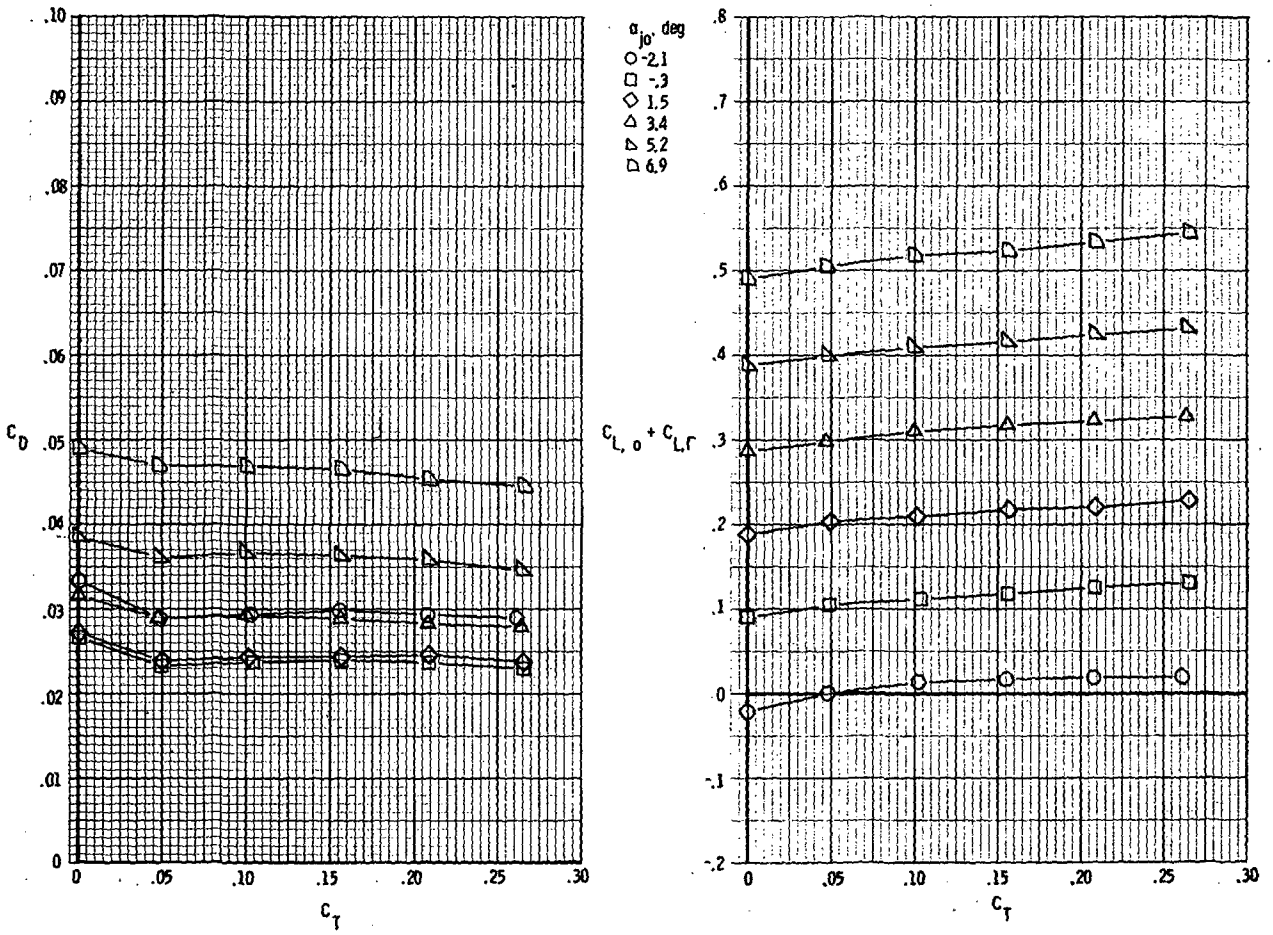

(c) M = 0.90.

Figure 34.- Continued.

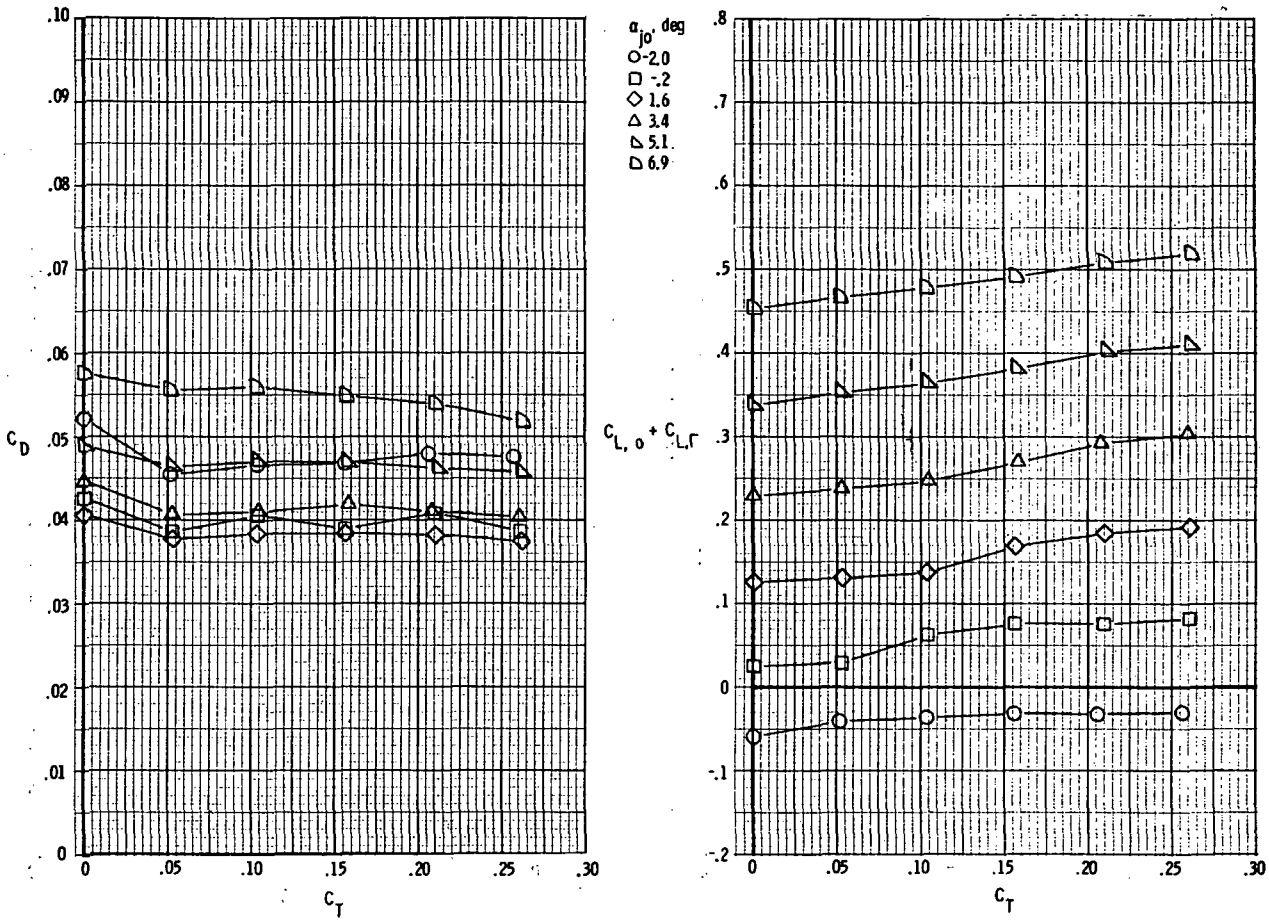

(d) M = 0.95.

Figure 34.- Concluded.

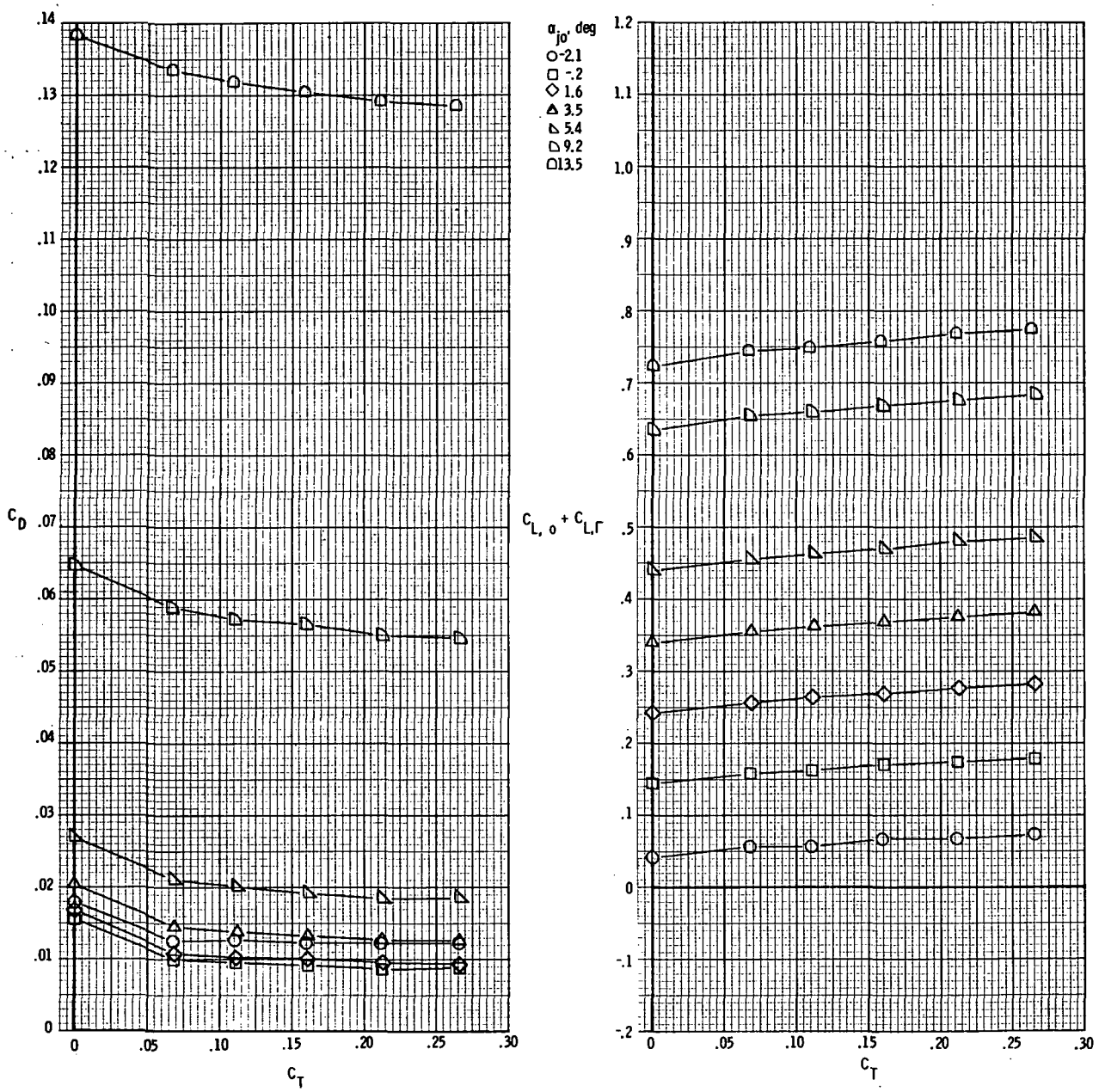

(a) M = 0.70.

Figure 35.- Drag and lift characteristics for model with rectangular exits; $x_e/c_r = 0.14$; $\delta_d = 30^{\circ}$.

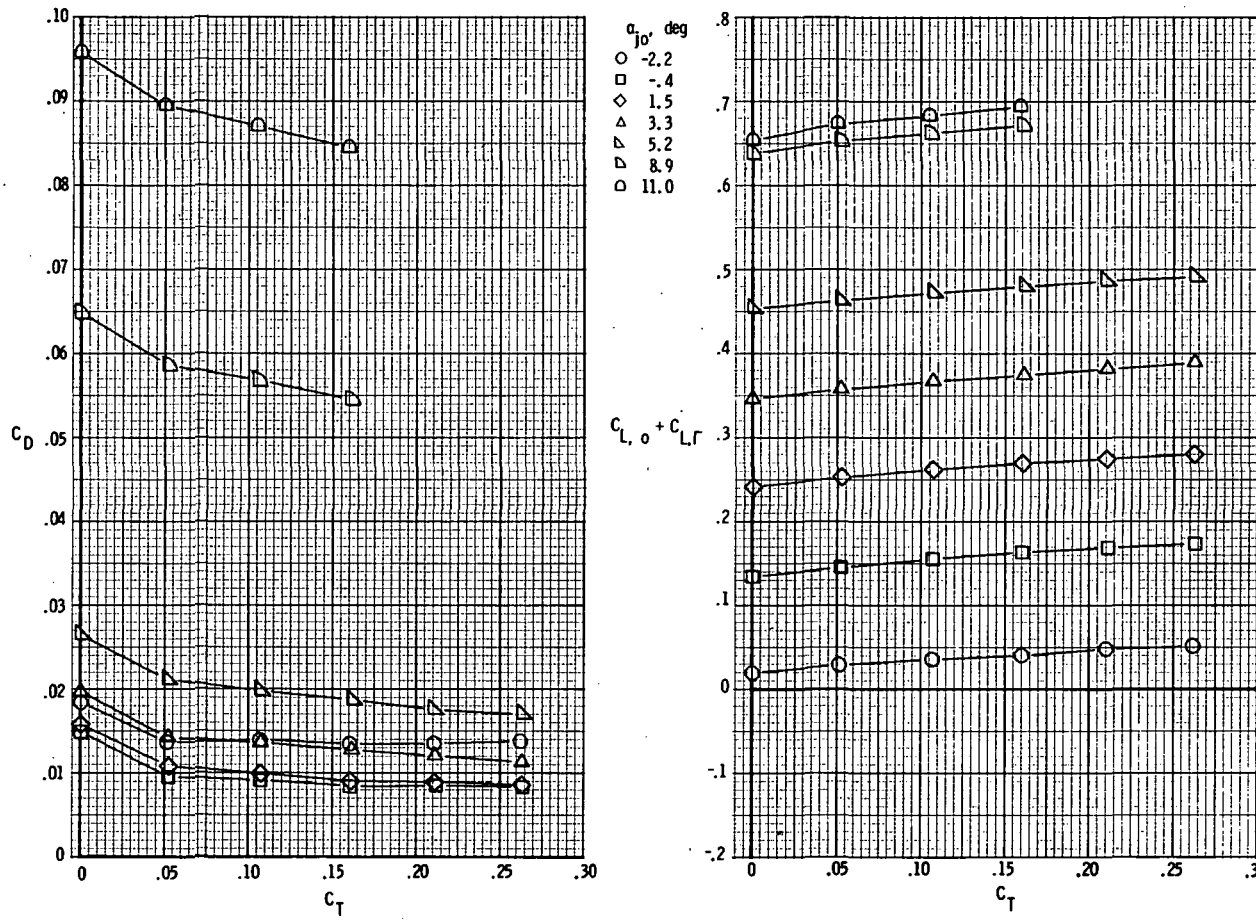

(b) M = 0.80.

Figure 35.- Continued.

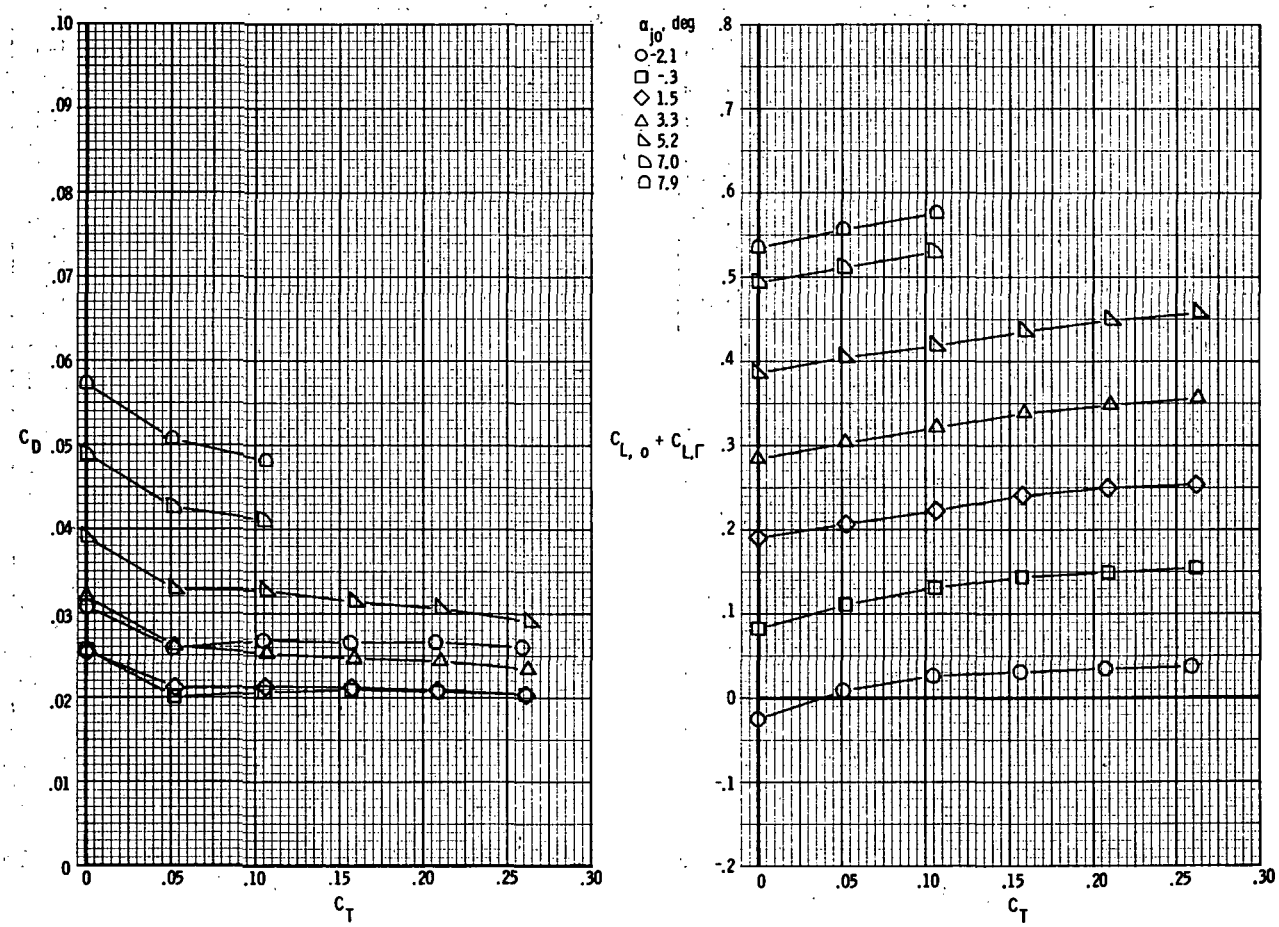

(c) M = 0.90.

Figure 35. - Continued.

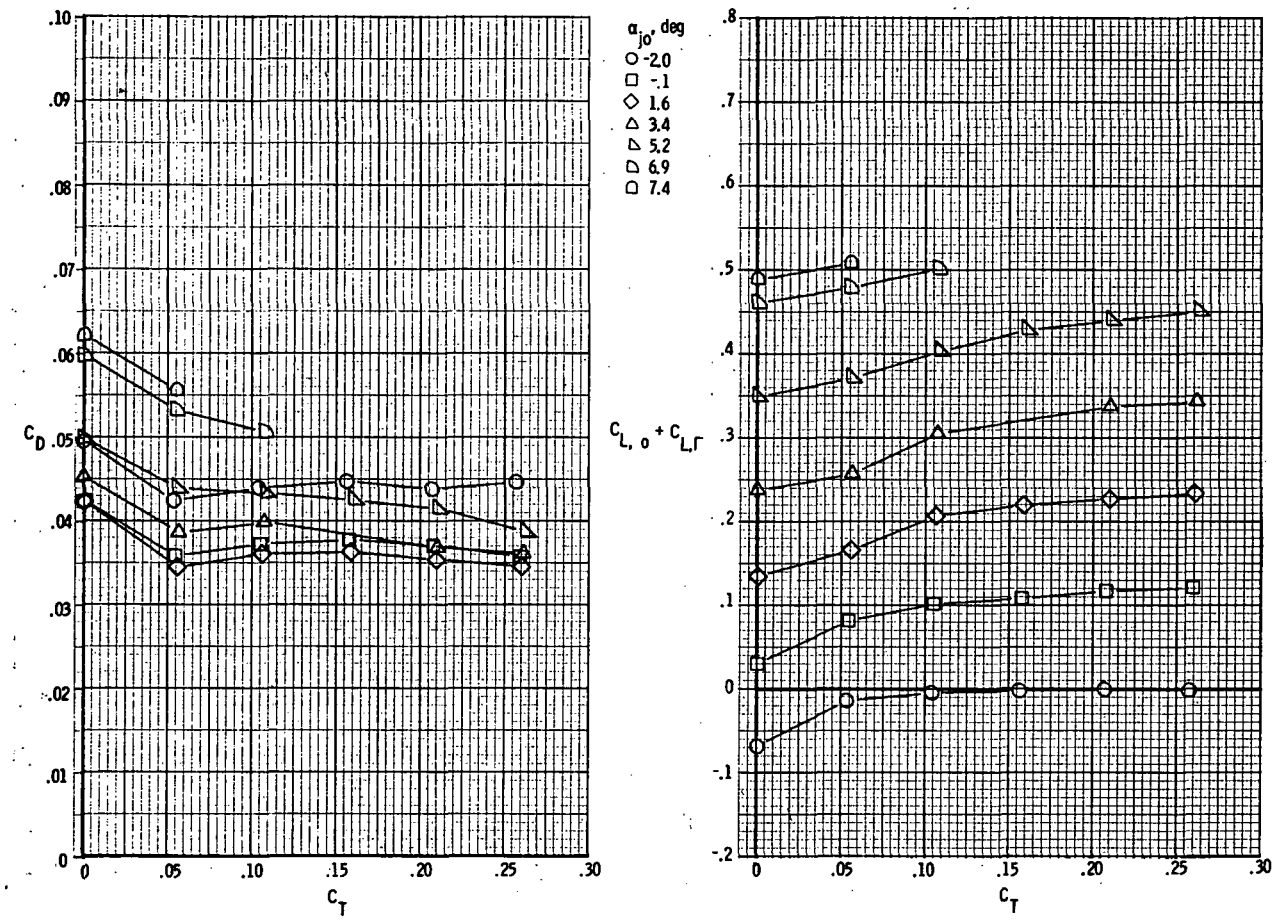

(d) M = 0.95.

Figure 35. - Continued.

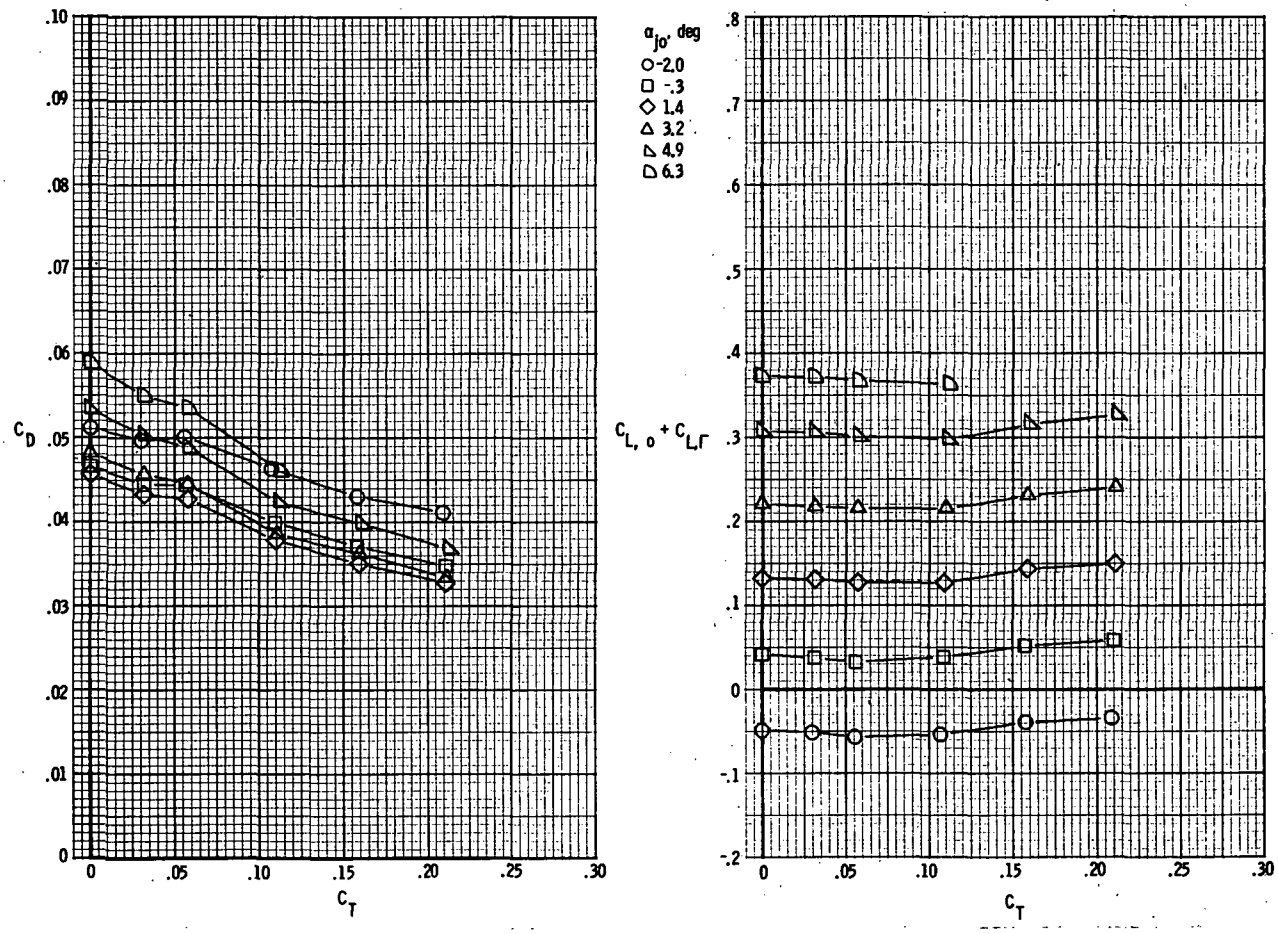

(e) M = 1.20.

Figure 35. - Concluded.

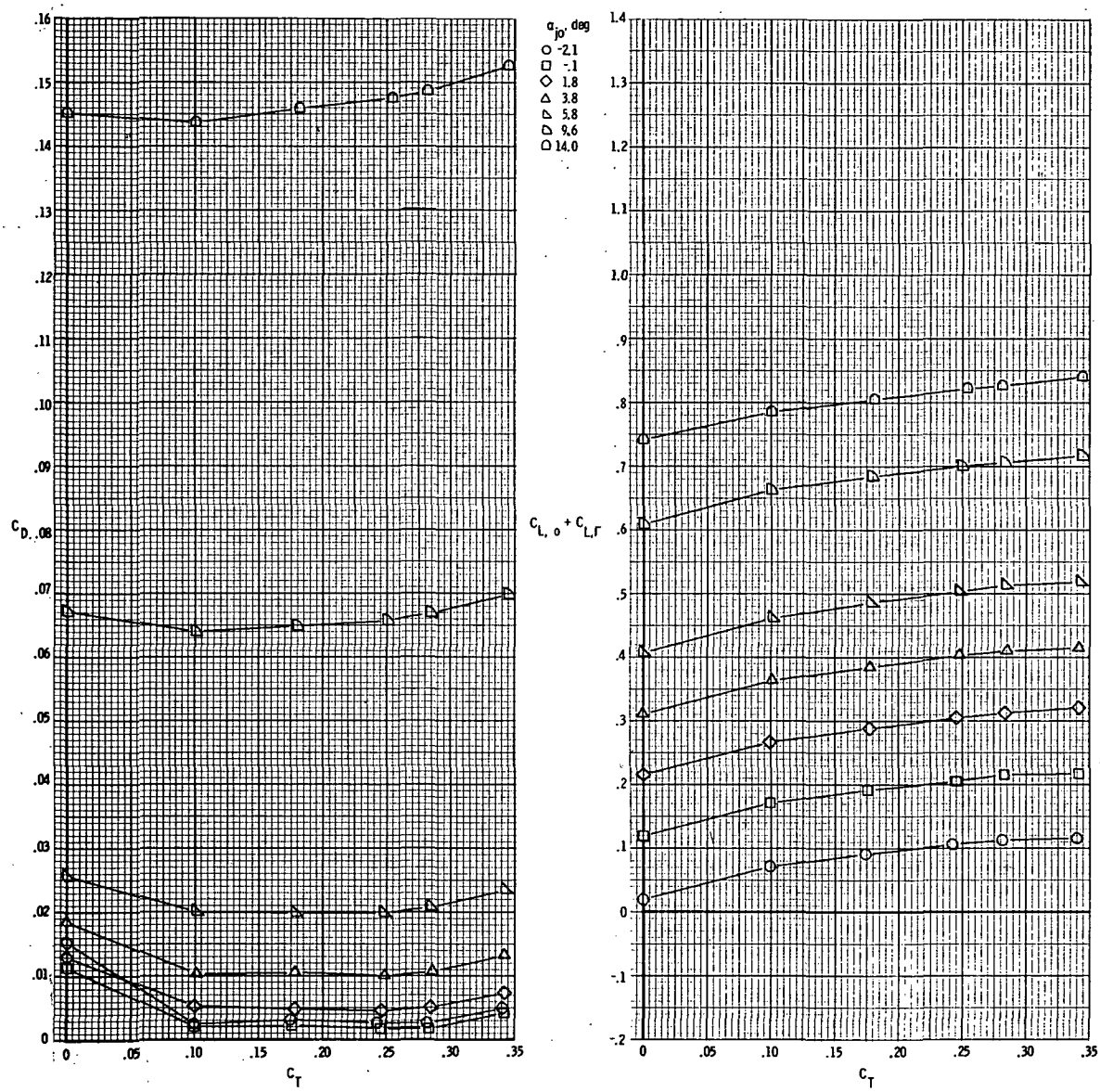

(a) M = 0.40.

Figure 36.- Drag and lift characteristics for model with rectangular exits; $x_e/c_r = 0.14$; $\delta_d = 45^{\circ}$.

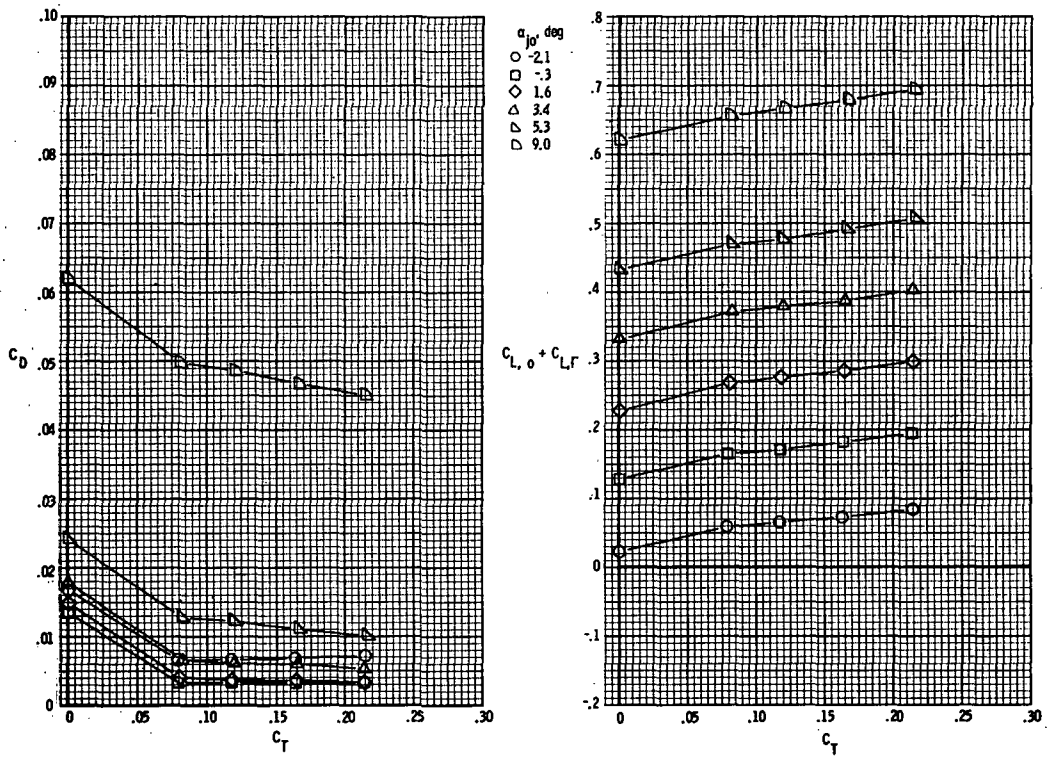

(b) M = 0.70.

Figure 36.- Continued.

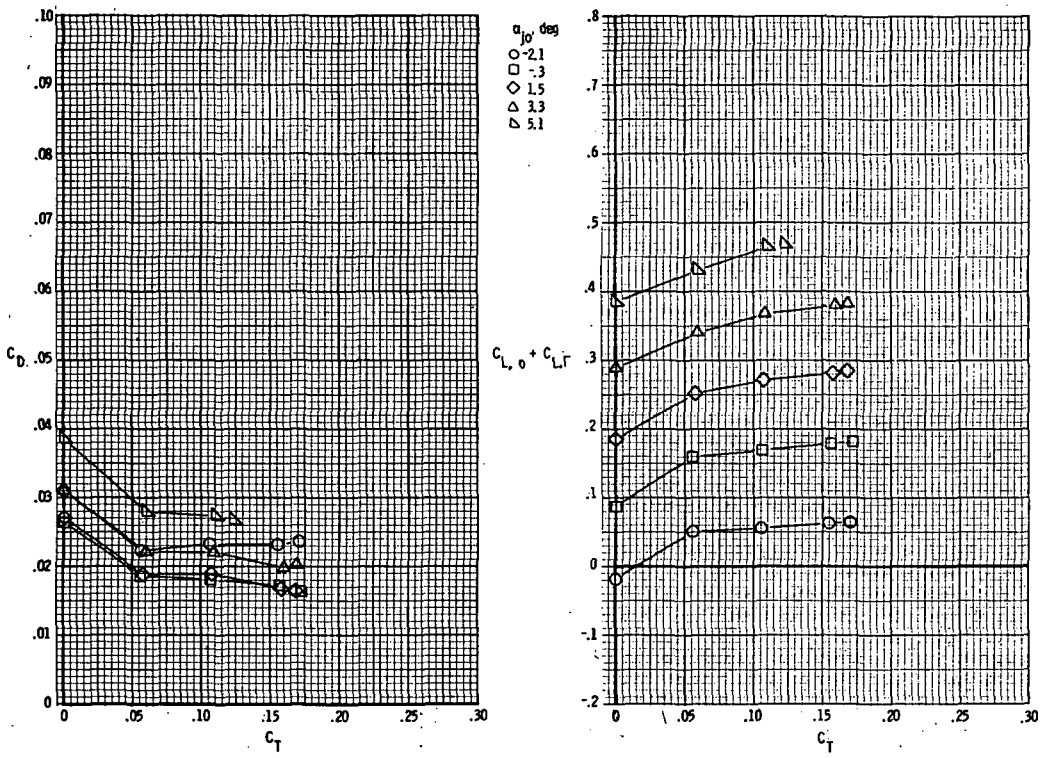

(c) M = 0.90.

Figure 36.- Concluded.

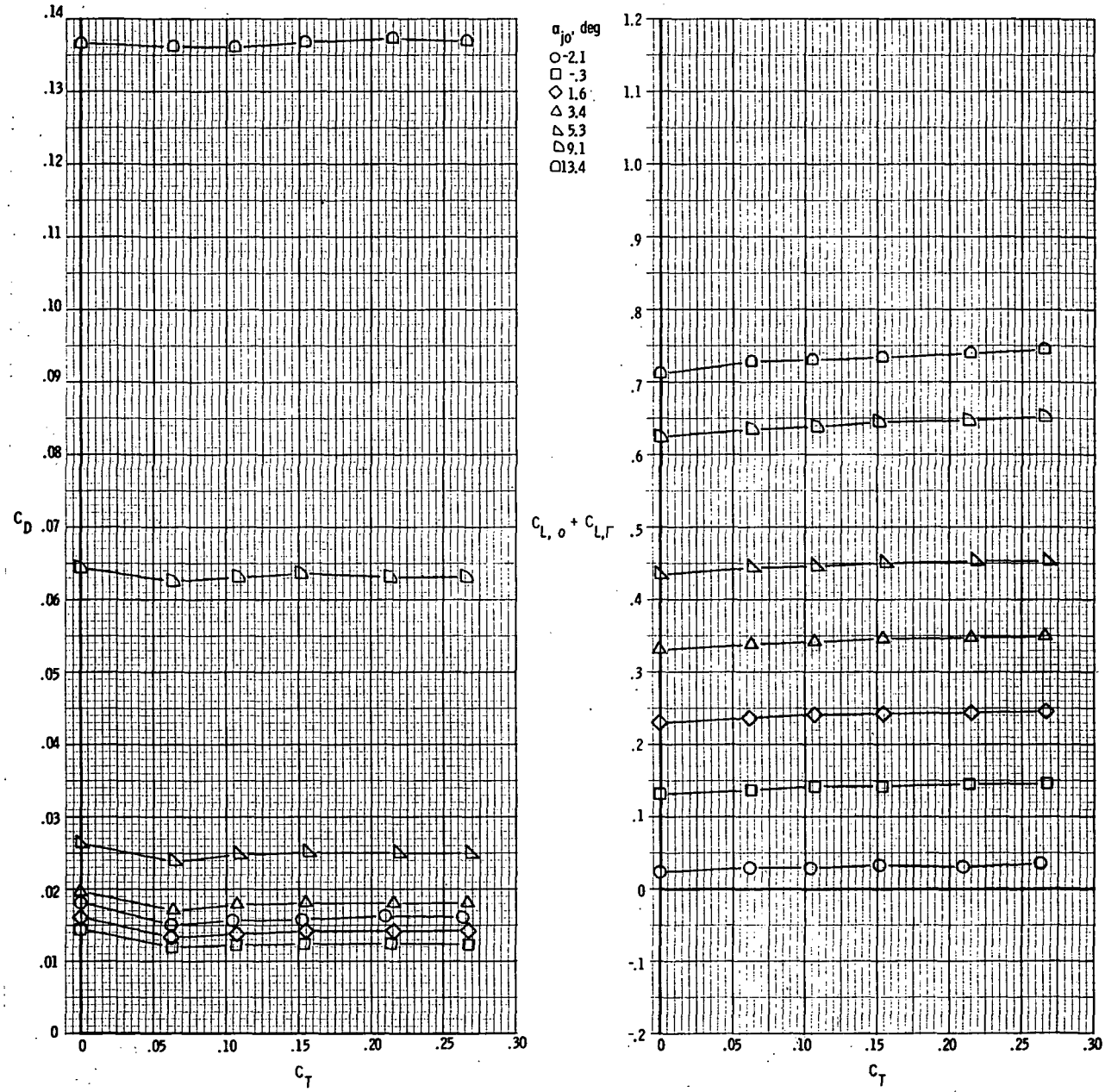

(a) M = 0.70.

Figure 37.- Drag and lift characteristics for model with rectangular exits; $x_e/c_r = 0.21$; $\delta_d = 15^o$.

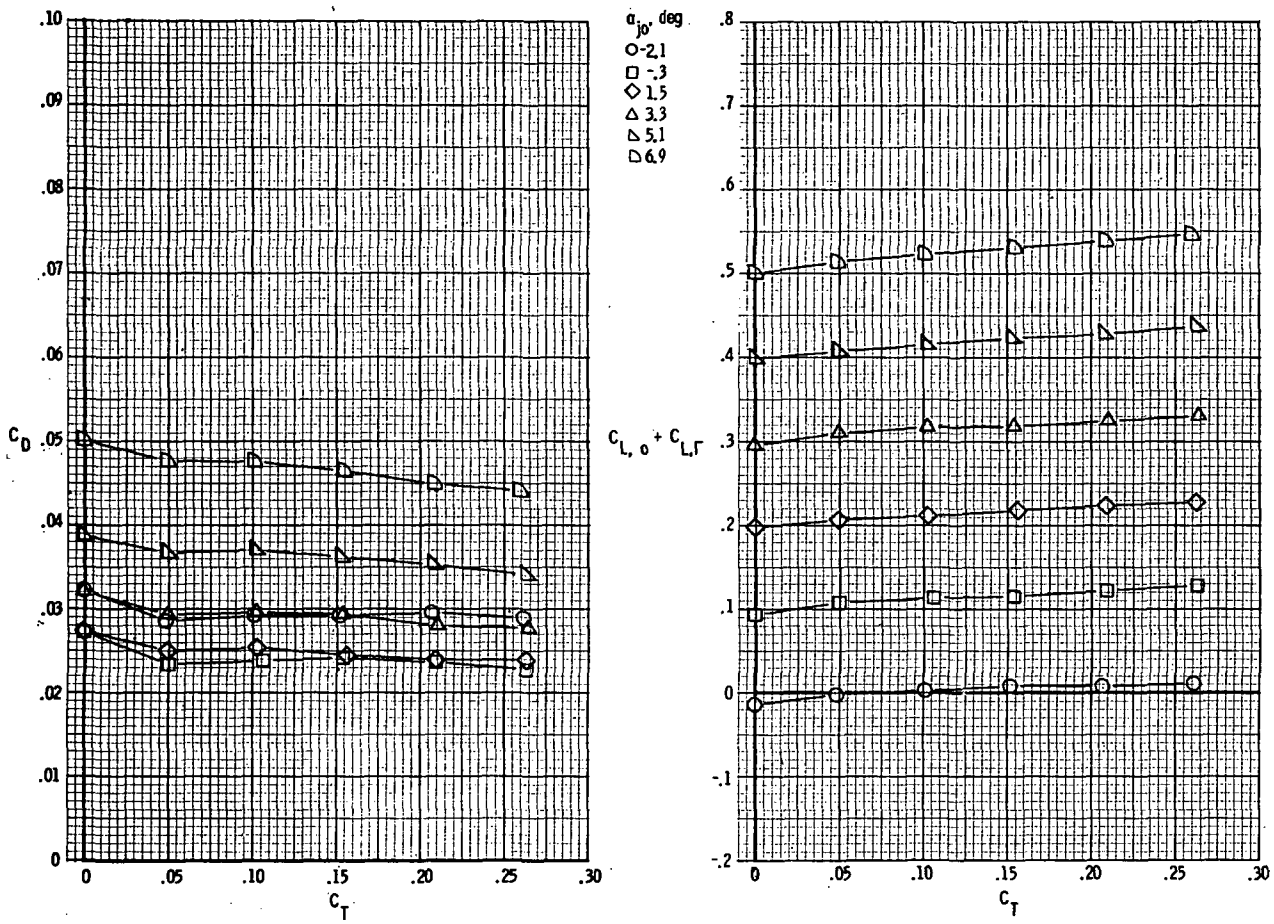

(b) M = 0.90.

Figure 37.- Concluded.

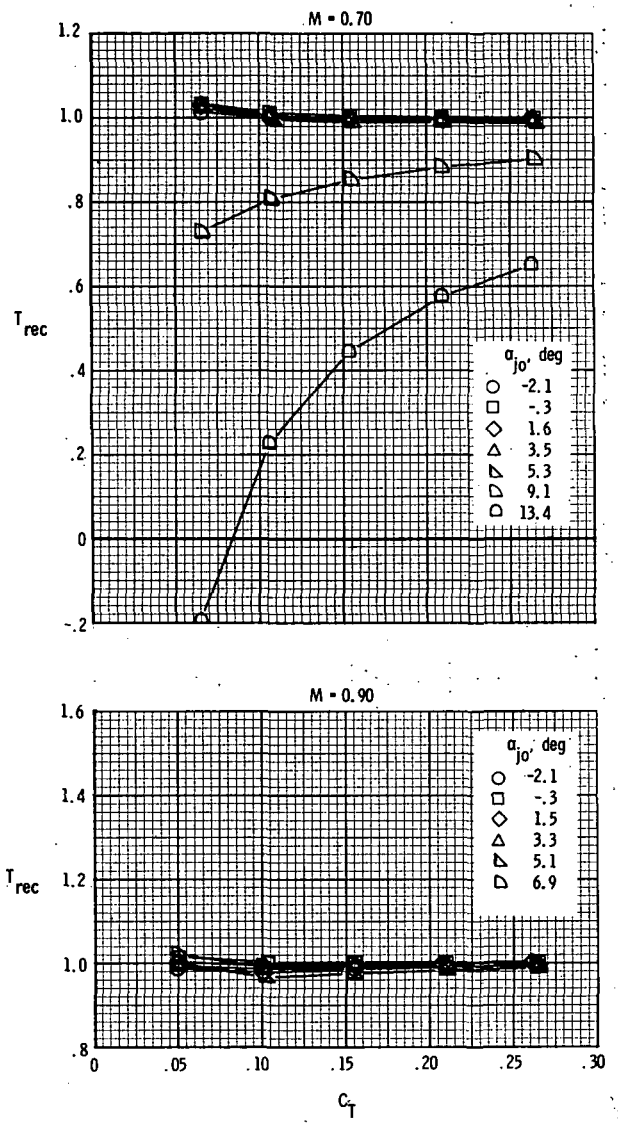

(a) $x_e/c_r = 0.07$; $\delta_d = 15^o$.

Figure 38.- Variation of thrust recovery with thrust coefficient for model with rectangular exits.

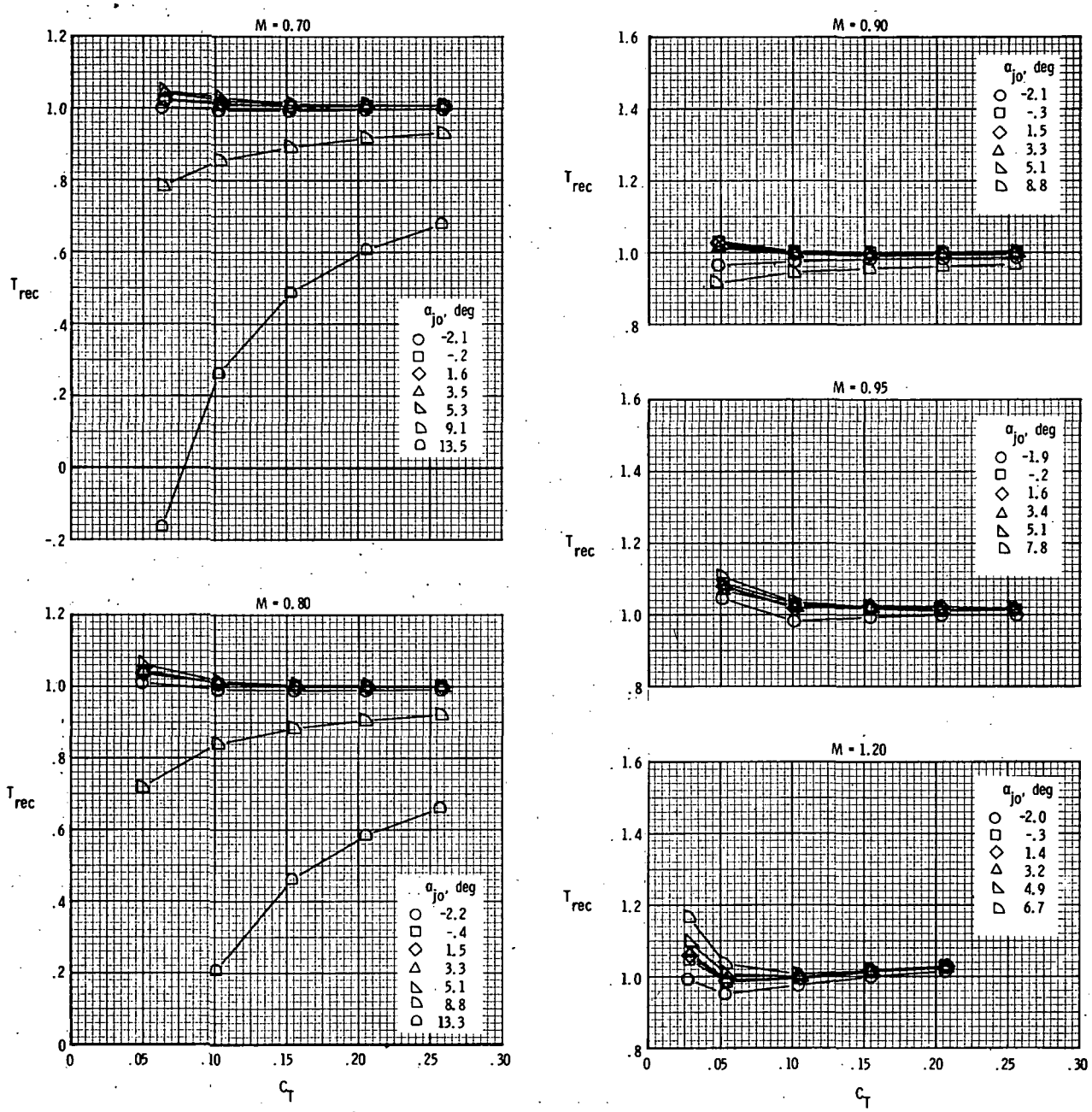

(b) $x_e/c_r = 0.14$; $\delta_d = 0^o$.

Figure 38.- Continued.

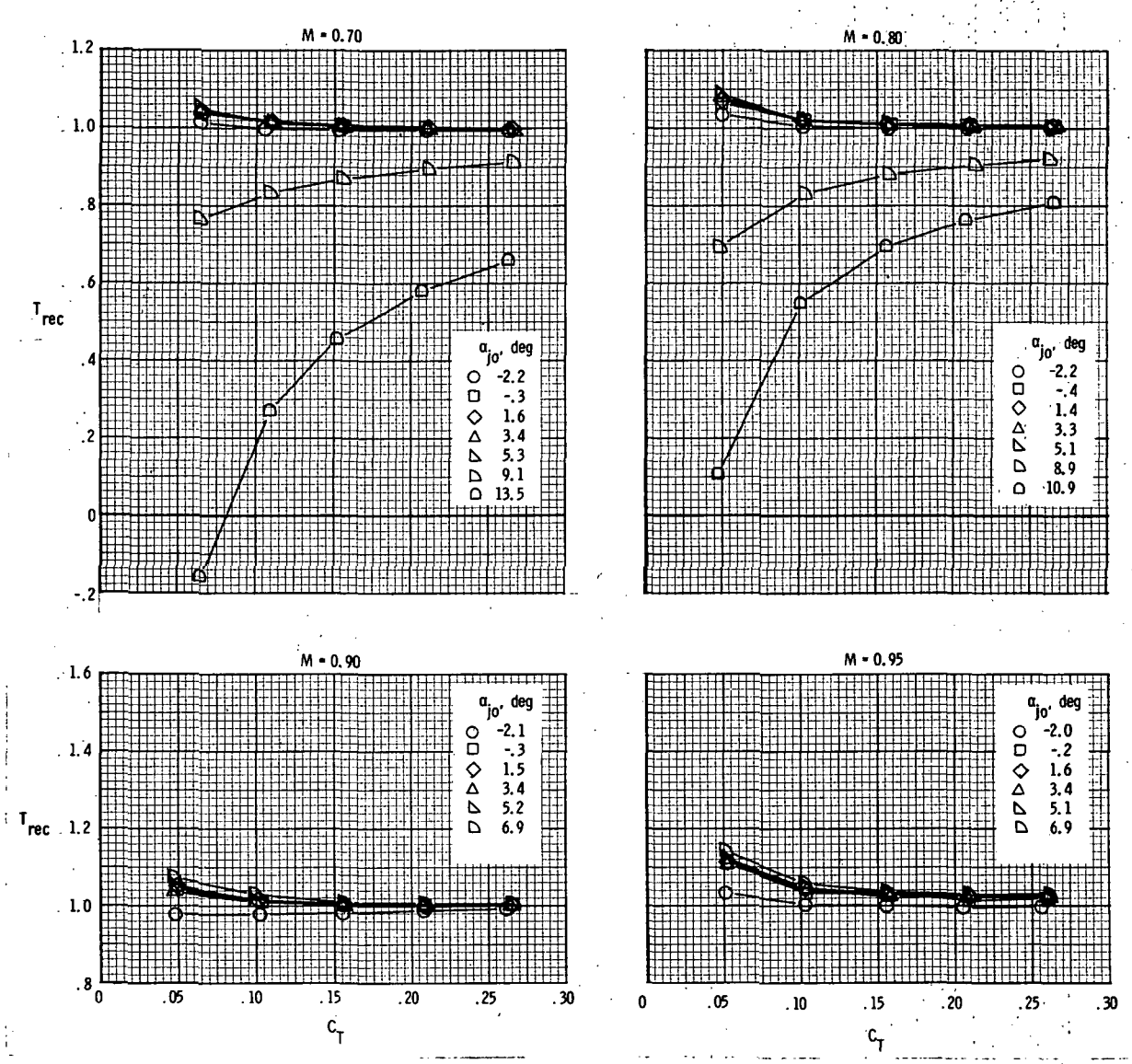

(c) $x_e/c_r = 0.14$; $\delta_d = 15^o$.

Figure 38.- Continued.

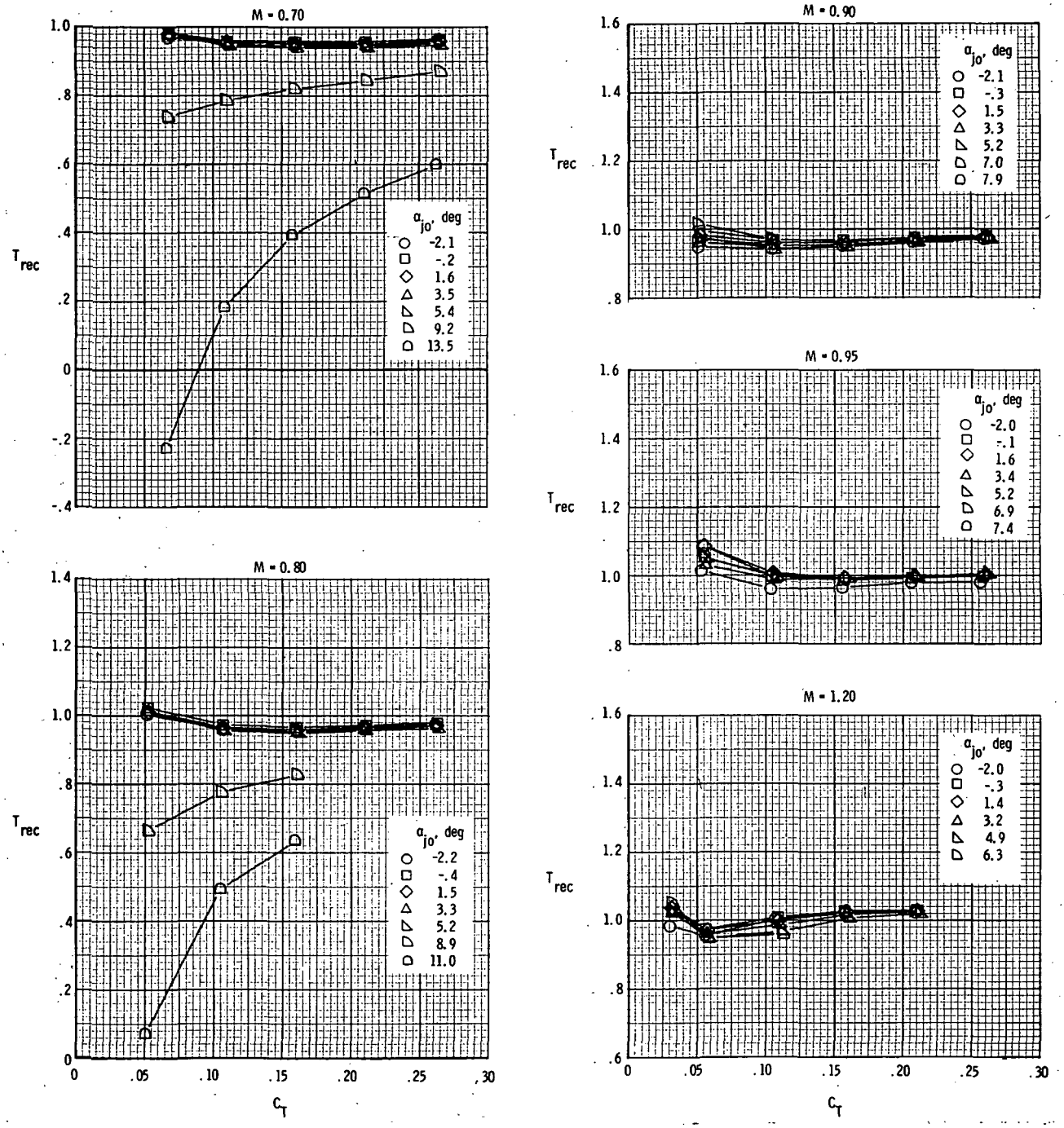

(d) $x_e/c_r = 0.14$; $\delta_d = 30^o$.

Figure 38.- Continued.

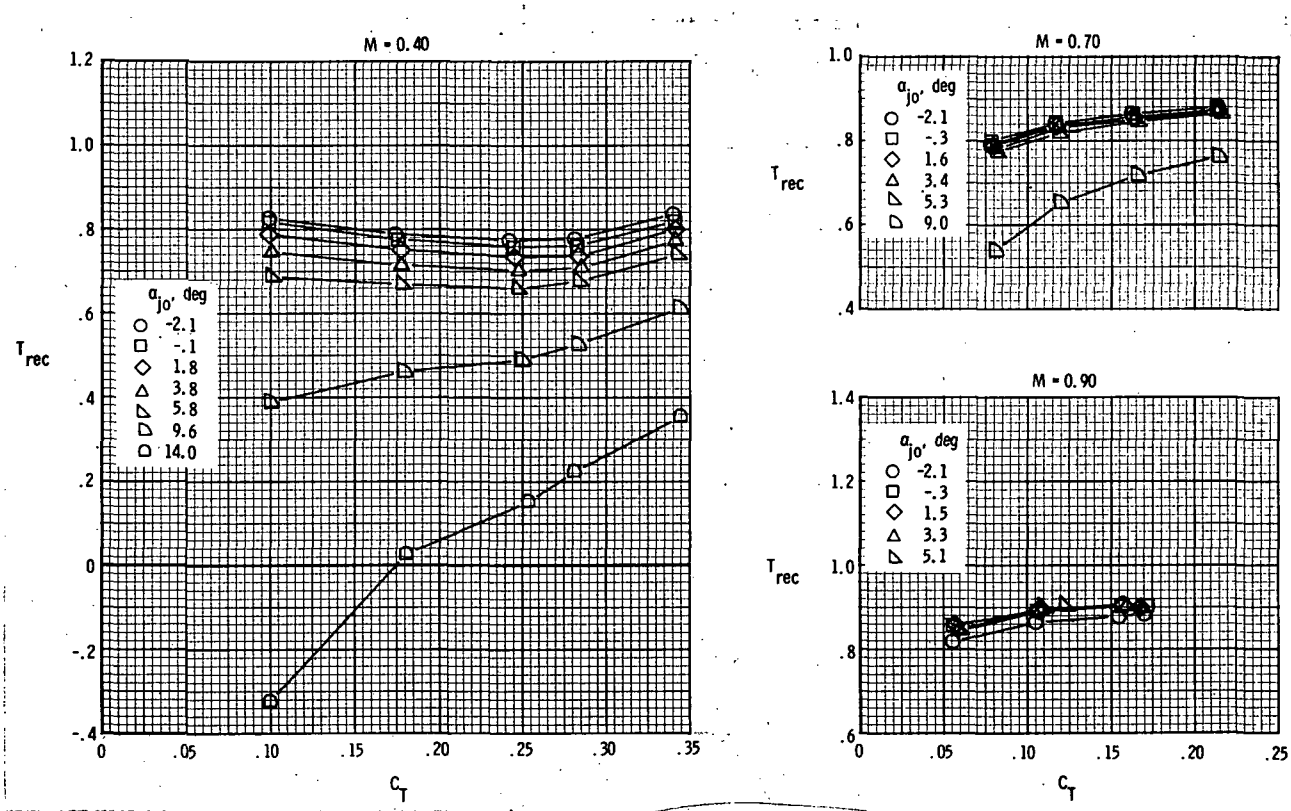

(e) $x_e/c_r = 0.14$; $\delta_d = 45^o$.

Figure 38.- Continued.

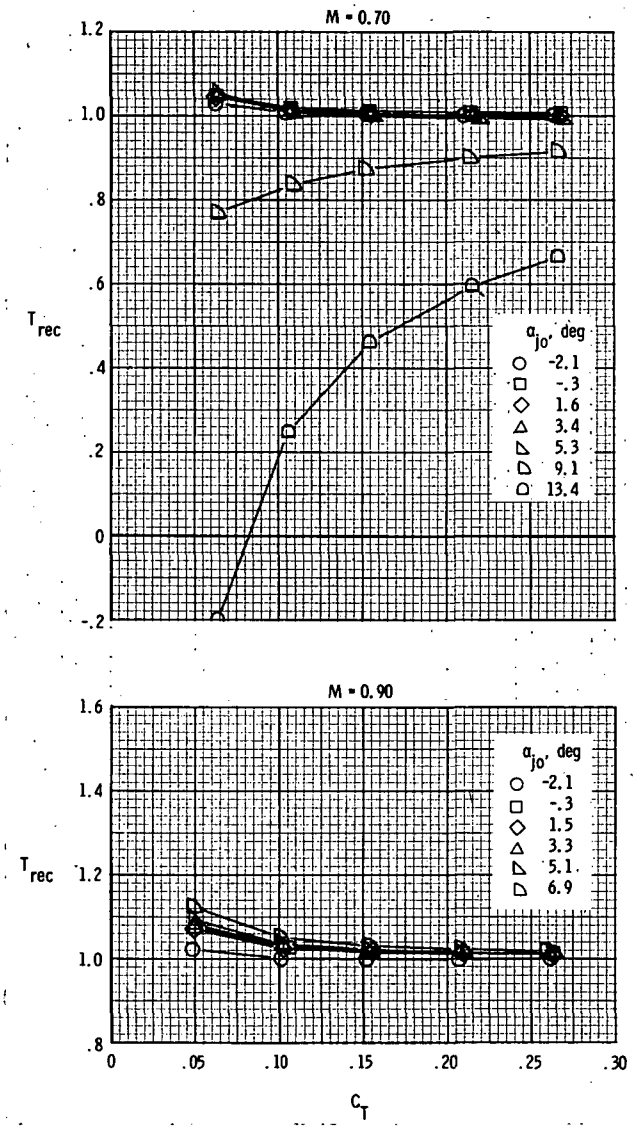

(f) $x_e/c_r = 0.21$; $\delta_d = 15^o$.

Figure 38.- Concluded.

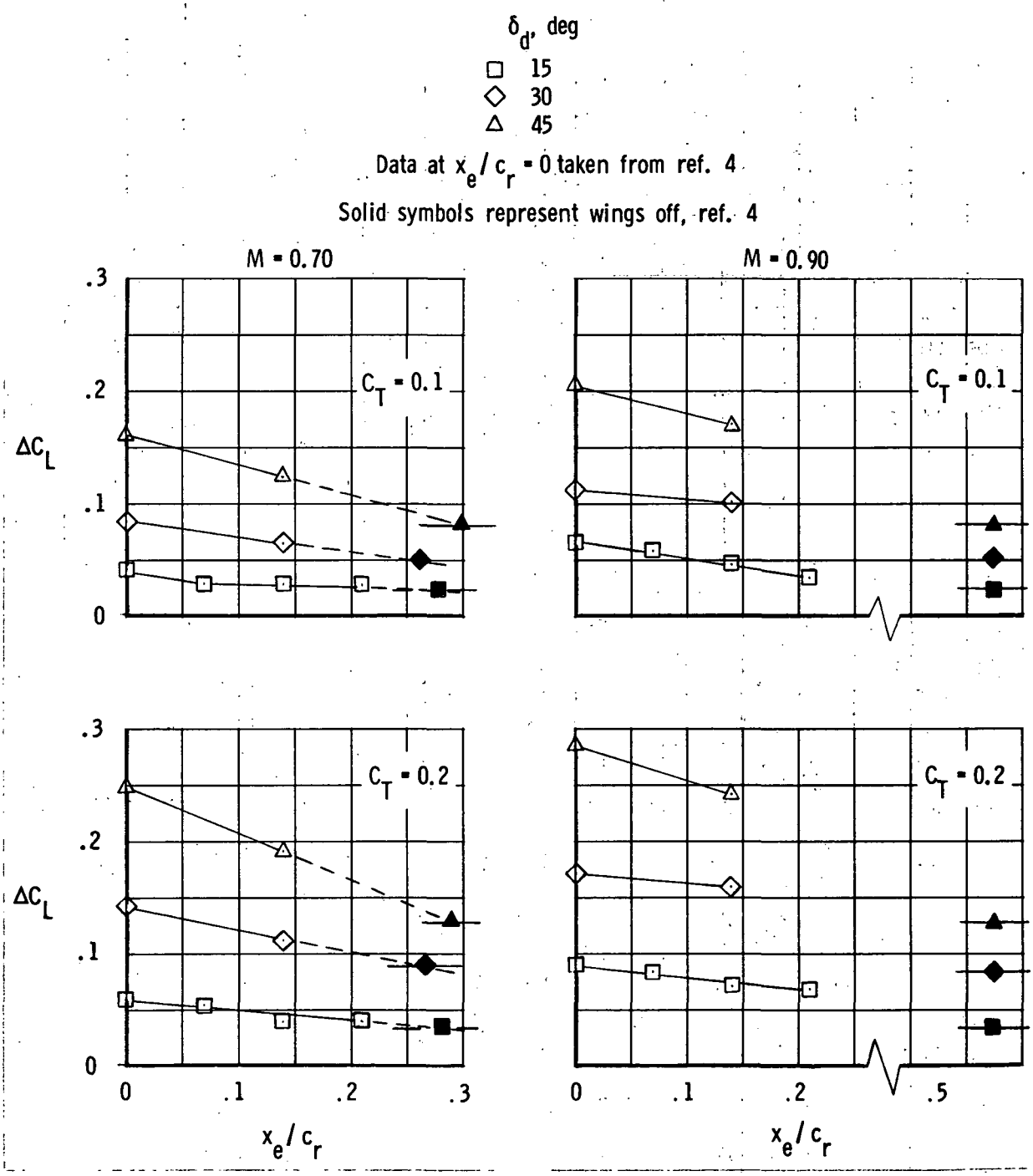

Figure 39.- Summary of incremental lift characteristics for model with rectangular exits for selected Mach numbers and thrust coefficients; $\alpha = 0^{\circ}$.

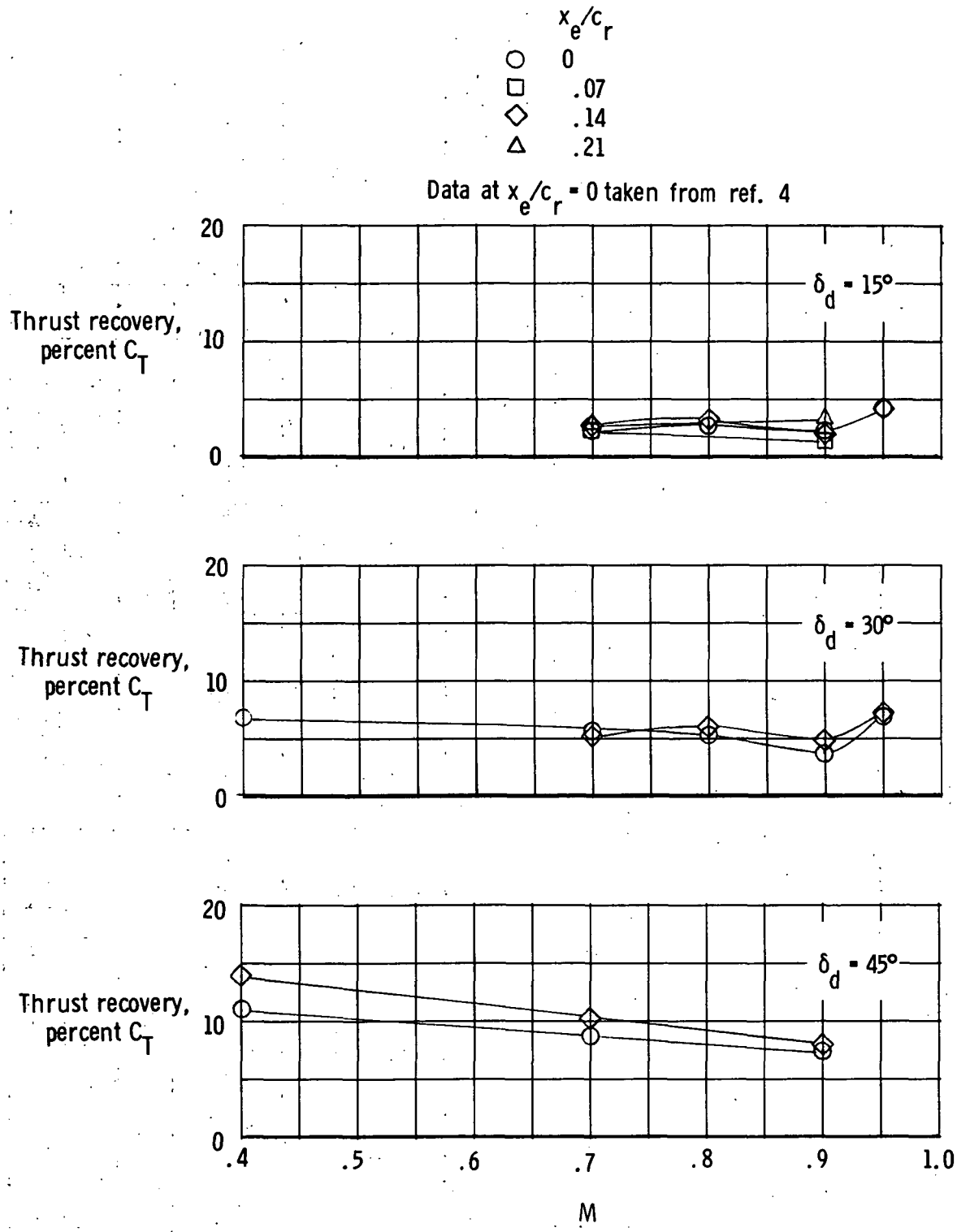

Figure 40.- Summary of thrust recovery characteristics for model with rectangular exits; $C_T = 0.1$; $\alpha = 0^{\circ}$.

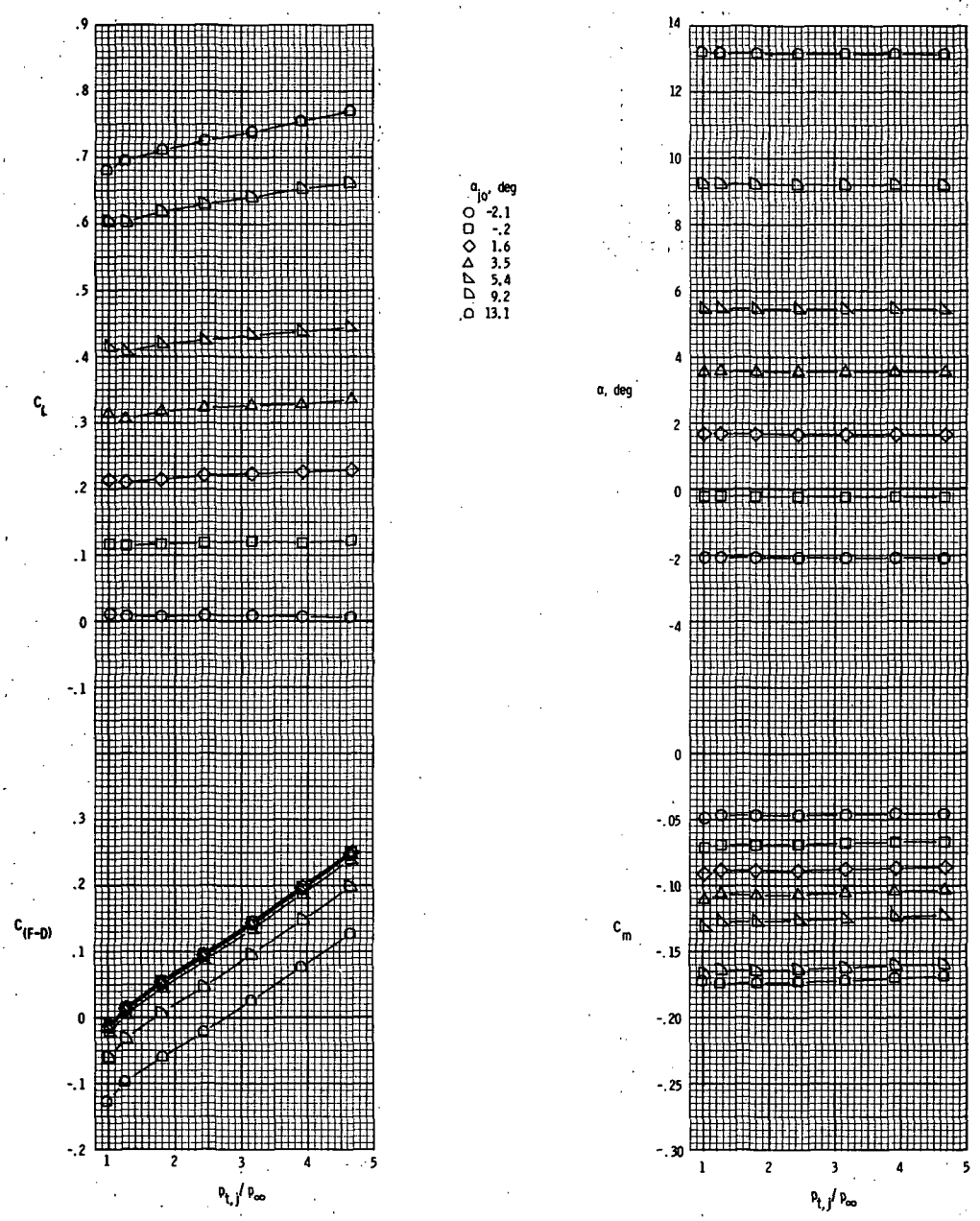

(a) M = 0.70.

Figure 41.- Variation of basic aerodynamic characteristics with nozzle pressure ratio for model with round nozzles; $\delta_d = 0^o$.

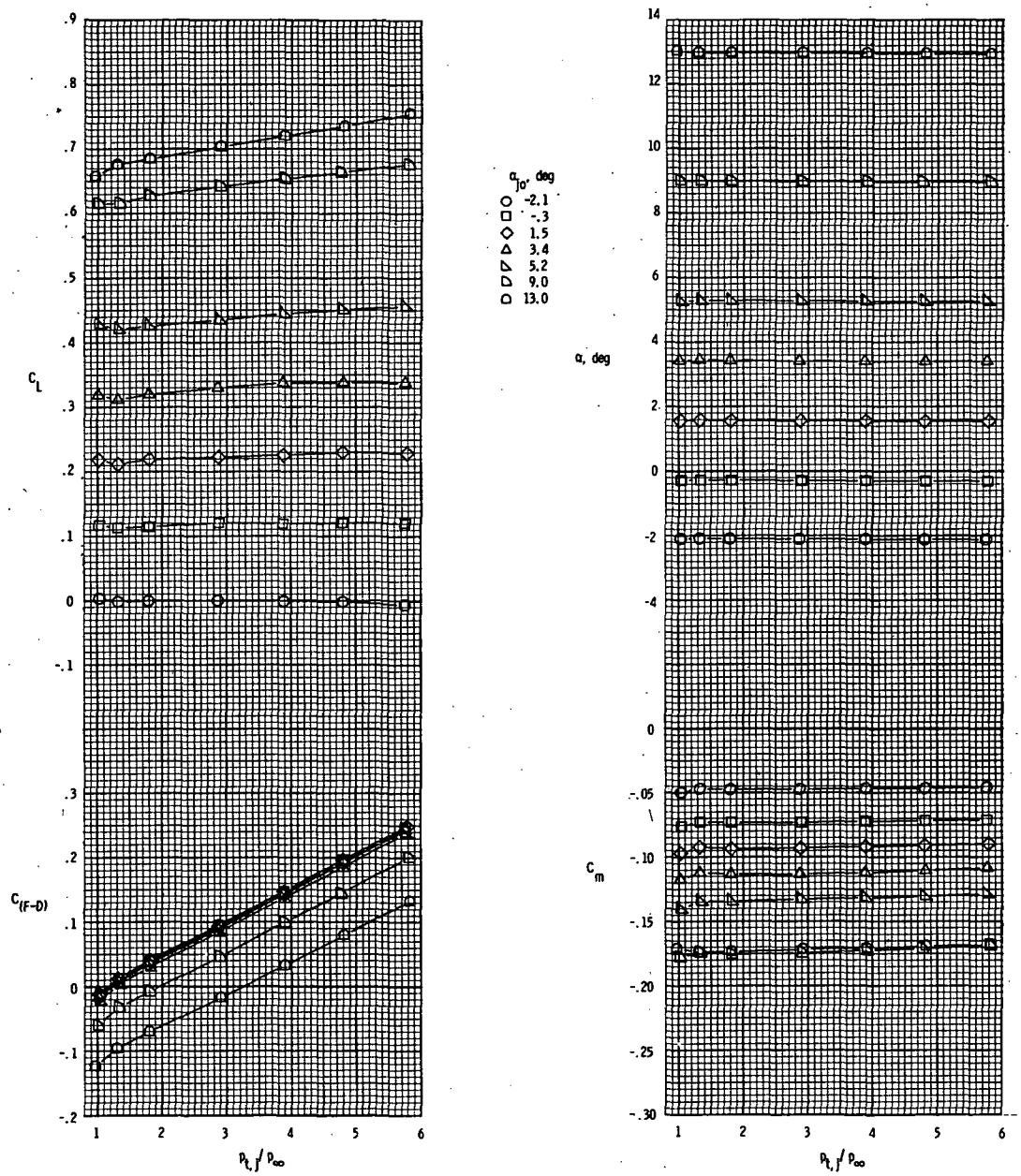

(b) M = 0.80.

Figure 41.- Continued.

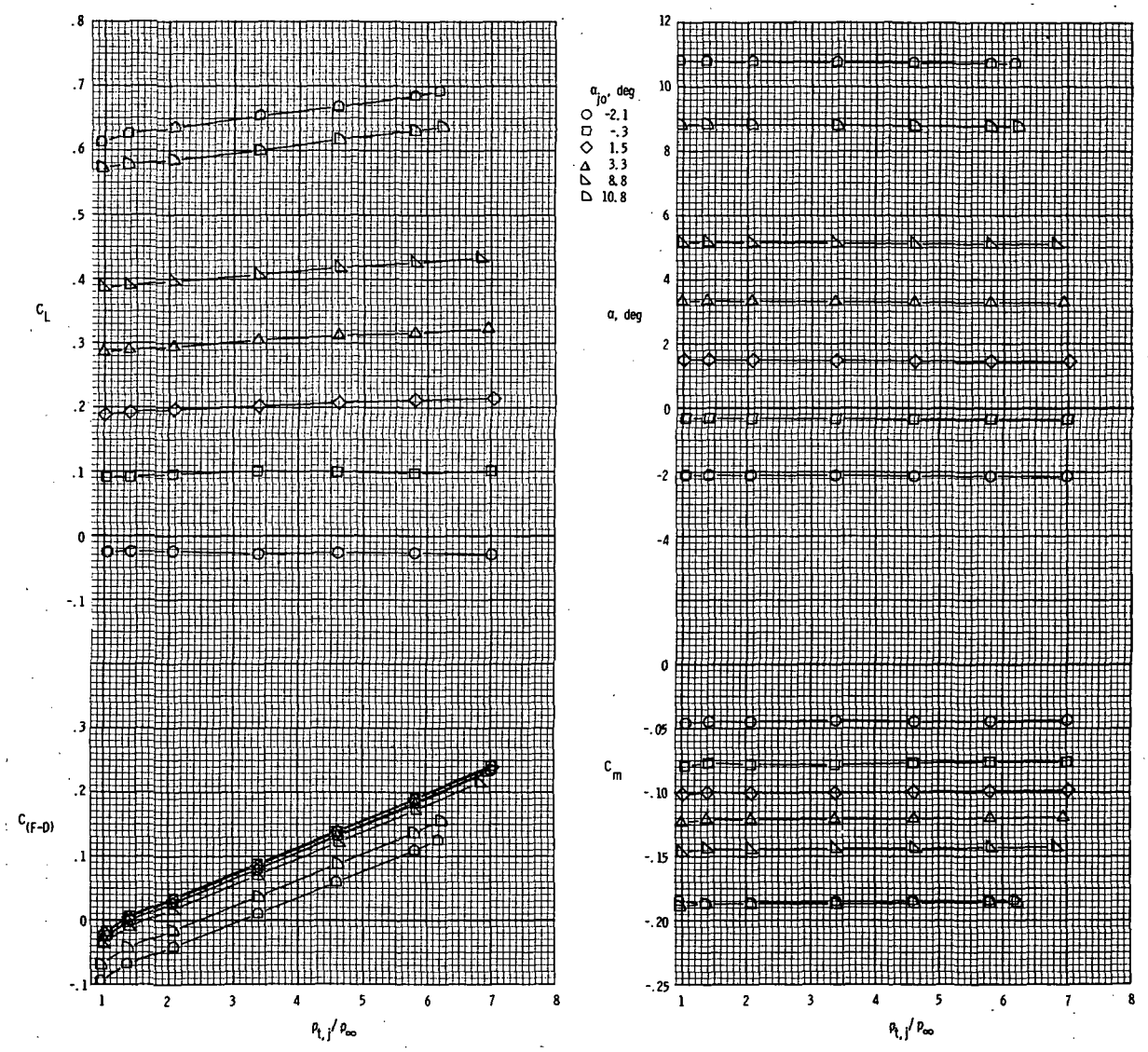

(c) M = 0.90.

Figure 41.- Continued.

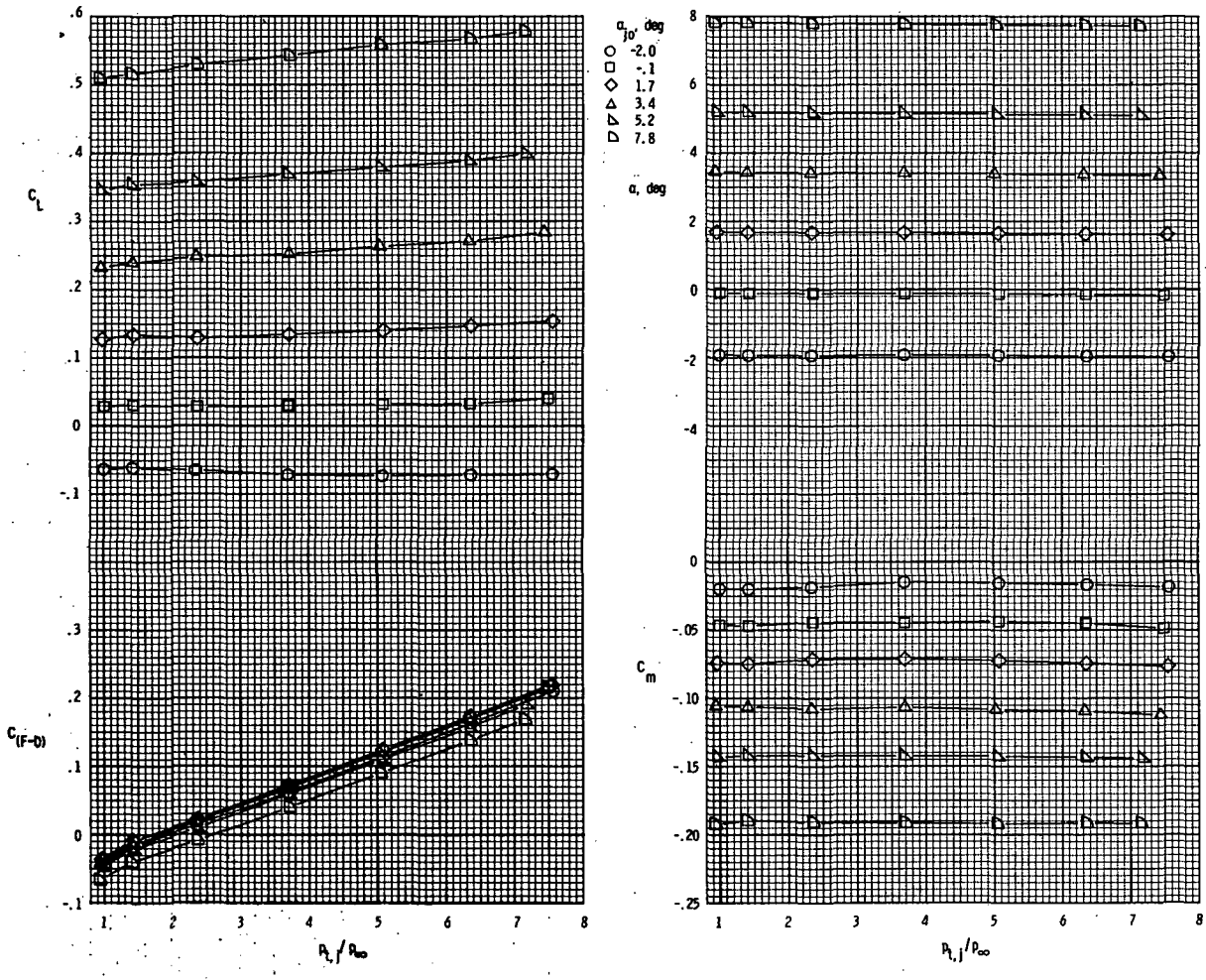

(d) M = 0.95.

Figure 41.- Concluded.

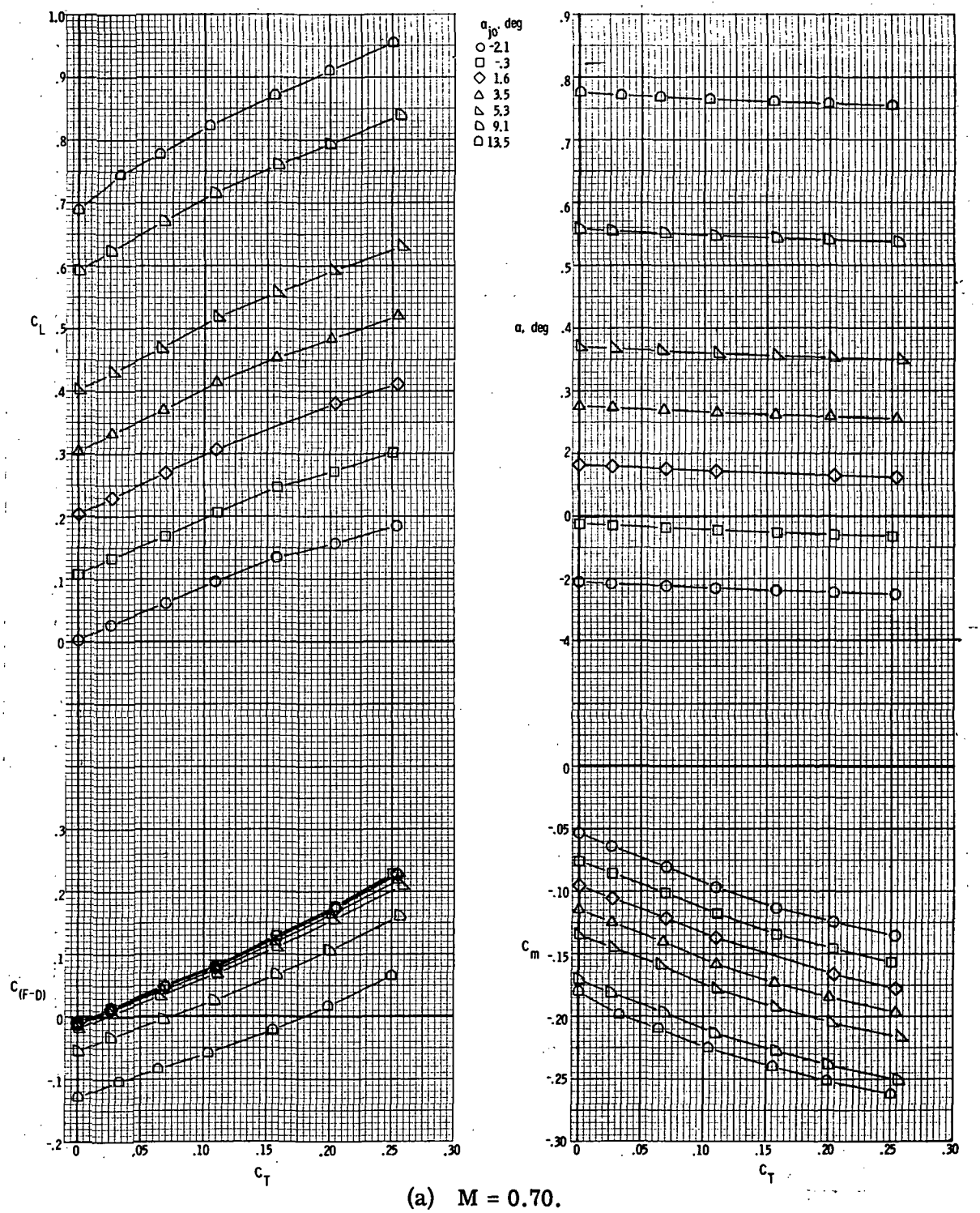

(a) M = 0.70.

Figure 42.- Basic aerodynamic characteristics for model with round nozzles; $\delta_d = 30^o$.

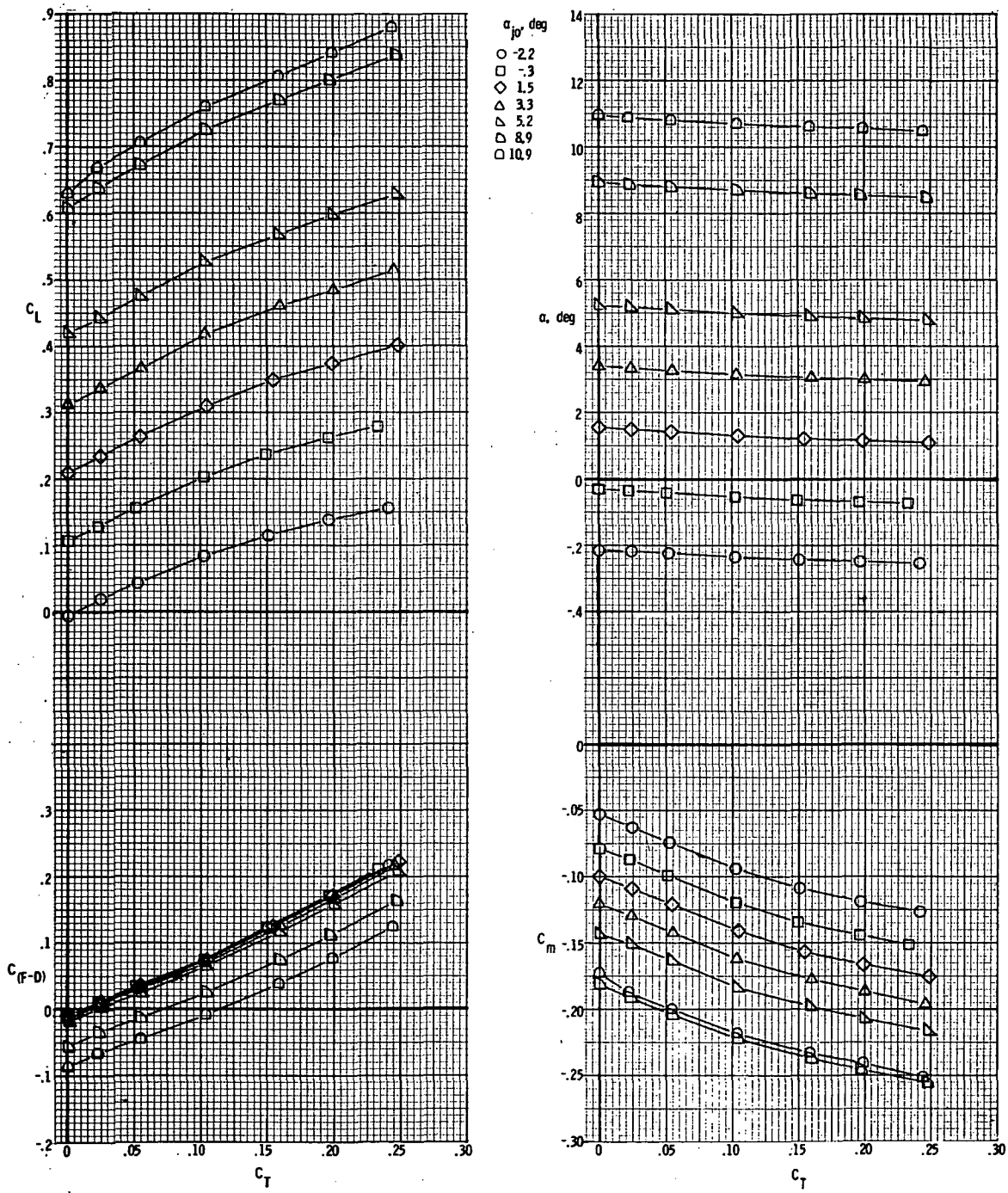

(b) M = 0.80.

Figure 42.- Continued.

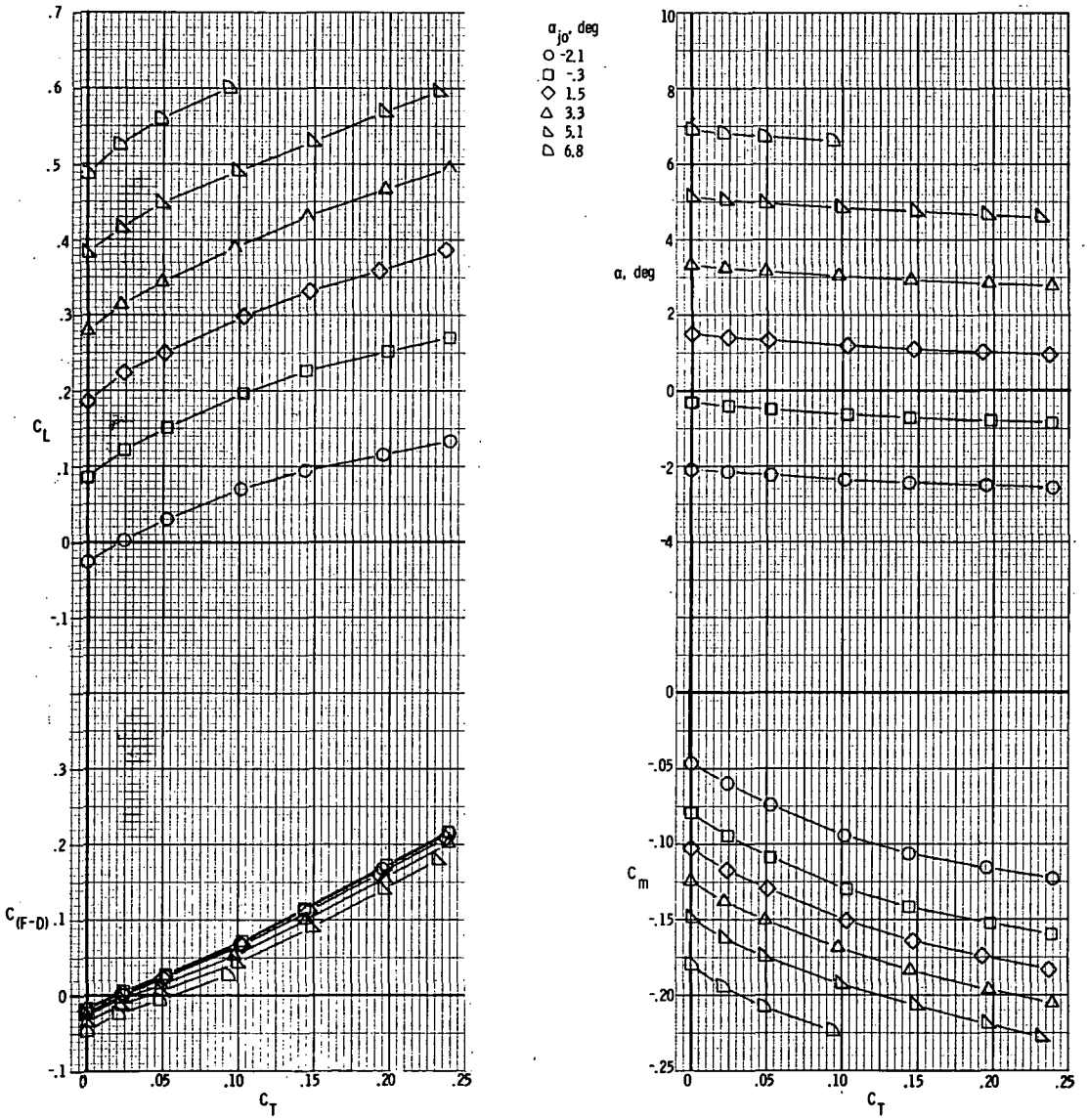

(c) M = 0.90.

Figure 42.- Continued.

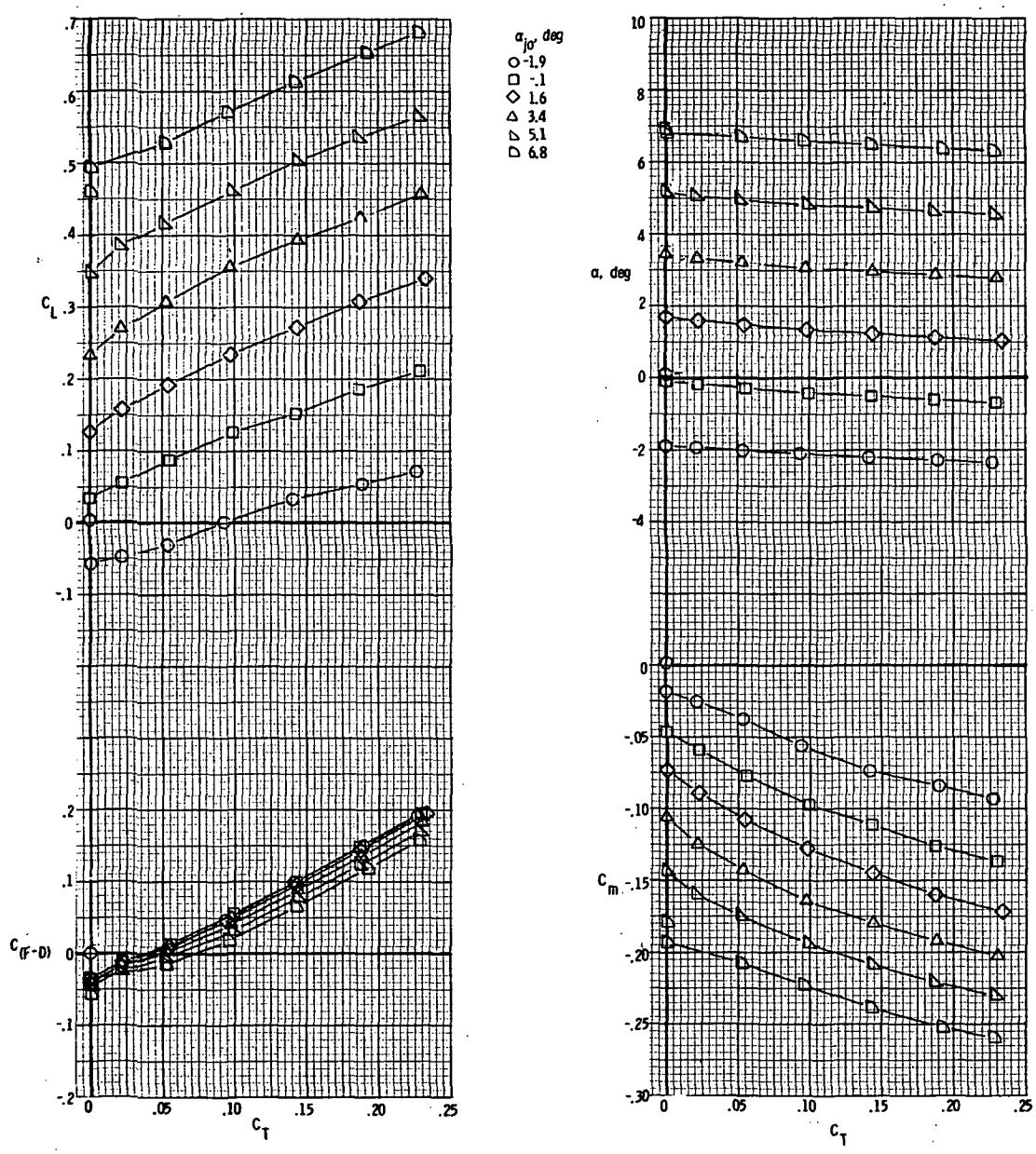

(d) M = 0.95.

Figure 42.- Concluded.

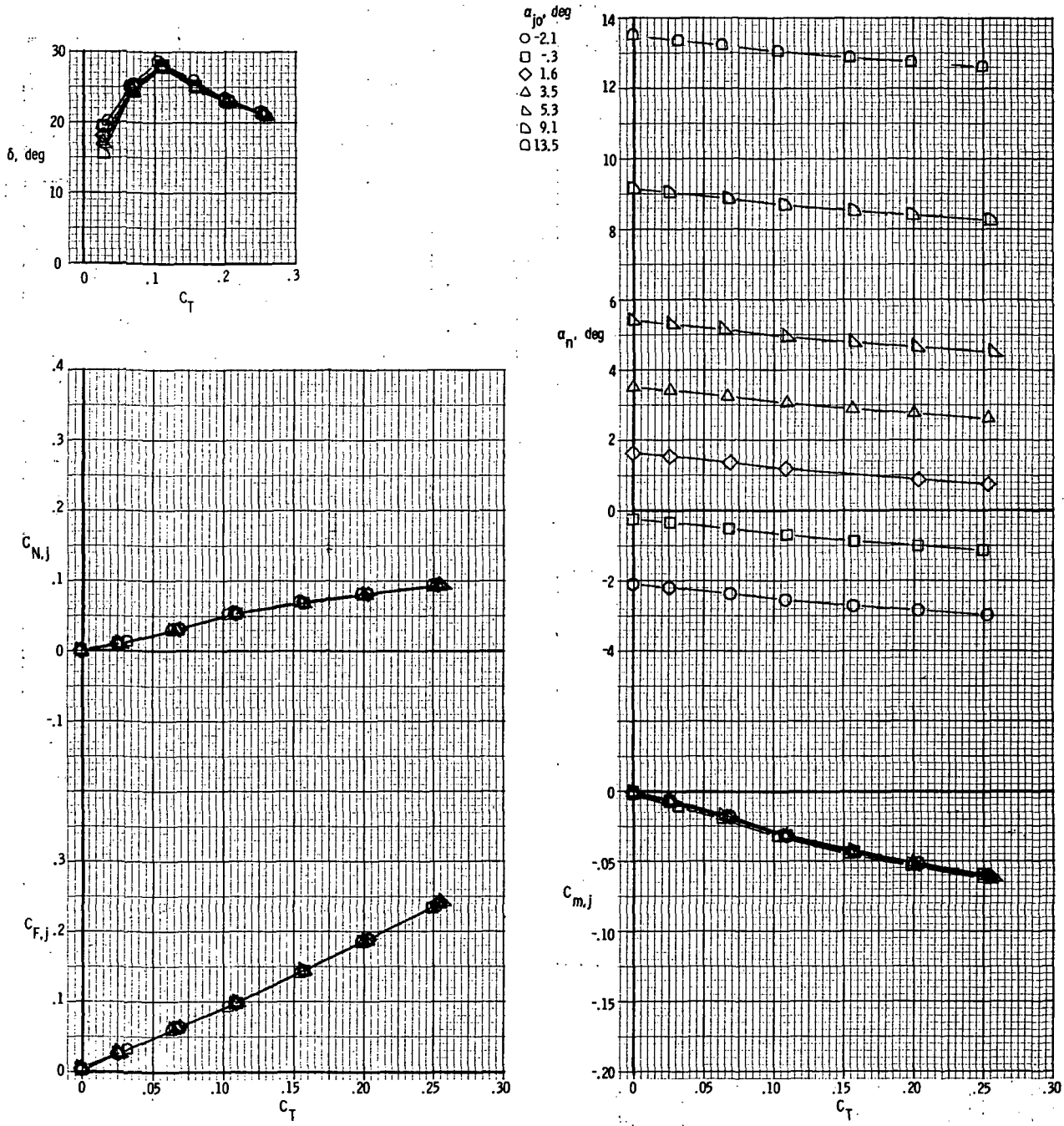

(a) M = 0.70.

Figure 43.- Basic nozzle thrust characteristics for model with round nozzles; $\delta_d = 30^{\circ}$.

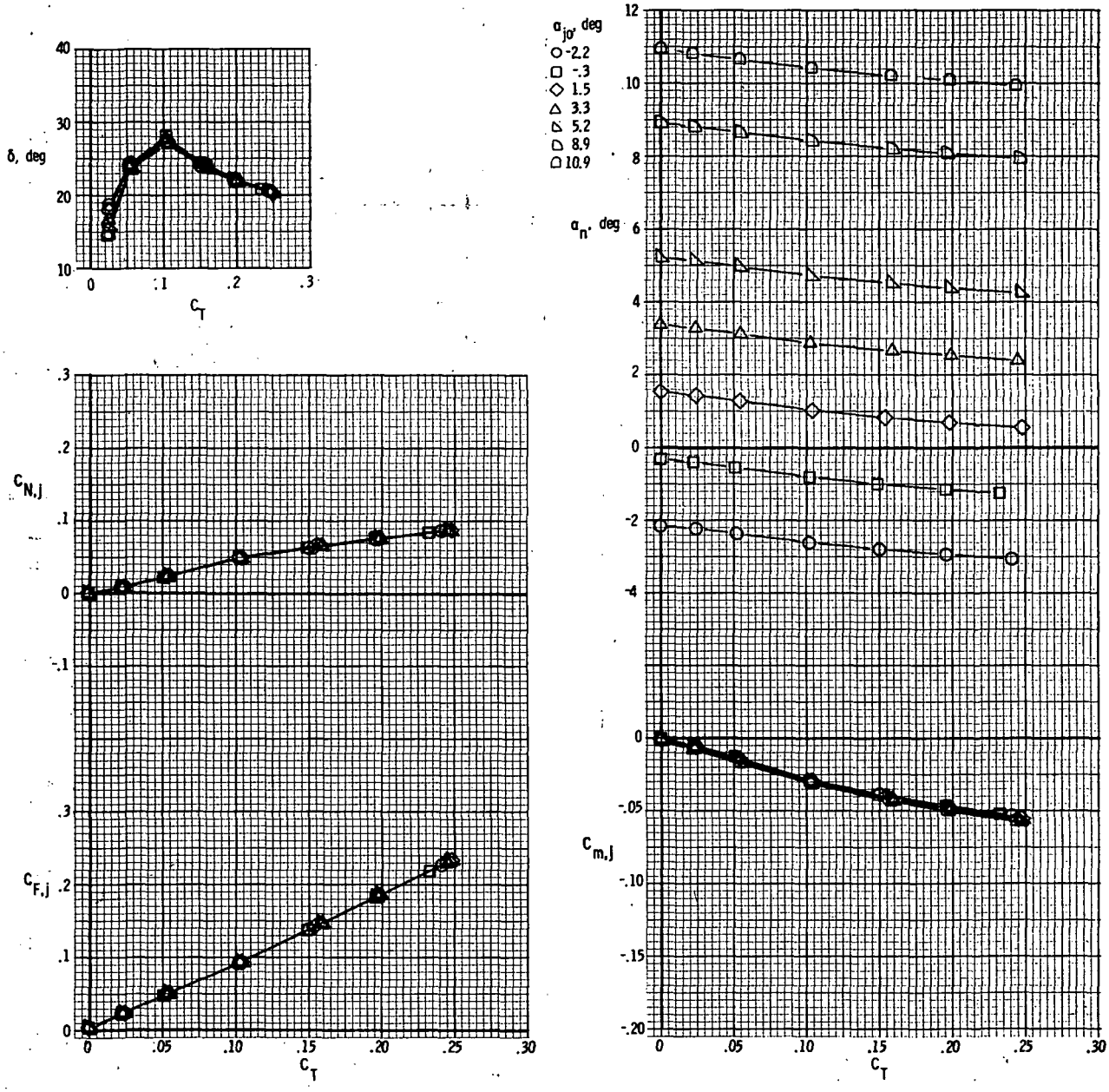

(b) M = 0.80.

Figure 43.- Continued.

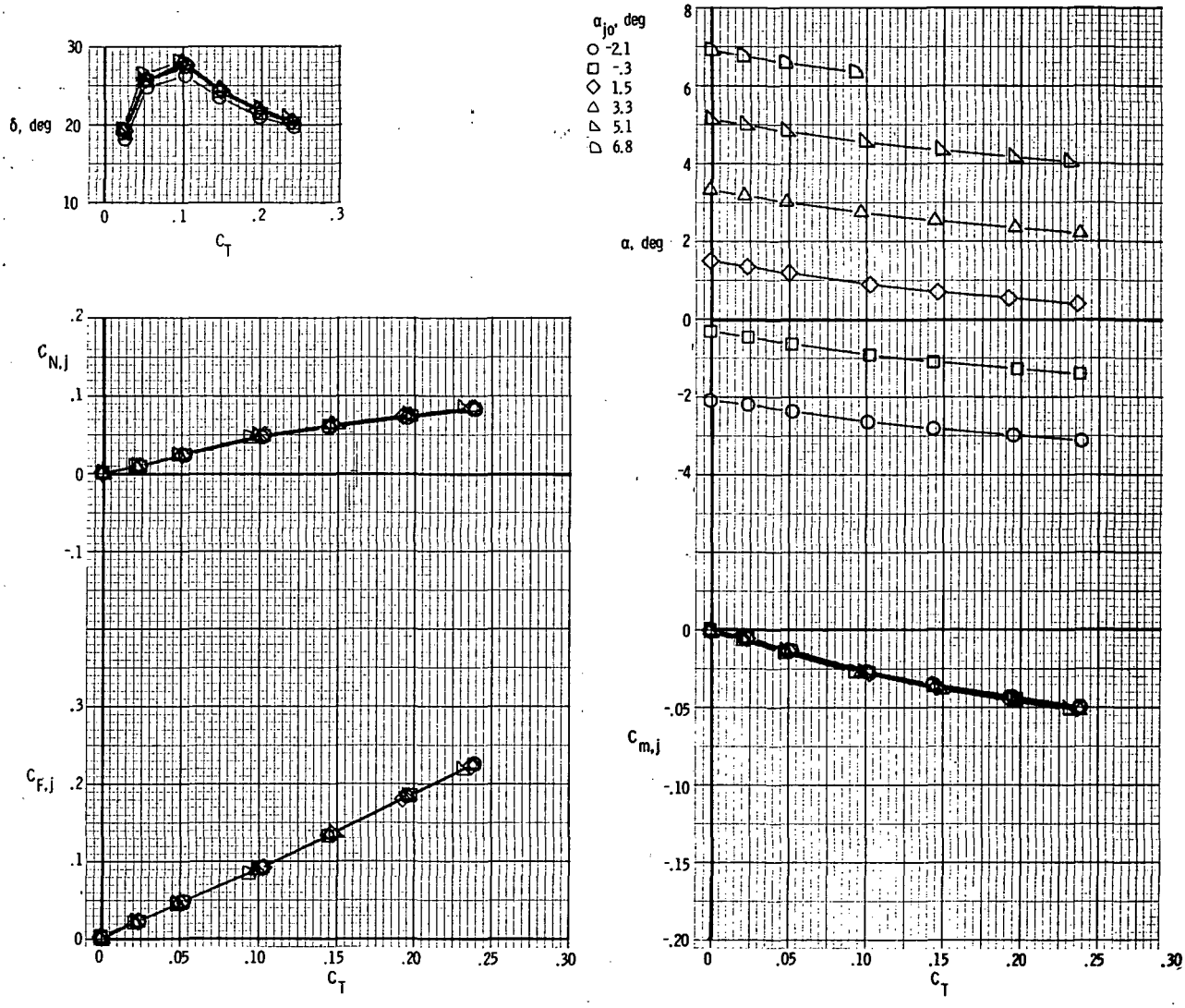

(c) M = 0.90.

Figure 43.- Continued.

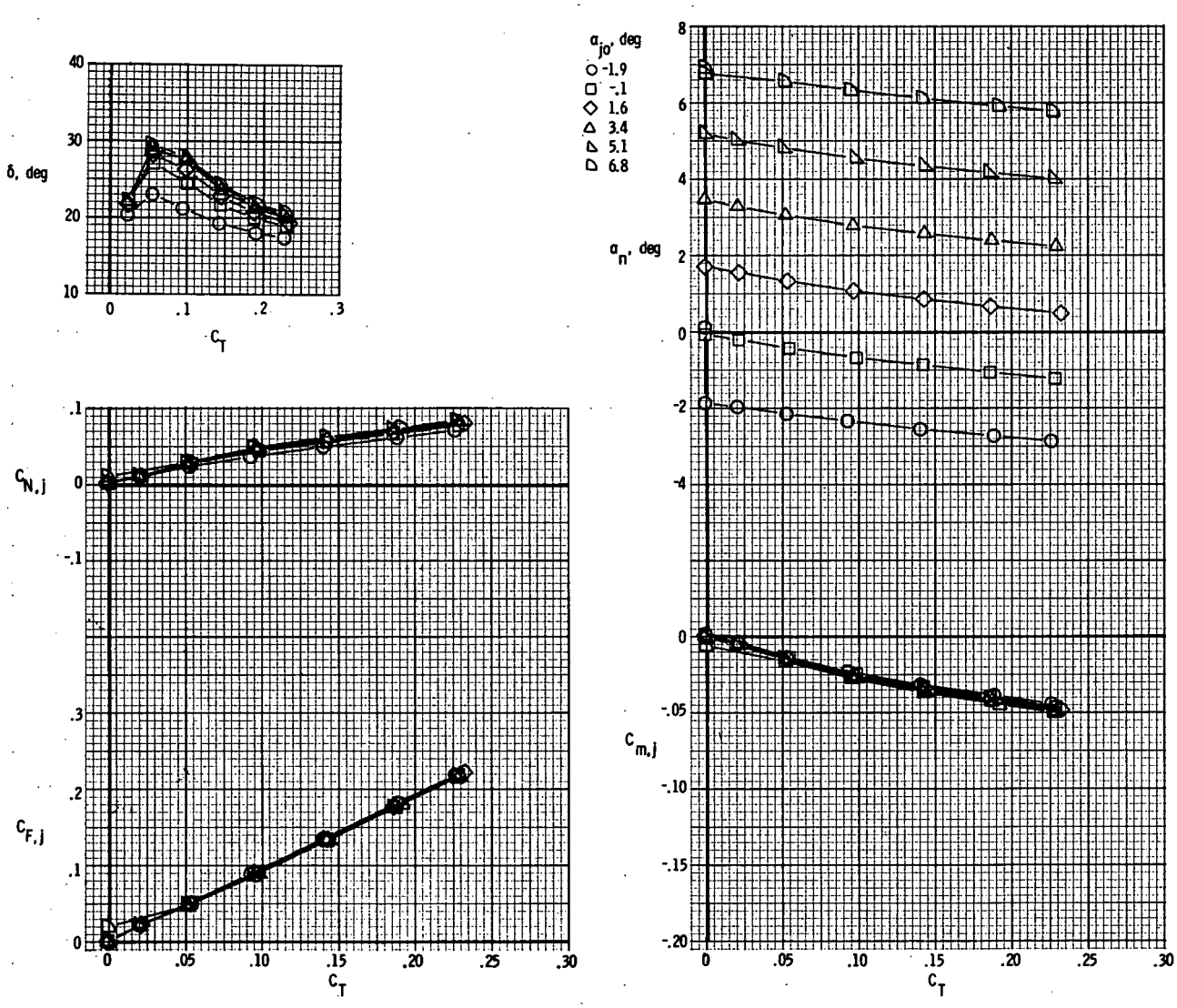

(d) M = 0.95.

Figure 43.- Concluded.

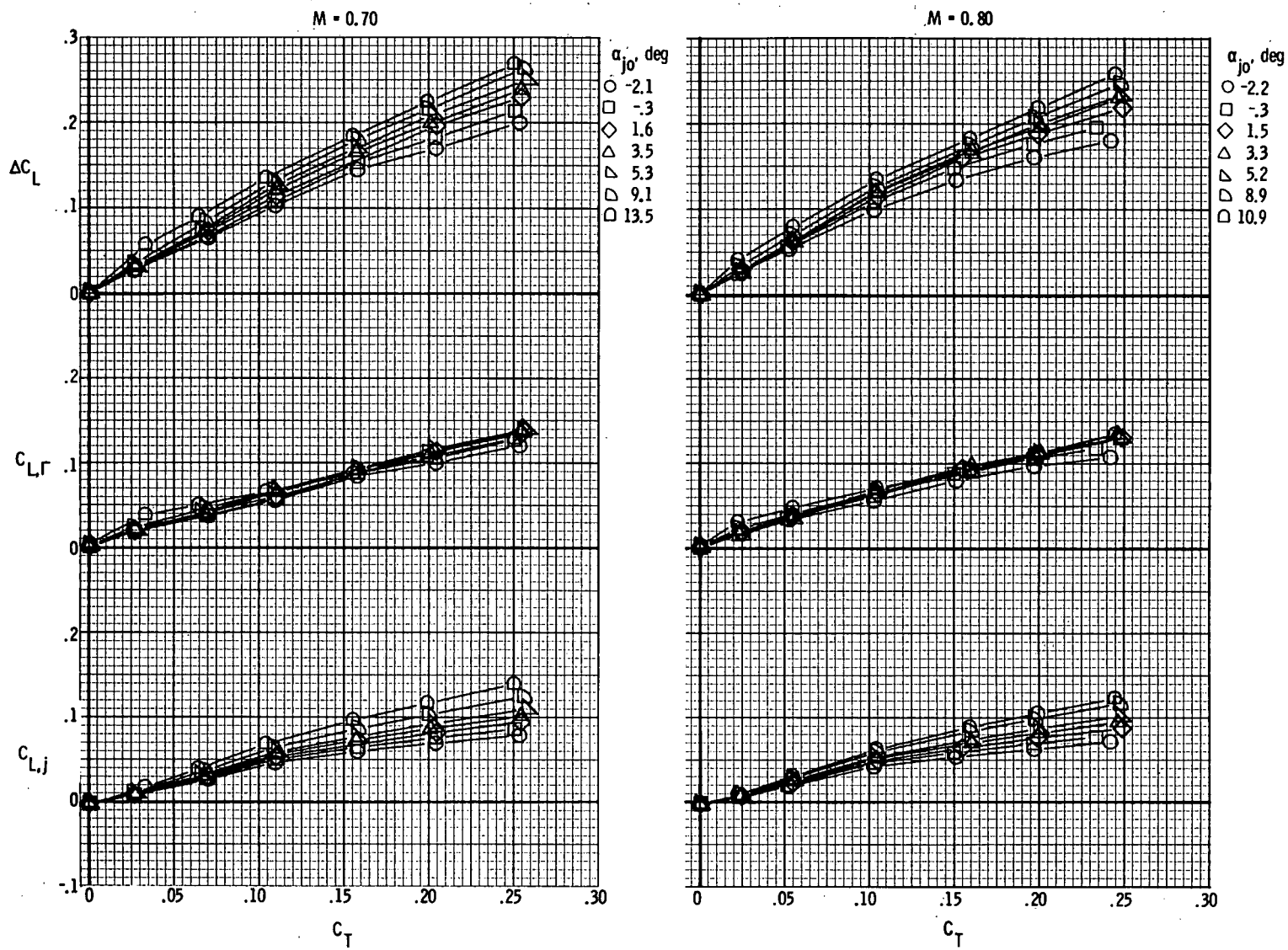

(a) M = 0.70 and 0.80.

Figure 44.- Jet lift, induced lift, and incremental lift for model with round nozzles; $\delta_d = 30^o$.

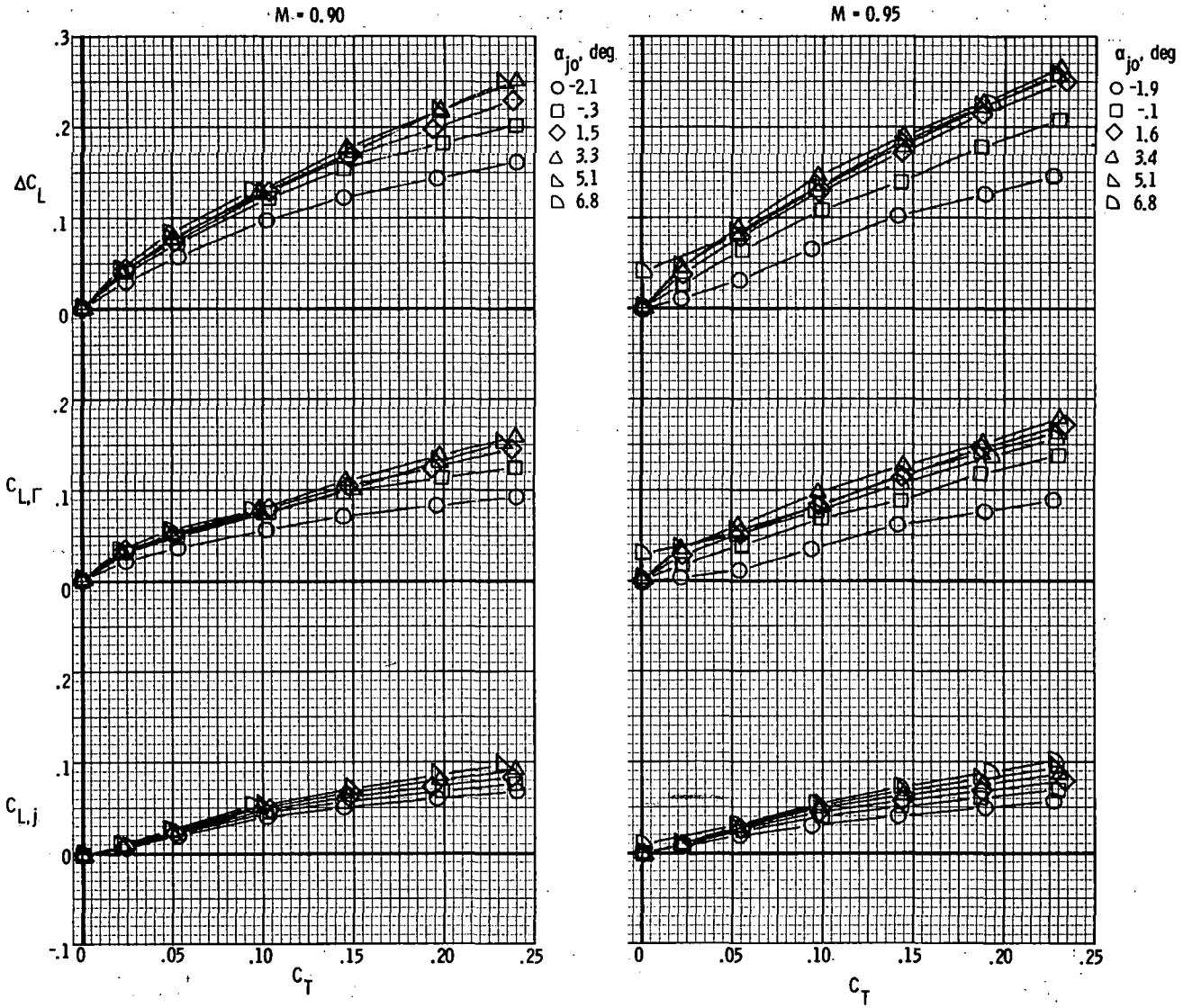

(b) M = 0.90 and 0.95.

Figure 44.- Concluded.

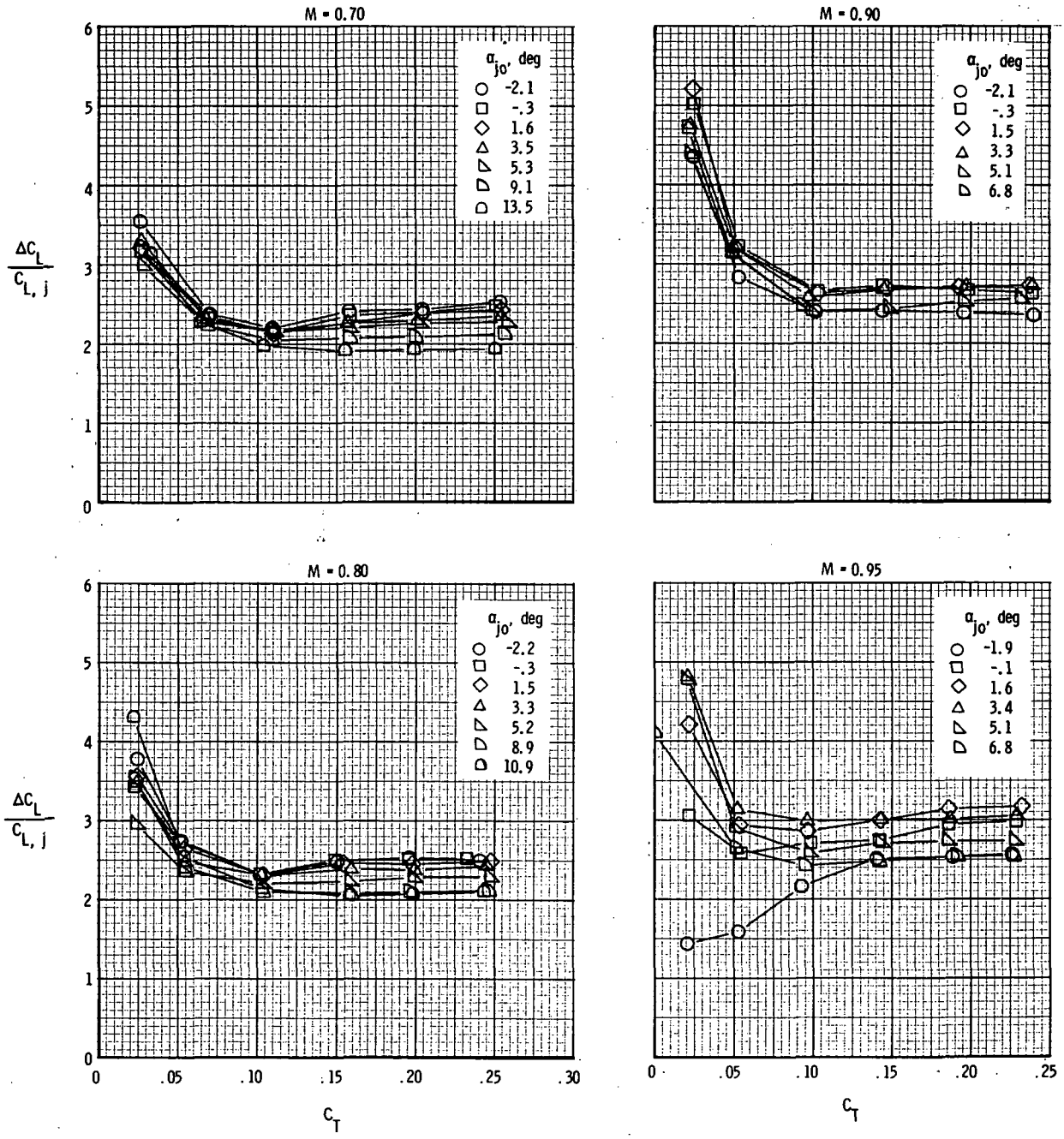

Figure 45.- Variation of lift augmentation factor with thrust coefficient for model with round exits; $\delta_d = 30^o$.

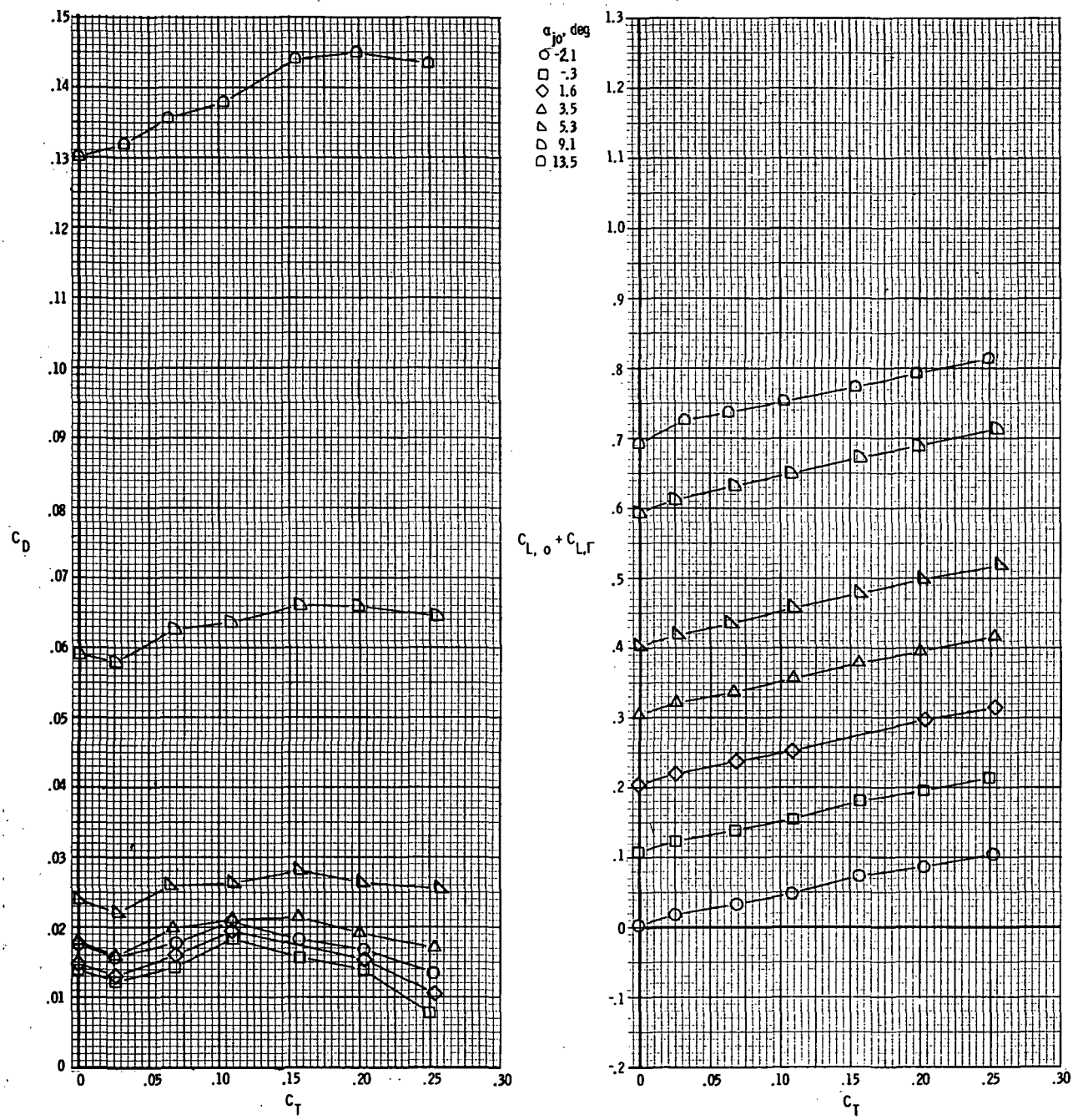

(a) M = 0.70.

Figure 46.- Drag and lift characteristics for model with round nozzle; $\delta_d = 30^{\circ}$.

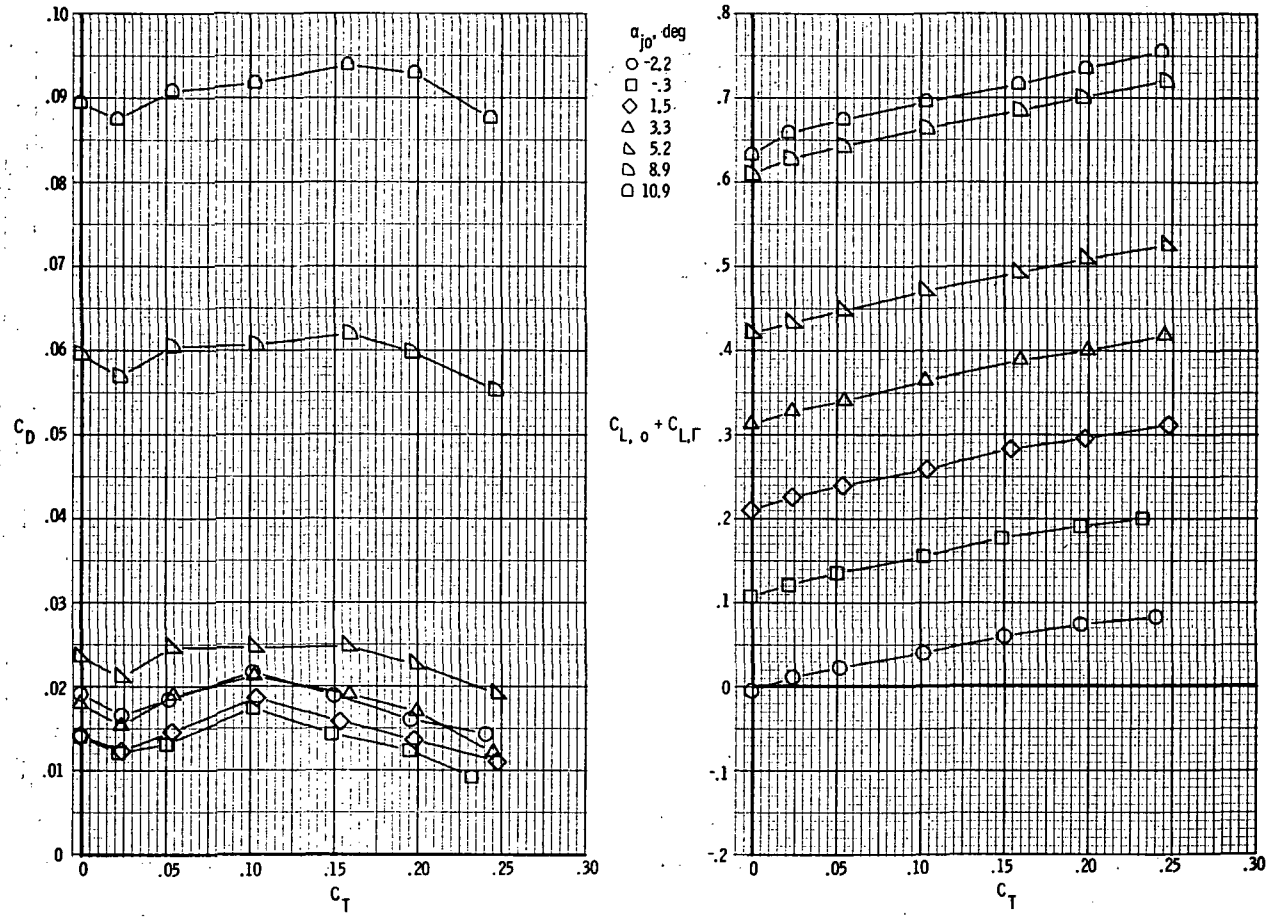

(b) M = 0.80.

Figure 46.- Continued.

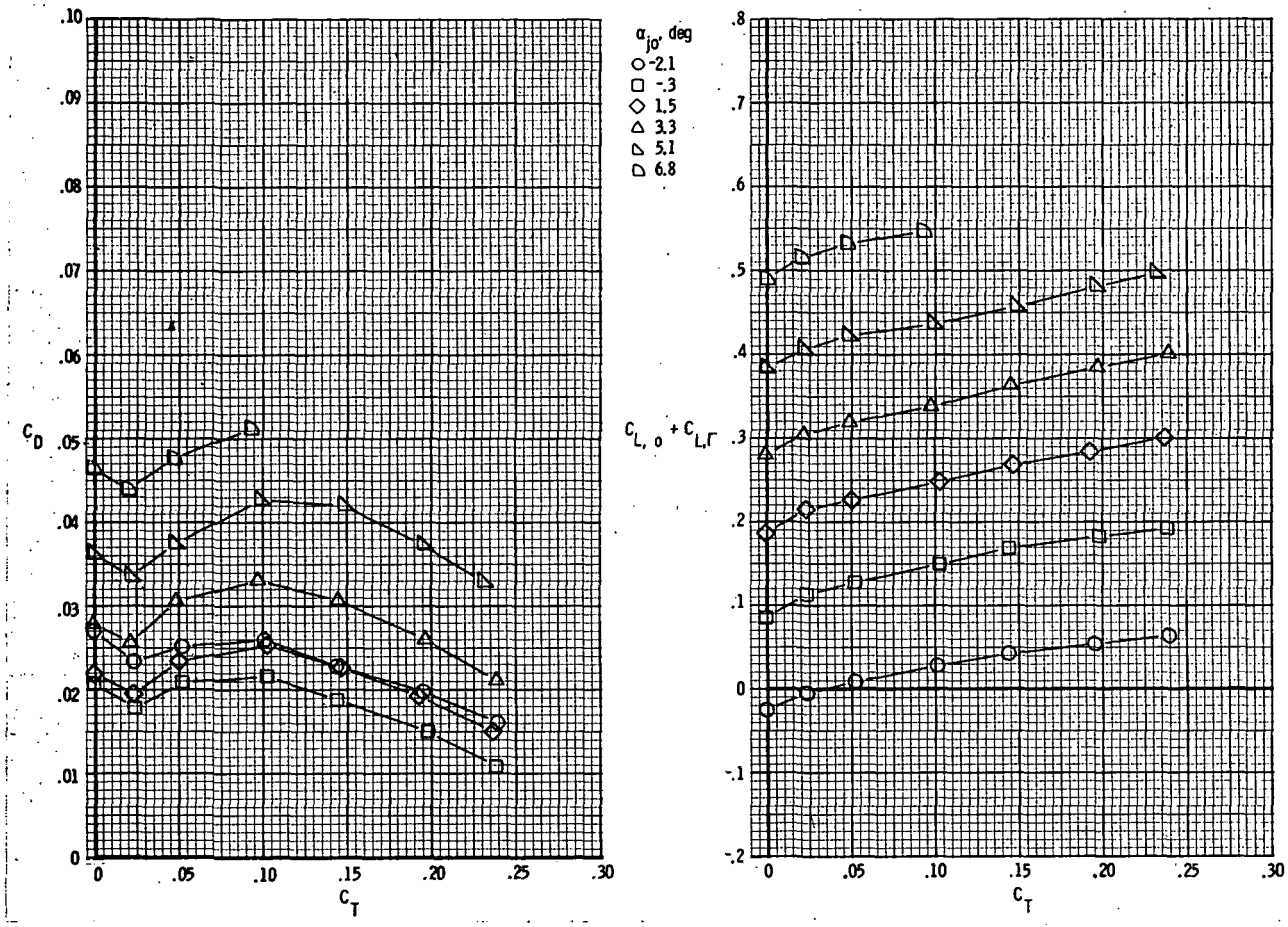

(c) M = 0.90.

Figure 46.- Continued.

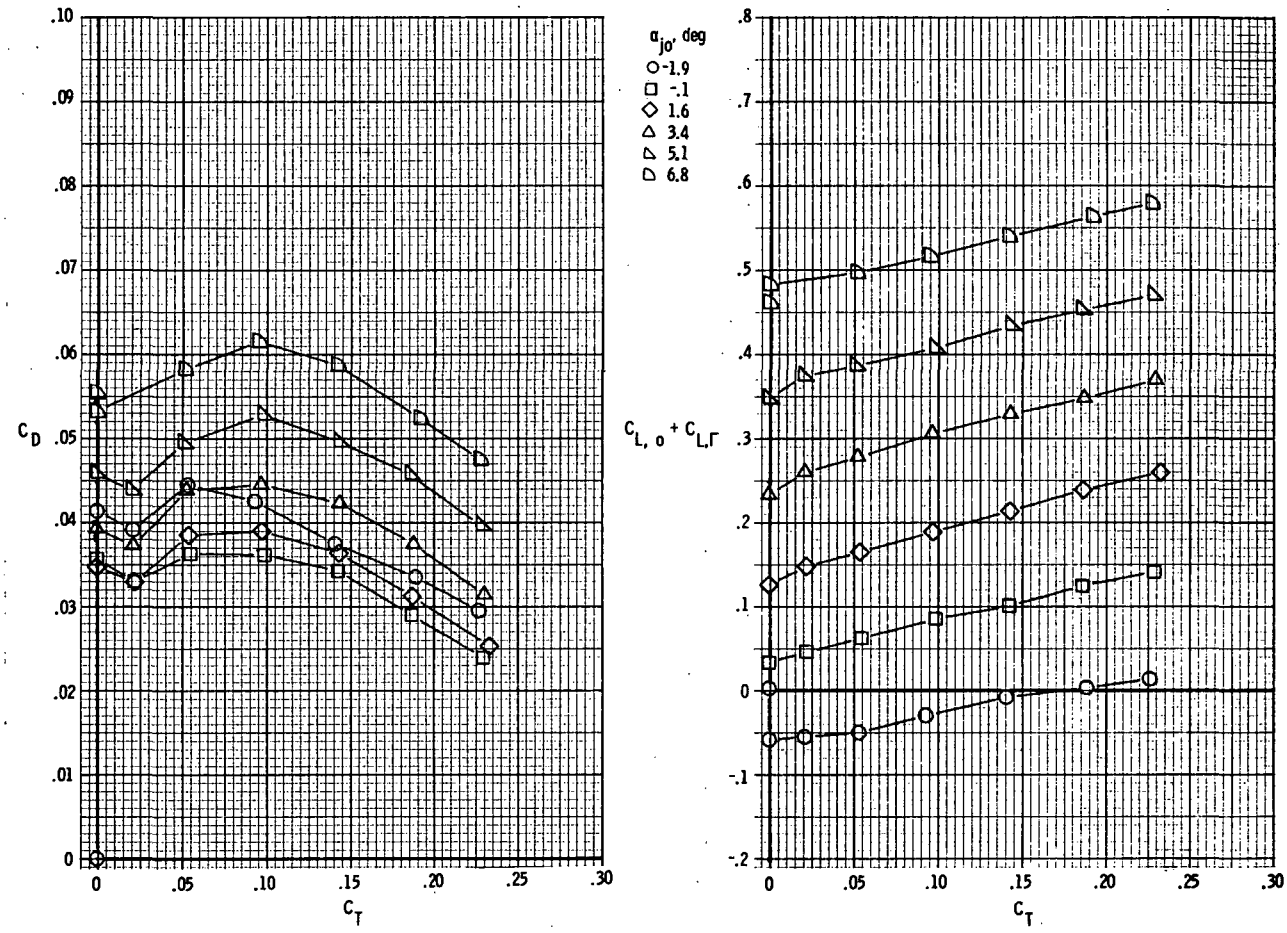

(d) M = 0.95.

Figure 46.- Concluded.

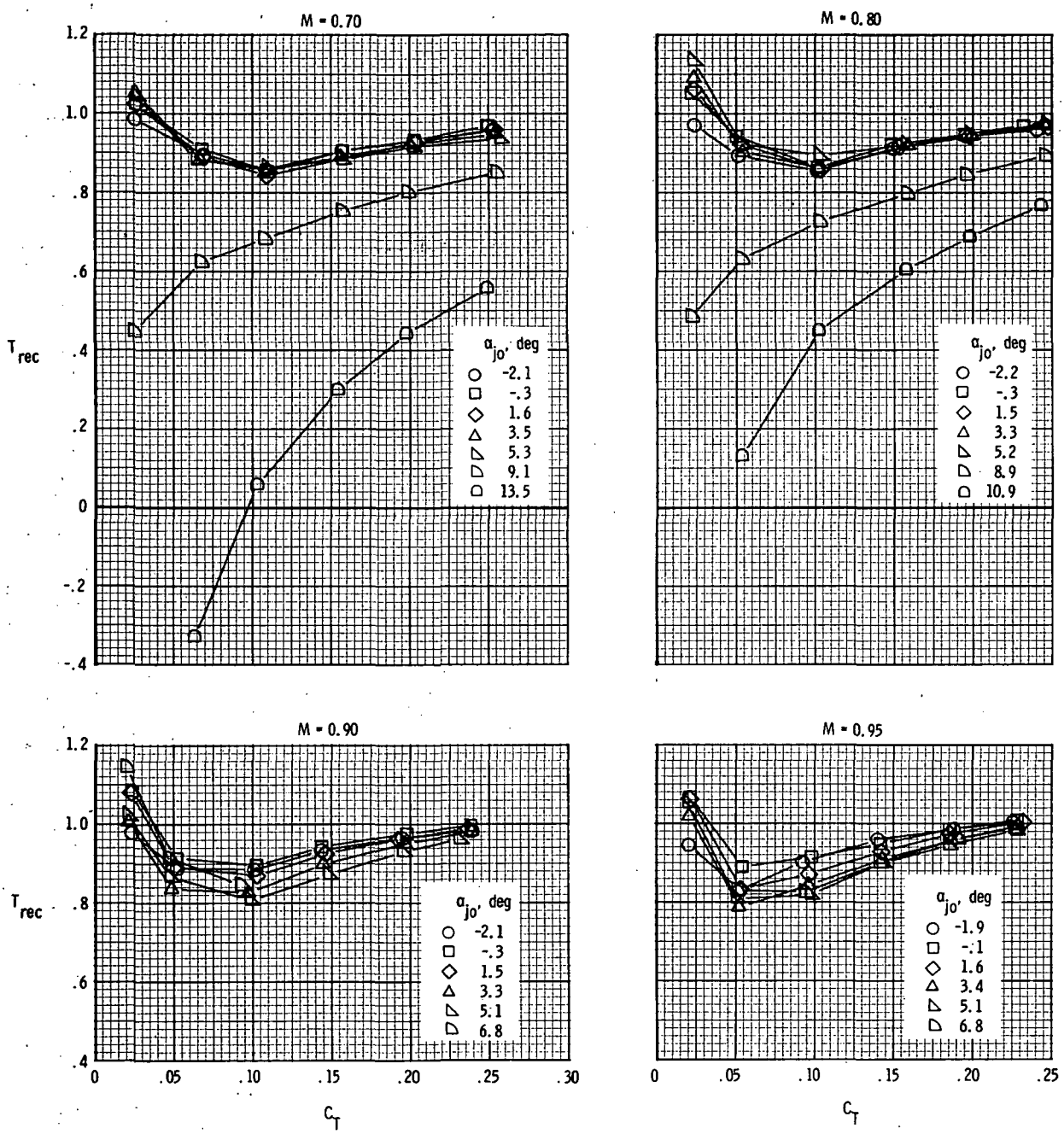

Figure 47.- Variation of thrust recovery with thrust coefficient for model with round exits; $\delta_d = 30^o$.

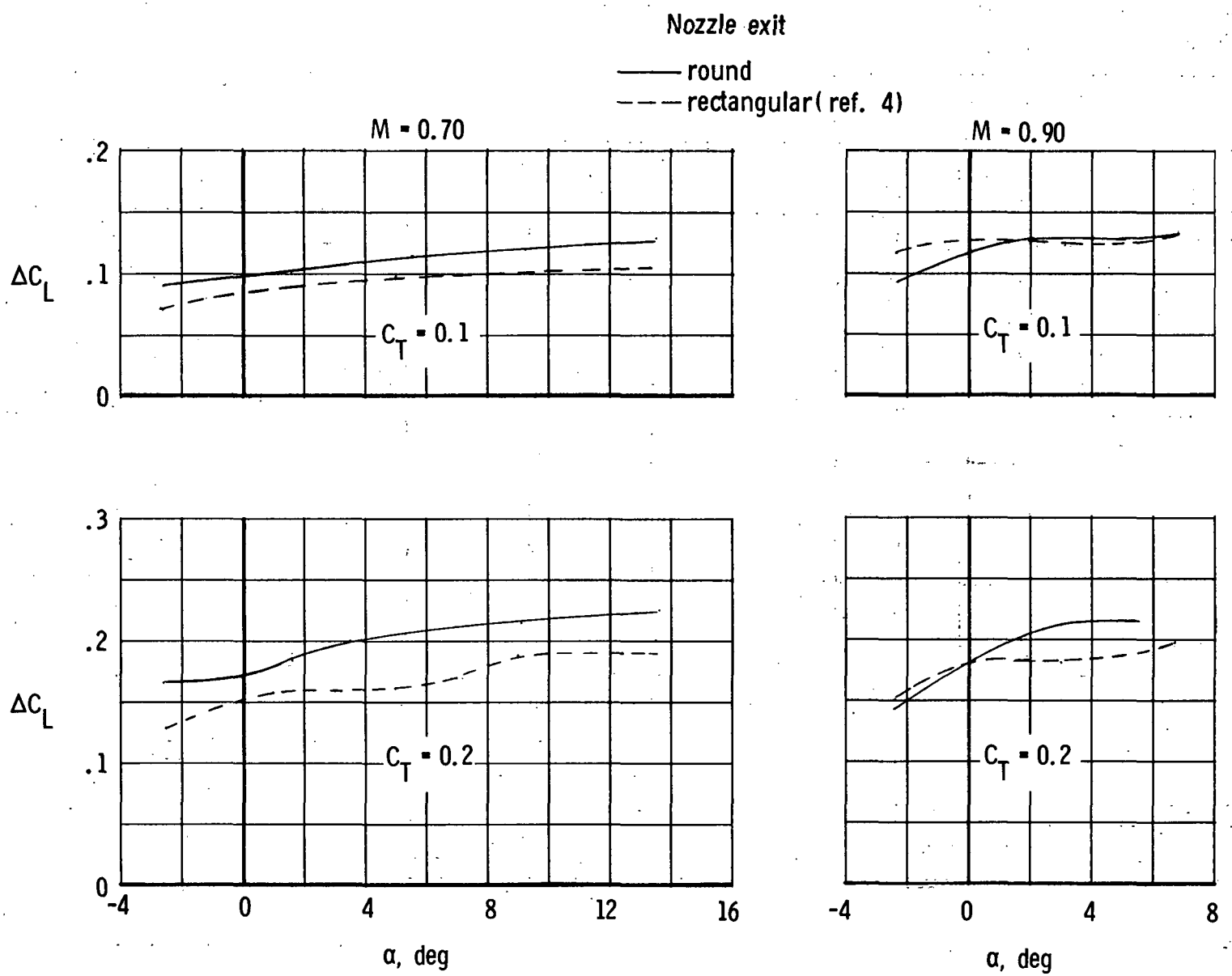

Figure 48.- Comparison of incremental lift characteristics for round and rectangular exits.

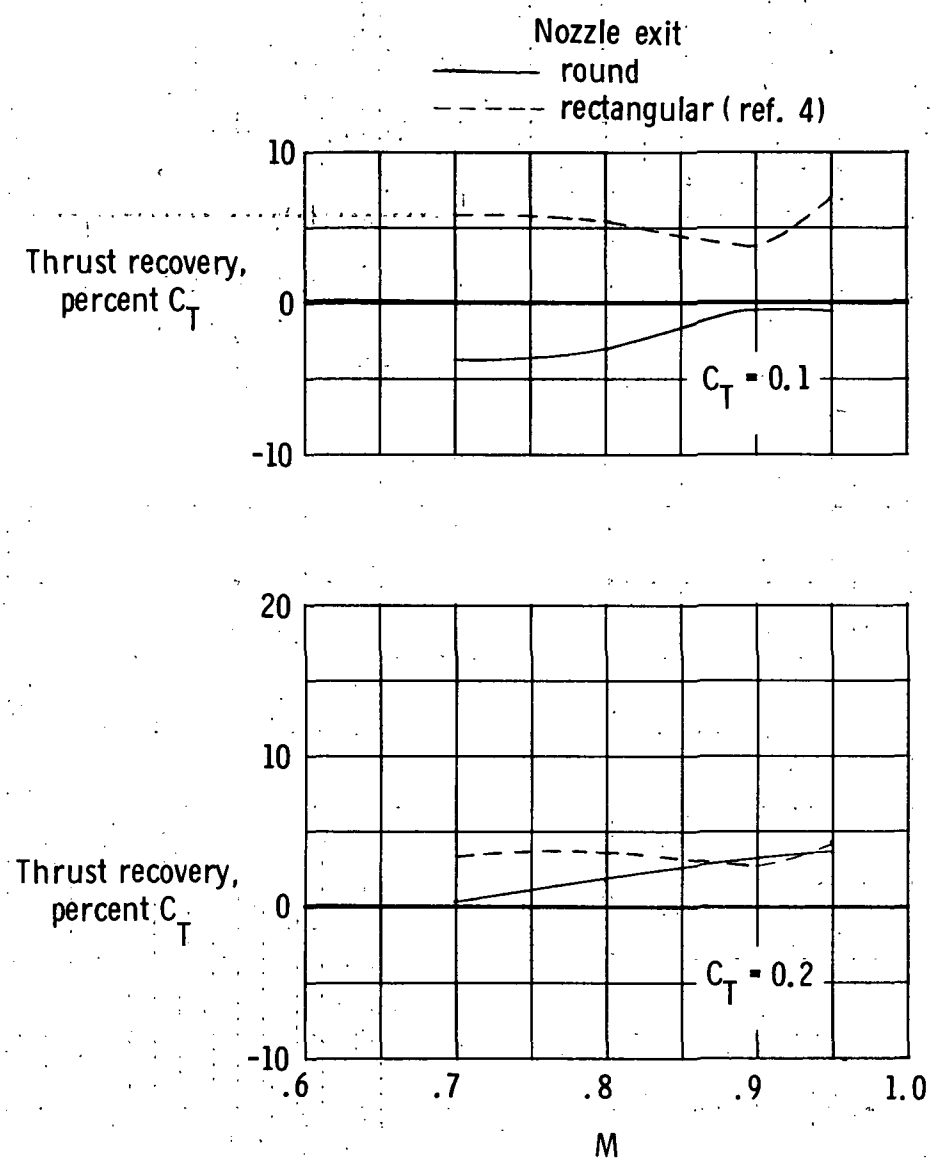

Figure 49.- Comparison of thrust recovery characteristics for round and rectangular exits; $\delta_d = 30^o$; $\alpha \approx 0^o$.

*U.S. GOVERNMENT PRINTING OFFICE: 1976 - 635-275/57

NATIONAL AERONAUTICS AND SPACE ADMINISTRATION
WASHINGTON, D.C. 20546

OFFICIAL BUSINESS
PENALTY FOR PRIVATE USE $300

SPECIAL FOURTH-CLASS RATE
BOOK

POSTAGE AND FEES PAID
NATIONAL AERONAUTICS AND
SPACE ADMINISTRATION
451

U.S.MAIL

POSTMASTER: If Undeliverable (Section 158 Postal Manual) Do Not Return

"The aeronautical and space activities of the United States shall be conducted so as to contribute . . . to the expansion of human knowledge of phenomena in the atmosphere and space. The Administration shall provide for the widest practicable and appropriate dissemination of information concerning its activities and the results thereof."

—NATIONAL AERONAUTICS AND SPACE ACT OF 1958

NASA SCIENTIFIC AND TECHNICAL PUBLICATIONS

TECHNICAL REPORTS: Scientific and technical information considered important, complete, and a lasting contribution to existing knowledge.

TECHNICAL NOTES: Information less broad in scope but nevertheless of importance as a contribution to existing knowledge.

TECHNICAL MEMORANDUMS: Information receiving limited distribution because of preliminary data, security classification, or other reasons. Also includes conference proceedings with either limited or unlimited distribution.

CONTRACTOR REPORTS: Scientific and technical information generated under a NASA contract or grant and considered an important contribution to existing knowledge.

TECHNICAL TRANSLATIONS: Information published in a foreign language considered to merit NASA distribution in English.

SPECIAL PUBLICATIONS: Information derived from or of value to NASA activities. Publications include final reports of major projects, monographs, data compilations, handbooks, sourcebooks, and special bibliographies.

TECHNOLOGY UTILIZATION PUBLICATIONS: Information on technology used by NASA that may be of particular interest in commercial and other non-aerospace applications. Publications include Tech Briefs, Technology Utilization Reports and Technology Surveys.

Details on the availability of these publications may be obtained from:

SCIENTIFIC AND TECHNICAL INFORMATION OFFICE

NATIONAL AERONAUTICS AND SPACE ADMINISTRATION

Washington, D.C. 20546